Fall 12-15-2017

Dynamic Modeling and Extreme Tension Analysis of Mooring System for a Floating Offshore Wind Turbine

Wei Ting Hsu
University of Maine, weiting.hsu@maine.edu

DYNAMIC MODELING AND EXTREME TENSION ANALYSIS OF MOORING SYSTEM FOR A FLOATING OFFSHORE WIND TURBINE

By

Wei-Ting Hsu

BSc, National Cheng Kung University, 2006

MASc, National Cheng Kung University, 2008

A DISSERTATION

Submitted in Partial Fulfillment of the

Requirements for the Degree of Doctor of Philosophy

(in Mechanical Engineering)

The Graduate School

The University of Maine

December 2017

Advisory Committee:

Krish P. Thiagarajan, Presidential Chair in Energy and Professor of Mechanical Engineering, Advisor

Lance Manuel, T. U. Taylor Professor of Engineering, Dept. of Civil, Architectural, and Environmental Engineering (CAEE), the University of Texas At Austin (UT-Austin).

Andrew J. Goupee, Libra Assistant Professor of Mechanical Engineering.

Vincent Caccese, Professor of Mechanical Engineering

Melissa E. Landon, Associate Professor of Civil and Environmental Engineering

DYNAMIC MODELING AND EXTREME TENSION ANALYSIS OF MOORING SYSTEM FOR A FLOATING OFFSHORE WIND TURBINE

By Wei-Ting Hsu

Dissertation Advisor: Dr. Krish P. Thiagarajan

An Abstract of the Dissertation Presented
in Partial Fulfillment of the Requirements for the
Degree of Doctor of Philosophy
(in Mechanical Engineering)
December 2017

For the offshore wind industry, exploiting the dynamic behaviors of mooring lines is of increasing importance in floating offshore wind turbine (FOWT) mooring system design. Currently, the design philosophy for structures and moorings is based on principles and practices adopted in offshore oil and gas, including mooring systems that are optimized for applications in deeper waters. However, the design of FOWT mooring systems is facing several challenges, including installation costs, the stability of light-weight minimalistic platforms, and shallow water depths (50 – 300m). The extreme tension in mooring lines of a light displacement platform in shallow water is dominated by snap loads. Hence the extreme tension values of the lines are one of the most important factors to consider for

safe design of permanent FOWT mooring system. Thus, there is also a need for dynamic performance assessment of FOWT mooring systems using numerical modeling while considering the extreme events on the mooring lines. The overall goal of the study is to investigate the extreme dynamic tension of mooring systems of a FOWT and propose a long-term distribution model which could improve the current approach to design tension of a mooring line.

This dissertation advances the current state-of-the-art with respect to mooring line design in the offshore wind industry by considering three interrelated issues. The first is to fundamentally understand the underlying physics of extreme dynamic tension of a mooring system. To reach the goal, the factors that can influence the snap events on vertical hanging cable system are investigated. In this issue, the nonlinearity of bilinear cable stiffness, hydrodynamic drag force as well as the pretension of the cable are considered. Therefore, the present work finds that potential exists for snap type impact to affect the mooring system of the FOWT. Here, the DeepCWind semi-submersible floating wind system proposed by phase II of Offshore Code Comparison Collaboration Continuation (OC4) project, is selected for this study. There is a reasonably strong correlation between the tension spikes and wave motion, as well as the vertical motion of the fairlead. Third, to estimate the extreme mooring line tension due to snap loads, a composite Weibull distribution (CWD) is proposed. The model is composed of two Weibull distributions with different characteristics on either side of a transition tension value, and whose parameters is estimated from test data. The proposed distribution model has a good fit to the measured tension data, particular in the extreme range.

Moreover, the research addresses the simulation of long, time-dependent mooring tension sequences by coupled AQWA-OrcaFlex-FAST. A number of comparisons between numerical modeling predictions and test data are done and have good quality results validation. Therefore, the focus is shifted to a probabilistic examination of snap load frequency and magnitude both in experimental data and in the simulation. The CWD model of the numerical data is also compared with the CWD model of test data.

DEDICATION

To my beloved Hear Chan Master -Wu Jue Miao Tian

ACKNOWLEDGEMENTS

I would like to express my deepest gratitude to my advisor, Prof. Krish Thiagarajan, for his excellent guidance, caring, encouraging and most of all patience throughout the entire process. I learnt how to do critical appraisals of research under his supervision.

I wish to thank Dr. Lance Manuel for his expertise on probability distribution model, as well as for his discussion and ideas on my dissertation. I would like to thank Dr. Andrew J. Goupee for providing access to the DeepCWind experimental data and the FAST codes for the 1:50 scale wind turbine model, whose generous advice was tremendously helpful in data analysis. I wish to thank Dr. Vincent Caccese and Dr. Melissa Landon for their discussion and feedback on my dissertation.

I gratefully acknowledge the funding sources that made my Ph.D. work possible. I was funded by the College of Engineering and Office of the Vice-President of Research and for years 1, and by the Bureau of Safety and Environmental Enforecement (BSEE), U.S. Department of the Interior (Contract no. E13PC00019 issued to Maine Marine Composites, LLC) for years 2 &3. I was honored to be a Michael Eckardt Dissertation fellow supported by the graduate school for year 4 and a teaching assistant supported by the department of Mechanical Engineering for year 5.

In addition, I would like to recognize Von Vogt, Steve, Richard Akers, Michael MacNicoll, and Toby Dewhurst of Maine Marine Composites, LLC who have provided access to use OrcaFlex. Thanks for their input and assistance on so many occasions during the use of OrcaFlex. Thanks for Dr. Kang Hooi Siang for generous support on the development of the Charm3D model.

In my later work of experimental study of cable model, Dr. Ray-Yeng Yang, Dr. Wen-Yang Hsu, Dr. Yun-Ta Wu and Tzu-Ching Chang of Tainan Hydraulic Laboratory made significant contributions to the tests. Thanks for their inspirational discussions with me regarding these experiments. I would like to recognize the members of the MOOR lab who have all contributed to the progress I have made. This would not have been possible without their support.

My time at UMaine was made enjoyable in large part of due to the friends that became a part of my life. I am grateful for time spent with Jui-Han, Dongmei, Yi, Danny, Geneva, Ango, Celine and Kan-ju and our memorable trips. My Ph.D. life was also enriched by Heart Chan group. Thanks for Amanda, Maggie, Winnie, Clare and Katherine.

Lastly, I would like to thank my family for their love and encouragement. For my parents who raised me with a love of science and supported me in all my pursuits. For my brother Cheng-Hao, who looked after my parents in Taiwan. And most of all for Chia-Tsen, whose faithful support during the final stage of this Ph.D. is so appreciated.

TABLE OF CONTENTS

LIST OF TABLES

LIST OF FIGURES

NOMENCLATURE

A	excitation amplitude
Af	Water-plane area of the floater
B_c	equivalent linear damping coefficient
B_{eq}	equivalent linear viscous damping coefficients
B_1, B_2	linear and quadratic damping coefficients
BFI	Benjamin-Feir index
CWD	composite Weibull distribution
C	internal damping of the cable
C_{e}	equivalent hydrodynamic damping coefficient
C_M	mass inertia coefficient
C_d	drag coefficient
C_A	added mass coefficient
CAML	Catenary Anchor Leg Mooring System
DNV	Det Norske Veritas
D	diameter of the vertical cylinder
FOWT	Floating Offshore Wind Turbine
FSO	Floating, Storage and Offloading
F_{total}	total tension
F_{st}	static tension
F_{dyn}	dynamic tension
$\mathcal{F}$	cumulative (Weibull) distribution function of tension cumulative (composite Weibull) distribution function of tension
f	Weibull probability density function of tension
g	acceleration due to gravity of earth (g =9.81 $\frac{m}{s^2}$)
H	Water depth
H_{tr}	transition wave height
H_s	significant wave height

H_{sub}	distance between sea-surface to the bottom of the submersible
$K_{c1,2}$	bilinear axial stiffness of the cable system (K_{c1} =1766 $\frac{N}{m}$, K_{c2} =127 $\frac{N}{m}$)
KC	Keulegen-Carpenter number
k	stiffness of the cable
L_c	length of the cable
LF	Low-Frequency components
M	mass of the floater
MPME	Most Probable Maximum Extreme
MLE	Maximum Likelihood Estimation
M_c	mass plus added mass per unit length of the chain
M_v	structural mass and the associated hydrodynamic added mass
M_y	Moment with respect to y-axis at the base of tower
NREL	National Renewable Energy Laboratory
N_L	maximum dynamic force at the lower end of hoisting cable
O&G	Oil and Gas Industry
OC4	Offshore Code Comparison Collaboration Continuation
OC3	Offshore Code Comparison Collaboration
PSD	Power Spectral Density
P	Exceedance probability
QQ-plot	quantile-quantile plot
RAO	Response Amplitude Operator
r_{xy}	correlation coefficient of variables *x* and *y*
Spar	Spar-buoy type floating offshore wind turbine
Semi	Semi-submersible floating Wind Turbine
SC	Design breaking strength
SF	Semi-submersible model with Froude scaled turbine
SP	Semi-submersible model with performance scaled turbine
TF	Tension Leg Platform model with Froude scaled turbine
T_P	spectral peak period

T_{FL}	the line tension at the fairlead position
T_H	the horizontal force from the cable on the vessel
$\hat{T}_{cr}$	the critical tension
T_{touch}	The tension at the touchdown point
T_L	resultant static force in the lower end of the rope
t_p	excitation time period
TLP	Tension Leg Platform
T	dynamic tension [kN]
T^{max}	local maximum dynamic tension [kN]
T^{min}	local minimum dynamic tension [kN]
T^n	dynamic tension not associated with a snap event [kN]
T_{rms}	root-mean-square dynamic tension [kN]
T^s	snap-induced tension [kN]
T_{C-mean}	characteristic mean line tension [kN]
T_{C-dyn}	characteristic dynamic line tension [kN]
T_{d-max}	maximum dynamic tension [kN]
T_{LF-max}	maximum low-frequency tension [kN]
T_{LF-sig}	significant low-frequency tension [kN]
T_{WF-max}	maximum wave-frequency tension [kN]
T_{WF-sig}	significant wave-frequency tension [kN]
T_o	pretension of a mooring line ($\mathrm{T_o} = 1124$) [kN]
T_ℓ	slack tension ($\mathrm{T_\ell} = 10\%\ \mathrm{T_o}$) [kN]
$\hat{T}$	non-dimensional dynamic tension ($\hat{\mathrm{T}} = \mathrm{T}/\mathrm{T_{rms}}$)
$\widehat{T^n}$	non-dimensional dynamic tension, not associated with a snap event ($\widehat{\mathrm{T^n}} = \mathrm{T^n}/\mathrm{T_{rms}}$)
$\widehat{T^s}$	non-dimensional snap-induced tension ($\widehat{\mathrm{T^s}} = \mathrm{T^s}/\mathrm{T_{rms}}$)
$\hat{T}_{d-max}$	non-dimensional maximum dynamic tension ($\hat{\mathrm{T}}_{\mathrm{d-max}} = \mathrm{T_{d-max}}/\mathrm{T_{rms}}$)
$\hat{T}_{C-dyn}$	non-dimensional characteristic dynamic line tension ($\hat{\mathrm{T}}_{\mathrm{C-dyn}} = \mathrm{T_{C-dyn}}/\mathrm{T_{rms}}$)
$\hat{T}_{C-mean}$	non-dimensional characteristic mean line tension ($\hat{\mathrm{T}}_{\mathrm{C-mean}} = \mathrm{T_{C-mean}}/\mathrm{T_{rms}}$)

$\hat{T}_{MPME}^{CWD}$	non-dimensional most probable maximum extreme dynamic tension based on the composite Weibull distribution ($\hat{\mathrm{T}}_{\mathrm{MPME}}^{\mathrm{CWD}} = \mathrm{T}_{\mathrm{MPME}}^{\mathrm{CWD}}/\mathrm{T}_{\mathrm{rms}}$)
$\hat{T}_{MPME}^{test}$	non-dimensional most probable maximum extreme dynamic tension of $\hat{\mathrm{T}}$ from the test data ($\hat{\mathrm{T}}_{\mathrm{MPME}}^{\mathrm{test}} = \mathrm{T}_{\mathrm{MPME}}^{\mathrm{test}}/\mathrm{T}_{\mathrm{rms}}$)
$\hat{T}_{MPME}^{WBL}$	non-dimensional most probable maximum extreme dynamic tension based on the Weibull distribution ($\hat{\mathrm{T}}_{\mathrm{MPME}}^{\mathrm{WBL}} = \mathrm{T}_{\mathrm{MPME}}^{\mathrm{WBL}}/\mathrm{T}_{\mathrm{rms}}$)
$\hat{T}_{tr}$	non-dimensional transition tension
$\hat{T}_{1,2}$	scale parameters of the composite Weibull distribution function of tension
T_z	mean zero up-crossing wave periods
WF	Wave-Frequency components
W_{pl}	Weight of payload
WBL	Weibull distribution
w	the weight per unit length of the mooring line
X	the horizontal distance from the anchor
X_{max}	the maximum surge motion over all 3-5hr surge motion histories
X_{mean}	the mean surge motion of the same dataset
X_{cr}	the critical surge motion
x1	forced motion of cable on the top
x2	motion of the floater (positive downward)
$\dot{x2}$	velocity of the floater
$\ddot{x2}$	acceleration of the floater
x_m	mean of variable *x*
x_{touch}	lateral position of the touchdown point
y_m	mean of variable *y*
Z_m	vertical displacement of the center of gravity of catenary part
α	non-dimensional oscillating frequencies of a mooring chain ($\alpha = Z_m\omega^2/g$)
β	dimensionless frequency parameter
$\beta_{1,2}$	shape parameters of the composite Weibull distribution function of tension
γ_{mean}	partial safety factor of DNV ($\gamma_{\mathrm{mean}} = 1.75$ for high safety class)
γ_{dyn}	partial safety factor of DNV ($\gamma_{\mathrm{dyn}} = 2.2$ for high safety class)

δ	empirical constant (δ equals to 1)
$\sigma_{x,y}$	standard deviation of variables *x* and *y*
σ_T	standard deviation of combined low- and wave-frequency components of line tension [kN]
σ_{T-LF}	standard deviation of low-frequency component of line tension [kN]
σ_{T-WF}	standard deviation of wave-frequency component of line tension [kN]
μ	dynamic viscosity of water
ε_{ABS}	absolute distribution fitting error
η	scale parameter of Weibull distribution function
η_{st}	static stretch of cable system
η_o	excitation amplitude
ξ	shape parameter of Weibull distribution function
$\mathcal{L}$	likelihood function
$\Delta x_{wave,s}$	significant wave-frequency motion amplitude
$\Delta x_{wave,max}$	maximum wave-frequency motion amplitude
ϖ	excitation frequency
Λ	non-dimensional frequency
ξ	damping ratio
τ	dimensionless displacement ratio ($\tau = \eta_{st}/\eta_o$)
Ψ_d	dynamic coefficient to estimate the probability of occurrence of snap forces in the hoisting cable
ρ_w	water density
$\forall$	volume of the floater

CHAPTER 1

INTRODUCTION

Over the current decade, the offshore wind industry has grown significantly. More and more governments worldwide are becoming aware that offshore wind resources are abundant and increased installation of offshore wind farms has made wind one of the most promising renewable energies. Recently, most of the offshore wind turbines are mounted on the various foundations based on the range of water depth (H).

0m < H < 30m: bottom-fixed foundations such as monopile structures, are usually used.

25m < H < 50m: bottom-fixed foundations such as jacket structures and tripod structures are typically used.

H > 50m: floating foundations such as Semi-submersible (Semi) type, Spar-buoy (Spar) type, and Tension Leg Platform (TLP) are applied.

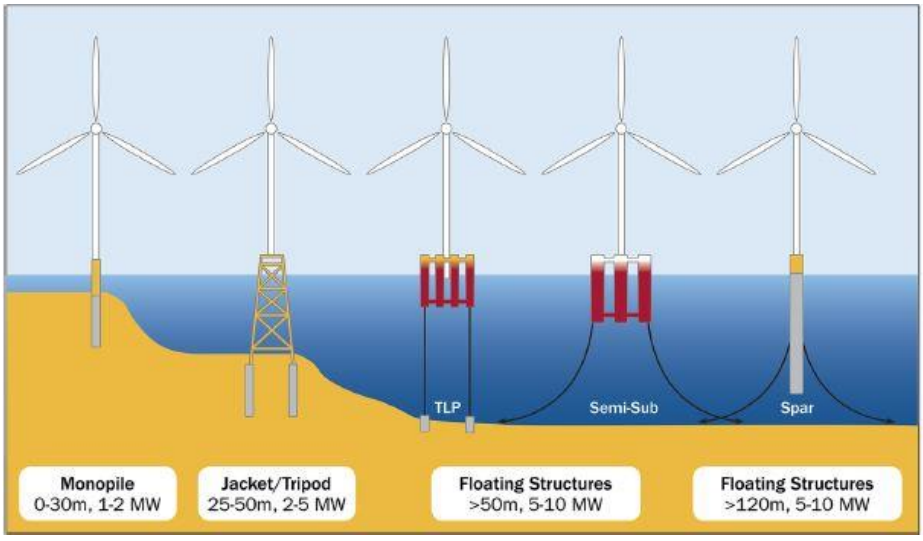

Fig. 1.1 Types of wind turbine foundations [1]

The monopiles support wind turbines are relatively simple to design. The turbine tower is supported by the monopile, either directly or through a transition piece. The pile is

penetrated into the seabed using either steam or hydraulic power hammers. The jacket structures are attached to the seabed through the soil piles and connected to the turbine tower using a transition piece. The fixed offshore wind turbines are constrained by the water depth. These types of foundations (monopile and jacket structures) are not suitable for the seafloor with continental shelf drops away suddenly and deeply. This can cause the installation of fixed structures much more difficult.

The floating offshore wind turbines (FOWTs) can eliminate the water depth constraint and ease turbine set-up. Moreover, installing an offshore wind farm in deeper water can reduce the visual and noise annoyances, and obtain more consistent and stronger wind resources. There are numerous platform configurations with various mooring systems and ballast options. A Spar is moored by catenary mooring lines and uses ballast to achieve stability. A TLP is anchored by rigid tendons to a seabed foundation to restrain vertical motions in waves. The tendon system is highly tensioned due to excess buoyancy of the platform hull. A Semi is moored by catenary mooring lines and has sufficient water-plane inertia to maintain stability. Nowadays, several prototypes using these floating concepts (Semi, Spar, and TLP) are launched and under operation: Hywind, developed by Statoil ASA (Stavanger, Norway) which is based on spar-buoy technology; WindFloat, developed by Principal Power Inc. (Seattle Washington) which are both based on semi-submersible technology. These successful operations increase the offshore wind industry's confidence on developing offshore wind power. However, there have been very few full-scale tests, and most of the prototype data is not available to the research community. A number of scaled FOWTs are developed and the experiments are conducted in wave tanks/basins worldwide: the 1:22.5 scale Spar tested in the National Maritime Research Institute (NMRI) in Tokyo,

Japan; the 1:105 scale WindFloat conducted at UC Berkeley; the 1:50 scale DeepCWind Spar, Semi and TLP tested in MARIN, Netherlands.

The DeepCWind consortium headed by the University of Maine performed model tests of three generic 1:50 scale FOWT concepts in MARIN's wave basin facility in the Netherlands in 2011 and 2013 [2-6]. In 2011, a Spar, a TLP, and a Semi were designed and tested, and various experiments were conducted, such as free decay tests, regular wave tests and irregular wave tests under various wind conditions. The wind turbine model was Froude-scaled based on the National Renewable Energy Laboratory (NREL) 5MW wind turbine. When the FOWTs are scaled by Froude number to reproduce realistic platform-wave interactions, they could underestimate wind loads on the tower and blades which are highly affected by Reynold number. In 2011, the DeepCWind FOWT models used the Froude scaling, and the wind speeds were increased to achieve the appropriate scaled thrust forces. Since the aerodynamic performance of the 2011 tests did not match expectations at the lower Reynolds numbers, the rotor of the scaled model is redesigned. In 2013, the semi-submersible model with a modified wind turbine model was tested in the same MARIN wave basin. The main properties and the model test details can be found in earlier works [2-6]. Several 2011 and 2013 DeepCWind test data provided by Dr. Andrew Goupee are used in this study.

For station-keeping of FOWTs, a proper mooring system is required to keep the translational motions in surge and sway and the rotational motions in yaw of the platform within an adequate range. The mooring concepts include taut and catenary systems. The catenary refers to the shape that a free hanging line assumes under the influence of gravity. The catenary system provides restoring forces through the suspended weight of the

mooring lines and its change in configuration arising from the platform motions. A taut leg system usually has an angle of 30 to 45 degrees, and the restoring forces are created through axial elastic stretching of the mooring line rather than geometry changes.

A moored floating offshore wind turbine is exposed to various environmental loads, including wind, wave, and current acting on the floating system. The response forces are a combination of added mass forces, wave drift damping forces, viscous forces, restoring forces and mooring line damping forces to the interaction with the mooring lines.

In regard to the DNV [7] the response of the floating platforms in a stationary, short-term, environmental state may conveniently be split into four components:

Mean displacement due to mean environmental loads.

Low-frequency displacements due to low-frequency wind loads, and second-order wave loads.

Oscillations in the frequency range of the incoming waves, due to first-order wave loads.

The vortex-induced motion shall be considered for deep draft floating platforms.

When taking due account of all these elements of excitation and responses, mooring line tensions can be categorized into two components: static and dynamic loads. The static mooring line tension is due to the line pretension and mean environmental loads. The dynamic mooring line tension includes low-frequency loads due to drift platform motions and wave-frequency loads due to first-order wave loads.

However, the design philosophy for structures and moorings is based on principles and practices adopted by offshore oil and gas (O&G), and these are optimized for applications in deeper waters (water depth >1000m). In deeper waters, a floating platform's response

largely filters the wave frequency forces thus leaving the mooring system to balance the low-frequency drift forces. Indeed, the offshore wind industry has observed very different mooring line dynamic performance compared with O&G. Mooring lines of FOWTs have experienced extreme tensions more often than lines of O&G. A mooring system for a FOWT must be developed considering criteria such as cost, the stability of lightweight minimal platforms (1000 – 14000 tonnes), and applications for relatively shallow water depths (50 – 500m). DOE cost of energy models indicate that if platform costs can be held near 25% of the total system capital cost then a cost goal of $0.05/kWh would be attainable [8]. The mooring system of a FOWT faces significant effects of wave-frequency forces related to a lighter displacement platform in the shallow water. When exposed to wave-induced motions, one particular loading condition a FOWT mooring system may be vulnerable to is snap type impact. A snap load is defined as a spike in tension as a mooring line re-engages immediately following a slack condition, typically of very short duration. Therefore, the mooring system of a FOWT may operate in an alternating slack-taut condition, which could cause the discontinuity in the elastic stiffness. In regard to the duration in which the line becomes taut, the transition from slack to the taut condition can cause a snap load which is usually 2 – 3 times the cyclic tension magnitude. Such an impact can result in shock on the line material leading to immediate failure or considerably reduced service life [9-14]. In 2011, the Navion Saga Floating, Storage and Offloading (FSO) vessel lost two steel wire ropes due to ductile overloaded [15]. The cause was identified to be high local dynamic snap loads that followed a slack event. In another example, a fiber rope mooring of a ship in the Hokkaido Tomakomai Port broke and snapped back during the berthing process, striking two workers [16]. In 2015

environmental changes in the Java Sea caused a rope that was fastened to a ship to snap and break during recovery efforts of AirAsia flight QZ8501 [17]. Snap loads on mooring lines have the potential to cause catastrophic failures resulting in the destruction of structures and fatal injuries to personnel.

A snap load can occur due to a combination of light pre-tension, shallow water depth and large platform motions in response to a survival storm condition. Together with these factors, the nonlinearity of mooring line stiffness and hydrodynamic drag force are considered as the important factors for snap events. Some studies have stated that snap loads are caused by the nonlinearity of bilinear stiffness, geometric and viscous wave force as well as the elastic wave propagation through the line after the impulse force [18-21]. Burgess studied towing systems and found that the most dramatic example of a dynamic hawser load is the snap load, caused by sudden large motions of the cable ends [18]. Such severe loading of the cable will cause a transient response in which elastic traveling waves may play an important role, so the solution for the cable dynamics must retain the complete elastic behavior of the cable. Umar et al. [19] studied the complex dynamics of slack mooring system under wave and wind excitations. Their research investigated the effect of non-linearities due to hydrodynamic damping, geometric nonlinearity due to mooring lines, nonlinearity due to restoring force and excitation forces using time domain integration scheme. They found that nonlinearity in the system causing the problem of instability is caused by the nonlinear restoring force of the mooring lines. The nonlinear force-excursion relationship of the mooring system was represented by a 5th order anti-symmetrical polynomial.

The focus of this research concerns how the nonlinearity of mooring line stiffness and hydrodynamic drag force affect the snap events of mooring systems. Therefore, this research reveals the underlying physics of extreme mooring line dynamic tensions for a FOWT. The parametric experimental study of a one-dimensional cable model (the vertical hanging cable model) was conducted. This research discusses the bilinear stiffness effects, hydrodynamic drag force effects and static tension effects on the dynamic line tension. The findings show that nonlinearity of line stiffness, hydrodynamic drag force along with low static tensions increase the occurrence probability and the amplitudes of snap loads.

It is always a challenge to predict environmental loads and dynamic responses of a coupled wind turbine, the platform, and the mooring system. Numerical modeling provides a cost-effective, reliable and sophisticated way to analyze the whole FOWT systems. A number of simulation codes are available to the offshore wind industry and capable of modeling FOWTs in a coupled time-domain dynamic analysis. Examples are FAST with AeroDyn and HydroDyn by NREL, FAST with OrcaFlex coupling by NREL and Orcina, SIMO/RIFLEX by MARINTEK and ADAM by MSC. However, numerical modeling has encountered the main challenge of obtaining accurate and reliable simulation results. Thus, the best way to develop confidence and validation on the codes is by taking measurements from physical-scale test or field data and comparing the measured data with the numerical simulation results. Snap events are found in several 1:50 scale DeepCWind test data sets under survival waves with various wind conditions. In this study, the 1:50 scale DeepCWind test data are used to validate the coupled FAST-OrcaFlex models. Once the confidence of the numerical model has been established, various environmental conditions are examined for the snap events study.

So far, this research has argued that the mooring system of a FOWT faces significant effects of wave-frequency forces related to a lighter displacement platform in shallow water, as well as the nonlinearity of line stiffness and hydrodynamic drag force. The resulting impact on a minimum strength requirement is two-fold: (i) an increase in the maximum tension during a typical survival condition (e.g., a 100-year storm); and (ii) a greater likelihood of snap-induced tension spikes. The former effect is comprehensively dealt with in current design practices, while the latter is generally approached on a case-by-case as-needed basis. To investigate the most probable maximum loads under 100-year return sea-states, this study proposes a model for the long-term extreme tension distributions of a mooring line subject to higher probability of snap events. This research is important because the snap-induced spikes in line tension could cause severe failure to the mooring system. Moreover, the causes, the consequences and the occurrence probability of snap loads are important for the design of a FOWT. The overall goal of the study is to investigate the extreme dynamic tension of mooring systems of a FOWT and to propose a long-term distribution model which could improve one aspect of the current approach toward mooring line tension design.

1.1 Background on the Mooring System of FOWTs

When compared to the mooring systems in O&G Industry, the mooring lines of FOWTs are more sensitive to the platform motions. To prevent the platform motion from capsizing as well as from experiencing large dynamic loads, the station keeping system is vital for keeping the wind turbine in an adequate range. Due to economic reasons, it is necessary to minimize system costs, while not exceeding mooring line breaking strength and platform

constraints [22]. The optimization of mooring system becomes a challenge for the offshore wind industry. Brommundt et al. [22] first proposed a new tool for the optimization of catenary mooring systems for floating wind turbines with a semi-submersible support structure based on frequency domain analysis. The authors were able to minimize the line length under the 100-year return environmental conditions. Two sites in the North Sea were chosen: the oil and gas production fields Troll (330m water depth) and the Greater Ekofisk area (75m water depth). They proposed that the low-frequency contributions from wind lead to excitations in platform pitch and hence in higher mooring line peak tension. Thus, wind spectral wind loads should be considered in mooring system design. In extreme environmental conditions, the ratio of spectral wind in comparison to the total spectral loads can be up to 38%, whereas the contribution in operational conditions can be up to 84%. It is crucial for the design of symmetrical mooring systems to properly define load cases and directional spreading to cover the most severe loads. Moreover, it can be expected that second-order low-frequency motions can lead to higher mooring stresses, which is not considered in their study.

Mooring analysis has to be performed to predict extreme responses such as line tensions, anchor loads and vessel offsets due to design loads. Relevant responses are subsequently checked against allowable values to ensure adequate strength of the system against overloading and sufficient clearance to avoid interference with other structures [23]. Benassai et al. [23] studied the catenary mooring system of a floating wind turbine with a tri-floater semi-submersible support structure. They focus on minimizing the line weight with reference to ultimate and accidental loads tuned for the South Tyrrhenian Sea with a water depth of 50 – 300m. The decoupled frequency domain analysis was applied to study

the mooring system behavior. The authors estimate the maximum dynamic offset relative to the typical storm duration of 3 hour by:

$$\Delta x_{wave,max} = \Delta x_{wave,s}\sqrt{\frac{1}{2}\ln(\frac{10800}{T_z})} \quad (1.1)$$

Where $\Delta x_{wave,s}$ is the significant wave-frequency motion amplitude and T_z is the sea-state mean zero up-crossing periods.

To reduce the cost in a potential floating wind farm, Fontana et al. [24] proposed a multiline anchor concept for the OC4 Semi-submersible floating system. A multiline mooring system using 3 anchors per turbine and 3 turbines per anchor was used to evaluate this concept. Mooring line and anchor dynamics were simulated via MoorDyn [25], a lumped-mass mooring model within FAST. The authors found that the multiline anchor experiences lower mean and maximum forces compared to the single-line anchor, but the forces are applied over a large directional range. Moreover, the distribution of force cycle amplitudes and number of cycles is very similar between single-line and multiline anchors.

Cordle and Jonkman [26] present an overview of the simulation codes available to the offshore wind industry that are capable of performing integrated dynamic calculations for floating offshore wind turbines. They found that the behavior of the fairlead tension was similar to that of the surge displacement, which confirms that platform surge is the factor that most influences fairlead tensions in a spar buoy. Moreover, that the mooring-line tensions are counteracting the thrust from the rotor, which means the fairlead tensions were higher when the wind turbine had a greater mean thrust.

Kim et al. [27] proposed a design procedure of mooring lines for FOWT to examine the operation feasibility of FOWT in a Korean environment. The OC4 DeepCWind semi-

submersible platform with the NREL standard 5MW wind turbine was selected for the study. Mooring lines were designed in regard to the water depth of 120m in the Jeju offshore area. The authors found that the maximum tension increases as the nominal diameter of mooring line increase due to the increase of the weight of catenary mooring lines. They also suggested that an increase of nominal diameter will result in an increase of dynamic tension.

Hong et al. [28] performed an experimental study using a model of a spar buoy-type floating offshore wind turbine. The model was moored by springs in a wave tank, with a 1:100 scale ratio for a 5MW wind turbine. The authors found that the scale model responded with large motion as the wave frequency approaches one of the natural frequencies in regular wave tests. They also presented that large surge or heave motion resulted in large changes in mooring lines and their spring constants also changed.

Nihei et al. [29] proposed a new type of floating wind turbine, in which the floater itself can rotate from the wind with a new single point mooring system. They examined two different configurations of the single point mooring system. One used a thrust bearing at the connecting point between the mooring and the floater. The other used both a thrust bearing and aligning bearing. They found that both of the static friction and the restoring yaw moment are less for the latter one.

Bae et al. [30] studied the performance changes of an OC4 DeepCWind semi-submersible FOWT with broken mooring lines. Regarding the numerical results, the drift distance with one mooring line broken can be over 700m, which could be a significant risk to neighboring FOWTs or offshore structure. In reality, the power cable is likely to be disconnected or broken and the wind turbine cannot produce power after that.

1.2 Background on Snap Loads on Mooring Systems of Floaters

Although rare, snap events have been documented in marine operations onboard floating platforms, such as the Navion Saga Floating, Storage and Offloading (FSO) vessel and the ship used in the recovery effort. Although there have been very limited studies on shock loads on mooring lines of FOWTs [31], there are several investigations on other marine systems.

Snap loads on mooring line of several floating systems has been investigated, such as, vertical hanging segmented cable systems [32], lifting and mooring cable systems[10], offshore cranes [33], lines for U.S. Navy ship use [34], marine cable systems [11, 35, 36], multi-cable hoisting systems [37], a Catenary Anchor Leg Mooring (CALM) buoy [38], a deep-sea tethered remotely operated vehicle [39, 40], and a submerged floating tunnel [41]. Some of these studies have investigated the causes and consequences of snap loads on mooring lines of different floating systems.

Liu [10] has defined a snap load as an impact load caused by the sudden re-tensioning of the line after a state of zero tension which occurs when the cable system is subjected to surface motions of large amplitude and/ or high frequency. The duration of a snap was observed to be short but its amplitude was found to be many times greater than the maximum dynamic load, depending upon the properties of the line and the payload. A Fortran IV computer program called SNAPLG was developed to solve transient, dynamic and snap load responses to surface excitation of any composite underwater cable system in any current conditions with fixed or weighted lower end boundary conditions.

Swenson [34] has presented a three-year investigation conducted by the U.S. Navy into the feasibility of developing a safer line for naval use. The author noted that the line snapback

is due to material parting. The approach taken to reduce snap-back was to fabricate the prototype line from a low stretch, load-bearing material.

Geoller and Laura [32] have presented a review of experimental and analytical investigations dealing with the dynamic response of vertically hanging segmented cable systems where the upper portion is a stranded steel cable and the lower segment is a nylon rope. Lumped parameter models were developed to predict cable forces during a snap condition that follows slackness in the cable. The authors observed that a spike in tension developed when the excitation frequency was below the natural frequency of the cable system. This impact load, which is a maximum at the top of the cable, can be of sufficient magnitude to cause premature failure even in cable systems with a high safety factor.

Strengehagen and Gran [33] have found that the mooring line dynamics have a limited role in influencing the surge and heave motions of a semisubmersible, but are significant when observing the line tensions in extreme sea-states. Suhara et al. [42] observed that a snap event happened when non-dimensional oscillating frequencies of a mooring chain were constrained as follows:

$$\alpha_S < \alpha < \alpha_F \tag{1.2}$$

where $\alpha = Z_m\omega^2/g$. Z_m represents the vertical displacement of the center of gravity of catenary part, ω is the circular frequency of forced oscillation, g is the acceleration due to gravity. Values of α_S are estimated by using the approximate calculation method as 0.35 – 0.6 and the value of α_F is 1.

Niedzwecki and Thampi [11] have developed single- and multi-degree of freedom models of a cable suspending a package and used these to study snap loads in regular seas. They

found that snap loads can be several orders of magnitude larger than normal static and dynamic loads and can become the dominant design consideration. They have defined the condition for impending slack in the cable or cable system when the cable distributed mass can be neglected. Their formula is based on non-dimensional frequency (Λ) and damping ratio (ξ) used in typical linear dynamic system formulations and is given by:

$$\frac{\Lambda^4+(2\xi\Lambda)^2}{\sqrt{\Lambda^4(\Lambda^2+4\xi^2-1)^2+(2\xi\Lambda)^2}} \geq \tau \tag{1.3}$$

$$\Lambda = \omega/\sqrt{K_c/M_v} \tag{1.4}$$

$$\xi = C_e/\left(2\sqrt{K_c M_v}\right) \tag{1.5}$$

Where ω is the excitation frequency, M_v is the structural mass and the associated hydrodynamic added mass, K_c is the axial stiffness of the cable system, C_e is the equivalent hydrodynamic damping coefficient,$\tau = \eta_{st}/\eta_o$ is the dimensionless displacement ratio. η_{st} is the static stretch of cable system and η_o is the excitation amplitude and The separation of slack and taut regions as adopted by DNV [7] are shown in Fig. 1.2.

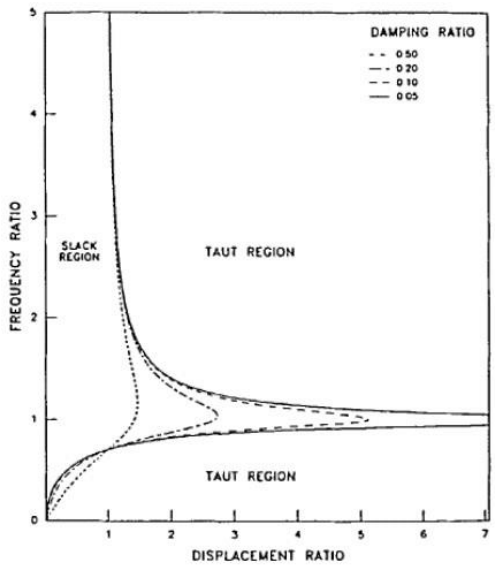

Fig. 1.2 Dimensionless curve for prediction of slack cable conditions [7, 11]

Huang and Vassalos [35] have presented a numerical lumped-mass modeling approach for predicting snap loads on marine cables operating in alternating taut-slack conditions. They noted that the possibility of a cable becoming slack exists whenever the tension temporarily falls to a level which is comparable to the distributed drag force along the cable. In these circumstances, in the presence of periodic environmental loadings, the cable will operate in alternating taut-slack conditions. Moreover, depending upon the rate at which the cable becomes taut, the transition from the slack to the taut state may cause high tension in the cable which can have detrimental effects and may even cause cable breakage. They observed that when the cable is under severe excitation (an amplitude of 0.075 m and frequency of 1 Hz), the response becomes distorted. The displacement is characterized by sharp troughs and flat crests, with flat troughs and sharp crests for the velocity. Moreover, the magnitude of the acceleration becomes much larger since the transition from slack to taut states involves a sudden change in velocity.

Hann [37] has developed a method for static and dynamic analysis of multi-cable hoisting systems typically comprised of hoisting and guide ropes, electrical cables, and anchor lines. A dynamic coefficient to estimate the probability of occurrence of snap forces in the hoisting cable was defined as:

$$\Psi_d = \frac{N_L(H_{sub})}{T_L(H_{sub})} \tag{1.6}$$

Here, N_L is the maximum dynamic force at the lower end of hoisting cable and T_L is the resultant static force in the lower end of the guide rope, both of which are functions of the distance from sea surface to the bottom of the submersible, H_{sub}. The limiting value of the coefficient corresponding to the rope becoming slack is $\Psi_d = 1$ under which conditions snap loads occur. The author's snap load assessments for moderate and severe sea states were found to be consistent with those found by Liu (1991).

Gobat and Grosenbaugh [14] have studied the dynamics of catenary moorings in the region surrounding the touchdown point. They defined a snap event as when the transverse wave speed in a line is smaller than the speed of the touchdown point of the mooring line. This criterion is

$$\left|\frac{dx_{touch}}{dt}\right| \geq \sqrt{\frac{T_{touch}}{M_c}} \tag{1.7}$$

Here x_{touch} is the lateral position of the touchdown point, T_{touch} is the tension at the touchdown point, and M_c is the mass plus added mass per unit length of the chain. The authors observed that shocks during upward motion of the mooring line led to a snap load in the tension record, while shocks during downward motion led to slack tension at the touchdown point. They also noted that the motion of the line along a sandy bottom

associated with unloading shocks led to significant trenching and potentially increased abrasion.

Zhu et al. [39] have formulated three-dimensional equations of motion for a marine tethered remotely operated vehicle system that support large elastic deformations and snap loads. The cable model was formulated using the lumped parameter approach. The authors have observed that the snap loads increased as the stiffness of the sling increased, even beyond the cable breaking strength. Also, while low flow speeds reduced the snap loads, the tether tension increased significantly as the speed of the current was increased.

Lu et al. [41] have investigated the dynamics of submerged floating tunnels supported by taut lines including snap loads on the tethers. They have studied the sensitivity of occurrences of slack tether events to wave height and wave period and showed that at large wave heights a submerged floating tunnel tether can go slack and experience snap loads during re-engagement.

Han et al. [36] have found that an entire mooring system is liable to fail suddenly once the most severely loaded line is broken. Such a break induces a large offset of the floating structure and causes sharply increased tensions in the adjacent mooing lines, eventually leading to the successive failure of the mooring system. Masciola et al. [31] have studied the influence of mooring line dynamics on the response of a floating offshore wind turbine and compared the results against an equivalent uncoupled mooring model. The authors have observed that the coupled and uncoupled platform responses differ when snap loads occur. The delay between a loss of cable tension and a snap load is short but is important enough to affect the outcome of the results. They also noted that a snap load results in a large force being applied to the platform due to rapid cable re-tensioning, and this reaction

explains why large differences occur between the coupled and uncoupled models in regions near snap loads. The variation of structural parameters and wave parameters except the wave period parameter has provided predictions about slack and snap phenomena. In this testing, it appears there are two types of slack. The first slack type is slight slack which causes the amplification of tether tension to be 1.5 – 3 times that of the maximum tension. The second slack type is normal slack which causes the amplification of tether tension to be 3 – 9 times that of the maximum tension. Moreover, tether stiffness has a strong correlation with the occurrence of slack and snap loads [43].

A flexible body with large structural flexibility and displacement, and more, under complex actions of ambient fluid loads, the movement of mooring-line often exhibits strong nonlinear characters which introduce significant challenge to the analysis of its restoring performance [44]. As water depth and structural length increase, the dynamic characters of mooring-line become more profound, which may consequently change top tension and, even, may introduce transiently large snap tension due to mooring line taut-slack [44]. Papazoglou et al. [45] showed that the nonlinear response of a catenary cable submerged in water is dominated by the elastic stiffness for sufficient high frequencies. This response is entirely due to the effects of nonlinear drag, which is the predominant nonlinearity until tension clipping occurs. Van Den Boom [46] conducted an extensive research program to gain further insight in the mechanism of the dynamic behavior of mooring lines and quantify the effects of important parameters, with special attention to the maximum tension, and to validate a numerical model. The author found that the nonlinearities coming from the geometry, elastic deformation and acting loads can significantly enlarge top tension. Zhang et al. [47] carried out an experimental investigation to obtain the dynamic tension

and discover the nonlinear characters while a mooring line transfers from taut to taut–slack. The authors showed once the taut-slack condition was observed, harmonics of higher-frequency components appear in the tension. Once the transformation from the taut to taut-slack condition occurs, chaos may appear, the tension amplitude is significantly enlarged, and there is a complex dynamic response. Gottlieb and Yim [48] examined a taut multi-point mooring system with a large geometric nonlinearity under wave and current excitation. This mooring system is found to exhibit local stability and global bifurcations leading to complex nonlinear and chaotic responses. This local bifurcation can lead to period doubling via an even ultra-subharmonic. The chaotic attractor found in the system excited by waves and current occurs for lower values of excitation amplitude than those of the system excited by waves alone. The authors identified the coupling of bias and periodic excitation as the generating mechanism of instability and sensitivity to initial conditions.

Gerber and Engelbrecht [21] modeled a large oil tanker moored to an articulated tower as a bilinear oscillator, which is a linear oscillator with different stiffness for positive and negative deflections due to the slackening of mooring lines. An increase in discontinuity of the mooring system resulted in an increase of oscillation amplitude, number of cycles and period of the response. Therefore, an increase in the discontinuity of the system led to a shift in the resonant peak to lower values of the natural frequency. Palm et. al., [49] presented a high-order discontinuous Galerkin formulation to capture snap loads in mooring cables. The proposed formulation is able to handle snap loads with good accuracy, with implications for both maximum peak load and fatigue load estimates of mooring cables. The authors observed snap-load propagation and snap-induced shock reflection for

a nonlinear mooring line material. The number of load cycles in the tension time history are noticeable high in small excitation period due to the propagation of the snap load.

Snap-induced impact on mooring line is a dominant problem for the offshore wind power industry. Several researchers have mentioned that the tensioned moorings of TLP should avoid to going slack which could quickly cause a taut condition again due to wave-induced platform motion [9, 10]. Masciola et al. [31] have studied the influence of mooring line dynamics on the response of a floating offshore wind turbine and compared the results against an equivalent uncoupled mooring model. Snap events were observed in 1:50 semi-submersible model tests under survival sea-states, Masciola et al. found that the delay between a loss of cable tension and a snap load is short, but is important enough to affect the outcome of the results [31]. Although the wind power industry is aware of the importance of snap events on mooring systems, there are no criteria for FOWT systems to avoid the associated extreme impact.

In the context of marine operations, Det Norske Veritas (DNV) [50] defines the total line tension in a crane wire as a linear sum of static and dynamic components, i.e.

$$F_{total} = F_{st} + F_{dyn} \tag{1.8}$$

Here the static load (F_{st}) is caused by the net effect of the weight of the mass lifted by the crane and changes in buoyancy when the mass enters the water. Noting that the dynamic force (F_{dyn}) can be opposite in direction to the static load, a snap condition is set to occur when the dynamic force exceeds 90% of the static load [7, 50], i.e.

$$F_{dyn} > 0.9F_{st} \tag{1.9}$$

It is also worth noting that [21, 22] recommend that snap conditions be avoided to the maximum extent possible during operations. In this research, snap load criteria proposed by DNV are applied to the investigations of FOWTs systems.

1.3 Objectives and Scope

The goal of this dissertation is to investigate extreme tensions due to snap loads on a floating offshore wind turbine system and to provide knowledge of the FOWT mooring system behavior which may benefit current practices. Out of that comes four objectives:

1. Study the causes and consequences of snap loads on the mooring system of a FOWT.
2. Analyze the platform motions and mooring line tensions during the snap events using test data.
3. Validate the results using a commercial coupled aerodynamics and hydrodynamics software and discuss the differences of the dynamic line tensions under different environmental conditions using the same numerical model.
4. Develop a long-term extreme tension distribution model of the mooring system of a FOWT.

The first objective is to fundamentally understand the underlying physics of extreme dynamic tension of a mooring system. Consequently, the parametric experimental study of the vertical hanging cable system was conducted. A theoretical approach was also applied to this system and compared with the test results.

The second objective is to study the relationship between the motions of a FOWT and its mooring line tensions while a snap event occurred. Therefore, the present work analyzes the test data of a 1:50 scale semi-submersible FOWT and finds that potential exists for snap type impact to affect the mooring system of the FOWT. There is a reasonably strong correlation between the tension spikes and wave motion, as well as the vertical motion of the fairlead.

The third objective is to calculate the floater's motions and the mooring lines' tensions using a commercial software. Moreover, the research addresses the simulation of long, time-dependent mooring tension sequences by the coupled AQWA-OrcaFlex-FAST programs. The results are validated by the 1:50 scale test data. A number of comparisons between numerical modeling predictions and test data are done and have good correlation. Therefore, by using this numerical model, the differences of the extreme dynamic tension on the mooring lines under different wind speeds are discussed.

The last objective is to develop the long-term extreme tension distribution model of the mooring system of a FOWT. To do so, the trend of exceedance probability is used to compare tension amplitudes of the snap events and the non-snap events. The exceedance probability curve in the higher tension ranges contributed by snap loads shows different characteristics compared to the lower tension range values related to non-snap events. There appears to be a transition point for this change in the curve characteristics. This study proposed a composite Weibull distribution. The results show that the composite Weibull distribution model has a good prediction on the extreme tension value of mooring line tension. To satisfy the ultimate limit system design, this study proposed that snap-induced

dynamic tension values have to be included. Alternatively, ignoring the snap loads would result in a more than doubling of the partial safety factor used in current practice.

1.4 Outline

The following chapters present the work that has been done to investigate the dynamic mooring line tension of a FOWT.

Chapter 2: develop a theoretical formulation which defines the snap load criteria of a vertical hanging cable system; investigate the effect of the nonlinearity of cable stiffness and water force on the dynamic tension of the vertical hanging cable system.

Chapter 3: investigate the extreme tensions on the mooring lines of a FOWT using test data of the 1:50-scale Semi and TLP models.

Chapter 4: develop the long-term extreme tension distribution model of the test data of the mooring systems of a FOWT.

Chapter 5: conduct a numerical analysis to evaluate the motions of a FOWT and dynamic tension of the mooring lines.

Chapter 6: develop the long-term extreme tension distribution model of the simulation results of the mooring systems of a FOWT and compare with the distribution model of the test data.

Chapter 7: demonstrate the summary of the research, discussion of snap load criteria, and future work.

CHAPTER 2

THEORETICAL BASIS FOR SNAP LOADS ON A CABLE SYSTEM

In this chapter, the goal is to understand the underlying physics of snap loads on a mooring line system. The mooring system includes an anchor system fixed to the seabed, a fairlead attached to the floater, and the lines. Snap loads are usually found on the line segments located in the fairlead and seafloor touchdown regions. In 1970, Goeller and Laura [51] investigated a hanging cable system exposed to a longitudinal excitation simulating ocean wave motion. The author proposed that a combination of wave amplitude and frequency can cause slack in the cable which subsequently becomes taut and experiences a severe impact load. The experiments were performed with 0.0016m and 0.0024m diameter stranded steel cables of length up to 21.3m with a 119.7N spherical payload attached to the lower end. The cables were suspended in a tank with a water depth of 19.8m and excited sinusoidally at the top end at amplitudes of 0.025 – 0.076m and frequencies from 0 – 3Hz. The maximum load during snap occurred at the top of the cable. Moreover, once snap was initiated, the cable force rose sharply with slight increases of the excitation frequency.

In this chapter, the vertical hanging cable system is studied regarding the model proposed by Goeller and Laura. Experiments were conducted to investigate the interaction of floater and mooring lines and its effects on snap events.

2.1 Theoretical Concept

While a FOWT operates in the sea, the wave-induced motions of the floater result in the mooring lines' tension on the fairlead. To understand the interaction of a FOWT and the

line tension around the fairlead, one could consider the floater, the fairlead and partial line nearby the fairlead as a system. The concept of this system is shown in Fig. 2.1. Here, we assume the length of the partial line is very short, and neglect the mass of the line. Thus, the tension at the fairlead corresponds to the difference of the net force on the floater (floater mass multiplied by the floater acceleration) with the tension acting on the end of the partial line.

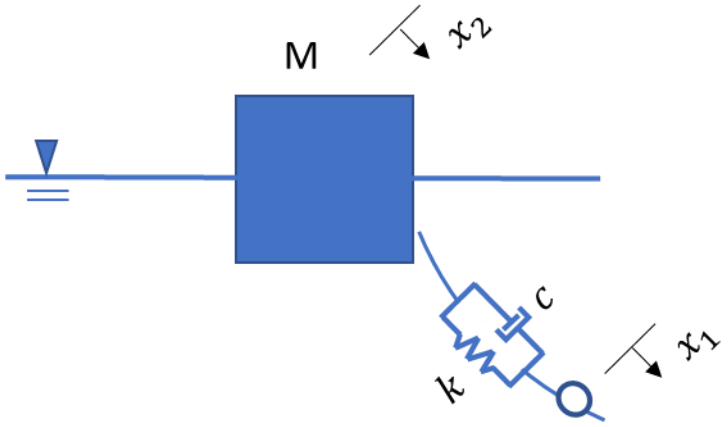

Fig. 2.1 The system of a floater, the fairlead and partial length of the mooring line

This three-dimensional physical problem could be seen as a one-dimensional system if the partial line is assumed to be straight with a very short length. This means that the line tension is always in the direction that is tangent to the line. Thus, the system could be simplified to the vertical hanging cable system as shown in Fig. 2.2. The vertical hanging cable system (Fig. 2.2) has the floater inside the water with the line holding the floater up, while for the system in Fig. 2.1, the floater is in the top with the line pulling the floater down. Although these two systems are opposites, they share similar physical phenomena.

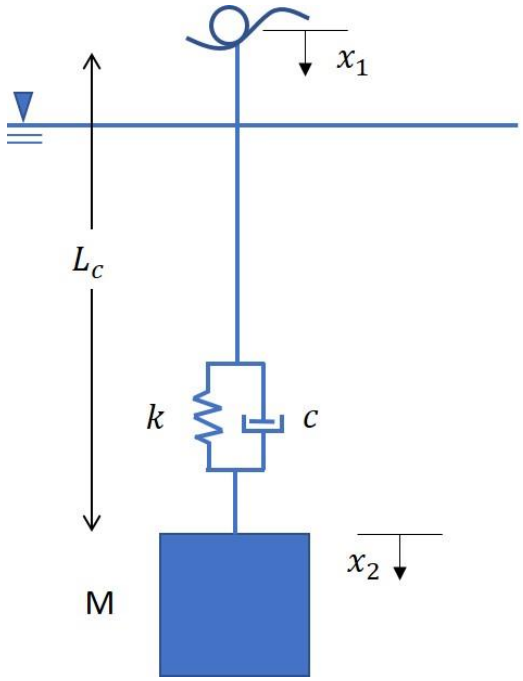

Fig. 2.2 The vertical hanging cable system

Fig. 2.2 shows the vertical hanging cable system. M is the mass of the floater, x_1 is the forced motion of cable on the top, where $x_1 = A\sin(\varpi t)$. A is the excitation amplitude, and ϖ is the excitation frequency. x_2 is the motion of the floater (positive downward), L_c and k are respectively the length and stiffness of the cable.

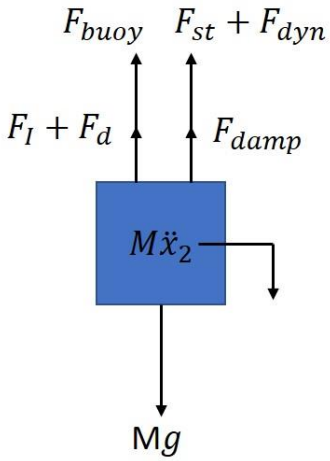

Fig. 2.3 Free body diagram

Fig. 2.3 shows the free body diagram of the floater.

$$F_{buoy} = \rho_w \forall g \tag{2.1}$$

$$F_{damp} = C(\dot{x}_2 - \dot{x}_1) \tag{2.2}$$

$$F_{st} = Mg - \rho_w \forall g \tag{2.3}$$

$$F_{dyn} = k(x_2 - x_1) \tag{2.4}$$

$$F_I = \rho_w C_A \forall \ddot{x}_2 \tag{2.5}$$

$$F_d = 0.5\rho_w C_d A_f |\dot{x}_2| \dot{x}_2 \tag{2.6}$$

Where, ρ_w is the water density, A_f and $\forall$ are respectively the cross sectional area and volume of the floater, and C is considered as the internal damping of the cable. This study assumes that the system is in still water and ignores the cable damping effect ($C = 0$). x_2, $\dot{x}_2$, and $\ddot{x}_2$ are respectively the motion, velocity, and acceleration of the floater.; C_d and C_A are respectively the drag and added mass coefficient. In order to study the snap loads of the vertical hanging cable system, the line tension is positive (taut) and stiffness is constant ($k = K_c$), when $K_c(x_2 - x_1) + F_{st} > 0$. The line tension is equal to zero (slack), and stiffness is zero ($k = 0$), when $K_c(x_2 - x_1) + F_{st} \leq 0$. Thus,

$$\begin{Bmatrix} (M + \rho_w C_A \forall)\ddot{x}_2 + 0.5\rho_w C_d A_f |\dot{x}_2| \dot{x}_2 + k(x_2 - x_1) = 0, \text{ for } K_c(x_2 - x_1) + F_{st} > 0 \\ (M + \rho_w C_A \forall)\ddot{x}_2 + 0.5\rho_w C_d A_f |\dot{x}_2| \dot{x}_2 = F_{st}, \text{for } K_c(x_2 - x_1) + F_{st} \leq 0 \end{Bmatrix} \tag{2.7}$$

There are two nonlinear terms in Eq. (2.6): K_c and $0.5\rho_w C_d A_f |\dot{x}_2| \dot{x}_2$. The nonlinearity of these two terms correspond to the bilinear stiffness and the hydrodynamic drag force, respectively. According to the earlier findings, snap loads occur because of the nonlinearity of bilinear line stiffness and hydrodynamic drag force [18-21]. For FOWTs, snap loads are

found because of their lightweight platform, which also operates in relatively shallow water depths. Therefore, in this study, the effects of the nonlinearity of bilinear line stiffness and hydrodynamic drag force, as well as the weight of payload on snap events are investigated using the vertical hanging cable model.

2.2 Theoretical Development

DNV defines the criteria of snap loads for a lowering crane system (Eq. 1.9). A snap condition is set to occur when the dynamic force exceeds 90% of the static load. Applying DNV's criteria of snap load to the vertical hanging cable system, Eq. (2.7) could be rewritten as

$$0.9F_{st} \leq F_{dyn} = -(M + \rho_w C_A \forall)\ddot{x}_2 - 0.5\rho_w C_d A_f |\dot{x}_2| \dot{x}_2 \tag{2.8}$$

Snap load occurs when the maximum value of the two terms of the right-side of Eq. (2.8) is larger in magnitude than $0.9T_{st}$. For a linear stiffness spring, one can assume that

$$x_2 = A \sin(\varpi t + \varphi) \tag{2.9}$$

$$\dot{x}_2 = A\, \varpi \cos(\varpi t + \varphi) \tag{2.10}$$

$$\ddot{x}_2 = -A\, \varpi^2 \sin(\varpi t + \varphi) \tag{2.11}$$

The drag force of circular cylinder can be interpreted in a Fourier-averaged sense [52] as

$$\frac{1}{2}\rho C_d A_f |\dot{x}_2| \dot{x}_2 = B_C \dot{x}_2 \tag{2.12}$$

Where B_C is the equivalent linear damping coefficient. For a vertical cylinder,

$$B_C = \frac{1}{3}\mu\beta D\, KC\, C_d \tag{2.13}$$

Where μ is the dynamic viscosity of water, β is the dimensionless frequency parameter, D is the diameter of the vertical cylinder, and KC is the Keulegen-Carpenter number

$$KC = \frac{2\pi A}{D} \tag{2.14}$$

In 1994, Thiagarajan and Troesch [52] investigated the hydrodynamic heave damping for tension leg platforms through model tests which were conducted at the University of Michigan. They also showed the curve of damping coefficients versus KC where KC ranged from 0 to 1. The authors also investigated a curve fit to the data and showed that,

$$B_C = a_1 \times KC + a_2 \tag{2.15}$$

Where $a_1 = 15.627 \ \frac{N-s}{m}$ and $a_2 = 3.424 \ \frac{N-s}{m}$. They also found that the mass inertia coefficient (C_M) of a vertical cylinder is independent of KC number, and equal to 1.13 for any KC smaller than 1, which indicates that the added mass coefficient C_A is equal to 0.13. Importantly, the values of a_1, a_2 and C_A were proposed for semi-submerged circular cylinders. The authors found that the form drag force is mainly due to flow separation and vortex shedding at the cylinder bottom, while the added mass is also affected by the cylinder bottom area. For a fully submerged circular cylinder the values of a_1, a_2 and C_A should be doubled. Moreover, the authors also presented that,

$$a_1 \propto \frac{D}{h_t} \tag{2.16}$$

$$a_2 \propto \beta^{-0.5} \tag{2.17}$$

The values of a_1, a_2 and C_A applied to this study are 50 $\frac{N-s}{m}$, 3.054 $\frac{N-s}{m}$ and 0.26 respectively. Thus, Eq. (2.8) becomes,

$$0.9F_{st} \leq (\mathrm{M} + \rho_w \forall C_A)A\varpi^2 \sin(\varpi t + \varphi) - [(a_1 \times KC + a_2) \times A\varpi \cos(\varpi t + \varphi)] \quad (2.18)$$

The maximum value of the right side of Eq. (2.18) is equal to, $\sqrt{[(\mathrm{M} + \rho_w \forall C_A)A\varpi^2]^2 + [(a_1 \times KC + a_2) \times A\varpi]^2}$

Thus, a snap occurs while,

$$(0.9F_{st})^2 \leq (\mathrm{M} + \rho_w \forall C_A)^2 A^2\varpi^4 + a_1^2 KC^2 A^2\varpi^2 + a_2^2 A^2\varpi^2 + 2a_1 a_2 \, KC \, A^2\varpi^2 \quad (2.19)$$

Rearrange the above equation,

$$\left(4\pi^2 \frac{a_1^2}{D^2}\varpi^2\right) A^4 + \left(4\pi \frac{a_1 a_2}{D}\varpi^2\right) A^3 + ((\mathrm{M} + \rho_w \forall C_A)^2\varpi^4 + a_2^2\varpi^2)A^2 - 0.81{T_{st}}^2 \geq 0 \quad (2.20)$$

In Eq. (2.20), assume $\varpi = 1$, the magnitude of each term is: $A^4 = \mathrm{O}(7)$, $A^3 = \mathrm{O}(4)$, $A^2 = \mathrm{O}(1)$, and constant term = $\mathrm{O}(1)$.

For the vertical hanging cable system,

$$\forall = \frac{1}{4}\pi h_d D^2 \propto D^2 \quad (2.21)$$

$$A = A(\varpi, M, D) \quad (2.22)$$

By solving the fourth order equation of A, we find that A is a function of forcing frequency and payload mass.

2.3 Experimental Model

To compare with the theoretical calculations and to further understand how these parameters affect the snap events, an experimental parametric study was carried out. The right and the left plots of Fig. 2.4, respectively, show the conceptual model and the test

model. This model includes the series springs and a payload. The top of the model was attached to one side of the tension sensor, and the other side of the load cell is connected to a fish wire, which is looped around two pulleys and attached to the wave maker. With the wavemaker on the left side of the pulleys, it is possible to create oscillatory motion acting on the top side of the model. Two springs with constants K_{c1} (top) and K_{c2} (bottom) connect in series supporting the payload, where K_{c1} is 14 times larger than K_{c2}. $K_{c1} =$ 1766N/m and $K_{c2} =$ 127N/m. The series springs are designed with bilinear stiffness, where the stiffness is equal to $\frac{1}{K_{c1}^{-1}+K_{c2}^{-1}}$ for elongation smaller than x_{cr}, and is equal to K_{c1} when the elongation of the series springs is greater than x_{cr} (see Fig. 2.5). There is a stopper system connected to the two ends of the soft spring, which allows the soft spring to have the maximum elongation of x_{cr}. This is a 1:2 scale model of a vertical hanging cable system proposed by Goeller and Laura in 1970. For the 1:2 scale model, the mass m range from 0.625kg to 18.95N and $D = 0.1$m. The details of the comparison of this scale model with prototype cable system, the experiment procedures, and the validation tests are shown in Appendix A. The bilinear spring model is designed to create nonlinear dynamic tension. To observe the significant nonlinear dynamic tensions, the stiffness with elongation smaller than x_{cr} is 15 times smaller than the stiffness with elongation larger than x_{cr}. Thus, while the springs' elongations vary from smaller to larger than x_{cr}, the dynamic tensions include an obvious nonlinearity. Moreover, the smallest value of payload weight is 6.13N and the static tension with spring elongation of x_{cr} is 5.43N, which means that as long as the dynamic tension is larger than 5.43N, the system experiences nonlinear dynamic tension. Substituting the parameters of this system into Eq. (2.8), the dynamic tensions larger than 5.43N were observed in some cases with excitation periods smaller than 0.8s. Once

nonlinear dynamic tensions were seen, the possibility of snap loads increased. Thus, this model was designed to assure that snap loads could be seen.

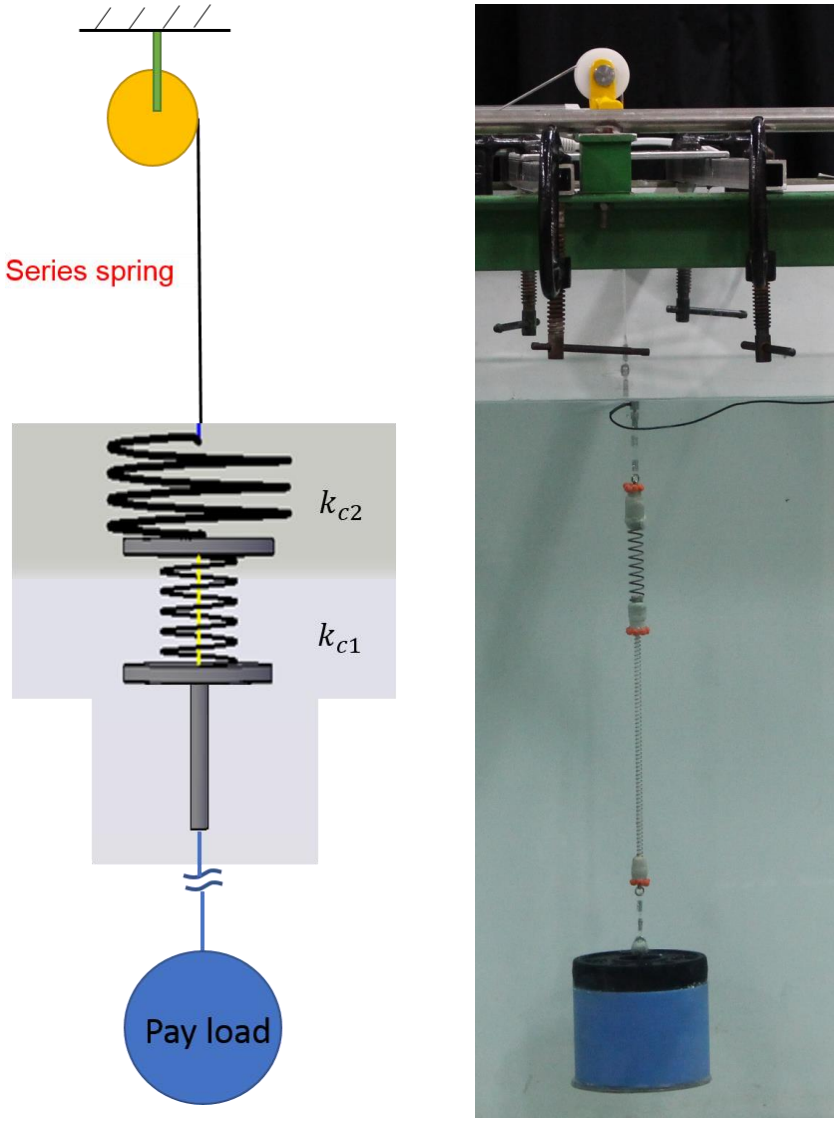

Fig. 2.4 The conceptual model (left) and the test model (right)

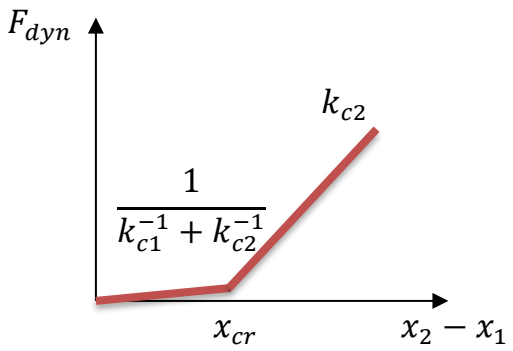

Fig. 2.5 The restoring force vs the series spring system elongations

2.4 Test matrix

Three main parameters analyzed for their influence on the snap events are

- Excitation (vertical) amplitude (A)
- Excitation time period (t_p)
- Weight of payload (W_{pl})

The test matrix is tabulated in Table 2.1.

Table 2.1 The test matrix

$\boldsymbol{A}$	0.01 – 0.04m
$\boldsymbol{t_p}$	0.5 – 2s
$\boldsymbol{W_{pl}}$	6.13 – 18.95N

To compare with the nonlinearity of a bilinear stiffness, a linear spring with a stiffness of 1766N/m supporting various payloads was also tested at different excitation amplitudes and excitation time periods. Here, the linear spring model and the bilinear springs model are represented by SP_1 and SP_2 respectively. Moreover, the effect of water force on the

nonlinearity of dynamic tension is studied. The tests carried out in water are compared to the tests carried out in air.

The static, minimum and maximum tension recorded over each cycle are noted and averaged over the number of cycles and are reported here. There are a total of 105 cases studied. For each case, 10 – 30 cycles are recorded regarding the different t_p values. The cases with $t_p = 0.5$s have 10 cycles while the other cases have 30 cycles. The static tension value is averaged by the record data of the first 3 seconds. In this period, the model is in the still condition, before the excitation motion begins. For each case, the first and last 20% of the cycles are removed and the other remaining 60% used for further calculation. For each case, all of the local maximum tension of the target cycles are averaged and defined as the maximum tension for that case. The minimum tension is defined in the same manner. Following these calculations, the tension range for each case is defined as the difference between the maximum and minimum tension.

The snap criteria defined in section 1.2 is applied to this study, which is a snap event is initiated after a local minimum tension value falls below the threshold tension (10% of the pre-tension value), and lasts until the tension spikes to a value greater than the pretension.

In this study, the F_{st} is equal to the dry weight and wet weight of the payload in air and in water respectively. It is important to mention that, for each payload, the static tension of the cases carried out in air is consistent with the static tension of the cases carried out in water. Thus, the static tensions of the cases carried out in water are adjusted by adding extra circular plates on the payloads to balance the buoyant force on the payloads. The reason for doing this is to compare the dynamic tension of the cases in air and the cases in water under the same static force. Thus, F_{st} in air = F_{st} in water = Mg.

Typical time histories of tension for non-snap, snap-like and snap events are respectively shown in Figs. 2.6-2.8. For the snap-like loads, their minimum tension values do not fall below 10% of the pre-tension value ($0.1F_{st}$) which means that it does not follow DNV's criteria of snap load. However, the tension cycles have flat troughs and peak crests. The cases are defined to be snap-like when their:

1. minimum tension values are larger than $0.1F_{st}$.
2. the ranges of F_{st} to maximum tension are two times larger than the range of minimum tension to F_{st}.

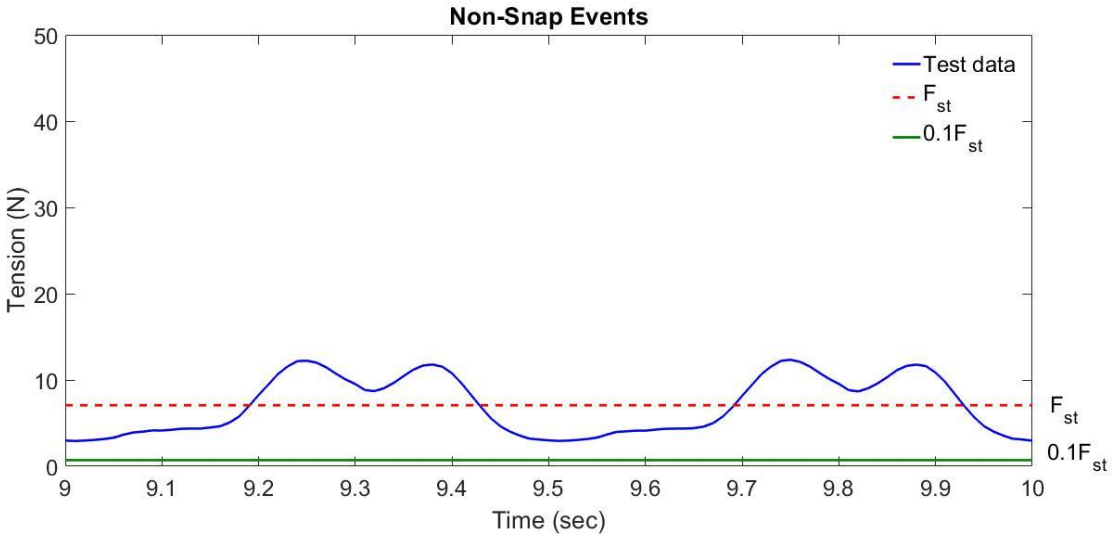

Fig. 2.6 Typical tension time history for SP_1 in air at an excitation amplitude of 0.35m, period of 0.5s and the payload weight of 6.13N

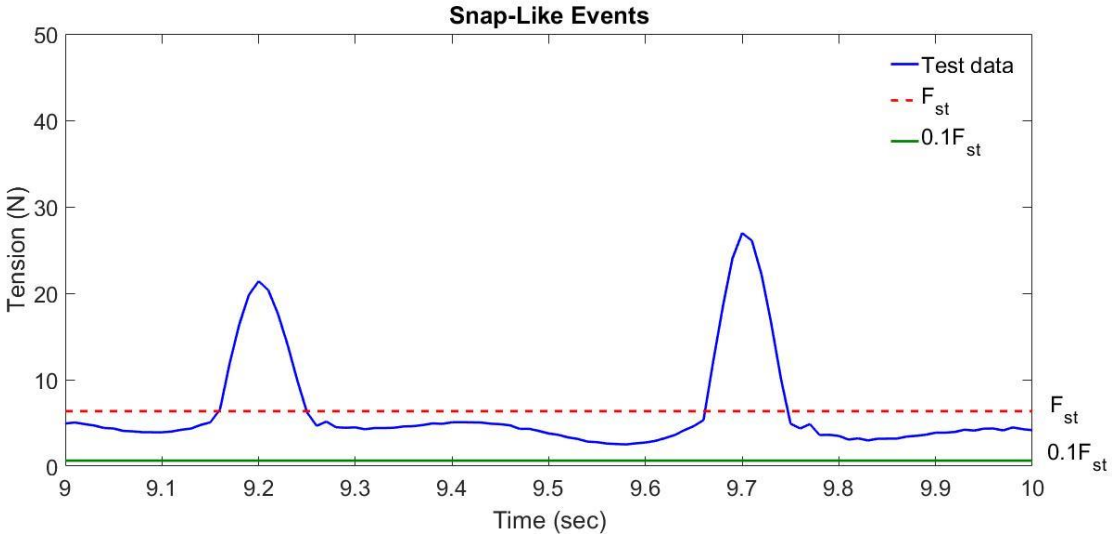

Fig. 2.7 Typical tension time history for SP_2 in air at an excitation amplitude of 0.35m, period of 0.5s and the payload weight of 6.13N

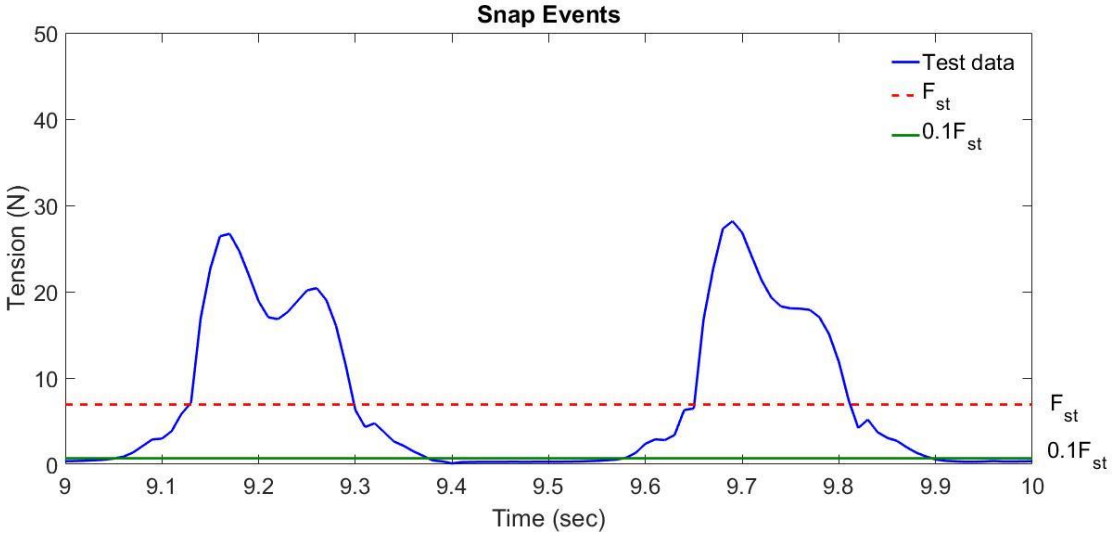

Fig. 2.8 Typical tension time history for SP_2 in water at an excitation amplitude of 0.35m, period of 0.5s and the payload weight of 6.13N

2.5 Influence of bilinear stiffness

To illustrate the differences in dynamic tensions between linear and nonlinear cable stiffness, tests of SP_2 in air are compared with those of SP_1. Sections 2.5.1 – 3 discusses the bilinear stiffness effect on payload weights (W_{pl}) equal to 6.13N, 14.25N and 18.95N respectively.

2.5.1 $W_{pl} = 6.13$N

Figs. 2.9 and 2.10 graphically show the test matrix of SP_1 and SP_2 under various excitation amplitudes (A) and excitation periods (t_p) respectively, for payload weight (W_{pl}) equal to 6.13N. The red squares indicate the tests where snap loads are observed, while the blue squares show the snap-like events. Finally, the black squares represent the non-snap events. For SP_2, the snap events are observed in the case with $A = 0.04$m and $t_p = 0.6$s. The snap-like events are observed here when A ranged from 0.015m to 0.035m and t_p ranged from 0.5s to 0.6s. However, for SP_1, no snap events were observed. Fig. 2.11 shows the variation of the normalized tension ranges of SP_1 (the top plot) and SP_2 (the bottom plot) for t_p ranging from 0.5s to 2s and A ranging from 0.01m to 0.04m. For both SP_1 and SP_2, the normalized tension ranges of each A value are close to zero for t_p ranging from 1s to 2s and slightly increase for t_p from 0.8s to 1s. For t_p < 0.8s, the normalized tension ranges of SP_2 are significantly larger than these of SP_1. Moreover, snap events are also observed in the region within t_p < 0.8s (see Fig. 2.11). Fig. 2.12 shows the tension histories of A = 0.04m and t_p = 0.6s of SP_1 (the blue line) and SP_2 (the red line). This case is the only one with the snap events observed (the red block in Fig.2.10). The local maximum tension values of SP_2 are three times larger than the values of SP_1. Moreover, the nonlinear dynamic tensions are also observed in the SP_2 while the dynamic tensions are linear for SP_1. For SP_2, there is a smaller peak following by each snap load with the periods equal to half of the t_p. Moreover, the local minimum tensions of the small peaks are close to the values of SP_1, but their local maximum tensions are 1.5 – 2.5 times larger than the values of SP_1. This indicates that the nonlinearity of stiffness along with small pretension value

could result in snap events with several times large tension ranges followed by smaller peaks with potential dangers to a floating structure.

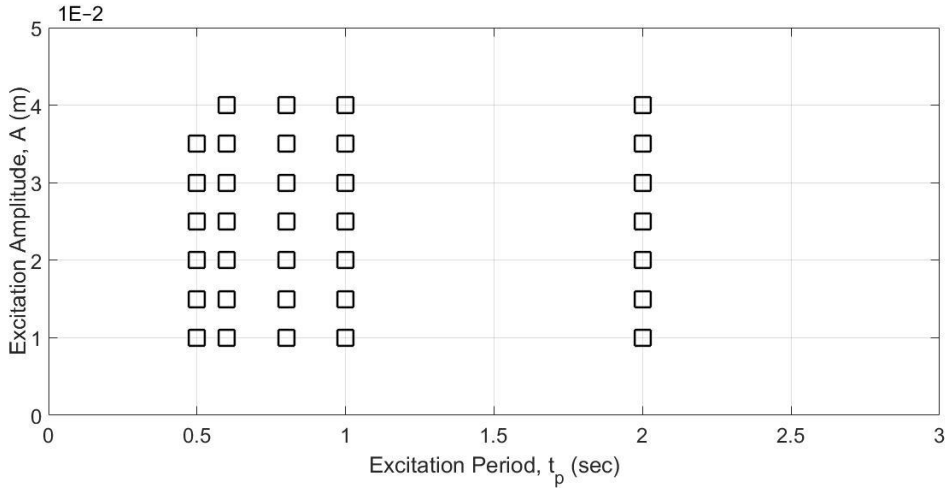

Fig. 2.9 The test matrix for SP_1 in air with the payload weight of 6.13N. The black markers denote the non-snap events

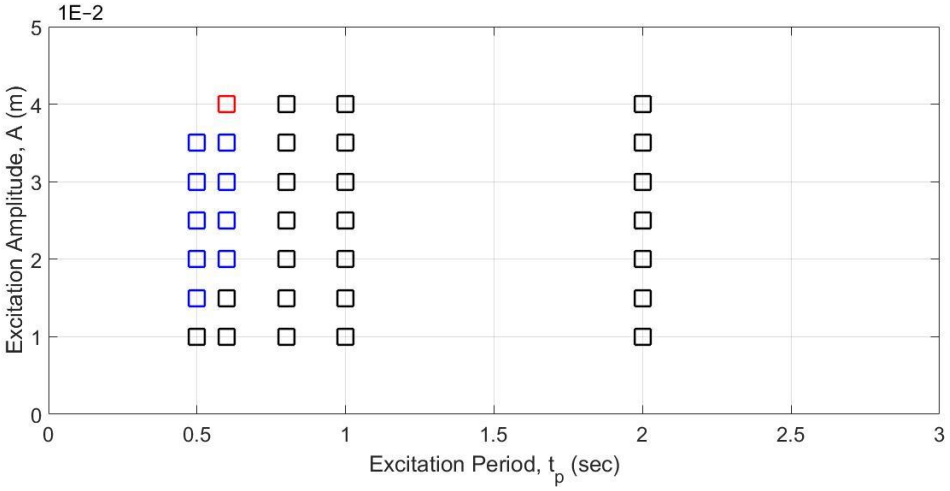

Fig. 2.10 The test matrix for SP_2 in air with the payload weight of 6.13N. The black, blue and red markers respectively denote the non-snap, snap-like and snap events

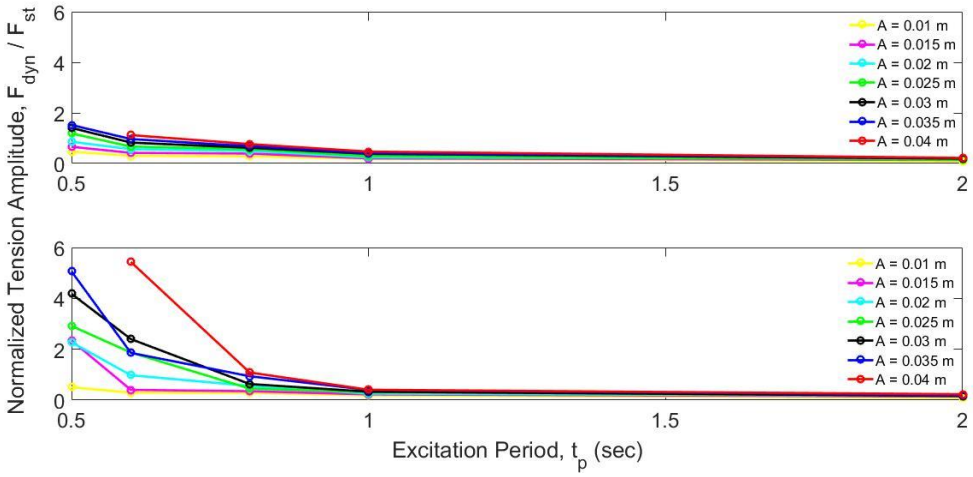

Fig. 2.11 Normalized tension range vs. excitation period for each excitation amplitude with the payload weight of 6.13N. Comparison of SP_1 in air (top) and SP_2 in air (bottom)

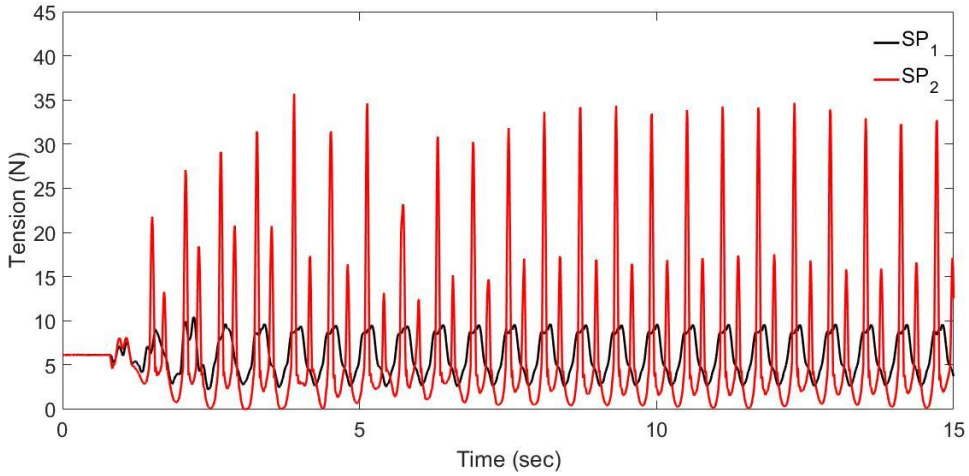

Fig. 2.12 The tension time series of SP_1 in air (black line) and SP_2 in air (red line) with an excitation amplitude of 0.4m, a period of 0.6s and the payload weight of 6.13N

2.5.2 $W_{pl} = 14.25$N

Figs. 2.13 and 2.14 respectively show the test matrix of SP_1 and SP_2 for W_{pl} = 14.25N. For SP_2, the cases with snap events decrease significantly while comparing to W_{pl} = 6.13N. This indicates that the increase of pretension value significantly decreases the occurrence of snap events. However, there are still two cases with snap-like events for A ranging from 0.03m to 0.35m when t_p equals 0.5s. However, cases of SP_1 are found to be non-snap

related. Fig. 2.15 shows the variation of the normalized tension ranges of SP_1 (the top plot) and SP_2 (the bottom plot) for t_p ranging from 0.5s to 2s and A ranging from 0.01m to 0.04m. The normalized tension ranges of most of the cases of SP_2 are very similar to the cases of SP_1, except the two cases, A =0.03m and $t_p = 0.5$s; A =0.35m and $t_p = 0.5$s. These two cases are also marked as blue blocks in Fig. 2.14, i.e. they are snap-like events. Fig. 2.16 shows the tension histories of SP_1 (the black line) and SP_2 (the red line) for A =0.03m and $t_p = 0.5$s. The local minimum tensions of SP_2 are larger than the 10% of the static tension value and very close to the values of SP_1. However, SP_2 has flat troughs and sharp crests as well as a smaller peak followed by each large tension spike. These characteristics are also seen in SP_2 of Fig. 2.6. Moreover, in Fig. 2.16, the local maximum tension values of SP_2 are two times larger than the values of SP_1.

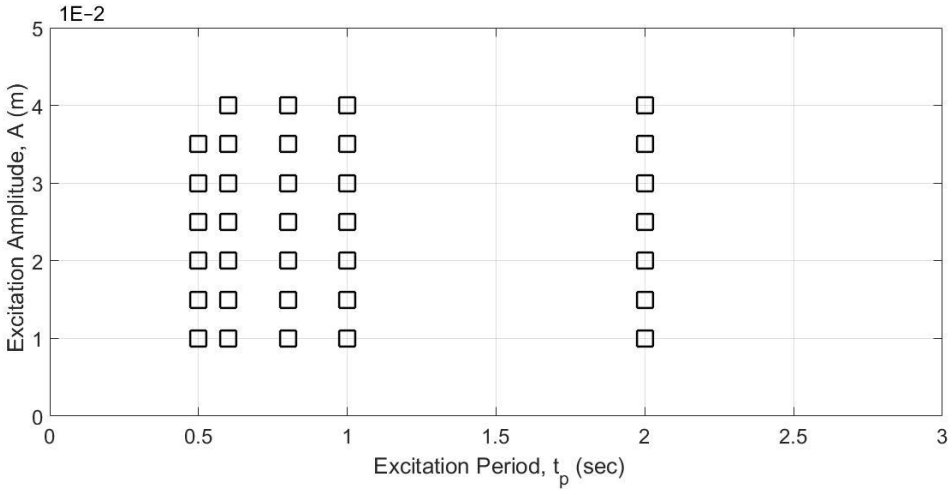

Fig. 2.13 The test matrix for SP_1 in air with the payload weight of 14.25N. The black markers denote the non-snap events

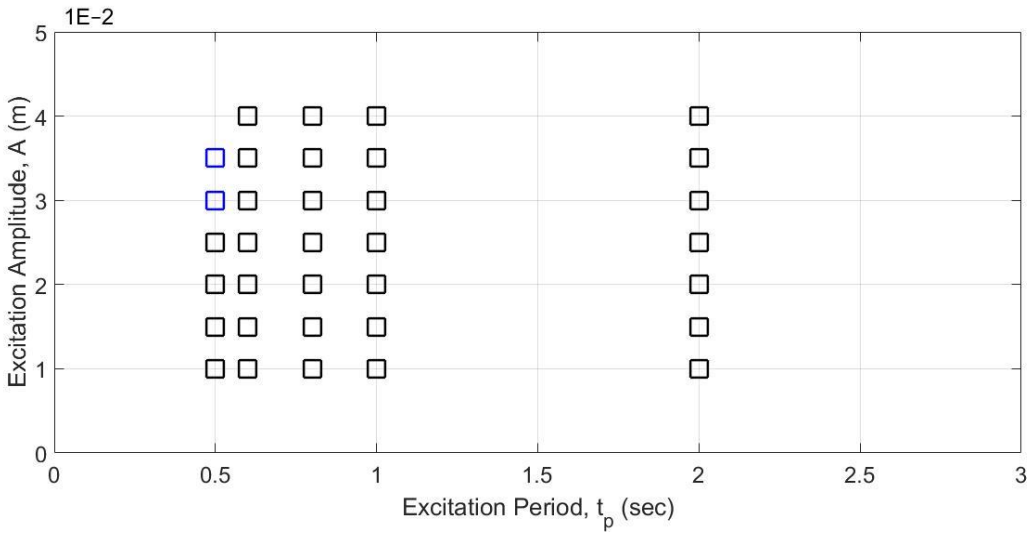

Fig. 2.14 The test matrix for SP_2 in air with the payload weight of 14.25N. The black and blue markers respectively denote the non-snap and snap-like events

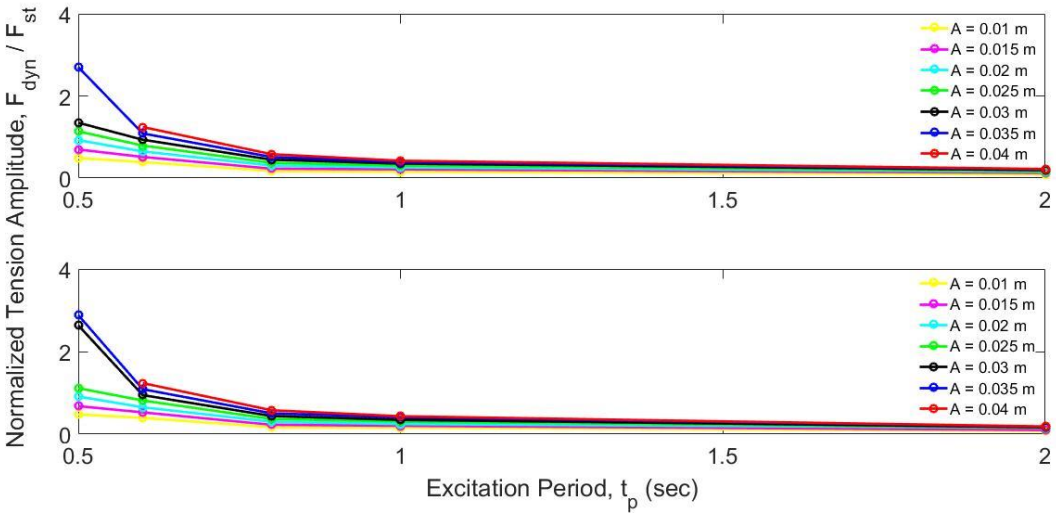

Fig. 2.15 Normalized tension range vs. excitation period for each excitation amplitude with the payload weight of 14.25N. Comparison of SP_1 in air (top) and SP_2 in air (bottom)

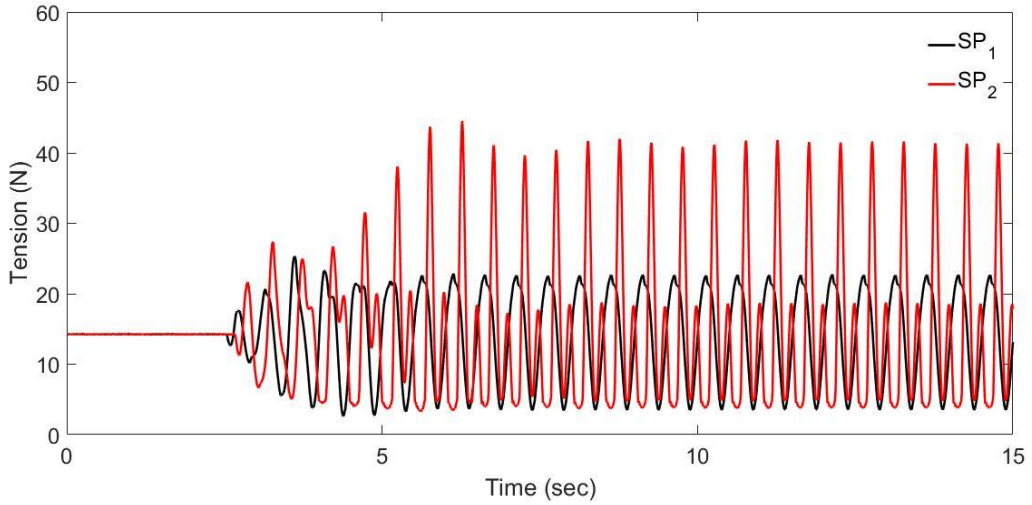

Fig. 2.16 The tension time series of SP_1 in air (black line) and SP_2 in air (red line) with an excitation amplitude of 0.3m, a period of 0.5s and the payload weight of 14.25N

2.5.3 $W_{pl} = 18.95$N

Relative to the cases considered in section 2.5.1 and 2.5.2, SP_2 with a higher pretension value could decrease the occurrences of snap events. In section 2.5.2, cases of W_{pl} = 14.25N are not found to have snap events. Therefore, for W_{pl} = 18.95N, cases are not expected to be snap related. For SP_1, no snap events cases are observed (see Fig. 2.17). Surprisingly, for SP_2, the snap events are found in the case with A = 0.35m and t_p = 0.5s (see Fig. 2.18). Fig. 2.20 shows the tension histories of SP_1 (the black line) and SP_2 (the red line) for A =0.35m and t_p = 0.5s. These linear dynamic tensions of SP_2 significantly deviate from the formation of snap loads (Fig. 2.12) and snap-like loads (Fig. 2.16), which have flat troughs and peak crests. While analyzing the variation of the normalized tension ranges for SP_1 and SP_2 (Fig. 2.19), the normalized tension ranges of all the cases of SP_2 (including the case with snap loads) are very similar to the cases of SP_1. This finding raises the question whether the dynamic tension in this case (SP_2 with A = 0.35m, t_p = 0.5s) can

be considered as a snap load with the similar tension performance of SP_1. This indicates that, DNV's criteria might not fit bilinear cable systems.

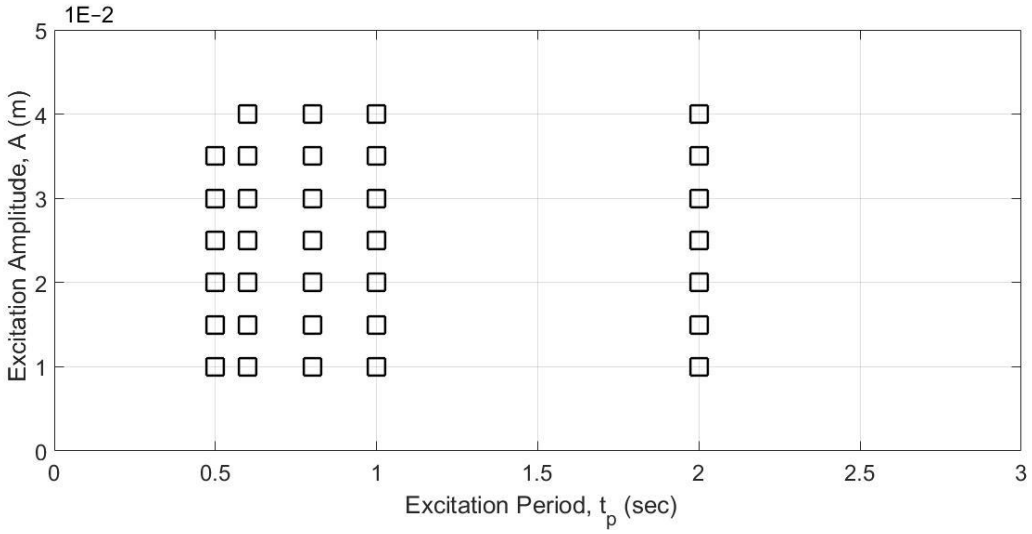

Fig. 2.17 The test matrix for SP_1 in air with the payload weight of 18.95N. The black markers denote the non-snap events

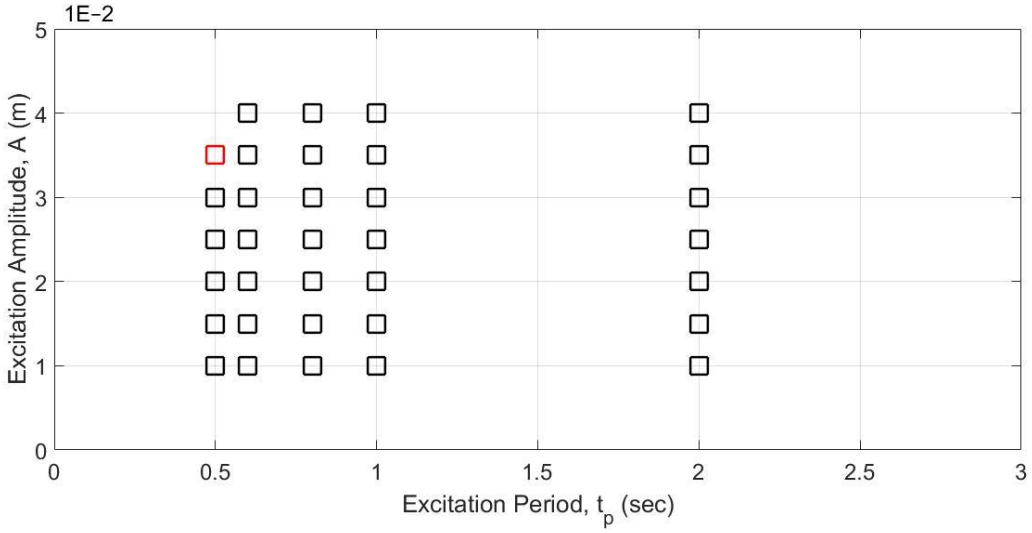

Fig. 2.18 The test matrix for SP_2 in air with the payload weight of 18.95N. The black and red markers respectively denote the non-snap and snap events

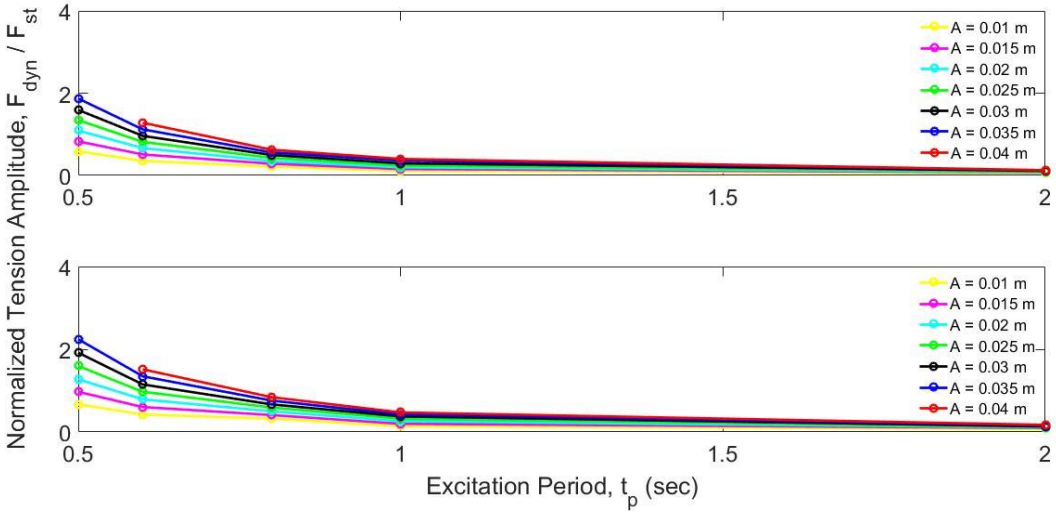

Fig. 2.19 Normalized tension range vs. excitation period for each excitation amplitude with the payload weight of 18.95N. Comparison of SP_1 in air (top) and SP_2 in air (bottom)

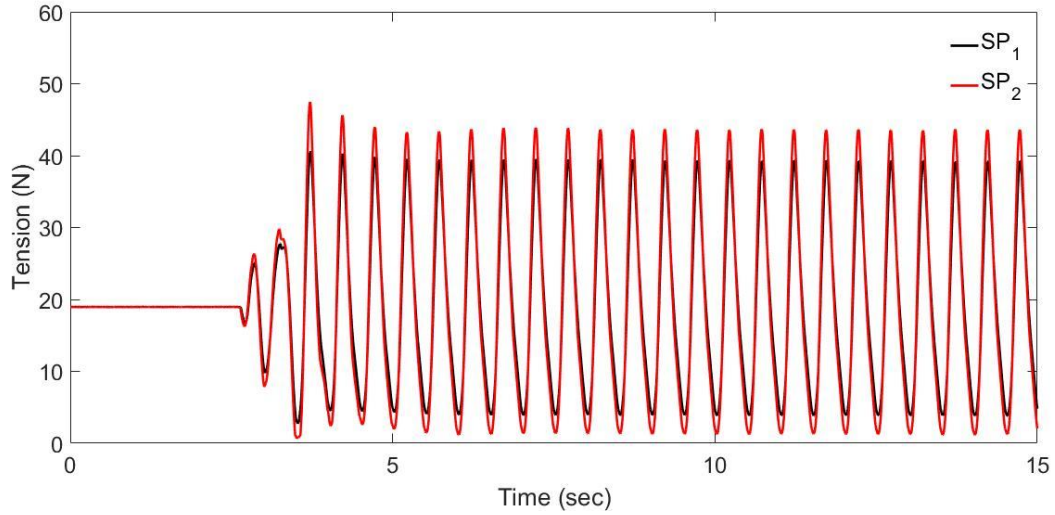

Fig. 2.20 The tension time series of SP_1 in air (black line) and SP_2 in air (red line) with an excitation amplitude of 0.35m, a period of 0.5s and the payload weight of 18.95N

2.6 Influence of Hydrodynamic Drag Force

To investigate the effect of water force on the cable dynamic tension, the tests of SP_2 carried out in water are compared to the tests carried out in air under various excitation amplitudes and excitation time periods. In the following section 2.6.1 – 3 respectively illustrate the difference between the tests in air and in water for payload weights W_{pl} equal

to 6.13N, 14.25N and 18.95N. The snap load criterion estimated by the theoretical formula (Eq. 2.20) is compared with the test results in each section.

2.6.1 $W_{pl} = 6.13$N

Fig. 2.21 shows the test matrix of SP_2 carried out in water for W_{pl} = 6.13N. The yellow line is the theoretical snap criterion. In Fig. 2.21, the test matrix has more red and blue blocks compared to the test matrix of SP_2 carried out in air (**Error! Reference source not found.**). Therefore, water force triggers snap loads that results in larger t_p and lower A for W_{pl} = 6.13N. The top area of the yellow dashed line in Fig. 2.21 indicates that snap loads have a higher probability of occurrence while the underside of the yellow dashed line is the non-snap area. The theoretical snap load criterion is consistent with the tests results when t_p < 1s. For t_p ranging from 1 – 2s, the theoretical criterion indicates that snap events could be found at A > 0.03m, while the test results show that snap loads are not observed in this region. This is possible because the theoretical formula assumes the spring system is massless while the spring system of the tests still has the weight of 0.29N which is 1.5 – 5% of the pretension. Moreover, the uncharacterized friction during the experiments might have resulted in decreasing the probability of snap events in the region of the higher excitation periods.

Fig. 2.22 shows the variation of the normalized tension ranges of tests of SP_2 conducted in air (the top plot) and the tests conducted in water (the bottom plot) for t_p ranged from 0.5s to 2s and A ranged from 0.01m to 0.04m. For SP_2 in air, the normalized tension ranges of each A value are close to zero when t_p ranged from 1s to 2s and significantly increased

when t_p < 1s. However, for SP_2 in water, the normalized tension ranges of each A value are close to zero when t_p > 1.5s, slightly increased when t_p ranged from 1.25s to 1.5s, and significantly increased when t_p < 1.5s. For each A value, the normalized tension ranges of SP_2 in water are larger than SP_2 in air. Therefore, higher excitation amplitudes result in higher dynamic tension ranges. Fig. 2.23 shows the tension histories of SP_2 in air (the black line) and in water (the red line) for A =0.04m and t_p = 0.6s. In this case snap loads are found in both water and air. The cases of SP_2 in water have flatter troughs and sharper crests compared to the cases of SP_2 in air. Moreover, the dynamic tension ranges of SP_2 in water are 30% larger than the values of SP_2 in water. This finding indicates that the hydrodynamic drag force can increase the dynamic tension ranges for W_{pl} = 6.13N.

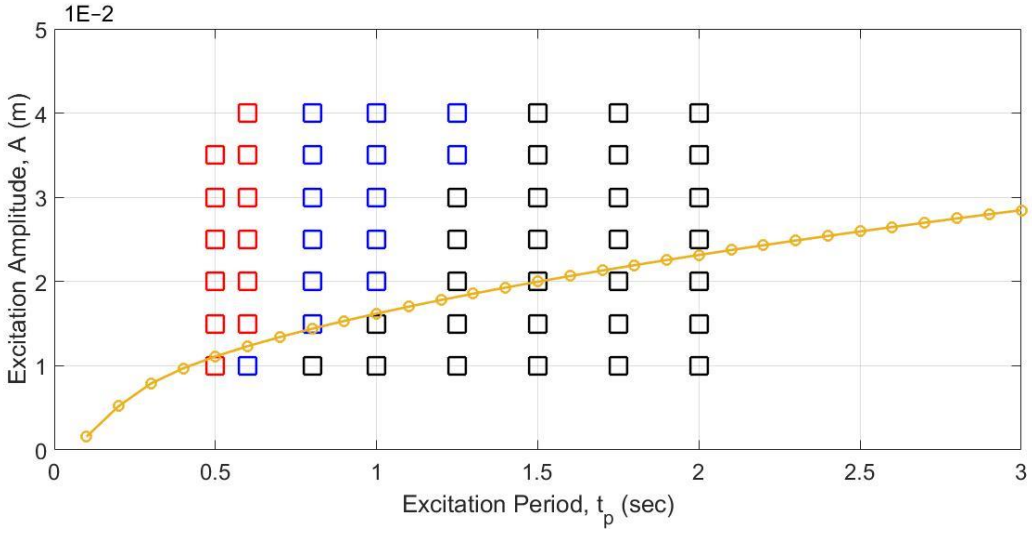

Fig. 2.21 The test matrix for SP_2 in water with the payload weight of 6.13N. The black, blue and red markers respectively denote the non-snap, snap-like and snap events. The yellow line denotes the theoretical snap criterion of Eq. (2.20)

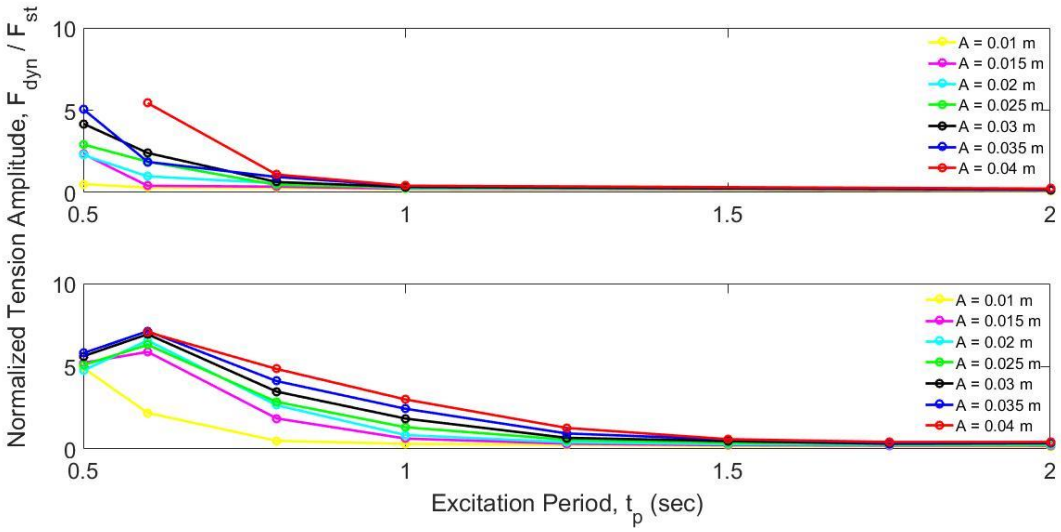

Fig. 2.22 Normalized tension range vs. excitation period for each excitation amplitude with the payload weight of 6.13N. Comparison of SP_2 in air (top) and SP_2 in water (bottom)

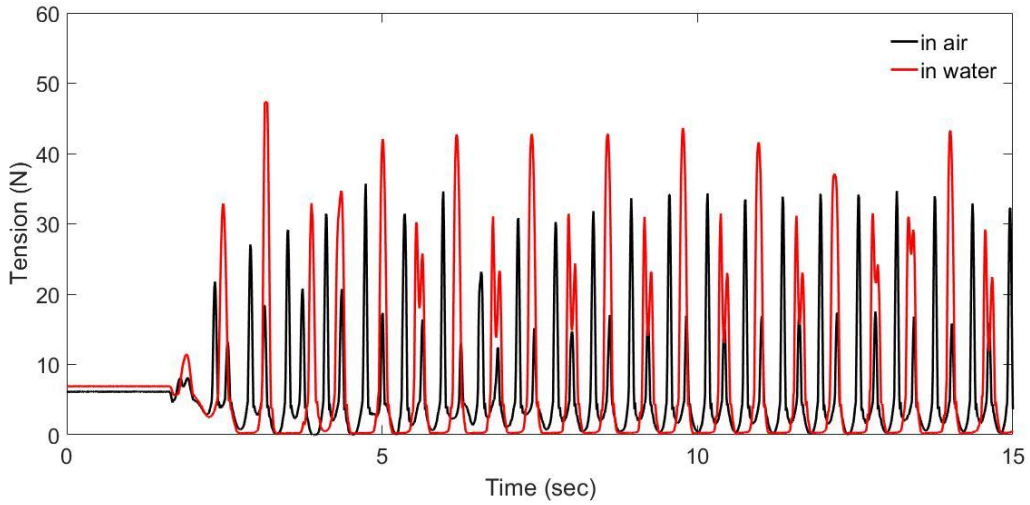

Fig. 2.23 The tension time series of SP_2 in air (black line) and SP_2 in water (red line) with an excitation amplitude of 0.4m, a period of 0.6s and the payload weight of 6.13N

2.6.2 $\mathbf{W_{pl} = 14.25N}$

Fig. 2.24 shows the test matrix of SP_2 carried out in water for W_{pl} = 14.25N. The yellow dashed line is the theoretical snap criterion. In Fig. 2.24, the number of red blocks is significantly lower than the number of SP_2 in water with W_{pl}=6.13N (see Fig. 2.21), but slightly higher than the number of SP_2 in air with W_{pl}=14.25N (see Fig. 2.14). Therefore,

for the bilinear stiffness model in water, the increase in pretension (W_{pl}) would result in the mitigation of snap loads. Under the same pretension the bilinear stiffness model has more snap events with the operations in water than in air. The theoretical criterion is consistent with the test data when $t_p = 0.5$s and deviates onto the prediction of test data with t_p ranged from 0.6 – 0.8s. Again, this is possible because friction is ignored in the theoretical formulation. The theoretical criterion (the yellow line) in Fig. 2.24 moves towards the left and upward compared to the line in Fig. 2.21. By increasing the pretension, higher excitation amplitudes and lower excitation periods are required to create snap loads.

Fig. 2.26 shows the tension histories of SP_2 in air (the black line) and in water (the red line) for A =0.03m and $t_p = 0.5$s. It is clearly seen that the recorded data of SP_2 in water are truncated at 4.9N near the peaks, because of the 5N range of the load cell used in the experiment. Moreover, there exist several cases with these filtered recordings in which A ranged from 0.02m to 0.04m and $t_p = 0.5$s. The same cases of SP_2 in water with W_{pl}=18.95N also found this problem. To obtain meaningful results, the crest values are estimated by using the quadratic extrapolation method. This approach is selected because the second-order curve has a good fit on the peak regions of the snap loads of W_{pl}=6.13N. In Fig. 2.25, the red dashed lines represent the predicted values using the quadratic extrapolation approach. Fig. 2.26 indicates that, snap loads are found in both SP_2 in water and SP_2 in air.

Fig. 2.25 shows the variation of the normalized tension ranges of the tests of SP_2 conducted in air (the top plot) and the tests conducted in water (the bottom plot) for t_p ranged from 0.5s to 2s and A ranged from 0.01m to 0.04m. The dashed circles represented the values

predicted by the quadratic extrapolation method. For SP_2 in air, the normalized tension ranges of each A value are close to zero for t_p ranging from 0.6s to 2s while for SP_2 in water the same phenomenon is found for t_p ranging from 0.8s to 2s. The normalized tension ranges of SP_2 in air and SP_2 in water respectively have significant increases for t_p < 0.6s and 0.8s. For each A value, the normalized tension ranges of SP_2 in water are larger than SP_2 in air. The cases of SP_2 in water have flatter troughs and sharper crests compared with the cases of SP_2 in air. In Fig. 2.26, the amplitudes of SP_2 in water are 2.5 times larger than the amplitudes of SP_2 in air.

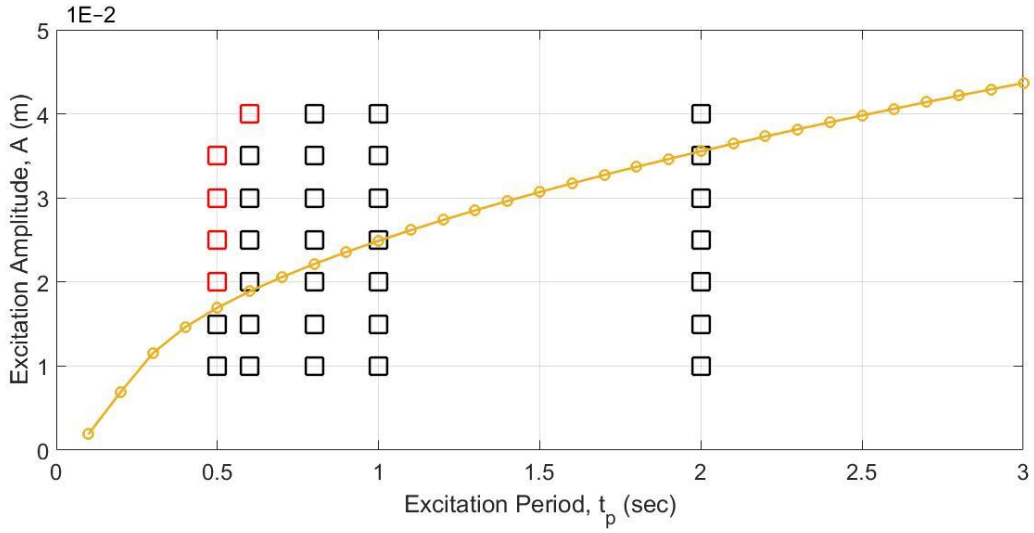

Fig. 2.24 The test matrix for SP_2 in water with the payload weight of 14.25N. The black and red markers respectively denote the non-snap and snap events. The yellow line denotes the theoretical snap criterion of Eq. (2.20)

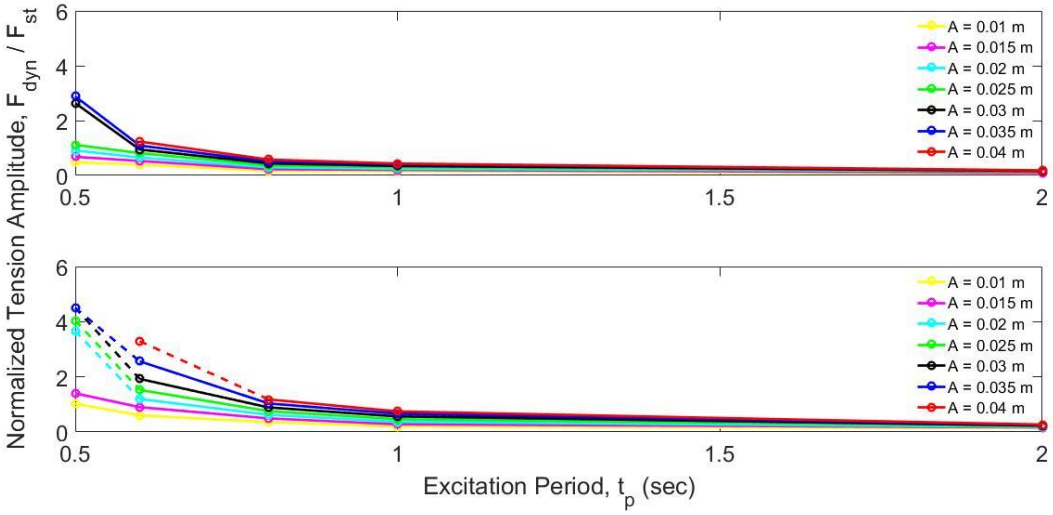

Fig. 2.25 Normalized tension range vs. excitation period for each excitation amplitude with the payload weight of 14.25N. Comparison of SP_2 in air (top) and SP_2 in water (bottom)

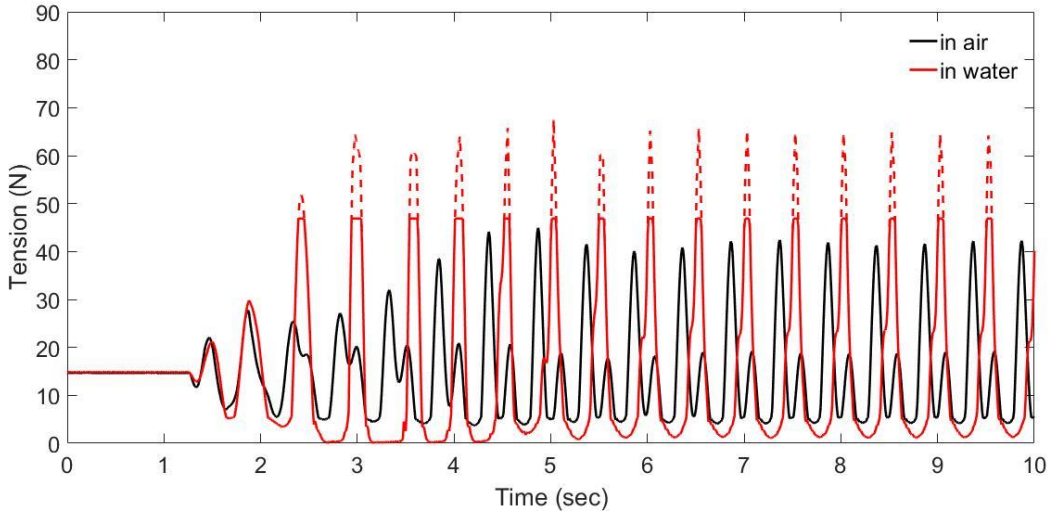

Fig. 2.26 The tension time series of SP_2 in air (black line) and SP_2 in water (red line) with an excitation amplitude of 0.3m, a period of 0.5s and the payload weight of 14.25N

2.6.3 $W_{pl} = 18.95$N

Fig. 2.27 shows the test matrix of SP_2 carried out in water for W_{pl} = 18.95N. The yellow dashed line is the theoretical snap criterion. In Fig. 2.27, the test matrix has the same number of red blocks as SP_2 in water with W_{pl}= 14.25N and has a blue block at A=3.5 and t_p = 0.6s. The theoretical criterion is consistent with the test data when t_p = 0.5s. The

theoretical criterion in Fig. 2.27 moves up and to the left compared to the line in Fig. 2.24. Due to the theoretical snap load criterion, the number of snap load cases decreases with the increase of the pretensions. Fig. 2.28 shows the variation of the normalized tension ranges for SP_2 in air (the top plot) and SP_2 in water (the bottom plot). For each A value, the normalized tension ranges of all the cases of SP_2 in water are slightly larger than the cases of SP_2 in water. Fig. 2.29 shows the tension histories of SP_1 (the black line) and SP_2 (the red line) for A =0.35m and t_p = 0.5s. The troughs and the crests of SP_2 in water are respectively slightly flatter and slightly sharper than these of SP_2 in air. The local minimum tensions of SP_2 in water are slightly lower than the values of SP_2 in air. The local maximum tensions of SP_2 in water are only 1.25 times larger than the values of SP_2 in air.

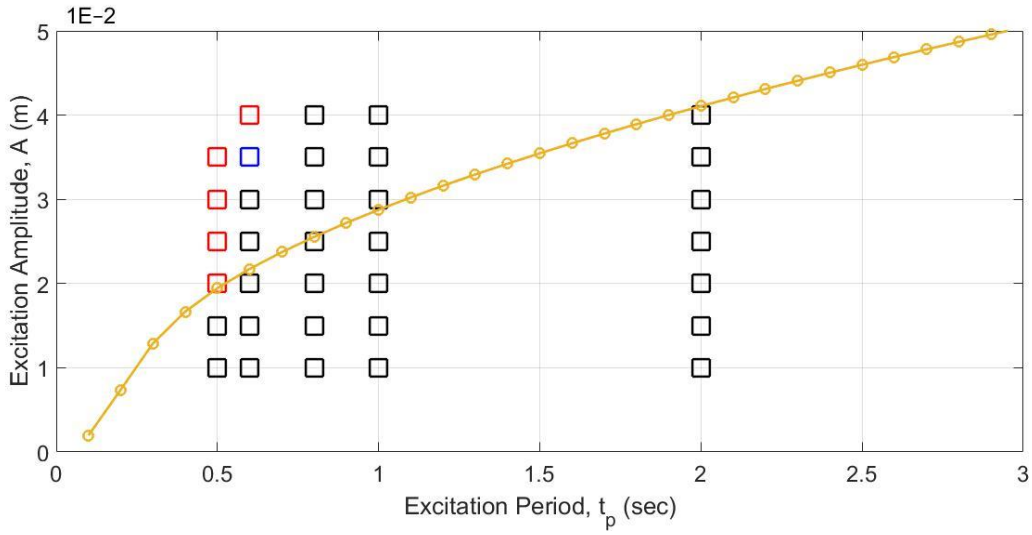

Fig. 2.27 The test matrix for SP_2 carried out in water with the payload weight of 18.95N. The black, blue and red markers respectively denote the non-snap, snap-like and snap events. The yellow line denotes the theoretical snap criterion of Eq. (2.20)

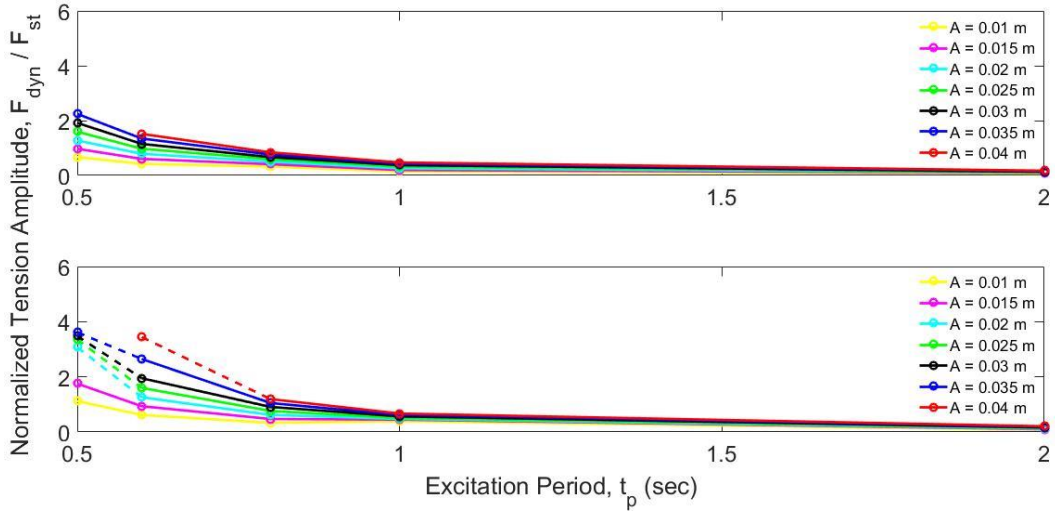

Fig. 2.28 Normalized tension range vs. excitation period for each excitation amplitude with the payload weight of 18.95N. Comparison of SP_2 in air (top) and SP_2 in water (bottom)

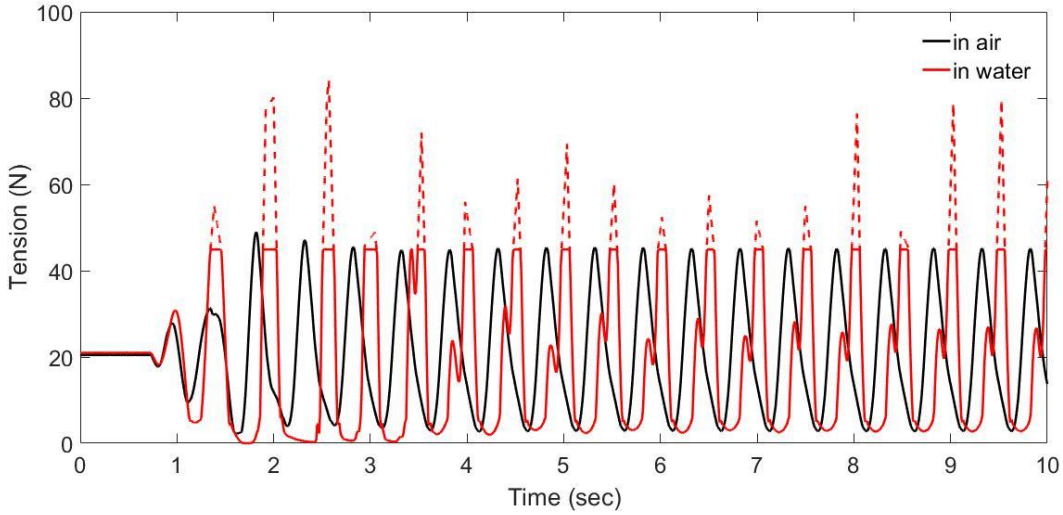

Fig. 2.29 The tension time history at an excitation amplitude of 0.35m, a period of 0.5s and the payload weight of 18.95N. Comparison of SP_2 in air (black line) and SP_2 in water (red line)

2.7 Influence of Weight of the Payload

To investigate the effects of static force on the cable dynamic tension, the cases of SP_1 in air, SP_2 in air, and SP_2 in water are compared and discussed. The excitation amplitudes (A) and time periods (t_p) are normalized as $A/t_p^2\, g$. In the following sections, 2.7.1 and 2.7.2 respectively illustrate the pretension effects on the occurrence of snap loads and on the

normalized tension ranges. The weight of the payloads is made non-dimensional in the following manner:

$$\widehat{W}_{pl} = W_{pl} \,/\, 14.25 \tag{2.23}$$

Where 14.25N is the weight of the second payload, which is the scaled weight of Goeller and Laura's model. Thus, $\widehat{W}_{pl}$ ranges from 0.43 to 1.33.

2.7.1 Effect on the Occurrence of Snap Loads

Figs. 2.30 –32 show the occurrence of snap loads for SP_1 in air, SP_2 in air, and SP_2 in water respectively. The range of $\widehat{W}_{pl}$ is from 0.43 to 1.33, which is the same in each of the three figures. The horizontal axis shows the dimensionless variable of $A/t_p^2\, g$, and the vertical axis shows weights of payloads ($\widehat{W}_{pl}$). The black, blue and red circles represent the cases with non-snap, snap-like, and snap events respectively. In Fig. 2.30, snap events are found in none of the cases of SP_1 in air. The snap and snap-like events are observed in SP_2 in air when $A/t_p^2\, g$ > 0.005, 0.012 and 0.014 for $\widehat{W}_{pl}$ = 0.43, 1 and 1.33 respectively. With the increases of $\widehat{W}_{pl}$, the snap events are found with larger $A/t_p^2\, g$ values, which is also found in the cases of SP_2 in water. The snap and snap-like events in SP_2 in water are observed when $A/t_p^2\, g$ > 0.002, 0.008 and 0.008 for $\widehat{W}_{pl}$ = 0.43, 1 and 1.33 respectively. This finding indicates that water force can result in a higher probability of snap loads and triggers snap loads with a lower $A/t_p^2\, g$ value. The yellow dashed line in Fig. 2.32 shows the theoretical criterion of a snap load which is calculated from Eq. (2.20). The right side of the line indicates that there is a high probability of snap loads, while the left side shows the non-snap region. The theoretical criterion is consistent with the test results. In regard

of the test results of $\widehat{W}_{pl}$ = 0.43, snap and snap-like events start to appear at $A/t_p^2\ g$ = 0.002 and 0.004 respectively. The yellow dashed line indicates that the occurrence of snap loads is strongly correlated with the pretension.

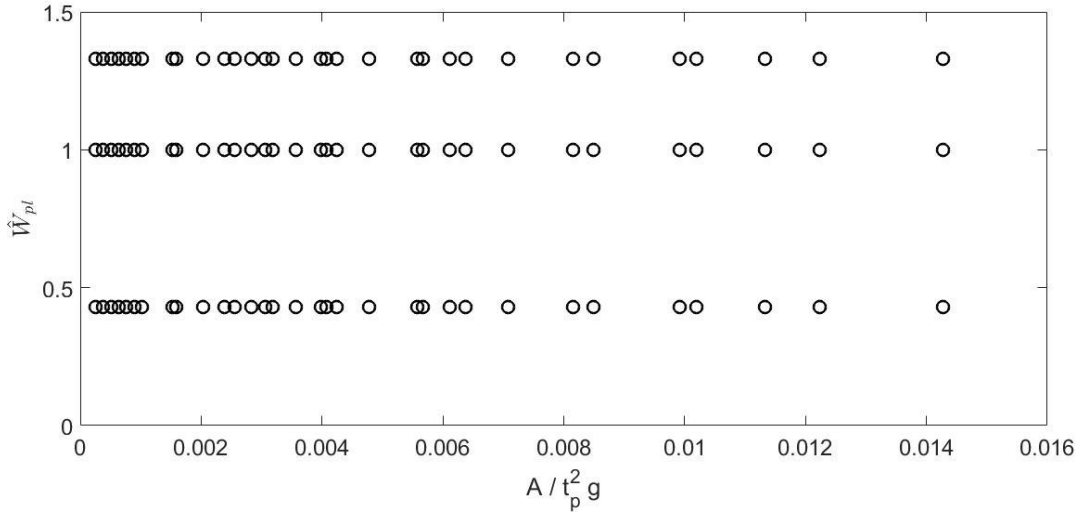

Fig. 2.30 The test matrix for SP_1 carried out in air with the various payload weights and $A/t_p^2\ g$ values. The black markers denote the non-snap events

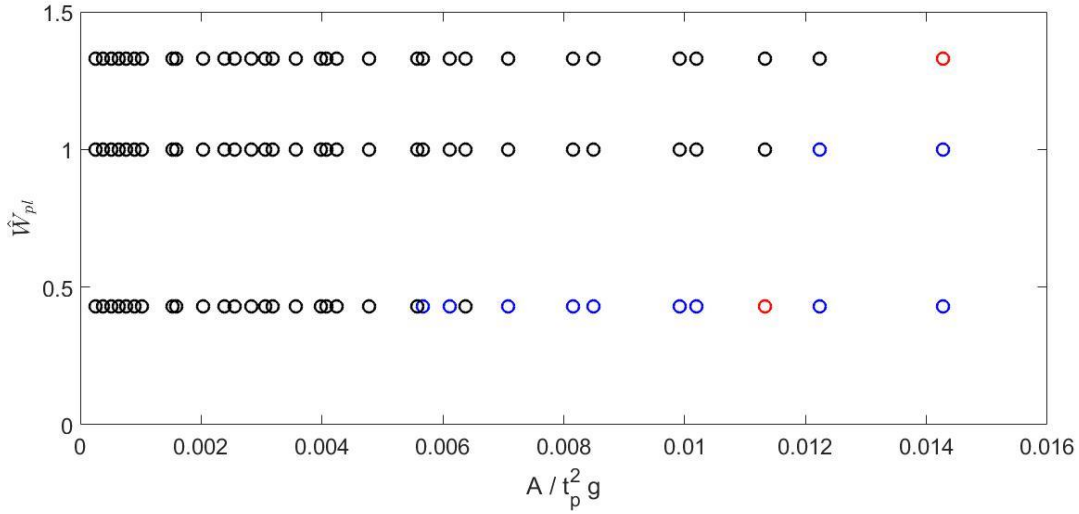

Fig. 2.31 The test matrix for SP_2 carried out in air with the various payload weights and $A/t_p^2\ g$ values. The black, blue and red markers respectively denote the non-snap, snap-like and snap events

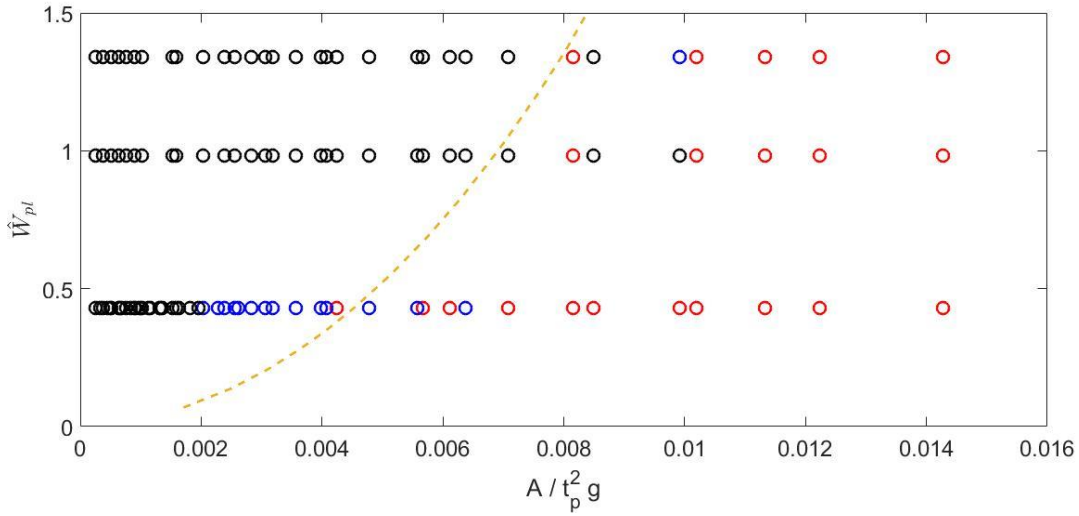

Fig. 2.32 The test matrix for SP_2 carried out in water with the various payload weights and $A/t_p^2\ g$ values. The black, blue and red markers respectively denote the non-snap, snap-like and snap events. The yellow line denotes the theoretical snap criterion of Eq. (2.20)

2.7.2 Effect on the Normalized Tension Ranges

In Fig. 2.33, the normalized tensions of the three different pretensions ($\widehat{W}_{pl}$) are very close for all $A/t_p^2\ g$ values. For all three W_{pl}, the normalized tension ranges grow as the $A/t_p^2\ g$ values increased, and all of them are smaller than 2. In Fig. 2.34, the normalized tension ranges of the three $\widehat{W}_{pl}$ are close when the $A/t_p^2\ g$ < 0.006. The amplitudes of $\widehat{W}_{pl}$ = 0.43 deviate from those of the other two when $A/t_p^2\ g$ > 0.006. For $\widehat{W}_{pl}$ = 0.43, the snap loads are observed when $A/t_p^2\ g$ > 0.006. This indicates that the normalized amplitudes of snap loads are significantly larger than those of non-snap events. Moreover, the smaller pretensions result in larger normalized tension ranges. For $A/t_p^2\ g$ > 0.006, the normalized tension ranges of $\widehat{W}_{pl}$ = 0.43 are 2 – 2.5 times larger than those of the other two payloads. In Fig. 2.35, the black markers ($\widehat{W}_{pl}$ = 0.43) deviate from the other two when $A/t_p^2\ g$ > 0.002. For $\widehat{W}_{pl}$ = 0.43, the normalized tension ranges in Fig. 2.35 are 1.5 times larger than the amplitudes in Fig. 2.34. These findings indicate that the water force together with the

small pretension could result in larger normalized tension ranges within the region of smaller $A/t_p^2\ g$ values.

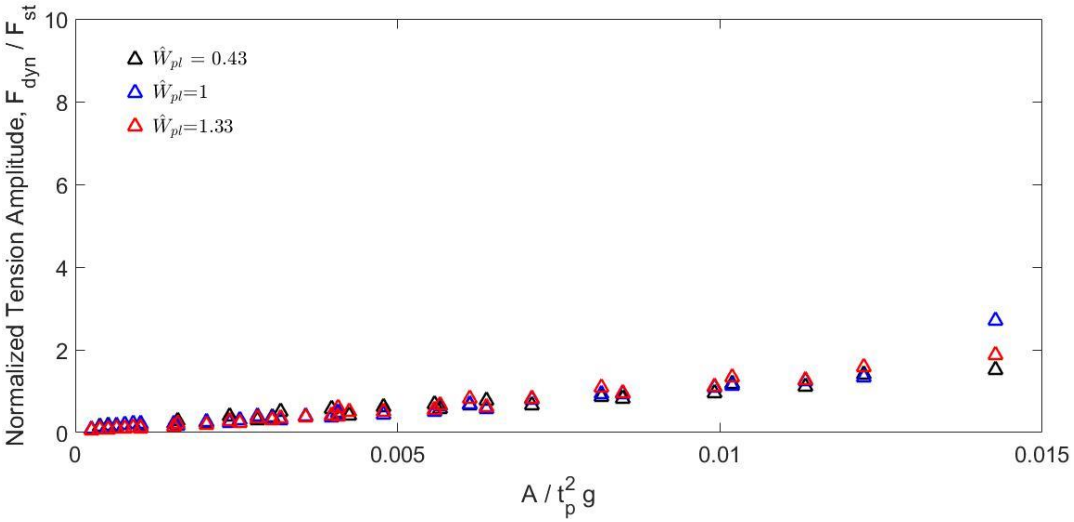

Fig. 2.33 Normalized tension range vs. $A/t_p^2\ g$ values for SP_1 in air. Comparison of $\widehat{W}_{pl}$ = 0.43, 1 and 1.33

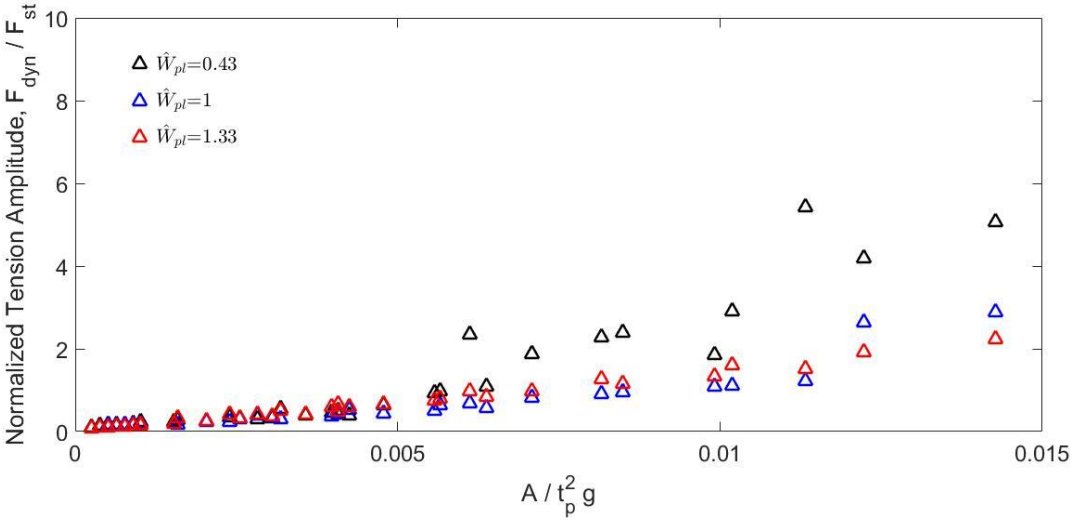

Fig. 2.34 Normalized tension range vs. $A/t_p^2\ g$ values for SP_2 in air. Comparison of $\widehat{W}_{pl}$ = 0.43, 1 and 1.33

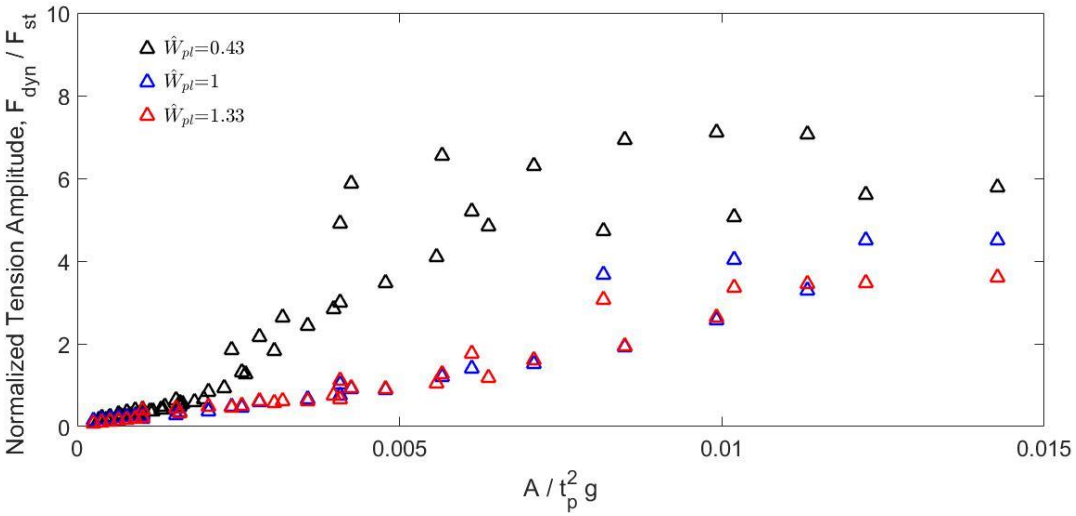

Fig. 2.35 Normalized tension range vs. $A/t_p^2\ g$ values for SP_2 in water. Comparison of $\widehat{W}_{pl}$ = 0.43, 1 and 1.33

CHAPTER 3

INVESTIGATION OF EXTREME TENSIONS IN FOWT MOORING SYSTEMS USING TEST DATA

In the previous chapter, snap loads on a nonlinear vertical cable model were investigated. The study suggests that nonlinearity of the line stiffness and hydrodynamic drag force can play important roles in the formation of snap loads. Moreover, the water force together with a small pretension could result in larger normalized tension amplitudes within the region of smaller $A/t_p^2\ g$ values.

In this chapter, the mooring systems of different types of FOWTs are investigated. The FOWT TLP is selected and compared with the mooring system of the FOWT Semi. A FOWT TLP is a vertically moored floating structure and incorporates taut (high-pretension) moorings. A FOWT Semi is a catenary moored platform with relatively lower pretension compared to a TLP. Moreover, the configurations of the two foundations are also very different. For example, the mass and the displacement of Semi are about 10 times that of a TLP. For a TLP, the natural frequencies of the roll, pitch, and heave are all much higher than Semi.

The floater motions and dynamic tensions of the mooring systems are studied using the 1:50 scale FOWT model tests. Several extreme tensions on FOWT mooring lines are observed in the DeepCWind 1:50 scale FOWT Semi models, as well as the TLP model. All results presented in this study are in full-scale units. Moreover, wind forces and turbine thrust coefficients have significant effects on the snap loads, and they are discussed herein.

3.1 DeepCWind FOWT

Snap loads are observed in the tests of both the semi-submersible model with the Froude scale wind turbine model in 2011 and the same semi-submersible model with the performance scaled wind turbine model in 2013 as well as the 2011 TLP model with the Froude scale wind turbine model. Following, these three models are respectively named as "SF", "SP" and "TF." These three models are selected to investigate snap loads in this chapter.

3.1.1 1:50 Scale Semi-submersible Model with Froude Scaled Turbine (SF)

The depth of the prototype platform draft is 20 m and the water depth is 200 m. Fig. 3.1 and Fig. 3.2, respectively, show the side and top view of the model, along with their principal dimensions. The main properties of the semi-submersible are shown in Table 3.1. Fig. 3.3 and Fig. 3.4 respectively show the semi model and the semi wind turbine model set-up in the basin. The prototype mooring system is comprised of three catenary chains oriented at 60, 180 and 300 degrees with respect to the *x*-axis. The lines are stud-less chains with properties as shown in Table 3.2. The mooring system used in the model experiments is made up of inextensible lines attached to linear springs located at the anchors to provide a close match to the prototype stiffness values. Table 3.3 shows the wind turbine properties of the 2011 turbine model.

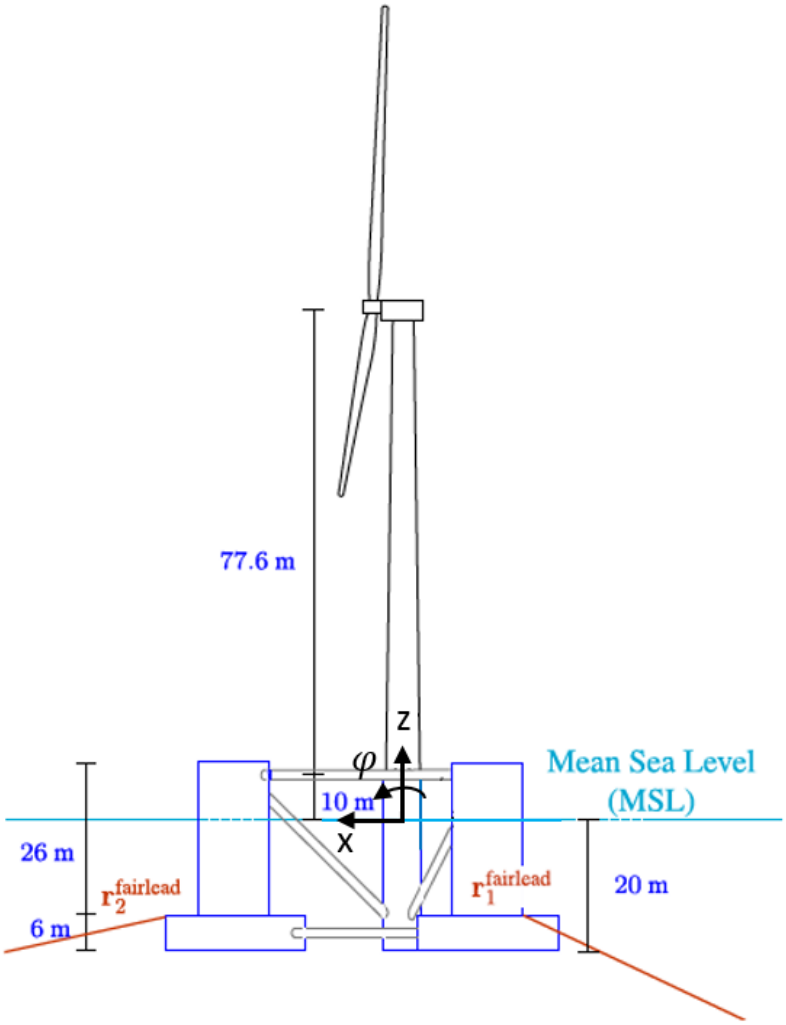

Fig. 3.1 Side view of Semi wind turbine model [5]

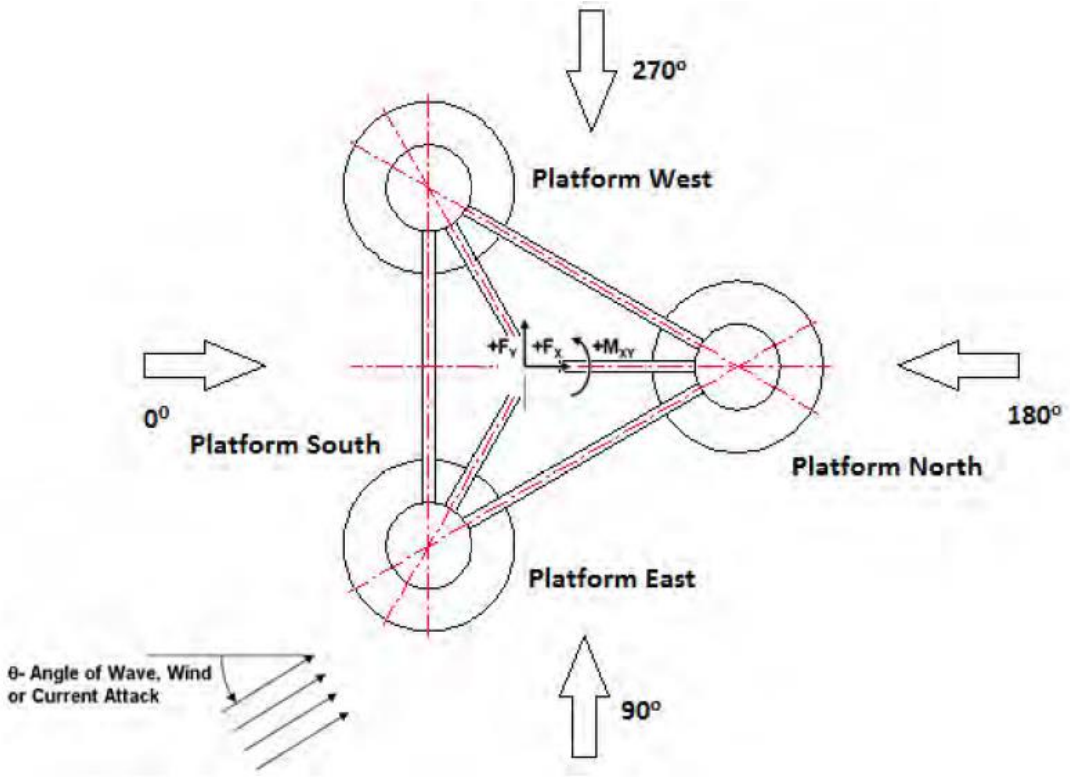

Fig. 3.2 Top view of Semi wind turbine model [5]

Fig. 3.3 Semi model

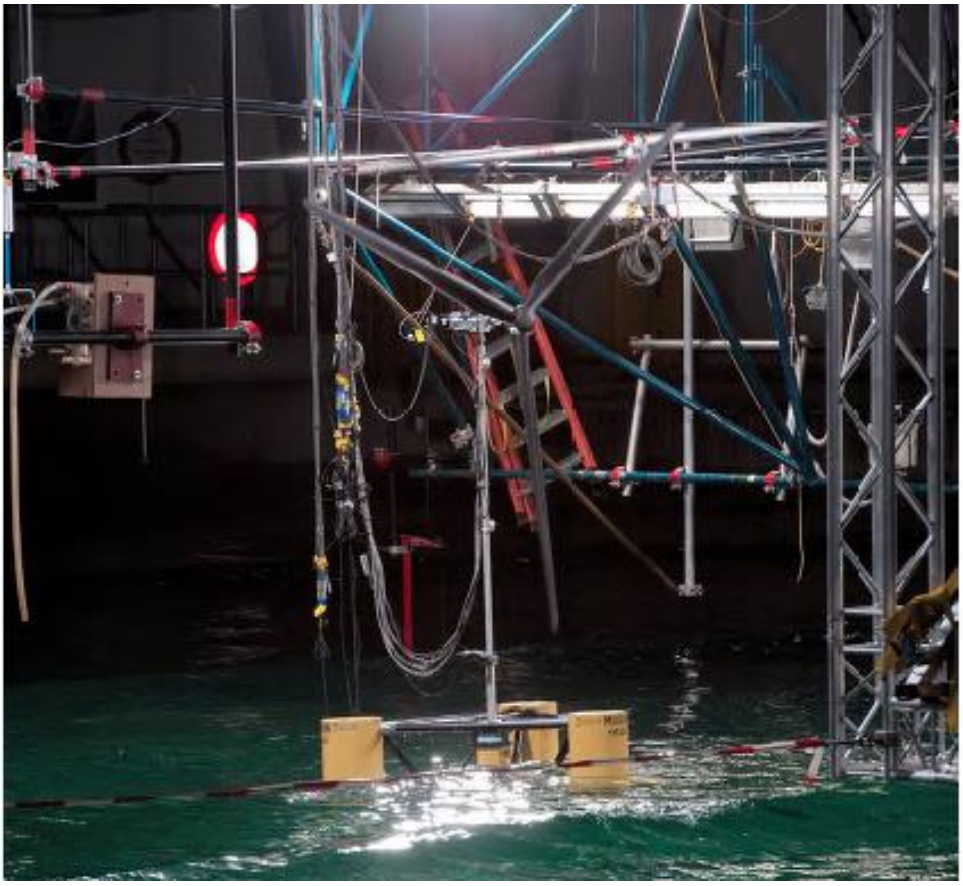

Fig. 3.4 Semi wind turbine model set-up in the basin [5]

Table 3.1 Main particular Semi with turbine of SF [5]

Designation	Magnitude	Unit
Mass	14,040	ton
Displacement	14,265	ton
Center of Gravity above keel	10.11	m
Roll radius of gyration in air	31.61	m
Pitch radius of gyration in air	32.34	m
Natural roll period (moored)	26.9	s
Natural pitch period (moored)	26.8	s
Natural heave period (moored)	17.5	s

Table 3.2 Mooring line properties of SF [5]

Designation	Magnitude	Unit
Radius to anchor	837.6	m
Depth of anchor	200	m
Radius to fairlead	40.9	m
Draft of fairlead	14	m
Un-stretched line length	835.5	m
Line diameter	0.08	m
Line mass density (dry)	123.8	kg/m
Line mass density (wet)	108.7	kg/m
Line extensional stiffness	752.9	MN

Table 3.3 Main properties of the wind turbine of SF

Designation	Magnitude	Unit
Rotor orientation, configuration	Upwind, 3 blades	
Rotor diameter	126.0	m
Hub diameter	3.0	m
Hub height above SWL	90.0	m
Height of tower-top flange above SWL	87.6	m
Total tower-top mass	397,160	kg

3.1.2 1:50 Scale Semi-submersible Model with Performance Scaled Turbine (SP)

In 2013, University of Maine commissioned MARIN to perform repeat model tests on the 5MW DeepCWind semi-submersible FOWT concept. The reason to repeat model tests was to improve the turbine blade performance. The blade shape was altered to improve performance with the same floater model. While the intent was to duplicate the 2011 main

particulars for the floating wind turbine system with the exception of wind turbine performance in the 2013 test, differences in the mass properties of the improved wind turbine yielded slightly different system properties. The main properties and the model test details can be found in earlier works [53]. The platform dimensions for the system which are identical for the 2011 and 2013 campaigns. Fig. 3.5 shows the side view of Semi wind turbine model. Fig. 3.6 shows the Semi wind turbine model set-up in the basin. Table 3.4 shows the gross quantities of interest for the two systems. The tower and wind turbine properties are different. Table 3.5 shows the natural periods and frequencies for the two systems.

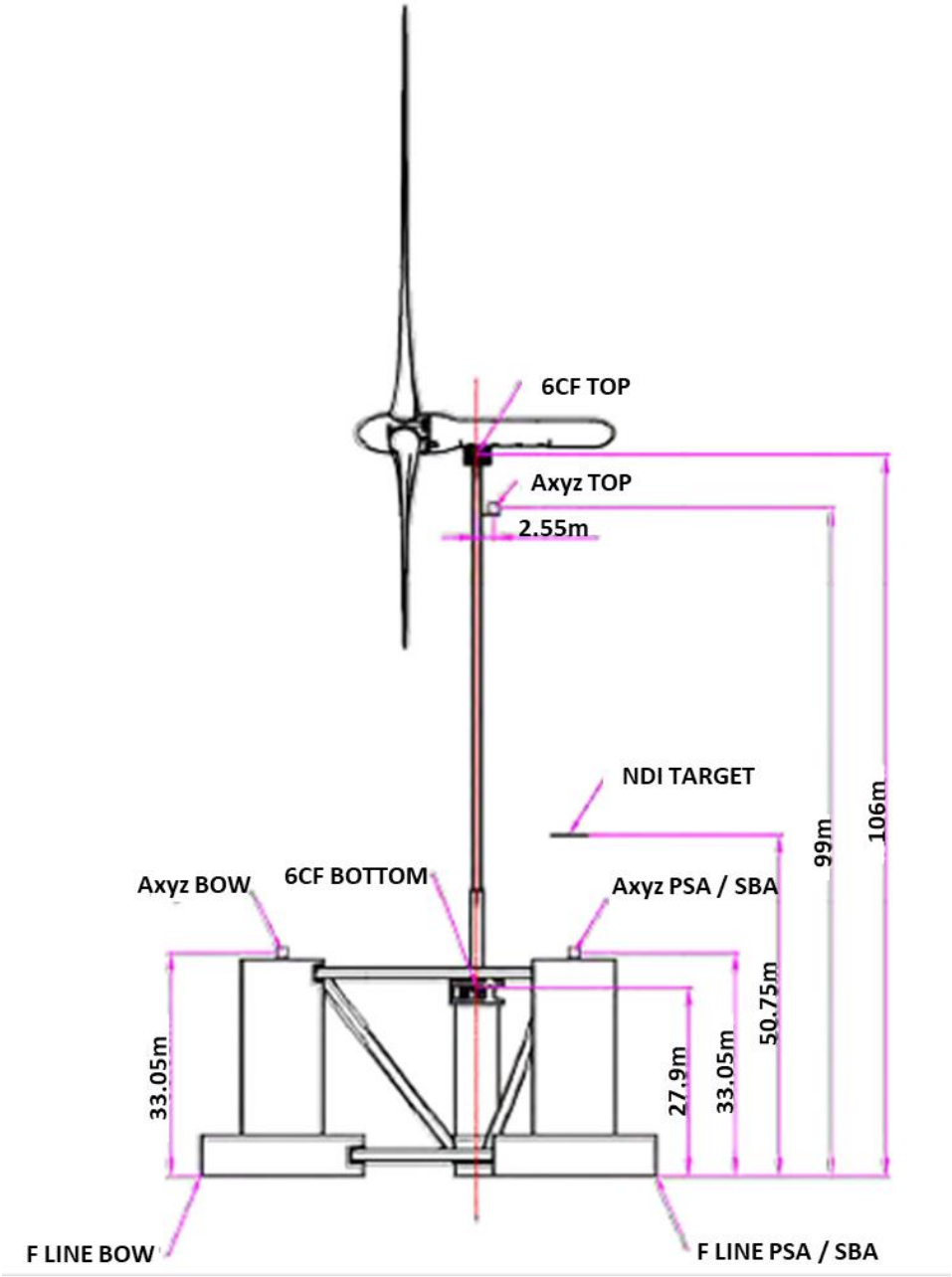

Fig. 3.5 Side view of Semi wind turbine model [54]

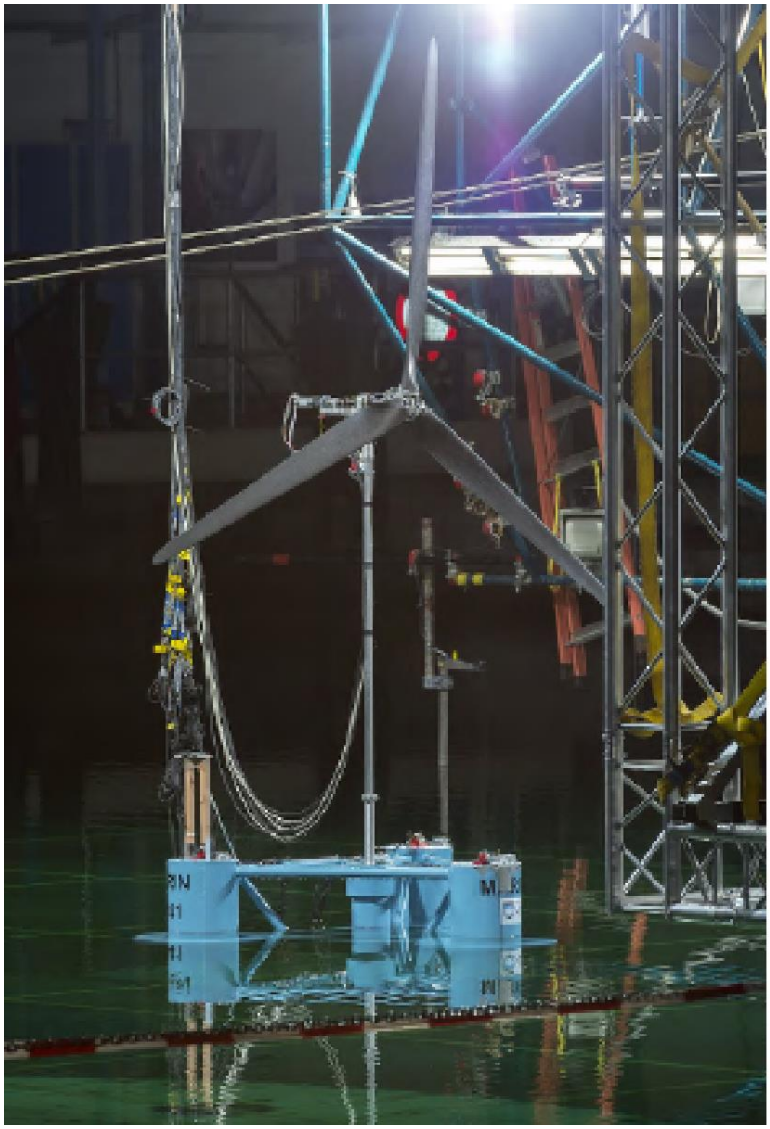

Fig. 3.6 Semi wind turbine model set-up in the basin [54]

Table 3.4 Gross properties of the SF and SP systems [53]

Quantity	2011	2013
Rotor Diameter (m)	126.0	126.0
Hub Height (m)	90.0	90.0
Draft (m)	20.0	20.0
Mooring Spread Diameter (m)	1675	1675
Mass w/ Turbine (MT)	14,040	13,958
Displacement (MT)	14,265	14,265
CG Above Keel (m)	10.11	11.93
Roll Radius of Gyration (m)	31.61	32.63
Pitch Radius of Gyration (m)	32.34	33.38

Table 3.5 Natural periods and frequencies for the SF and SP systems [53]

DOF	2011	2013
Surge (s)	107	107
Sway (s)	112	112
Heave (s)	17.5	17.5
Roll (s)	26.9	32.8
Pitch (s)	26.8	32.5
Yaw (s)	82.3	80.8
Tower Fore-aft Bending (Hz)	0.35	0.32
Tower Side-side Bending (Hz)	0.38	0.34

3.1.3 1:50 Scale Tension Leg Platform Model with Froude Scaled Turbine (TF)

The prototype water depth is 200 m and the platform draft is 30m. Fig. 3.7 shows the TLP model with a wind turbine. The main properties of the TLP are shown in Table 3.6. Figs. 3.8 and 3.9 respectively show the top view and side view of the model along with their principal dimensions. The three tendons are oriented at 60, 180 and 300 degrees with respect to the *x*-axis. The three tendons used in the model tests are constructed from stainless steel tubes as shown in Table 3.7. The tubes are closed at both ends by brazed metal caps and attached to a linear spring located at the anchors to provide a close match to prototype stiffness value.

Fig. 3.7 TLP model with wind turbine [5]

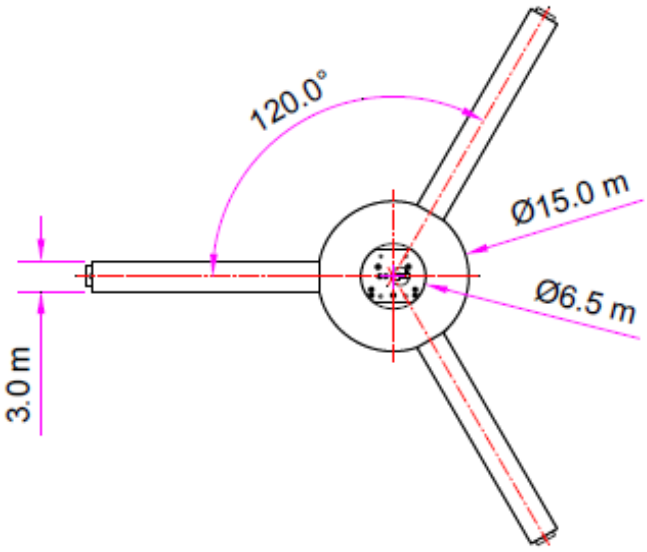

Fig. 3.8 Top view of TLP wind turbine model [5]

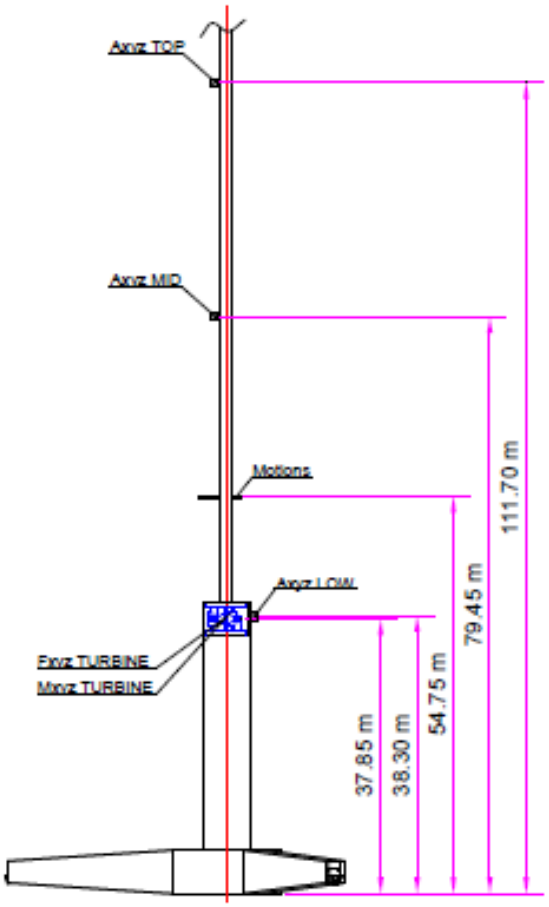

Fig. 3.9 Side view of TLP wind turbine model [5]

Table 3.6 Main particular TLP with turbine [5]

Designation	Magnitude	Unit
Mass	1,361	ton
Displacement	2,840	ton
Center of Gravity above keel	64.06	m
Roll radius of gyration in air	52.61	m
Pitch radius of gyration in air	52.69	m
Natural roll period (moored)	3.7	s
Natural pitch period (moored)	3.7	s
Natural heave period (moored)	1.25	s

Table 3.7 TLP tendon properties [5]

Designation	Magnitude	Unit
Radius to anchor	30	m
Depth of anchor	200	m
Radius to fairlead	30	m
Draft of fairlead	30	m
Un-stretched line length	171.4	m
Line diameter	0.6	m
Line mass density (dry)	301.2	kg/m
Line mass density (wet)	10.5	kg/m
Line extensional stiffness	7500	MN

3.2 Description of the Experimental Data Set

For both SF and SP, snap loads are found under the survival sea-state while for TF, snap loads are observed in both operational and survival sea-states. To compare the snap loads of these three models, this study only considers cases under survival storm conditions (i.e., a 100-year storm). Thus, all the cases correspond to a survival sea state described by a JONSWAP spectrum with a significant wave height of 10.5 m, peak wave period of 14.3 s, and peak enhancement factor of 3.0, the waves act on the platform for a test duration of 3.5 hours. The prototype water depth is 200m while the wind speed is varied from 0 to 30.5 m/s. The wind conditions range from a steady wind to turbulent wind characterized by a NPD spectrum. It is notable that MARIN requests a half hour to settle in the model. Therefore, the tests have reached the steady-state by the time a half hour (full-scale time) has passed. Several snap events were also observed in the first half hour tension time history for SF, SP and TF. Since the snap events are infrequent, to include all the snap events for extreme tension analysis, the 3.5hr data are used for this study. The statistical analysis and tension maxima analysis of 3.5hr data and 3hr data (removing the first half hour data) are compared in Appendix B. The statistical differences are about 1.5% which indicates the 3.5hr test data are suitable to use for this study. Tables 3.8 - 10 show the environmental conditions that snap loads were observed for SF, SP, and TF respectively.

Table 3.8 Wave and wind conditions for Cases 1 - 7 corresponding to experimental data of SF (* indicates the cases with a nacelle yaw error of 20 degrees)

Case	Wave Conditions			Wind Conditions		
	H_s (m)	T_p (s)	Γ	V_w (m/s)	Wind Type	Ω (rpm)
1	10.5	14.3	3	0	-	0
2	10.5	14.3	3	21	Turbulent	12.73
3*	10.5	14.3	3	21	Turbulent	12.73
4	10.5	14.3	3	21	Steady	12.73
5*	10.5	14.3	3	21	Steady	12.73
6	10.5	14.3	3	30.5	Turbulent	0
7	10.5	14.3	3	30.5	Steady	0

Table 3.9 Wave and wind conditions for Cases 1 – 3 corresponding to experimental data of SP

Case	Wave Conditions			Wind Conditions		
	H_s (m)	T_p (s)	Γ	V_w (m/s)	Wind Type	Ω (rpm)
1	10.5	14.3	3	0	-	0
2	10.5	14.3	3	13	Steady	12.1
3	10.5	14.3	3	13	Turbulent	12.1

Table 3.10 Wave and wind conditions for Cases 1 - 5 corresponding to experimental data of TF

Case	Wave Conditions			Wind Conditions		
	H_s (m)	T_p (s)	Γ	V_w (m/s)	Wind Type	Ω (rpm)
1	10.5	14.3	3	0	-	0
2	10.5	14.3	3	21	Steady	12.73
3	10.5	14.3	3	21	Turbulent	12.73
4	10.5	14.3	3	30.5	Turbulent	0
5	10.5	14.3	3	30.5	Steady	0

Table 3.11 shows the five environmental conditions that comprise the data set used in this study. For SF and TF, constant wind speeds of 0 and 21m/s are selected while for SP, a constant wind speed of 13m/s is selected. The reason of choosing a lower wind speed of 13m/s for SP is that the revised blade profile improved the blade performance and lead to a thrust force similar to SF with a wind speed of 21m/s.

The directions of the wind and waves are 180o with respect to the x-axis (Fig. 3.1). Fig. 3.10 shows sample tension time histories in the prototype units for the three mooring lines corresponding to SF1. For the windward line (line 1), several spikes in tension, with maximum values ranging from 3000 to 6000 kN, occur randomly during the 3.5-hr time record. Comparatively, the tension in Lines 2 and 3 range from 500 to less than 1500 kN. The same phenomenon is observed in SF2, SP1, SP2, and TF2. However, snap loads are found in three tendons of TF2 (Fig. 3.11). The static tensions of Tendon 2 and 3 are higher than Tendon 1. However, the number of snap events in Tendon 2 and 3 are much lower than in Tendon 1. The windward line (line 1) of all the cases are considered in this study.

The data from the model tests are used to study how the snap force of the mooring lines may influence the floater motion and vice versa.

Table 3.11 Environmental Conditions of five cases

Case	Wave Conditions			Steady Wind Conditions	
	H_S (m)	T_p (s)	Γ	V_w (m/s)	Ω (rpm)
SF1	10.5	14.3	3	0	0
SF2	10.5	14.3	3	21	12.73
SP1	10.5	14.3	3	0	0
SP2	10.5	14.3	3	13	12.1
TF2	10.5	14.3	3	21	12.73

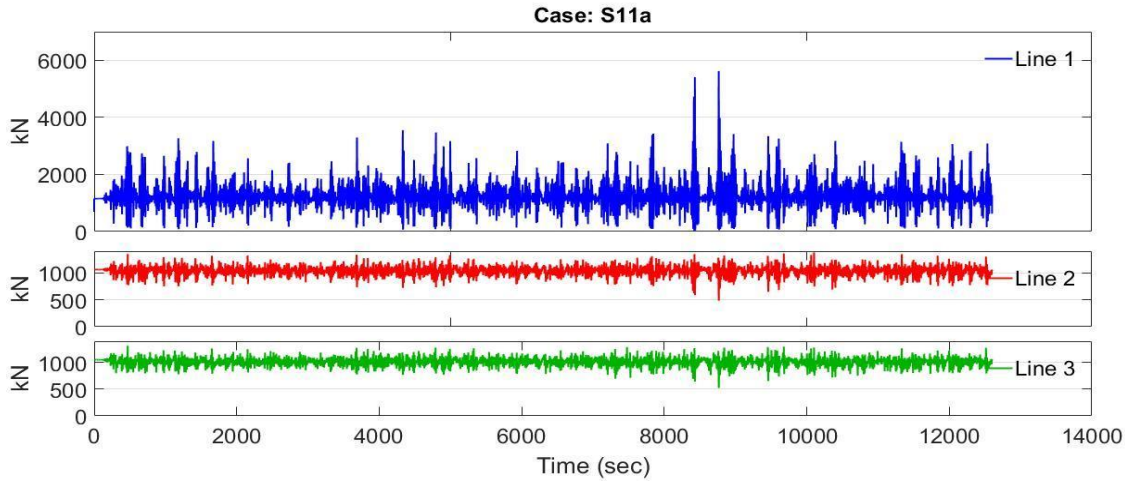

Fig. 3.10 Three-and-one-half hour long mooring line histories for lines 1, 2, and 3 corresponding to case SF1

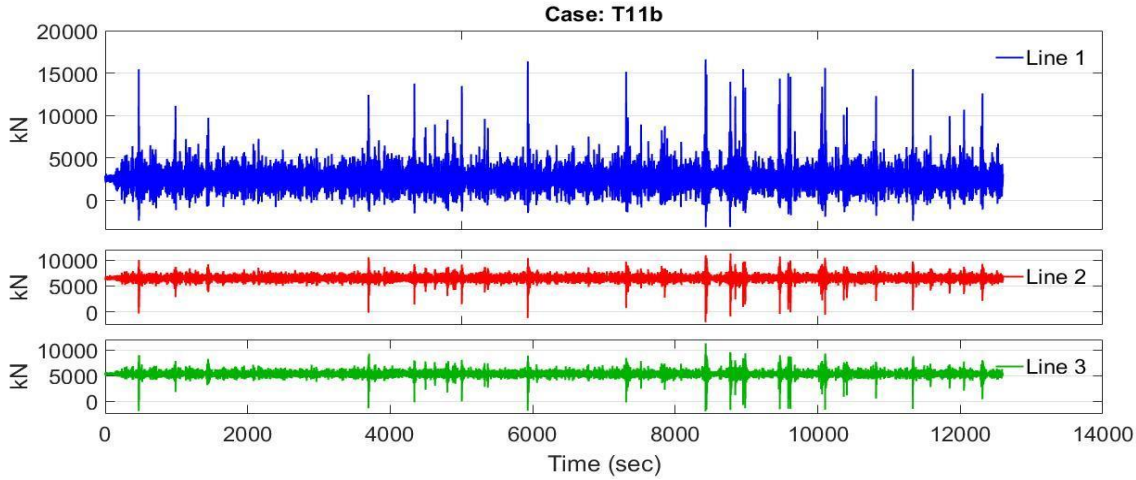

Fig. 3.11 Three-and-one-half hour long mooring line histories for Lines 1, 2, and 3 corresponding to case TF2

3.3 Snap Load Criteria

This study investigates line tensions measured during experiments conducted on a 1:50-scale semi-submersible FOWT [55]. Using DNV's snap condition criterion (Eq. 1.9), the potential existence of snap loading on the mooring system of a FOWT is presented. Fig. 3.12 shows an illustrative line tension time history obtained from experiments of the semi-submersible FOWT subject to survival storm conditions [55]. For this case, the significant height, peak wave period and steady wind speed were 10.5 m, 14.3 s, and 30.5 m/s, respectively.

Following Eq. (1.9), a threshold minimum is defined as 10% of the pre-tension value. A snap event is initiated after a local minimum tension value falls below the threshold tension, and lasts until the tension spikes to a value greater than the pretension.

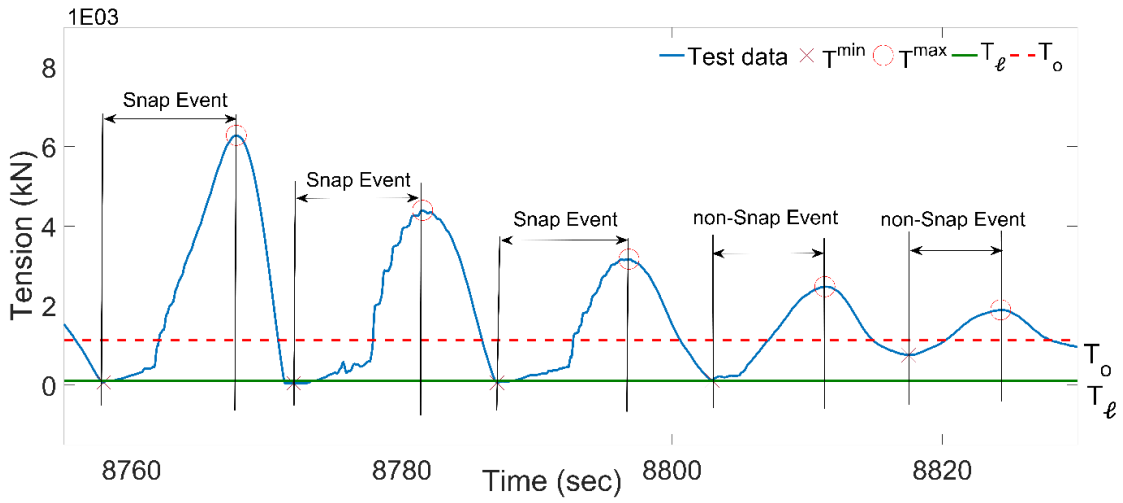

Fig. 3.12 Demonstration of mooring line time history along with snap events

Consistent with [56] the dynamic tension (T_i) is defined as the range extending from a local minimum to an immediately following maximum (shown in Fig. 1.2), i.e.

$$T_i = T_i^{max} - T_i^{min}, i = 1\ to\ r \tag{3.1}$$

where r is the total number of measurements of dynamic tension values from a time history. The set of cyclical dynamic tensions are separated into snap induced dynamic tensions (T^s) and those that are not associated with a snap event (T^n). The latter could be labeled as non-snap events. The distinction between T^n and T^s is based on whether the range exceeds the minimum and maximum thresholds, i.e.

$$T_j^n = T_j^{max} - T_j^{min}\ \ for \begin{cases} T_j^{max} > T_o \\ T_j^{min} > T_\ell \end{cases}, j = 1\ to\ p \tag{3.2}$$

$$T_k^s = T_k^{max} - T_k^{min}\ \ for \begin{cases} T_k^{max} > T_o \\ T_k^{min} \leq T_\ell \end{cases}, k = 1\ to\ q \tag{3.3}$$

Here T_o is the pretension of the mooring line and T_ℓ is the slack tension, equal to 10% of T_o. In the context of Eq. (1.9), the static load strictly refers to the pretension (T_o) plus the contribution due to the mean load from the waves. Thus, using the pretension as a proxy

for the static load implies a stricter application of the DNV criterion. The three series—i.e., T, T^n and T^s—for each 3.5-hour storm test data set are made non-dimensional in the following manner:

$$\hat{T} = T/T_{rms} \tag{3.4}$$

$$\hat{T}^n = T^n/T_{rms} \tag{3.5}$$

$$\hat{T}^s = T^s/T_{rms} \tag{3.6}$$

where T_{rms} represents the root-mean-square (rms) maximum dynamic tension. This rms value has conventional importance in determining mooring system response and is widely used in the study of floating platform motions [57-59]. Henceforth, the non-dimensional dynamic tension (Eq. 3.7) is referred to as dynamic tension for simplicity. The tension history data are made non-dimensional in the following manner:

$$\hat{T}_{dyn}(t) = T_{dyn}(t)/T_{rms} \tag{3.7}$$

3.4 Dynamic Line Tensions and Platform Motions Analysis of TLP and Semi

The dynamic line tensions and the platform motions of the TLP model and the Semi model are compared under no wind condition (SF1 and TF1). The following characteristics of the snap loads are investigated: their amplitudes, their frequencies, and the correlation coefficient (Eq. 3.8) of floater motions with mooring line tensions.

$$r_{xy} = \frac{\sum_{i=1}^{n}(x_i - x_m)(y_i - y_m)}{(n-1)\sigma_x\sigma_y} \tag{3.8}$$

Here r_{xy} is the correlation coefficient of the variables *x* and *y*. x_m and y_m are respectively the mean values of random variables *x* and *y*. σ_x and σ_y are respectively the standard

deviations of the random variables x and y, and n is the total number of the variables. Time histories of various measurements corresponding to the described storm conditions are shown in Figs. 3.13 and 3.14 for SF1 and TF1, respectively. For both models, the correlation coefficients of some of these measurements with the mooring tension are shown in Fig. 3.15. Fig. 3.13 – 1 and Fig. 3.14 – 1 show the normalized line tension variation versus time of SF1 and TF1, respectively. Figs. 3.13 – 2, – 3, and – 4 show the fairlead lateral displacement, fairlead vertical displacement, and fairlead pitch motion of SF1, respectively. The displacement in the x-direction has a phase shift that is absent in the z-direction. When a slack condition occurs, the floater is at its lowest vertical position and line tension is close to zero. Immediately afterward, when a snap force occurs the fairlead is at its highest vertical position. The vertical position of the fairlead has a high correlation with the line tension as seen in Fig. 3.15., and the correlation coefficient is 0.675. It is found from the experiments that there is a phase shift between the lateral displacement of the fairlead and the line tension. When compared to the vertical position, the lateral displacement has a relatively lower correlation coefficient of 0.222. The pitch motion lags in time with respect to the mooring line tension. The pitch angle increases as the mooring line tension decrease. The pitch motion has a negative correlation to line tension (the correlation coefficient is 0.243).

Figs. 3.14 – 2, – 3, and – 4 show the fairlead lateral displacement, fairlead vertical displacement, and fairlead pitch motion of TF1, respectively. Compared to SF1, the phases of the lateral displacement and the pitch motion of TF1 are not very different. The vertical position, lateral motion, and pitch motion have high correlations with the line tension as seen in Fig. 3.15., and the correlation coefficients are 0.884, 0.675 and 0.907, respectively.

These findings indicate that the dynamic line tensions have a higher impact on the platform motions (surge, heave, and pitch) of the TLP model than the Semi model under a no wind condition. Moreover, the range of normalized tensions, vertical movement, and pitch motions of TF1 are smaller than SF1. This means the TLP model has lower dynamic tensions and platform motions. By observing the lateral measurements, SF1 has a drift motion with an average displacement of -2.3m while TF1 does not.

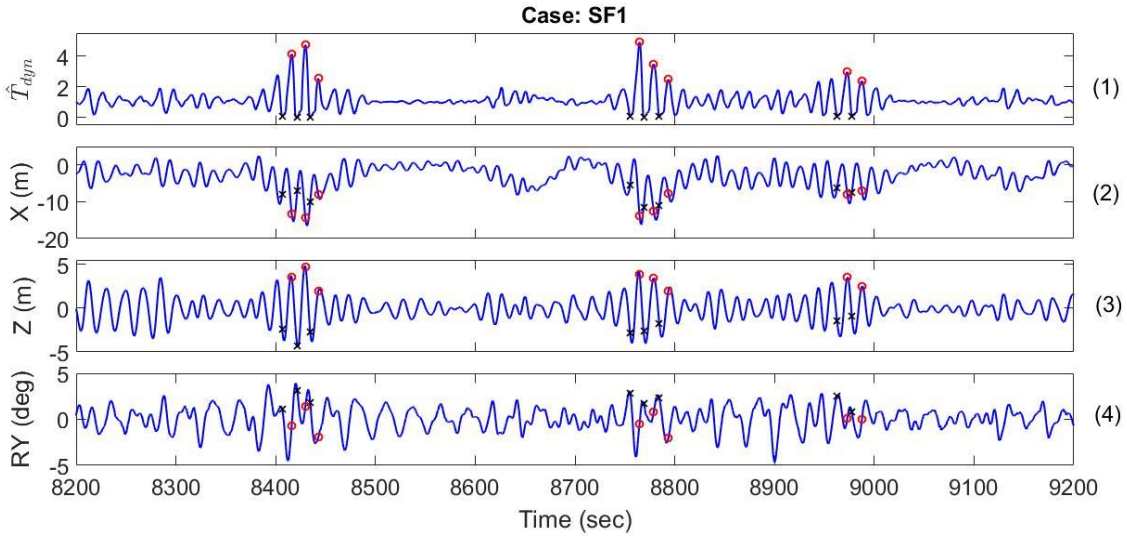

Fig. 3.13 The time series of experimental measurements of case SF1. (1) Normalized Mooring line tension (2) Fairlead lateral displacement (3) Fairlead vertical location (value zero means the origin position) (4) Pitch motion of the floater

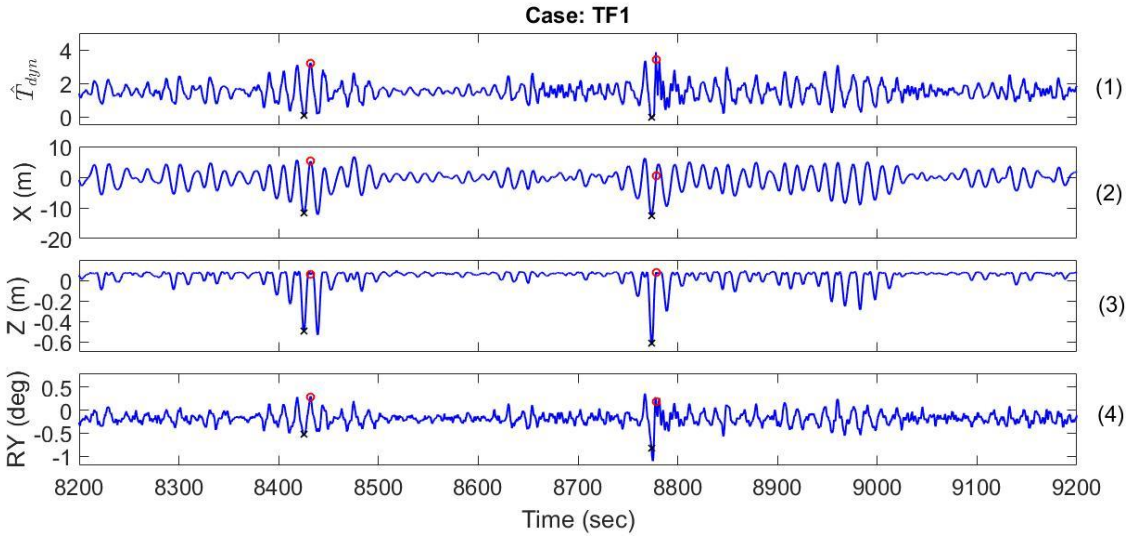

Fig. 3.14 The time series of experimental measurements of case TF1. (1) Normalized Mooring line tension (2) Fairlead lateral displacement (3) Fairlead vertical location (value zero means the origin position) (4) Pitch motion of the floater

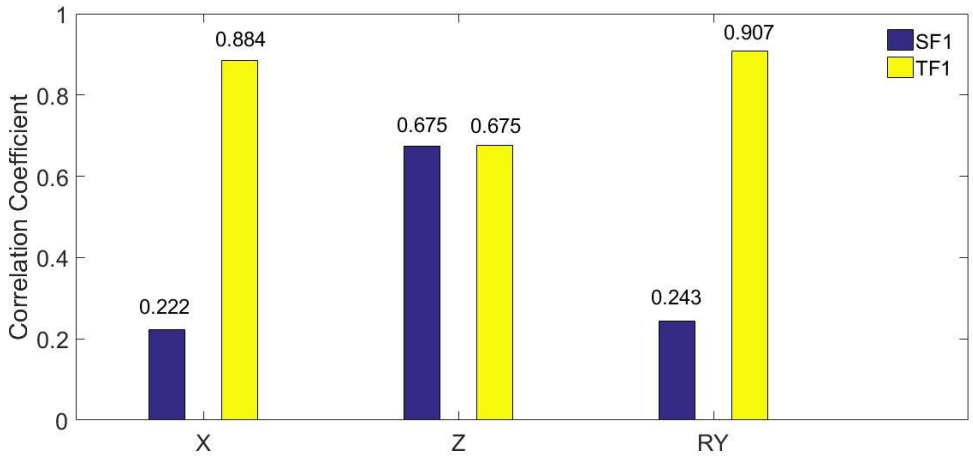

Fig. 3.15 Correlation coefficients between mooring line tension and floater motions of SF1 and TF1

Regarding the snap and the slack criteria defined in Section 3.3, Eqs. 3.1 – 6 are applied to the test data to find the non-dimensional maximum dynamic tension ($\hat{T}$), cyclical tension ($\hat{T}^n$), and snap loads ($\hat{T}^s$).

Table 3.12 summarizes data on $\hat{T}$, $\widehat{T^n}$, and $\widehat{T^s}$ for the case SF1 and TF1. In general, snap events of both SF1 and TF1 are infrequent, occurring on average about once for every 40

and 140 non-snap cyclic events, respectively. A total of 21 and 10 snap events are recorded during 3.5-h storm duration tests of SF1 and TF1, respectively. With the wave peak period of 14.3s, the number of wave cycles is 881 (=3.5hrs/14.3s), which bodes well with the number of $\widehat{T^n}$ cycles of SF1. However, TF1 has 50% more cycles than that for SF1. This is because the heave and pitch natural periods of TF are much smaller (7 – 26 times) than that for SF. The greatest snap event is observed in SF1. For SF1, the snap event durations range from 8.0 – 10.1 s while the duration of the snap events in TF1 are shorter than SF1 and range from 7.6 – 8.5 s. For SF1 and TF1, snap-induced dynamic tension ($\widehat{T^s}$) is in the range of 1.75 – 4.83 and 1.96 – 3.26, respectively, while their non-snap counterparts, $\widehat{T^n}$, are in the range of 0.09 – 2.88 and 0.04 – 2.76, respectively. The TLP exhibits fewer occurrences of snap loads as well as the dynamic tension values, when compared to the Semi.

Table 3.12 Normalized tension ranges, number of cycles, and duration for $\hat{T}$, $\widehat{T^n}$ and $\widehat{T^s}$ in the case SF1 and TF1 of test data

Case	$\hat{T}$		$\widehat{T^n}$			$\widehat{T^s}$			
	Tension range		Number	Tension range		Number	Duration range	Tension range	
	Min	Max	of cycles	Min	Max	of cycles	(sec / cycle)	Min	Max
SF1	0.09 -	4.83	904	0.09	2.88	21	8.0 - 10.1	1.75	4.83
TF1	0.04 -	3.26	1432	0.04	2.76	10	7.6 – 8.5	1.96	3.26

3.5 Wind effects on the Dynamic Line Tensions and the Platform motions

To investigate wind effects on snap loads, the mooring line tensions and the platform motions of the TLP and Semi models under steady wind are compared with the no wind condition. Thus, the measurements of SF1, SF2, SP2, TF1, and TF2 are discussed.

3.5.1 Semi

The wind speed of SF1, SF2 and SP2 are respectively 0m/s, 21m/s and 13m/s. The performance-scaled turbine model with a wind speed of 13m/s (SP2) has similar thrust force with the Froude-scaled turbine model with a wind speed of 21m/s. The moment with respect to the y-axis at the base of tower (M_y) includes the inertia of the turbine and tower, the thrust force acting on the wind turbine and wave forces acting on the platform. As such, this is a good way to compare the influence of aerodynamics between these two datasets. The mean value of the recorded M_y data of SF2 and SP2 are respectively -95,691.79kNm and -106,733.83kNm. The root mean squares of the recorded M_y data are 98,241.98kNm and 110,494.39kNm for SF2 and SP2 respectively. The difference of the mean value and root mean square value between SF2 and SP2 are 10.35% and 12.47% respectively.

Time histories of normalized line tension, fairlead lateral displacement, fairlead vertical location, and pitch motion corresponding to the described storm condition are shown in Figs. 3.16 – 17 for SF2 and SP2 respectively. When comparing Fig. 3.16, Fig. 3.17 and Fig 3.13, the relationship between the snap loads and the floater motions is very similar for SF1, SF2, and SP2. The range of the normalized tension of SF2 and SP2 are all close to that of SF1. This indicates that the wind forces have little influence on the dynamic tensions. The drift motions are larger with steady wind conditions (SF2 and SP2) than the no wind condition. The ranges of the vertical displacement of SF2 and SP2 are both close that of SF1. There is an offset of -3.9deg and -4.7deg for the pitch motions of SF2 and SP2 while there is no offset of SF1. The surge, heave, and pitch motions have a little higher correlation coefficients with the line tension for SF2 when compared to the values of SF1 and SP2 (Fig. 3.18.). Table 3.13 summarizes data on $\hat{T}$, $\widehat{T^n}$, and $\widehat{T^s}$ for the cases of SF1, SF2 and

SP2. In general, the snap events of both SF1, SF2 and SP2 are infrequent, occurring on average about once every 40, 32 and 21 non-snap cyclic events, respectively. A total of 21, 30 and 47 snap events are recorded during 3.5-h storm duration tests of SF1, SF2 and SP2, respectively. Therefore, the highest snap events are observed for SP2 than for SF1 and SF2. It is notable that, the difference in mean values of M_y between SF2 and SP2 is small (10.35%). However, the turbine performance of SP2 is different than for that of SF2. Due to the higher root mean square of M_y, SP2 has a higher number of snap events than SF2. The greatest snap load is observed for SF1, while the maximum snap load of SF2 is very close to SP2. For SF2, the snap event durations range from 8.1 – 10.4 s, which are very close to SF1. For SF2, the snap-induced dynamic tension ($\widehat{T^s}$) and non-snap counterparts ($\widehat{T^n}$) are in the ranges of 1.73 – 4.04 and 0.05 – 2.78 respectively. For SP2, the snap-induced dynamic tension ($\widehat{T^s}$) and non-snap counterparts ($\widehat{T^n}$) are in the ranges of 1.77 – 4.05 and 0.06 – 2.83 respectively. Both the ranges of $\widehat{T^s}$ and $\widehat{T^n}$ for SP2 are very close to the ranges of SF2. The results indicate the wind forces cause a 23% increase in snap events, and a 16% decrease in the maximum dynamic tension amplitude.

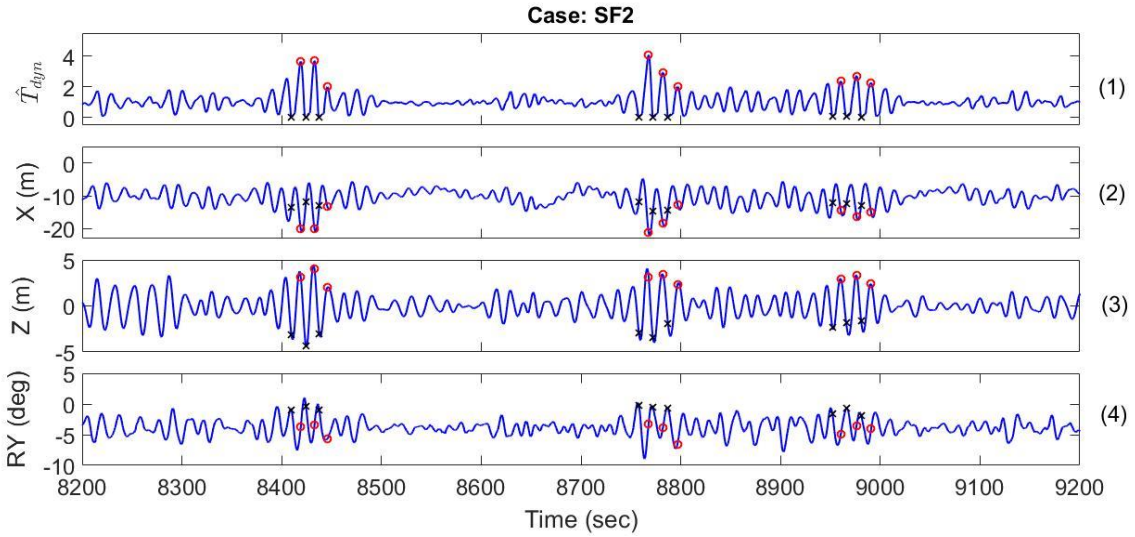

Fig. 3.16 The time series of experimental measurements of case SF2. (1) Normalized Mooring line tension (2) Fairlead lateral displacement (3) Fairlead vertical location (value zero means the origin position) (4) Pitch motion of the floater

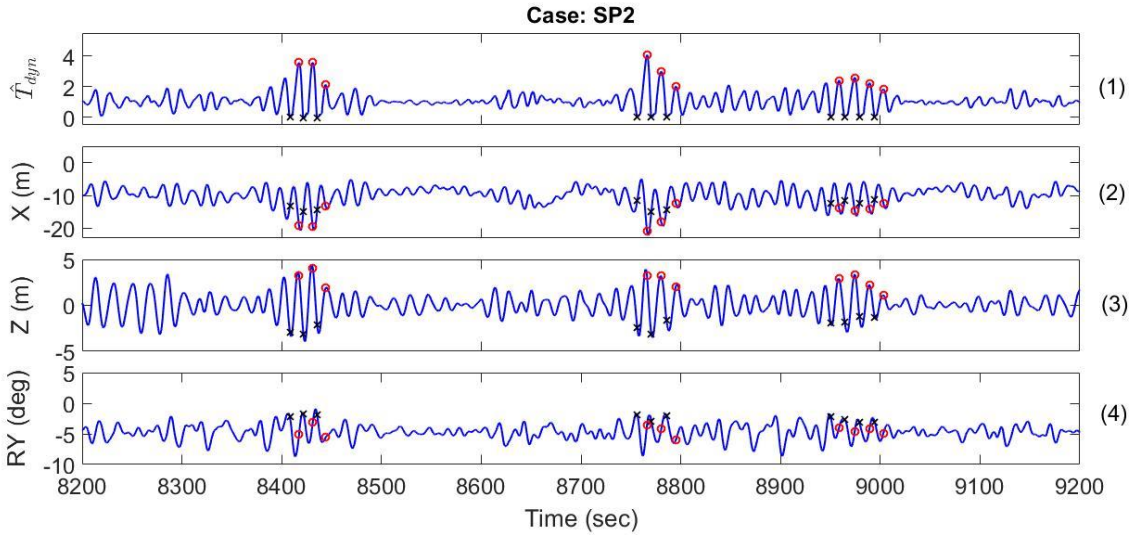

Fig. 3.17 The time series of experimental measurements of case SP2. (1) Normalized Mooring line tension (2) Fairlead lateral displacement (3) Fairlead vertical location (value zero means the origin position) (4) Pitch motion of the floater

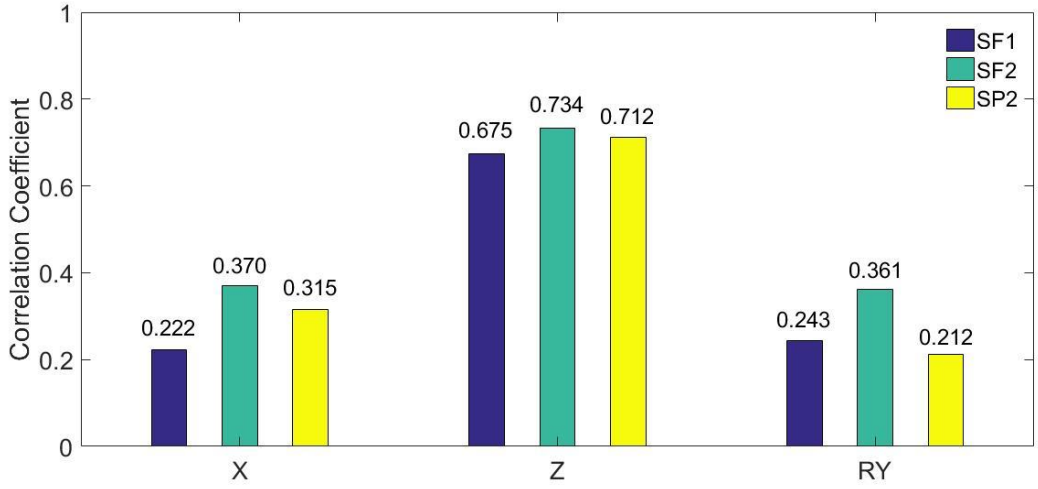

Fig. 3.18 Correlation coefficients between mooring line tension and floater motions of SF1, SF2, and SP2

Table 3.13 Normalized tension ranges, number of cycles, and duration for $\hat{T}$, $\widehat{T^n}$ and $\widehat{T^s}$ in the case SF1, SF2, and SP2 of test data

Case	$\hat{T}$		$\widehat{T^n}$			$\widehat{T^s}$			
	Tension range		Number	Tension range		Number	Duration range	Tension range	
	Min	Max	of cycles	Min	Max	of cycles	(sec / cycle)	Min	Max
SF1	0.09 -	4.83	904	0.09	2.88	21	8.0 - 10.1	1.75	4.83
SF2	0.05 -	4.04	970	0.05	2.78	30	8.1 - 10.4	1.73	4.04
SP2	0.06 -	4.05	966	0.06	2.83	47	7.3 - 10.1	1.77	4.05

3.5.2 TLP

Time histories of normalized line tension, fairlead lateral displacement, fairlead vertical location, and pitch motion corresponding to the described storm condition of TF2 are shown in Fig. 3.19. Compared to TF1 (no wind condition), the phases of the lateral displacement and the pitch motion for TF2 (steady wind speed) are not very different. Importantly, the range of the normalized tension of TF2 is much larger than TF1.

The drift motions are larger for TF2 than TF1. The range of the vertical displacement for TF2 is much larger than TF1. The mean pitch values are -0.2deg and -0.3deg for TF1 and TF2 respectively; however, the range of pitch motion of TF2 is much larger than TF1. There is a 93% increase in snap events under the steady wind condition. The surge and pitch motions have a little lower correlation coefficients with the line tension for TF2 when compared to the values of TF1 (Fig. 3.20). Moreover, the heave motion has a little higher correlation coefficient with the line tension for TF2 when compared to the values of TF1.

Table 3.14 summarizes data on $\hat{T}$, $\widehat{T^n}$, and $\widehat{T^s}$ for the cases of TF1 (no wind condition) and TF2 (steady wind condition). In general, the snap events of TF1 are infrequent, occurring on average about once every 140 non-snap cyclic events. While the snap events of TF2 are frequent, occurring on average about once every 9 non-snap cyclic events. A total of 10 and 142 snap events are recorded during 3.5-h storm duration tests of TF1 and TF2, respectively. Therefore, significant increases in snap events are observed for TF2 when compared to TF1. The greatest snap event is observed for TF2. For TF2, the snap event durations range from 8.4 – 10.1 s, which is little higher than the range TF1. The snap-induced dynamic tension ($\widehat{T^s}$) and non-snap counterparts ($\widehat{T^n}$) of TF2 are in the range of 1.34 – 4.63 and 0.04 – 3.07 respectively. The maximum values of $\widehat{T^s}$ and $\widehat{T^n}$ are both higher than the values of TF1. The results indicate that the wind forces cause a 93% increase of the snap events, and a 42% increase of the maximum dynamic tension amplitude.

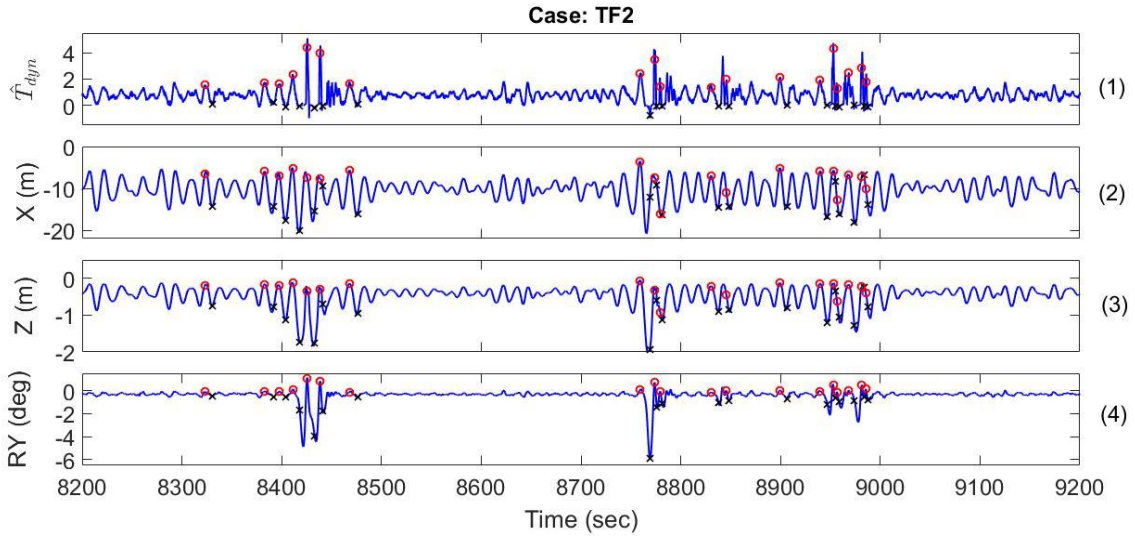

Fig. 3.19 The time series of experimental measurements of case TF2. (1) Normalized Mooring line tension (2) Fairlead lateral displacement (3) Fairlead vertical location (value zero means the origin position) (4) Pitch motion of the floater

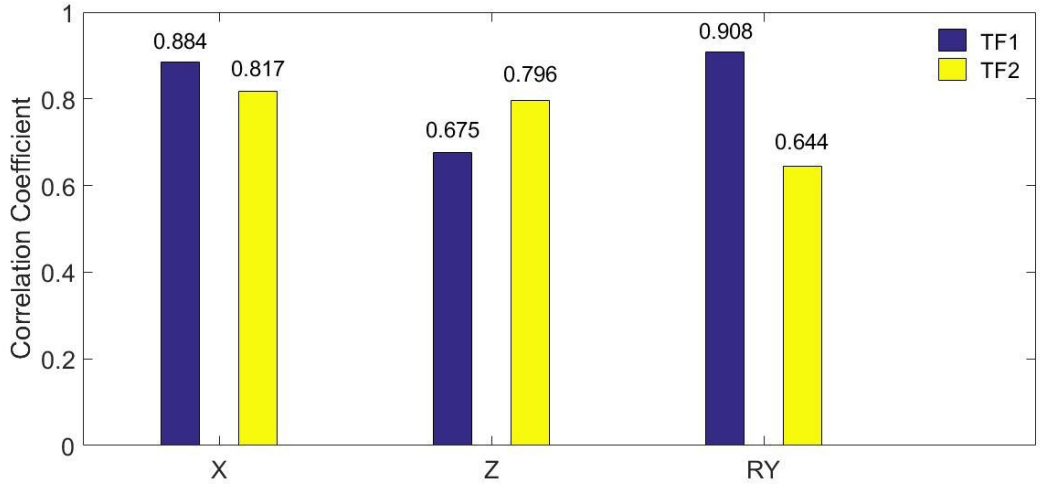

Fig. 3.20 Correlation coefficients between mooring line tension and floater motions of TF1 and TF2

Table 3.14 Normalized tension ranges, number of cycles, and duration for $\hat{T}$, $\widehat{T^n}$ and $\widehat{T^s}$ in the case TF1 and TF2 of test data

Case	$\hat{T}$		$\widehat{T^n}$			$\widehat{T^s}$			
	Tension range		Number	Tension range		Number	Duration range	Tension range	
	Min	Max	of cycles	Min	Max	of cycles	(sec / cycle)	Min	Max
TF1	0.04 -	3.26	1432	0.04	2.76	10	7.6 – 8.5	1.96	3.26
TF2	0.04 -	4.63	1345	0.04	3.07	142	8.4 – 10.1	1.34	4.63

3.6 Discussion and Conclusions

In regard to the results of the above, the dynamic line tensions have a higher impact on the platform motions (surge, heave, and pitch) for the TLP model than for the Semi model under a no wind condition. For the no wind condition, the TLP exhibits fewer snap loads as well as less dynamic tension values when compared to the Semi. The wind forces cause the surge motions of the Semi model to slightly decrease and there is no effect on the pitch motions of the Semi model. For SF2, the root mean squares of surge and pitch motions are respectively 10.63m and 1.1deg, while for SF1, the root mean squares of surge and pitch motions are respectively 3.37m and 1.1deg. Moreover, for the Semi model, the wind forces cause a decrease in the maximum $\widehat{T^s}$ value (4.04 for SF2 and 4.83 for SF1). These findings support our earlier study that the turbine thrust coefficients are affected by the structure pitch motions. Moreover, Thiagarajan et al. [60] studied the nonlinear pitch decay of a FOWT by developing theoretical analysis. The authors revealed that the mean offset position has an important role in the stiffness, damping and the natural period of pitch motion. For the discussion of wind effects on different Semi models (SF1, SF2 and SP2), the highest snap events are observed for SP2 rather than for SF1 and SF2. It is notable that

the difference in mean values of M_y between SF2 and SP2 is small (10.35%). However, the turbine performance of SP2 is different to that of SF2. Due to the higher dynamic wind loads, SP2 has higher snap events than SF2.

In regard to the results of the previous sections, wind forces have a higher influence on the pitch and heave motions of the TLP model than these motions for the Semi model. Therefore, higher heave and pitch motions could result in higher probability of the snap events and higher amplitudes of the dynamic line tensions. This is due to the TLP model's unique property of extreme high pretension. Therefore, the wind thrust acting on the turbine of the TLP model does not increase the pitch damping. Moreover, the wind forces have pronounced influence on the dynamic tensions of the TLP model and have a less pronounced influences on the dynamic tensions of the Semi model. In this section, it reveals that the TLP model with the increase of the pitch motions results in significant rises of the snap events. It is notable that the TLP model used in this study were undersized by 50%. Thus, a well-designed TLP FOWT is not expected to have as many snap events as the ones in this study.

CHAPTER 4

THEORETICAL EXTREME TENSION DISTRIBUTION MODELS OF TEST DATA

This study investigates seven experimental tests of the moored FOWT semi-submersible (SF) under survival storm conditions (i.e., a 100-year storm). The environmental conditions of these seven cases were listed in Table 3.8. For all these cases, the significant wave height and peak wave period were held constant at 10.5m and 14.3s, respectively, while the wind speed was varied from 0 to 30.5 m/ s. The wind conditions ranged from a steady wind to turbulent wind characterized by a NPD spectrum. The directions of the wind and waves were 180^o with respect to the *x*-axis. Several snap events are found to result in the windward mooring line. This chapter proposes a composite Weibull probability distribution for the mooring line dynamic tension that incorporates the effects of snap events. The proposed distribution model provides a good fit to the measured tension data, particularly in the extreme value range.

4.1 Analysis of Tension Maxima

In this study, the normalized cyclic dynamic tension ($\hat{T}$), snap-induced tension ($\widehat{T^s}$) and those that are not associated with a snap event ($\widehat{T^n}$) are investigated. Table 4.1 summarizes data on $\hat{T}$, $\widehat{T^n}$ and $\widehat{T^s}$ for all the seven cases described in Table 3.8. In general, snap events are infrequent, occurring on average about once for every 30 non-snap cyclic events. The greatest number of snap events is observed for Cases 3 and 5, where the wind speeds are different and for the rotor at 12.73 RPM. The smallest number of snap events occurred

when there is no wind. Overall, the snap event durations range from 7.7 to 10.5 s. Snap-induced dynamic tension ($\widehat{T^s}$) are in the range of 1.70 to 4.83, while their non-snap counterparts, $\widehat{T^n}$, are in the range of 0.05 to 2.95. In the no-wind condition (Case 1), the largest $\widehat{T^s}$ value of 4.83 is observed. A nacelle yaw error could cause $\widehat{T^s}$ to decrease for turbulent winds (Cases 2 vs. 3) and increase for steady winds (Cases 4 vs. 5). For both steady and turbulent winds, $\widehat{T^s}$ values are larger for higher wind speeds with a stationary rotor (Cases 6 and 7) compared to lower wind speeds with the rotor in operating conditions (Cases 2 and 4).

Table 4.1 Normalized tension ranges, number of cycles, and duration for $\widehat{T}$, $\widehat{T^n}$ and $\widehat{T^s}$ in the seven cases of the test data

Case	$\widehat{T}$		$\widehat{T^n}$			$\widehat{T^s}$			
	Tension range		Number	Tension range		Number	Duration range	Tension range	
	Min	Max	of cycles	Min	Max	of cycles	(sec / cycle)	Min	Max
1	0.09 -	4.83	904	0.09	2.88	21	8.0 - 10.1	1.75	4.83
2	0.06 -	4.50	971	0.06	2.89	37	8.0 - 10.5	1.70	4.50
3	0.06 -	4.27	958	0.06	2.71	38	7.8 - 10.5	1.72	4.27
4	0.05 -	4.04	970	0.05	2.78	30	8.1 - 10.4	1.73	4.04
5	0.06 -	4.43	966	0.06	2.95	38	8.1 - 10.5	1.81	4.43
6	0.08 -	4.65	938	0.08	2.87	30	7.7 - 10.3	1.77	4.65
7	0.07 -	4.55	934	0.07	2.87	25	7.8 – 10.0	1.76	4.55

Exceedance probability (P) estimates are commonly used for characterizing the probability that a variable of interest may exceed a specified threshold value. For a threshold value, $\widehat{T}_j$, the exceedance probability of a line's dynamic tension, $\widehat{T}$, in a given sample is computed as:

$$\mathrm{P}\left(\hat{T}_j\right) = \mathrm{P}\left[\hat{T} > \hat{T}_j\right] = 1 - n_j/(r+1) \tag{4.1}$$

where r is the total number of values of $\hat{T}$, and n_j is the number of tension values that exceed the threshold. Also, j indicates the serial number of the threshold in a sequence of increasing tension values; it ranges from 1 to r. Fig. 4.1 compares the exceedance probabilities of the dynamic tension ($\hat{T}$) for the stationary rotor, i.e., steady wind Cases 1 and 7, while Fig. 4.2 does the same for the turbulent wind Cases 3 and 6. The number of data points plotted corresponds to r, the total number of measurements (tension values) in the sample. The snap and non-snap tensions are distinguished by filled and hollow markers, respectively. The contrasting markers allows one to identify deviations in the probability curves and the larger values resulting from snap-induced tension in a straightforward manner. In both figures, exceedance probability curves for the higher tension ranges contributed to by $\widehat{T^s}$ show different characteristics compared to the lower tension range values that are mostly related to $\widehat{T^n}$. There appears to be a transition point associated with a change in the curve characteristics. This transition ranges from approximately 2.7 to 2.9 for all the four cases, irrespective of the wind speed and other influences. Over this range of transition, there is some overlap of tension values from non-snap and snap events, but no $\widehat{T^n}$ values occur beyond this transition. Furthermore, beyond the transition range, the probability curves are somewhat similar across the four cases with some insignificant variations. This was uniformly observed for all the seven cases studied.

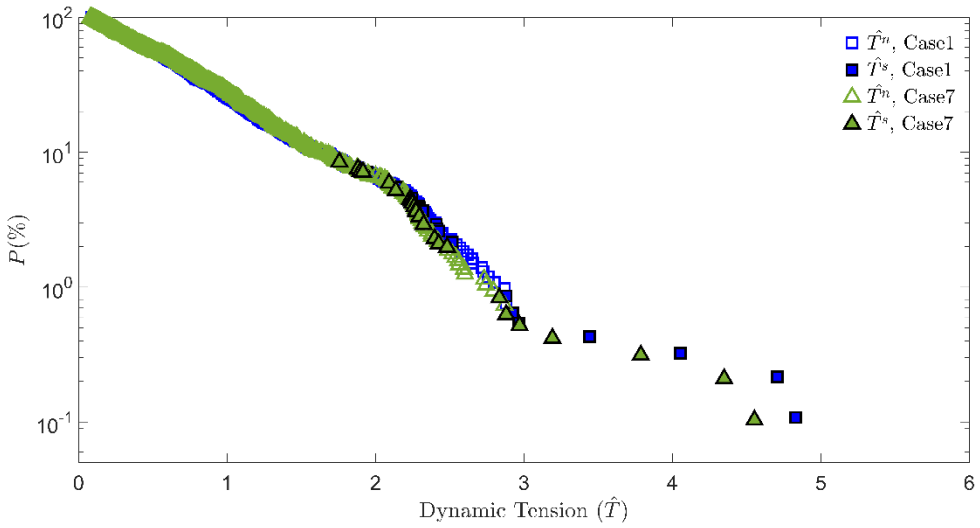

Fig. 4.1 A comparison of exceedance probability curves for $\widehat{T^n}$ (hollow markers) and $\widehat{T^s}$ (solid markers) for Case 1 (square) and Case 7 (triangle)

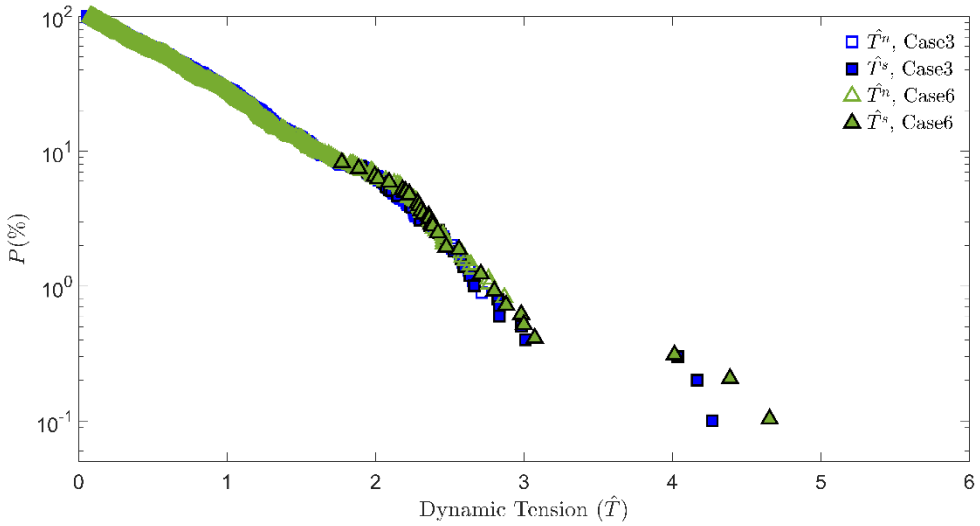

Fig. 4.2 A comparison of exceedance probability curves for $\boldsymbol{\widehat{T^n}}$ (hollow markers) and $\boldsymbol{\widehat{T^s}}$ (solid markers) for Case 3 (square) and Case 6 (triangle)

Figs. 4.3 and 4.4 present exceedance probability curves for $\hat{T}$, $\widehat{T^n}$ and $\widehat{T^s}$ for the same combination of cases in an alternate manner. Unlike Figs. 4.1 and 4.2 in which the distributions of $\widehat{T^n}$ and $\widehat{T^s}$ are combined into a single distribution of $\hat{T}$, Figs. 4.3 and 4.4 present exceedance probability curves for $\widehat{T^n}$ and $\widehat{T^s}$ separately as well as combined together as $\hat{T}$. To arrive at the exceedance probability of $\widehat{T^n}$ or $\widehat{T^s}$ alone, the total number

of tension values employed in Eq. (4.1) is correspondingly changed from *r* to either *p* or *q*. Figs. 4.3 and 4.4 highlight the advantage of being able to observe differences between $\widehat{T^n}$ and $\widehat{T^s}$ beyond the transition ranges. It appears that at selected tension levels, both $\widehat{T^n}$ and $\widehat{T^s}$ have higher exceedance probability levels with lower steady wind speeds and higher turbulent wind speeds. There appears to be a strong correlation between the point where $\hat{T}$ transitions to a different slope and the point where $\widehat{T^n}$ stops changing (i.e., where it falls off almost vertically). This leads us to postulate that the transition point may be modeled and correlated to the maximum dynamic non-snap tension in an extreme storm event.

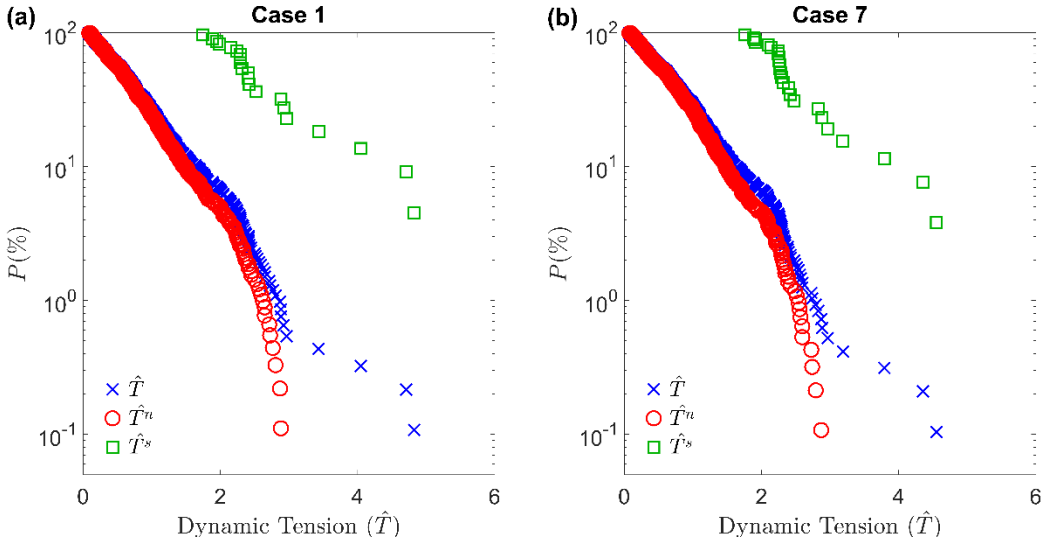

Fig. 4.3 A comparison of exceedance probability curves for $\widehat{\boldsymbol{T}}$ (crosses), $\widehat{\boldsymbol{T^n}}$ (hollow circles) and $\widehat{\boldsymbol{T^s}}$ (hollow squares) for: (a) Case 1 and (b) Case 7

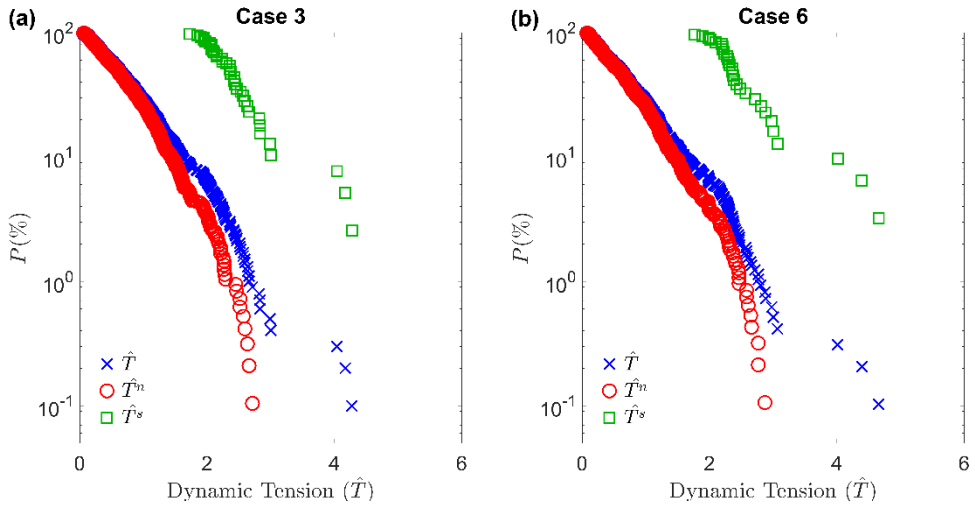

Fig. 4.4 A comparison of exceedance probability curves for $\widehat{\boldsymbol{T}}$ (crosses), $\widehat{\boldsymbol{T^n}}$ (hollow circles) and $\widehat{\boldsymbol{T^s}}$ (hollow squares) for: (a) Case 3 and (b) Case 6

4.2 Estimation of Extreme Tensions

It is clear that the exceedance probability curves for $\hat{T}$ in Figs. 4.1 – 4 suggest that $\hat{T}$ will likely follow a heavy-tailed probability distribution that has heavier-than-exponential tails [61]. In developing an understanding of probability models as they would apply to line tensions in the presence of snap events, it is instructive to examine extreme value distributions of comparable physical phenomena such as ship slamming and freak waves. In studies of such related phenomena, researchers have used Weibull distribution models with varying degrees of success. This may perhaps be due to the heavy tailed nature of the accompanying distributions.

4.2.1 Weibull Distribution Applied to Slamming and Freak Wave Events

A slamming impact is often interspersed among more conventional cyclic wave-induced loads on the bow of a ship hull, particularly when traveling in large waves. During a slamming event, the bow can emerge clear of the water surface and then fall back, causing

a ship hull to experience large impact pressures [62]. Razola et al. [63] presented a statistical analysis of accelerations experienced by a high-speed craft in waves. They found that lower acceleration levels are closely related to harmonic wave-hull interaction, while higher levels are related to the slamming impact pressure propagation. The Weibull model did not fit the tail of the slamming impact probability distribution and the 95% confidence interval for the most probable largest values were $\pm$20% of the most probable maximum extreme (MPME) value for most conditions [63].

Freak waves develop in rough seas that persist for a long duration and typically are a consequence of large steepness and small directional spreading associated such sea states. The probability of occurrence of freak waves is considered to increase when wave steepness increases and when the wave spectrum narrows [64]. Petrova et al. [65] investigated the short-term statistical representation of wave crests in sea states with abnormal waves. They found that the Forristall (perturbed Weibull) distribution model fit observations well until approximately 0.5 – 0.6 times the significant wave height, but underestimated the occurrence of freak waves. Onorato et al. [66] studied the generation of freak waves in a random sea state characterized by a JONSWAP spectrum. When the Benjamin-Feir Index (BFI) denoted nonlinearity in the wave elevation as being large, it was found that the probability distribution departed from the Rayleigh distribution, which is a special case of the Weibull distribution.

The Weibull distribution (WBL) function is initially employed to represent mooring line tension extreme values. Following [67], the WBL cumulative distribution function is given by

$$\mathcal{F}(\hat{T}) = 1 - \exp\left[-\left(\frac{\hat{T}}{\eta}\right)^{\xi}\right] \text{ for } \hat{T} \geq 0, \text{and } \eta, \xi \in \mathbb{R} \quad (4.2)$$

where η and ξ (both greater than zero) are the so-called scale and shape parameters, respectively. As defined, the scale parameter (η) of WBL is a threshold value associated with an exceedance probability of 36.8% [68]. Although a normalized tension quantity in the present study, the symbol η is retained to be consistent with conventional notation.

The method of Maximum Likelihood Estimation (MLE) is applied to estimate the WBL model parameters η and ξ [68]. The likelihood function, $\mathcal{L}$, for a given set of observations $\hat{T}_i$, $i = 1,2, \ldots r$ in terms of η and ξ that must be estimated is calculated as:

$$\mathcal{L}(\eta, \xi) = \prod_{i=1}^{r} f(\hat{T}_i | \eta, \xi) \quad (4.3)$$

where f is the Weibull probability density function and r represents the number of available data values. The method is used to obtain parameter estimations of $\hat{T}$, $\widehat{T^n}$ and $\widehat{T^s}$ for the seven experimental cases, and the results are given in Table 4.2. As can be seen from this table, the estimates of η and ξ for the seven cases suggest a weak correlation with wind conditions. The WBL parameter estimates for $\widehat{T^s}$ are larger than those for $\hat{T}$ and $\widehat{T^n}$, which are similar in magnitude; η estimates for $\hat{T}$ and $\widehat{T^n}$ are in the range of 0.775 – 0.863, while η estimates for $\widehat{T^s}$ are in the range of 2.607 – 3.007. Thus for $\widehat{T^s}$, the normalized 36.8%-ile exceedance probability tension is larger than even the "significant" $\widehat{T^n}$ value (i.e., the mean of the highest 33.3% of $\widehat{T^n}$).

Table 4.2 Scale (η) and shape (ξ) parameters for WBL distributions fitted to $\hat{T}$, $\widehat{T^n}$ and $\widehat{T^s}$ for the seven cases of test data

Case	$\hat{T}$		$\widehat{T^n}$		$\widehat{T^s}$	
	Scale (η)	Shape (ξ)	Scale (η)	Shape (ξ)	Scale (η)	Shape (ξ)
1	0.831	1.282	0.790	1.351	3.007	3.205
2	0.842	1.286	0.781	1.368	2.700	3.858
3	0.843	1.292	0.779	1.382	2.708	3.965
4	0.863	1.334	0.815	1.395	2.607	4.120
5	0.840	1.283	0.777	1.368	2.701	3.902
6	0.829	1.266	0.775	1.344	2.842	3.644
7	0.840	1.291	0.796	1.356	2.827	3.515

Weibull distributions, showing the probability of exceedance, with the estimated parameters for Cases 1 and 4 are shown in Fig. 4.5 and Fig. 4.6; these figures serve to assess the WBL fits to the snap and non-snap extreme tension values. Fig. 4.5 suggests that the distribution of $\widehat{T^n}$ is well represented by a Weibull model with a large shape parameter ($\xi > 1$). For $\xi > 1$, the exceedance probability plots for the Weibull model decrease gradually in the low tension range but fall more steeply at higher values. This same behavior is also seen in the exceedance probability of $\widehat{T^n}$ for the other cases of the seven studies. On the other hand, the exceedance probability plots for $\widehat{T^s}$ deviate considerably from the WBL distribution beyond the low tension range (Fig. 4.6). The exceedance probability data for $\widehat{T^s}$ stay high initially and decrease only gradually beyond the transition range. The plots indicate that the WBL model does not the fit $\widehat{T^s}$ data very well.

Fig. 4.7 shows exceedance probability plots of $\hat{T}$ along with fitted WBL distribution models for Cases 1 and 4. Since the probability curve over the higher tension ranges are contributed to by $\widehat{T^s}$, it is seen that $\hat{T}$ data have larger right tail probability levels than the corresponding probability levels predicted by the Weibull distribution. Thus, it is clear that the WBL models underestimate the upper tail of the cyclic extreme tension values that include snap events. This observation is consistent with the findings of Razola et al. [63], Petrova et al. [65] and Onorato et al. [64] related to the probability distributions of slamming impact forces and freak wave heights.

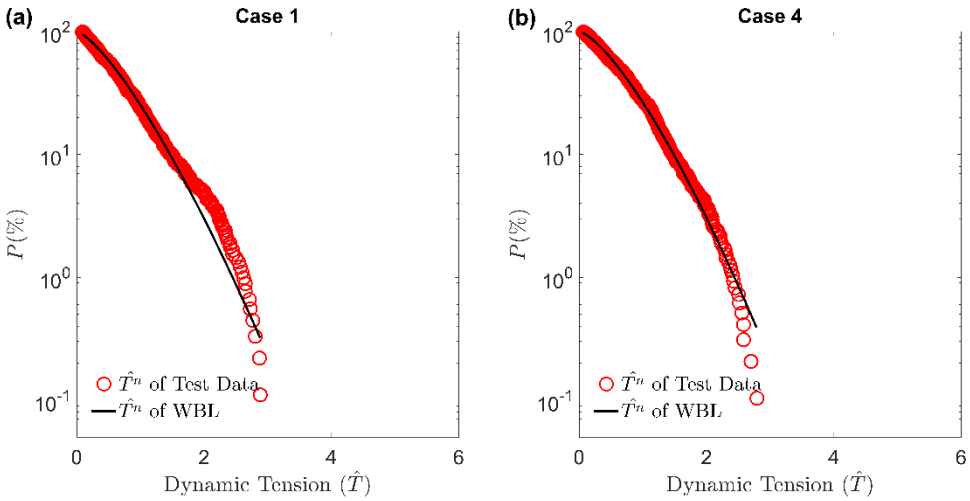

Fig. 4.5 A comparison of exceedance probability curves for $\widehat{T^n}$ between test data (hollow circles) and WBL (solid line) for: (a) Case 1 and (b) Case 4

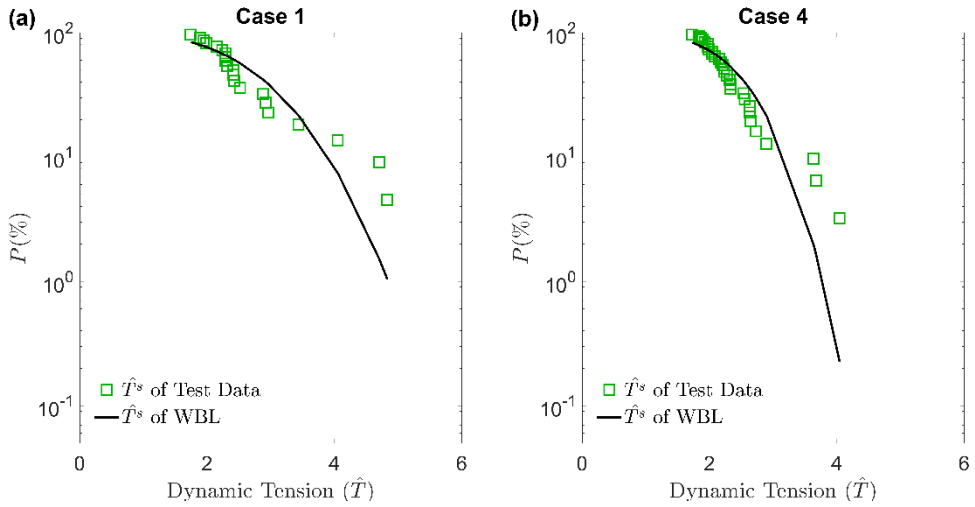

Fig. 4.6 A comparison of exceedance probability curves for $\widehat{T^s}$ between test data (hollow circles) and WBL (solid line) for: (a) Case 1 and (b) Case 4

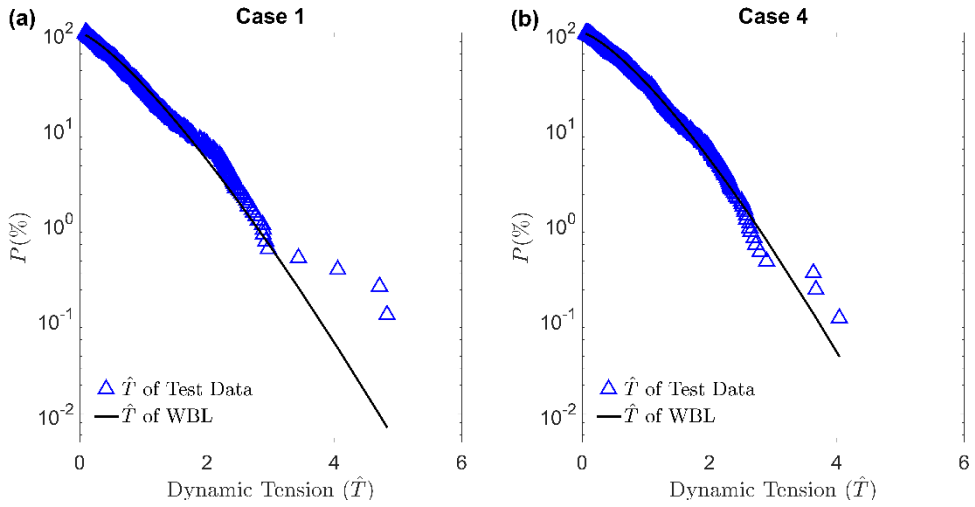

Fig. 4.7 A comparison of exceedance probability curves for $\hat{T}$ between test data (hollow circles) and WBL (solid line) for: (a) Case 1 and (b) Case 4

4.2.2 A Composite Weibull Distribution

Battjes and Groenendijk [69] observed that the wave height distribution in shallow foreshores was different from that in deep water and proposed a composite Weibull distribution that applied across various depths, with different shape and scale parameters on either side of a transition wave height (H_{tr}). The latter was defined in terms of relevant

physical parameters like the foreshore slope and water depth. Following [69], a composite Weibull distribution (CWD) model is applied to the non-dimensional dynamic tension ($\hat{T}$) that has the following form:

$$\mathcal{F}(\hat{T}) = \begin{cases} \mathcal{F}_1(\hat{T}) = 1 - \exp\left[-\left(\hat{T}/\hat{T}_1\right)^{\beta_1}\right], \ \hat{T} \le \hat{T}_{tr} \\ \mathcal{F}_2(\hat{T}) = 1 - \exp\left[-\left(\hat{T}/\hat{T}_2\right)^{\beta_2}\right], \ \hat{T} \ge \hat{T}_{tr} \end{cases} \tag{4.4}$$

Here $\mathcal{F}(\hat{T})$ is the cumulative composite Weibull probability distribution of $\hat{T}$; also, β_1, β_2 are the shape parameters and $\hat{T}_1, \hat{T}_2$ are the scale parameters. Note that $\hat{T}_{tr}$, is conceptually similar to H_{tr} defined by Battjes and Groenendijk [69]; it represents a transition tension that delineates non-snap cyclic tension maxima from snap-induced tension maxima. As was seen in Fig. 4.1, $\hat{T}_{tr}$ is strongly correlated with the maximum dynamic tension value for non-snap tension distribution. Thus, one may resort to the maximum dynamic tension (T_{d-max}) encountered by a mooring system in an extreme storm event, as defined by DNV [70], (Kwan [71] and Larsen and Sandvik [72]):

$$T_{d-max} = \begin{cases} T_{WF-max} + T_{LF-sig}, & \text{for } T_{WF-max} > T_{LF-max} \\ T_{WF-sig} + T_{LF-max}, & \text{for } T_{LF-max} > T_{WF-max} \end{cases} \tag{4.5}$$

where

$$T_{WF-max} = \sigma_{T-WF}\sqrt{2\ln N_{WF}} \tag{4.6}$$

$$T_{WF-sig} = 2\sigma_{T-WF} \tag{4.7}$$

$$T_{LF-max} = \sigma_{T-LF}\sqrt{2\ln N_{LF}} \tag{4.8}$$

$$T_{LF-sig} = 2\sigma_{T-LF} \tag{4.9}$$

Here subscripts *WF* and *LF* denote wave- and low-frequency components, while "*max*" and "*sig*" denote maximum and significant values, respectively. Thus, σ_{T-WF} and σ_{T-LF} are the standard deviations of the wave-frequency and low-frequency components, and N_{WF} and N_{LF} are the corresponding number of tension random process crossings over the duration of the environmental state. To account for uncertainty arising from the dependence of wave-frequency tension on low-frequency motions, T_{d-max} is often evaluated by a combined-spectrum approach, where the standard deviation is calculated by combining the wave- and low-frequency line tensions (see, for example, Kwan [71] and Larsen and Sandvik [72]). Thus, we have:

$$T_{d-max} = \sigma_T \sqrt{2 \ln N_T} \tag{4.10}$$

where σ_T is the standard deviation of the combined low- and wave-frequency line tensions, while N_T is the number of combined low- and wave-frequency platform oscillations over the duration of the environmental state under consideration. For the seven cases under consideration, N_T equals 881 corresponding to a peak period of 14.3 s and a 3.5-hour duration. The transition tension, $\hat{T}_{tr}$, represents a range and can thus be equated to twice the maximum dynamic tension (T_{d-max}) described in (4.10) by employing an empirical constant, δ. Thus, we have:

$$\hat{T}_{tr} = \delta \cdot 2(T_{d-max})/T_{rms} \tag{4.11}$$

This empirical constant is set equal to unity based on observations of the vertical trends of $\widehat{T^n}$ in Figs 4.3 – 4. Finally, $\hat{T}_{tr}$ values based on Eq. (4.11) for the seven cases are presented in the second column of Table 4.3. The normalized T_{rms} has to equal unity and could be expressed in terms of β_1, β_2, $\hat{T}_1$, $\hat{T}_2$ and $\hat{T}_{tr}$ using the incomplete Gamma functions:

$$\sqrt{\hat{T}_1^2\gamma\left(\frac{2}{\beta_1}+1,\left(\frac{\hat{T}_{tr}}{\hat{T}_1}\right)^{\beta_1}\right)+\hat{T}_2^2\Gamma\left(\frac{2}{\beta_2}+1,\left(\frac{\hat{T}_{tr}}{\hat{T}_2}\right)^{\beta_2}\right)}=\hat{T}_{rms}=1 \quad (4.12)$$

The background derivation of Eq. (4.12) can be found in [69]. For each of the seven cases, β_1 and $\hat{T}_1$ are assumed to equal to ξ and η for $\hat{T}$ (Table 4.2), respectively. The reason is that the WBL distributions fit the $\hat{T}$ data very well in the lower tension range (Fig. 4.7). Once $\hat{T}_{tr}$, and the first guess values of $\beta_1$and $\hat{T}_1$ are found, Eq. (4.12) combined with the continuity constraint at the transition tension value are used to obtain the shape parameter, β_2, and the scale parameter, $\hat{T}_2$. A composite Weibull distribution fit with these parameters is established by a least-squared error minimization technique—i.e., if the guessed ξ and η values are not the best estimates of β_1 and $\hat{T}_1$, further iterations are conducted to minimize the least square error (error tolerance: 1E-06) to find β_1, β_2, $\hat{T}_1$, and $\hat{T}_2$, that yield a best fit to the data. These parameters are presented in Table 4.3.

Table 4.3 The transition tension ($\hat{\boldsymbol{T}}_{\boldsymbol{tr}}$), shape parameters ($\boldsymbol{\beta_1}$; $\boldsymbol{\beta_2}$) and scale parameters ($\hat{\boldsymbol{T}}_{\boldsymbol{1}}$; $\hat{\boldsymbol{T}}_{\boldsymbol{2}}$) for the CWD for the seven cases

Case	$\hat{T}_{tr}$	$\hat{T}_1$	β_1	$\hat{T}_2$	β_2
1	2.710	0.792	1.279	0.345	0.763
2	2.875	0.826	1.228	0.364	0.741
3	2.845	0.824	1.241	0.361	0.744
4	2.845	0.855	1.269	0.364	0.741
5	2.839	0.822	1.228	0.364	0.741
6	2.785	0.803	1.222	0.361	0.744
7	2.770	0.816	1.243	0.360	0.745

Table 4.3 suggests that the values for β_1, β_2, $\hat{T}_1$, $\hat{T}_2$ and $\hat{T}_{tr}$ have a weak correlation with the wind conditions, and average values for all these parameters may be used to represent all loading situations. The average values for β_1 and β_2 are 1.244 and 0.746, while those for $\hat{T}_1$, $\hat{T}_2$ and $\hat{T}_{tr}$ are 0.820, 0.360 and 2.810 respectively. These average values are used in the analysis that follows, and also applied to Eq. (4.4).

Figs. 4.8 – 10 show exceedance probability plots for $\hat{T}$ estimated using the composite Weibull distribution for Cases 1, 2 and 7. The graphs support the validity of the CWD model in a qualitative sense.

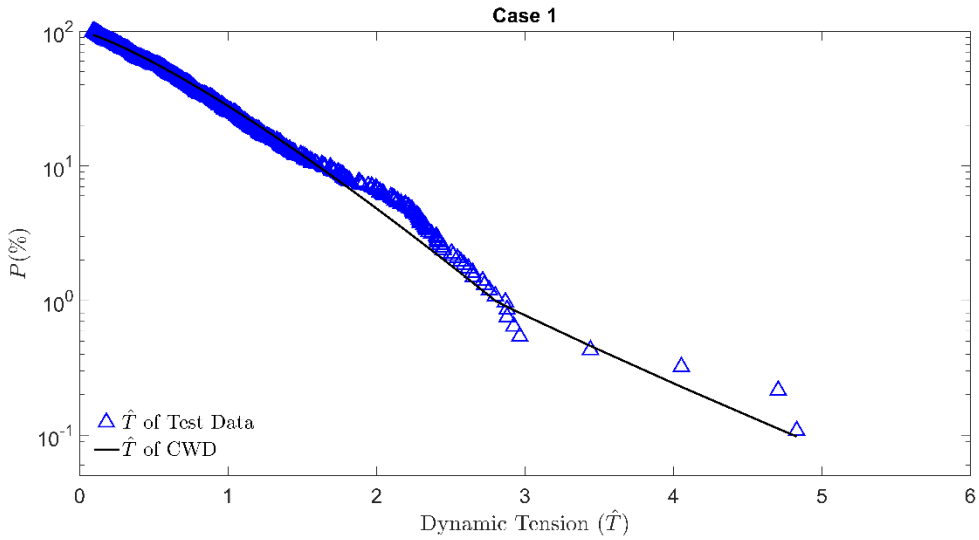

Fig. 4.8 A comparison of exceedance probability curves for $\hat{T}$ between test data (hollow triangles) and CWD (solid line) for Case 1

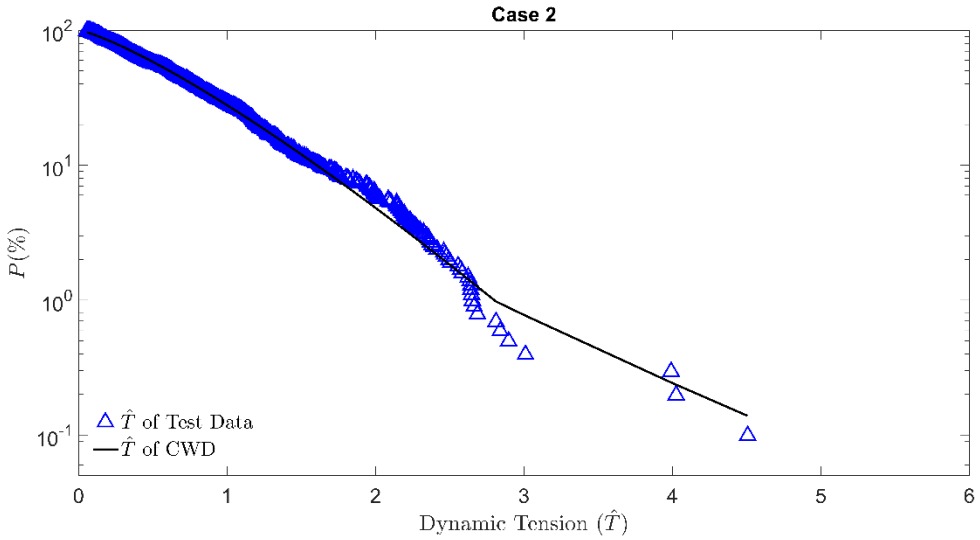

Fig. 4.9 A comparison of exceedance probability curves for $\hat{T}$ between test data (hollow triangles) and CWD (solid line) for Case 2

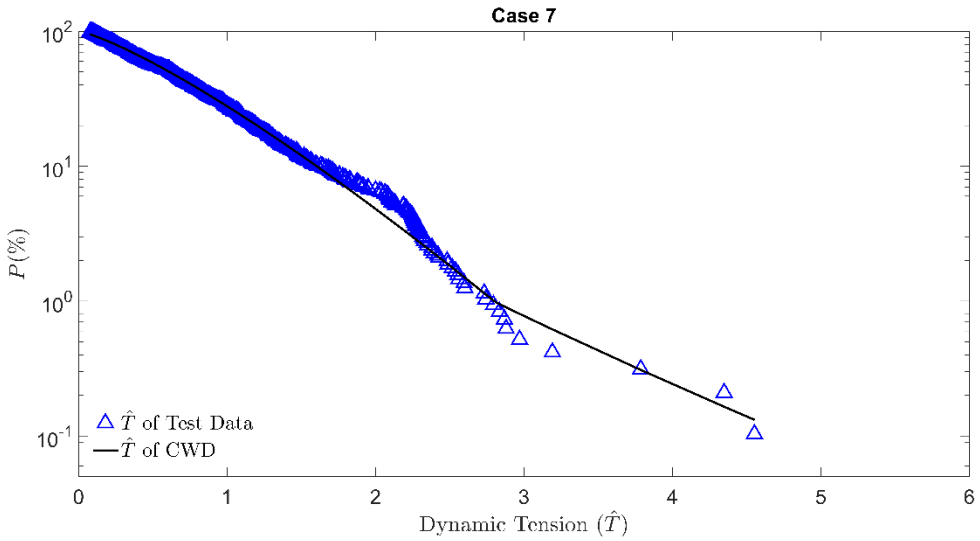

Fig. 4.10 A comparison of exceedance probability curves for $\hat{T}$ between test data (hollow triangles) and CWD (solid line) for Case 7

4.2.3 Extreme Value Prediction by CWD and WBL Models

The goodness of fit estimates for the CWD and WBL distribution function models are evaluated by computing the absolute distribution fitting error (ε_{ABS}), defined as [43]:

$$\varepsilon_{ABS} = 1/r \times \sum_{j=1}^{r} \left\| \mathrm{P}_{data}\left(\widehat{T}_j\right) - \mathrm{P}_{theo}\left(\widehat{T}_j\right) \right\| \tag{4.13}$$

where r denotes the number of identified observations (of $\widehat{T}$). $\mathrm{P}_{data}\left(\widehat{T}_j\right)$ is the exceedance probability based on test data as defined in Eq. (4.1), while $\mathrm{P}_{theo}\left(\widehat{T}_j\right)$ is the exceedance probability computed using the theoretical distribution model, as obtained with the cumulative probability distribution functions for both WBL and CWD defined in Eqs. (4.2) and (4.4) respectively. Fig. 4.11 shows a comparison of the absolute fitting errors for both models in Cases 1 – 7. The fitting errors with the CWD model range from 0.9% (Case 3) to 1.6% (Case 1), while the corresponding errors with the WBL model are slightly higher, ranging from 1.1% (Case 4) to 2.1% (Case 1). Although these errors with both distribution models are lower than 2.1%, the upper tails of the CWD distribution models show better fits with the experimental data.

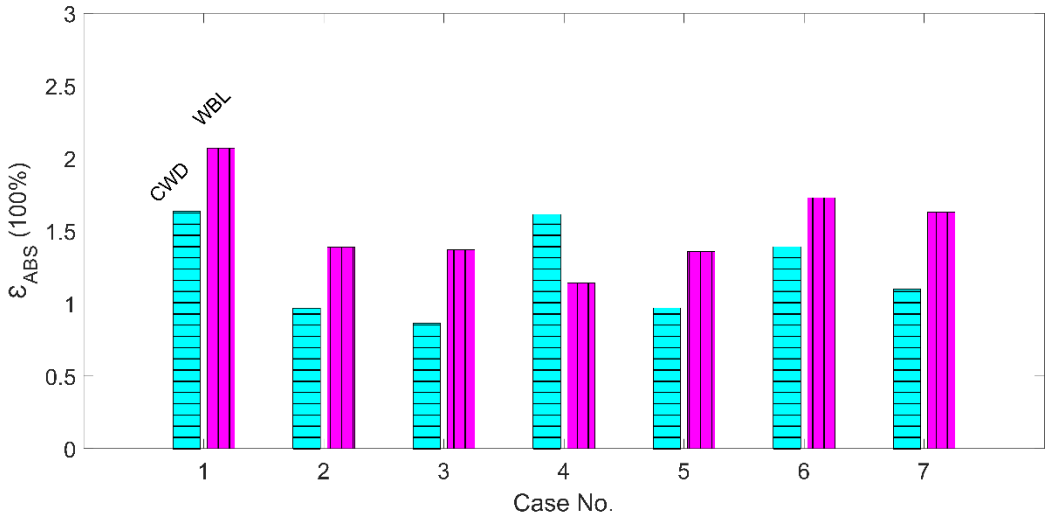

Fig. 4.11 Absolute fitting error ($\boldsymbol{\varepsilon_{ABS}}$) in percent for the exceedance probability distribution based on the CWD (horizontal line pattern) and WBL (vertical line pattern) models for Cases 1 – 7

For extreme value predictions, capturing the tail of the distribution (i.e., the largest values) is of primary importance [63]. The MPME (most probable maximum extreme) value is an extreme value statistic commonly used in the offshore industry [63, 73, 74]. The extreme value of vessel motion and structure response quantities that occur in a storm is often expressed using MPME values. Following [63, 74], the MPME value based on the WBL model is computed as:

$$\hat{T}_{MPME}^{WBL} = \eta[\ln(r)]^{1/\xi} \tag{4.14}$$

Similarly, the MPME dynamic tension based on the CWD model is

$$\hat{T}_{MPME}^{CWD} = \hat{T}_2[\ln(r)]^{1/\beta_2} \tag{4.15}$$

Computed values based on Eqs. (4.14) and (4.15) are shown in Table 4.4, and are also presented in the form of quantile-quantile plots (QQ-plots) [75] in Fig. 4.12. Table 4.4 compares $\hat{T}_{MPME}^{WBL}$, $\hat{T}_{MPME}^{CWD}$ and $\hat{T}_{MPME}^{test}$ for the seven cases, where $\hat{T}_{MPME}^{test}$ represents the maximum value of $\hat{T}$ observed from the test data. Note that absolute differences of $\hat{T}_{MPME}^{CWD}$ relative to the test date range from 2.07% (Case 1) to 19.06% (Case 4), while the WBL model systematically underestimated MPME values with differences ranging from 8.91 % (Case 4) to 22.98% (Case 1). In Fig. 4.12, QQ-plots for Cases 1, 2 and 7 are presented. It can be seen that the CWD model performs far more favorably compared to the WBL model for all the cases except Case 4. The CWD model fits the data very well, especially so in the upper tail, and deviations over the entire $\hat{T}$ range are relatively small; on the other hand, the WBL model shows maximum discrepancies relative to $\hat{T}$ test data that are approximately 2.87, 2.86 and 2.94 for Cases 1, 2 and 7, respectively. The QQ-plots in Fig.

4.12 also indicate that the proposed CWD model performs very well for potential extreme value prediction.

Table 4.4 The most probable maximum extreme dynamic tension based on test data ($\hat{T}_{MPME}^{test}$), the predicted MPME value for the WBL model ($\hat{T}_{MPME}^{WBL}$) and for the CWD model ($\hat{T}_{MPME}^{CWD}$) under the seven cases, including the differences between $\hat{T}_{MPME}^{WBL}$, $\hat{T}_{MPME}^{CWD}$ and $\hat{T}_{MPME}^{test}$

Case				The absolute difference w.r.t. $\hat{T}_{MPME}^{test}$ (%)	
	$\hat{T}_{MPME}^{test}$	$\hat{T}_{MPME}^{WBL}$	$\hat{T}_{MPME}^{CWD}$	$\hat{T}_{MPME}^{WBL}$	$\hat{T}_{MPME}^{CWD}$
1	4.83	3.72	4.73	22.98	2.07
2	4.50	3.79	4.81	15.78	6.89
3	4.27	3.76	4.80	11.94	12.41
4	4.04	3.68	4.81	8.91	19.06
5	4.43	3.79	4.81	14.45	8.58
6	4.65	3.80	4.78	18.28	2.80
7	4.55	3.74	4.77	17.80	4.84

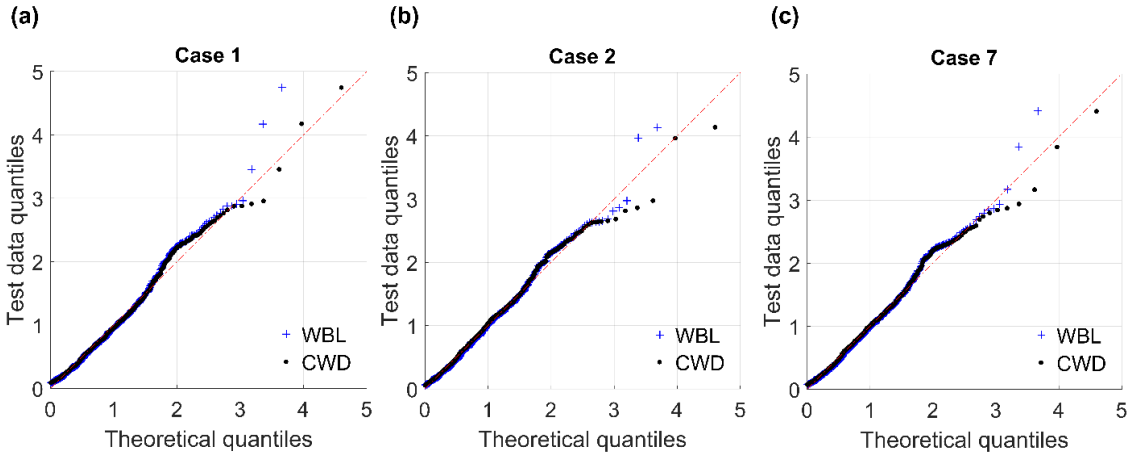

Fig. 4.12 Quantile-Quantile (Q-Q) plots for the WBL and CWD models versus test data for $\hat{T}$ considering (a) Case 1, (b) Case 2, and (c) Case 7

4.3 Discussion and Conclusions

In this study, the extreme value distributions of mooring tensions for a floating offshore wind turbine are investigated. A semi-submersible FOWT was tested at the 1:50-scale at the MARIN wave basin facility and reported in earlier works. A detailed examination of the mooring line tensions from the experiments revealed that the largest values of snap-induced tension ($\widehat{T^s}$) are 1.6 times that of the cyclic dynamic tension ($\widehat{T^n}$); this suggests that the maximum tension on FOWT mooring systems may be underestimated if snap events are not considered. Normalized snap-induced dynamic tension ($\widehat{T^s}$) are in the range of 1.70 – 4.83, compared to normalized non-snap tension values ($\widehat{T^n}$) that are in the range of 0.05 – 2.95. For both of the steady and turbulent winds, $\widehat{T^s}$ values are found to be larger for the higher wind speeds and with a stationary rotor (Cases 6 and 7) compared to cases with lower wind speeds and with the rotor in an operating condition (Cases 2 and 4). Although higher steady and turbulent winds result in a higher range of line tensions, they do not significantly influence the distribution of tension maxima. This might be caused by a mismatch in Reynolds number between full scale and the 1:50 model scale. Thus, the wind turbine underperformed greatly [76]. Moreover, in a previous chapter, it was found that wave height and heave motion are strongly correlated with snap events. It thus appears that wave characteristics play a dominant role in bringing about snap loads on a mooring line.

The probability distribution of dynamic tension ($\widehat{T}$) in the higher tension ranges is dominated by snap-induced tension maxima ($\widehat{T^s}$); as a result, $\widehat{T}$ distributions exhibit larger right tail probability levels than are associated with the Weibull (WBL) distribution. It is clear from this study that WBL models underestimate the upper tail of dynamic tension

that include snap events. A composite Weibull distribution (CWD) model with different shape and scale parameters on either side of a transition tension ($\hat{T}_{tr}$) is proposed that appeared to fit available data very well. This CWD model performs especially favorably in representing the upper tail of the tension distributions.

The implications of including snap-induced tension maxima in ultimate limit state evaluations may prove to be significant. For a FOWT, the ultimate limit state (ULS) design checks ensure that each mooring line has adequate strength to withstand loads imposed by extreme environmental conditions associated with a return period of 50 years [70]. The design maximum tension is the sum of two factored characteristic components, namely the characteristic mean line tension (T_{C-mean}) due to pre-tension and mean environmental loads, and the characteristic dynamic line tension (T_{C-dyn}) induced by low-frequency and wave-frequency motions. The ULS criterion per DNV [70] is

$$T_{C-mean}\gamma_{mean} + T_{C-dyn}\gamma_{dyn} \leq S_C \tag{4.16}$$

Here γ_{mean} and γ_{dyn} are partial safety factors equal to 1.75 and 2.2, respectively, for the high safety class. Also, S_C is the design breaking strength, defined as 95% of the minimum breaking strength. In many marine applications, the dynamic tension in catenary mooring lines is usually greater than the static tension corresponding to the dynamic behavior of the floaters [77]. This is especially true for FOWT systems and, thus, the second term in Eq. (4.15) is likely to be a more dominant factor in ULS design.

Considering that Eq. (4.16) is developed for systems where snap loads are generally non-existent or of very low probability, direct application of this equation to FOWT mooring systems is likely to be non-conservative. Following the line of analysis developed in the

present study, one can assume that $\hat{T}_{C-dyn}$ in Eq. (4.16) simply equals $\hat{T}_{d-max}$ (Eq. 4.10) which is one-half of the transition tension (0.5 $\hat{T}_{tr}$), thus disregarding the tension spikes from snap events.

If snap-induced dynamic tension values are to be included in the ULS design, one could consider equating $\hat{T}_{C-dyn}$ to the MPME value minus 0.9 $\hat{T}_{C-mean}$, where the MPME value is predicted using the composite Weibull distribution (Eq. 4.15) proposed in this study. As a case study, a 100-year storm of 3.5-hour duration with wave peak period of 14.3s is considered; this leads to a value of r equal to 881. For this particular case, if one assumes $\hat{T}_{C-dyn}$ based on the CWD model with the earlier proposed values of β_2 and $\hat{T}_2$ (0.746 and 0.360), it can be seen in Table 4.5 that the resulting $\hat{T}_{C-dyn}$ values will be 2.6 – 2.8 times larger than the $\hat{T}_{C-dyn}$ values based on the DNV criteria (0.5 $\hat{T}_{tr}$). This suggests the need for more than a doubling of the partial safety factor, γ_{dyn}.

Table 4.5 The characteristic dynamic line tension ($\hat{T}_{C-dyn}$) with the CWD model and the DNV standard (assuming one-half of transition tension, 0.5 $\hat{T}_{tr}$) for the seven cases, along with the ratio between the two

Case	$\hat{T}_{C-dyn}$ of CWD	$\hat{T}_{C-dyn}$ of DNV	Ratio
1	3.73	1.36	2.8
2	3.79	1.44	2.6
3	3.78	1.42	2.7
4	3.80	1.42	2.7
5	3.77	1.42	2.7
6	3.77	1.39	2.7
7	3.78	1.38	2.7

CHAPTER 5

NUMERICAL PREDICTION OF EXTREME TENSION IN FOWT MOORING SYSTEMS USING COUPLED ORCAFLEX-FAST

This chapter presents a comparative analysis of a semi-submersible based FOWT exposed to the 100-year storm conditions based on model test data and numerical simulations using coupled OrcaFlex-FAST software. The data is obtained from a 1:50 scale FOWT with the wind turbine modeled after the NREL 5MW wind turbine. OrcaFlex is used for numerical simulations of the mooring system. NREL's FAST software is coupled to OrcaFlex to obtain aerodynamic loads along with hydrodynamic loads for FOWT analyses. The numerical simulation of the moored FOWT in a 3.5-hour storm is executed in both the frequency-domain and the time-domain to determine the dynamic behavior of the platform and mooring system, respectively. Snap-type impact events are also observed in both test data and numerical simulation.

5.1 Numerical Setup of a Semi-submersible FOWT

State-of-the-art software tools are used to conduct simulations of the semi-submersible, including wind turbine dynamics, hydrodynamic platform responses, and a fully coupled mooring model. The tools are described briefly here.

Rhino 3D – a commercial 3D computer graphics and computer-aided design (CAD) application software developed by Robert McNeel & Associates was used to develop the model geometry [78].

ANSYS AQWA – is a suite of engineering analysis tools commonly used for the investigation of the effects of wave, wind and currents on floating and fixed offshore and marine structures. ANSYS AQWA has a frequency domain boundary element solver for floating bodies in an ocean environment. The mesh, linear and second-order hydrodynamic database are developed in this program [79].

OrcaFlex – a package for the dynamic analysis of offshore marine systems. OrcaFlex includes a time domain solver to find locations of stresses on flexible elements in an offshore system, including structural and fatigue analysis. This software requires as input, hydrodynamic coefficients of the floating body from an appropriate boundary element solver, e.g. ANSYS AQWA. The second order difference/sum frequency excitation force calculated by the QTF method is applied, since the influence of wave-induced second-order force in Semi FOWT has been observed [80, 81]. The mooring dynamics are modeled using OrcaFlex with a non-linear finite element model [82].

FASTLink – a coupler that enables access to FAST within the OrcaFlex environment to obtain aerodynamic loads along with hydrodynamic loads for FOWT analysis in OrcaFlex. This coupling is among the most robust tools for modeling FOWTs currently available [26]. A discussion of the implementation and use of FASTLink is provided by Masciola et al. [83]. Turbine aerodynamic analysis is often conducted using the NREL-FAST code, which has been applied to FOWTs for research, design, and development of government standards [84-87]. A discussion of the theory of FAST in offshore applications is provided by Jonkman [88]. The Froude-scale aerodynamic model is used in this study [81].

Fig. 5.1. and Fig. 5.2. show the geometry and converged panel models of the semi-submersible respectively. The main properties of the semi-submersible were shown in

Table 3.2. The prototype water depth is 200m and the draft is 20m. The wind turbine model is based on the NREL 5MW wind turbine, whose main properties are shown in Table 3.3. Fig. 5.3. shows the Semi wind turbine model set-up in the basin. The prototype mooring system includes three catenary lines oriented at 180, 60 and 300 degrees with respect to the *x*-axis. The lines are stud-less chains with properties as shown in Table 3.2. The mooring system used in the model experiments are made up of inextensible chains attached to linear springs located at the anchors to provide a close match to the prototype stiffness values. These properties are also the inputs to the program.

The chosen time series corresponds to a survival sea state described by a JONSWAP spectrum with a significant wave height of 10.5m, and a mean wave period of 14.3s acting on the platform for a duration of 3.5 hours. The encounter direction is 180 degrees with respect to the *x*-axis. Among various measurements made during the experiment, the platform motions and mooring line tensions are made available for this study. The snap events are found on the mooring chain oriented at 180 degrees with respect to the *x*-axis, thus the tension data of this mooring line is presented in this study. All results presented in this research are converted to full-scale units.

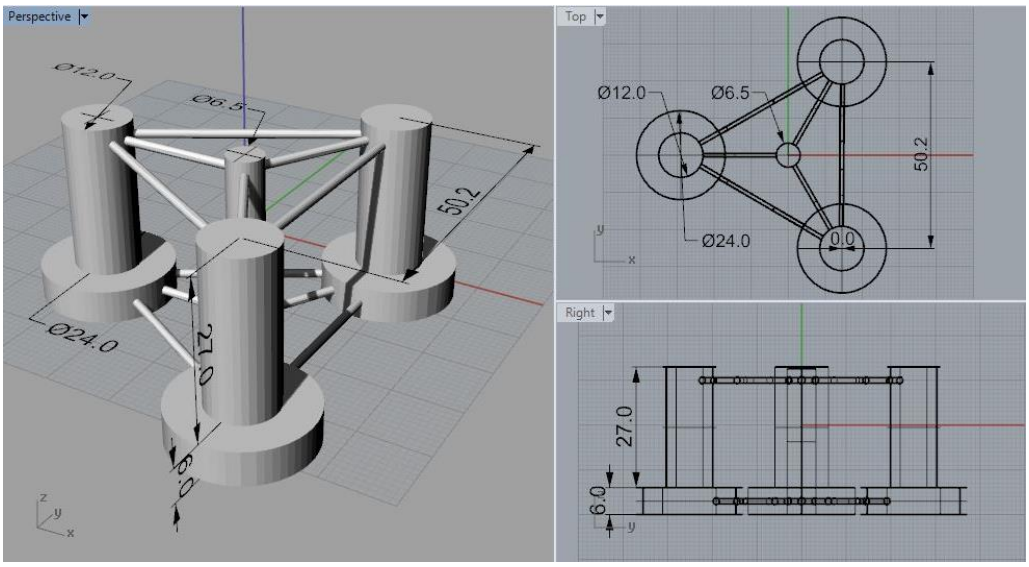

Fig. 5.1 Geometry Model

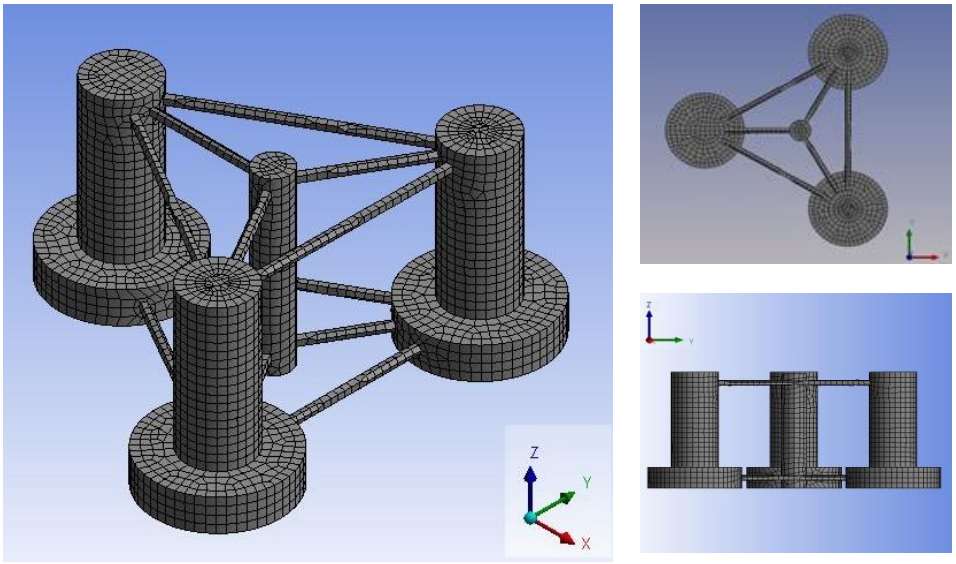

Fig. 5.2 Panel model used in AQWA

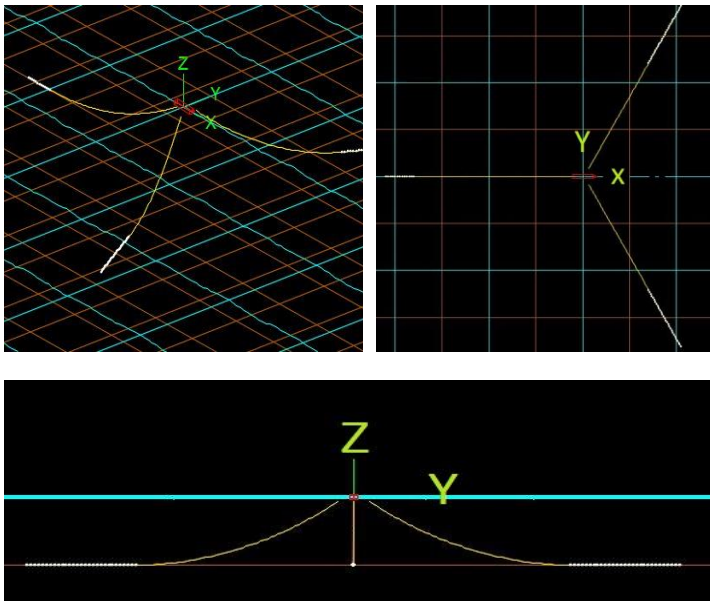

Fig. 5.3 The semi wind turbine model set-up in the basin

5.2 System 1-D and Software Validation

Prior to conducting simulations, several validation tests are performed with the software tools AQWA and Orcaflex to validate the model. These tests include:

1. Static offset tests
2. White noise tests and response amplitude operators (RAO)
3. Natural period, damping and free decay tests

The simulation results are compared with experimental data to provide the necessary validation of the simulation prior to further simulation runs for different sea state conditions.

5.2.1 Static Offset Tests

The platform model is given an initial offset in the *x*- and *y*-directions without wind, and the mooring line tension are measured. A plot of tension vs. offset provides the restoring

force characteristics of the mooring system. Fig. 5.4. and Fig. 5.5., respectively, show the comparison of mooring line restoring forces in the *x*- and *y*-directions between FASTLink simulations and experimental results. Offset values are incremented by 5m in accordance with experiments. In Fig. 5.4, the simulation results are in good agreement with each other and show good agreement with experimental results for lines 2 and 3. Tensions measured from simulations of line 1 are slightly larger than the tests. Since line 1 is collinear with the *x*-axis, it is heavily loaded and displays strong nonlinearity in the simulation, which is not captured in the experiments.

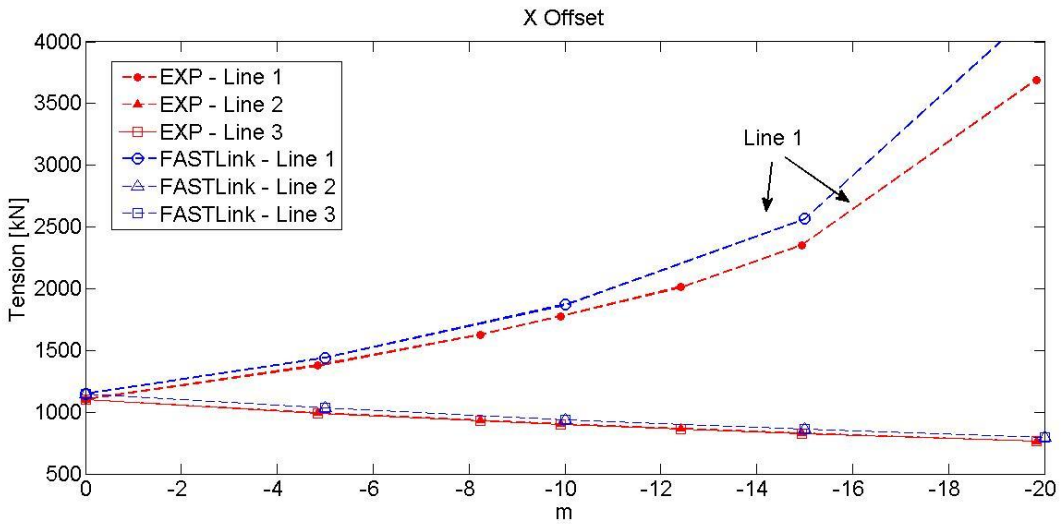

Fig. 5.4 Comparison of mooring line restoring force in *x*-direction between FASTLink and test data

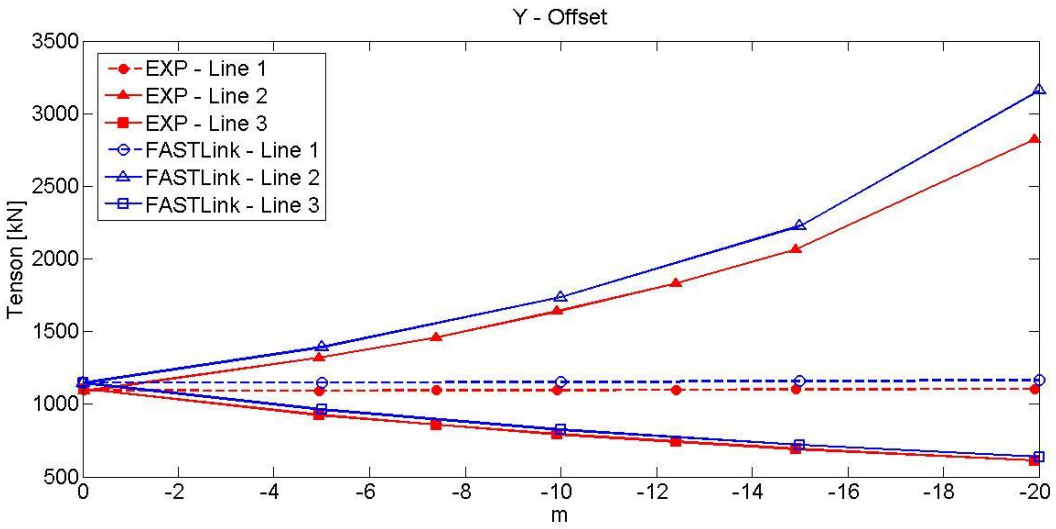

Fig. 5.5 Comparison of mooring line restoring force in the *y*-direction between FASTLink and test data.

5.2.2 White Noise Tests and Response Amplitude Operators (RAO)

The RAO of a floating platform in a degree of freedom describes the response amplitude per unit wave amplitude as a function of wave frequency. A random wave condition based on a white noise spectrum is applied to the structure to obtain responses at various frequencies simultaneously. The white noise power spectral density (PSD) given by S_i has energy spread evenly over the frequency range from 0.05 to 0.2 Hz (period 5 – 20 s). The RAO (R_i) is then calculated as

$$R_i = (P_i/S_i)^{\frac{1}{2}},\ for\ i = 1, 2, \ldots, M/2 \tag{5.1}$$

The PSD of the structure is P_i, and the index i = 1, 2, …, M/2 denotes the components at frequencies f_i, which are integer multiples of the FFT's fundamental frequency.

Fig. 5.6 – 8. show the comparison of the RAOs in the surge, heave, and pitch motions, respectively. These RAOs are obtained without wind effects but include the three mooring

lines for model tests and simulation tests. Both the surge and heave RAOs show good agreement between the experimental data and simulation results. The pitch RAO is in excellent agreement for a period range from 5 to 13s, beyond which the simulations consistently differ with the experiments. This is likely due to decreases in the wave amplitude at lower frequencies (approaching the end of the white noise spectrum) in the experiments, which leads to an artificially higher RAO (division by a small number).

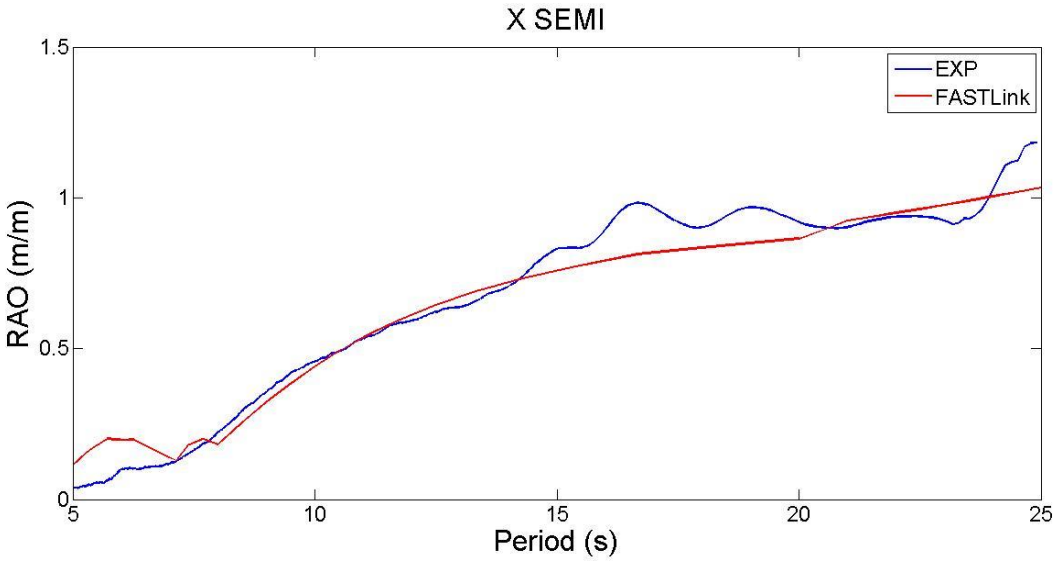

Fig. 5.6 Comparison of RAO in surge between FASTLink and test data

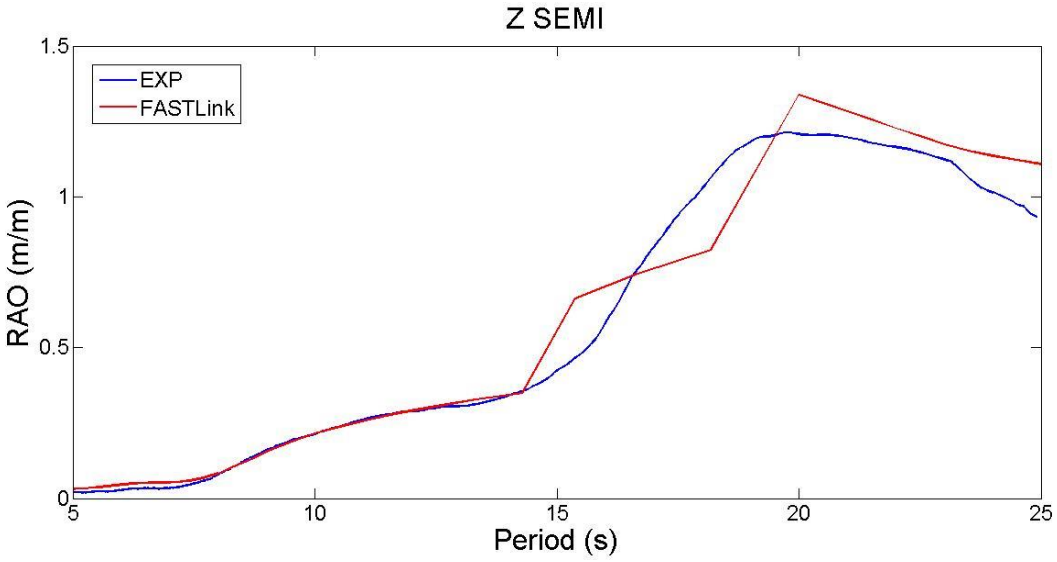

Fig. 5.7 Comparison of RAO in heave between FASTLink and test data

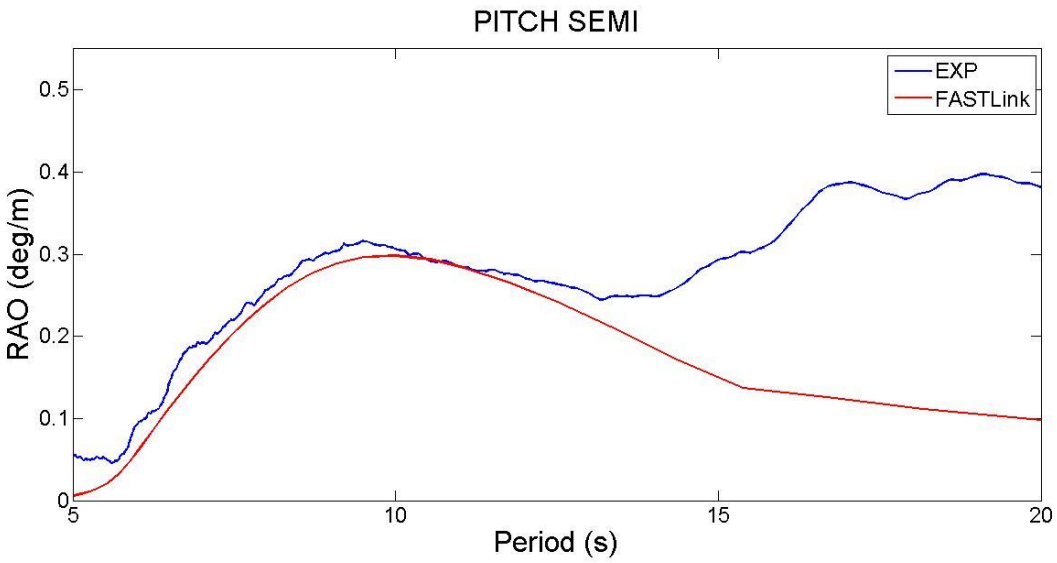

Fig. 5.8 Comparison of RAO in pitch between FASTLink and test data

5.2.3 Natural Period, Damping and Free Decay Tests

For the semi-submersible platform, flow-separation-induced drag is a large component of the total hydrodynamic damping. However, the hydrodynamic database developed through ANSYS AQWA simulations uses potential flow theory to model the hydrodynamic forces, which defines the radiation loads for structures without viscous effects. As such, the linear radiation damping is augmented with a viscous damping model. The platform viscous damping and linear damping are replaced by the equivalent linear viscous damping.

$$B_{\mathrm{eq}ij} = B_{1ij} + B_{2ij}\frac{8}{3\pi}A_{ij}\omega_{ij},\ \ i,j = 1,2,\cdots 6 \tag{5.2}$$

Where $B_{\mathrm{eq}ij}$ are the equivalent linear viscous damping coefficients, B_{1ij} and B_{2ij} are the linear and quadratic damping coefficients, A_{ij} are amplitudes and ω_{ij} are the frequencies. B_{1ij} and B_{2ij} are determined via the platform motion free-decay tests, which were conducted in the experiments. The values for the equivalent damping coefficients are evaluated and applied to the FASTLink simulations.

Fig. 5.9 – 11. show the comparison of free decay in three directions between basin tests and simulations. The natural periods of the surge, heave, and pitch are calculated for both experimental results and FASTLink simulations and show good agreement. The difference of the natural period in heave, pitch, and surge between FASTLink and the basin tests are 0.56%, 0.37%, and 2.7%, respectively. The simulations decay quicker than the tests. This is possible because the simulations use linear damping that overestimates the damping at lower amplitude motions.

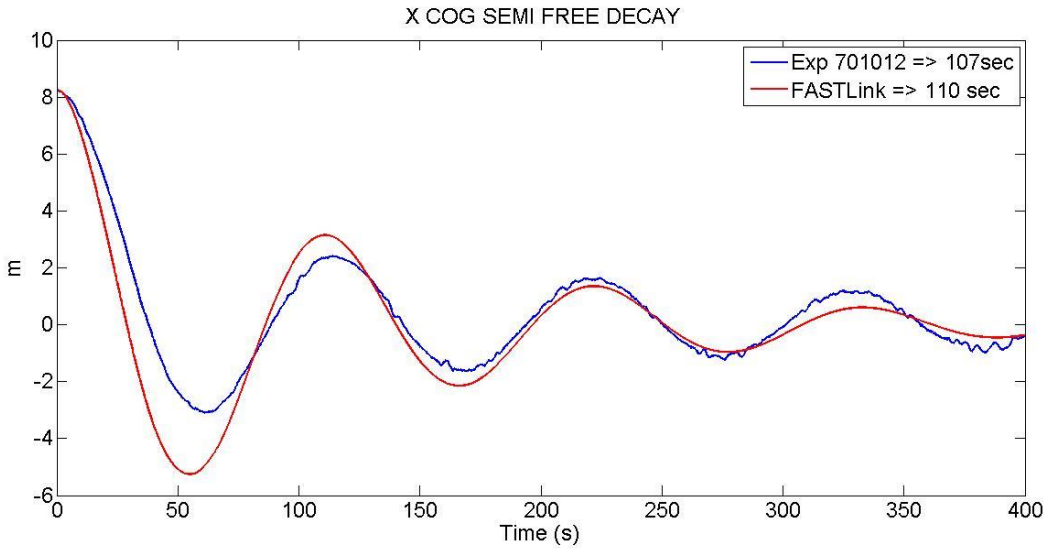

Fig. 5.9 Comparison of free decay in surge between FASTLink and test data

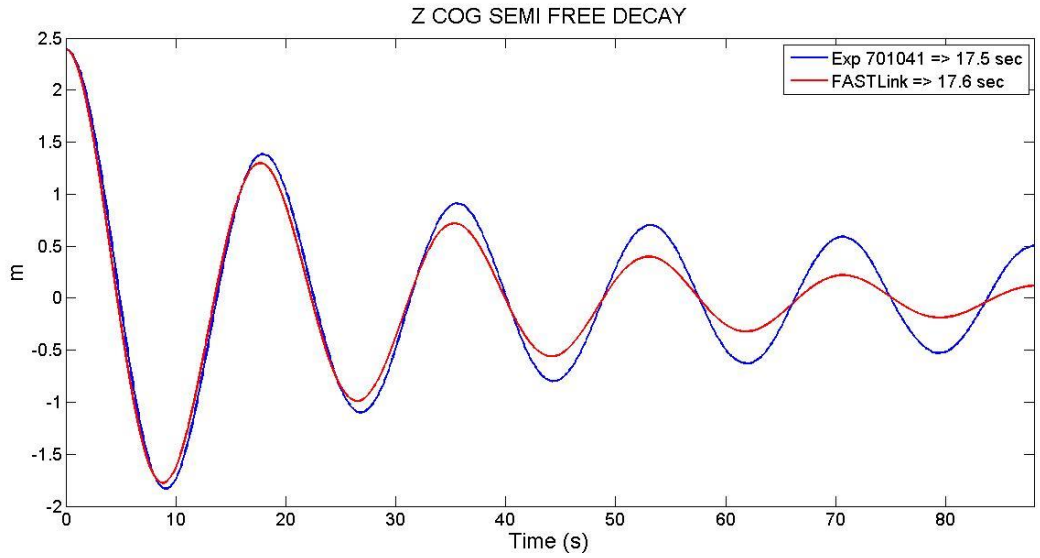

Fig. 5.10 Comparison of free decay in heave between FASTLink and test data

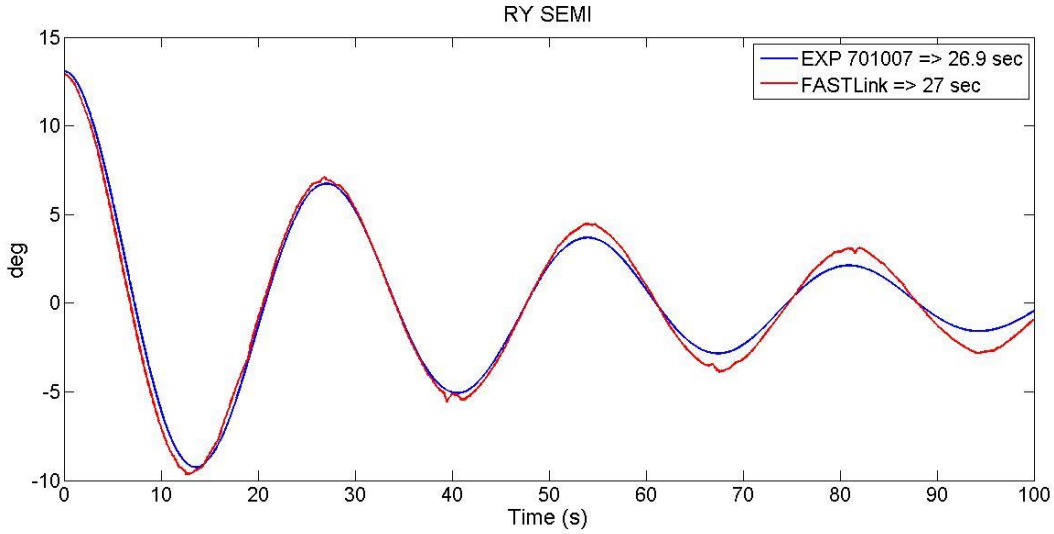

Fig. 5.11 Comparison of free decay in pitch between FASTLink and test data

5.3 Platform motions and Mooring Tension Prediction In a 100-yr Storm

A typical sea-state is described by a spectrum model (e.g. JONSWAP), that depends on characteristic parameters like significant wave height (H_s) and spectral peak period (T_p). In experiments, a typical sea spectrum is used to generate a random time series signal, which is input into the wave maker. The generated waves are measured by a wave probe at the location of the structure model (without the structure being physically present) and

analyzed to reveal the measured spectrum. The wavemaker transfer function is adjusted to obtain a good agreement between the measured and desired spectral conditions. The time series of the wave as output by the probe is a good indicator of the wave field "seen" by the model.

In this case study, the time series of the wave elevation are obtained from a wave spectrum to create a random time series input. The chosen time series corresponds to a survival sea-state described by a JONSWAP spectrum with H_s = 10.5m, T_p = 14.3s. This research investigates the global performance of the Semi FOWT and compares the results between numerical modeling and test data. The global performance includes motions in surge, heave and, pitch, mooring line tensions of three mooring lines. The time series, PSD and statistical analysis are presented. The Parzen window function [89] is applied to the power spectral density analysis. The sea-state combined with the no wind condition and the steady wind of 21m/s are compared with the test data (SF1 and SF2 in Table 3.11).

5.3.1 Wave and Platform Motions

Figs. 5.12, 5.14, 5.16 and 5.18 show the time series comparisons for wave, surge, heave, and pitch between experiments and FASTLink respectively. Figs. 5.13, 5.15, 5.17 and 5.19 show the PSD comparisons for wave, surge, heave and pitch between experiments and FASTLink respectively. The wave elevation time history and spectra agreement is fairly close as would be expected. The surge motion time history shows a higher absolute mean value under the steady wind condition than the absolute mean value under the no wind conditions. The comparison for the surge PSD is fairly good in the wave-energy range (0.04 to 0.2 Hz), while the simulation results are significantly lower at the low-frequency

range corresponding to the surge natural period of 0.0095 Hz. The differences are 47% and 27% for the no wind and steady wind condition respectively. Moreover, the surge PSD of the no wind condition is slightly higher at the low-frequency range than the surge PSD under the steady wind speed of 21m/s.

The heave motion time history shows a common mean value and overall behavior, however, the simulation PSDs in the wave frequency range of 0.06 to 0.1Hz are 73% and 55% lower than that of the test data under no wind and steady wind conditions, respectively. Furthermore, the PSDs of FASTLink at the heave natural frequencies of 0.056Hz are 20% and 26% lower than that of the test data under the no wind and steady wind conditions, respectively. This could be attributed to the heave RAO difference between the test data and the simulations in the wave frequency range.

The pitch motion time history shows a higher absolute mean value under steady wind conditions than the value under the no wind condition. The pitch PSDs of the FASTLink model are much lower at the wave frequency range and at the frequency of 0.035Hz than the test data. At the wave frequency range, the differences are 45% and 76% for the no wind and the steady wind conditions respectively. At the frequency of 0.035Hz, the differences are 89% and 73% for the no wind and the steady wind conditions respectively. The discrepancy of the surge and pitch PSDs in the low-frequency range between FASTLink model and test model could be attributable to second-order hydrodynamic effects not captured in the numerical model [31, 81]. The largest discrepancy, in regard to the PSD simulations, occurs with the pitch motion. It is believed that pitch motions are strongly affected by the turbine aerodynamics, and hence simulation results often show discrepancies.

Table 5.1 and Table 5.2 show the comparisons of statistics in wave heights, surge, heave and pitch motions for the no wind and the steady wind conditions, respectively. In these three motions of both SF1 (no wind condition) and SF2 (steady wind condition), root mean squares of test data are all larger than the root mean squares of FASTLink simulations. For SF1, the root mean square difference in surge, heave, and pitch are 27.74%, 23.63%, and 41.46% respectively. For SF2, the root mean square difference in surge, heave, and pitch are 9.41%, 20.8%, and 12.61%, respectively. It is notable that the magnitude of both heave and pitch motions are quite small. Hence the differences between the test data and the FASTLink results are not significant.

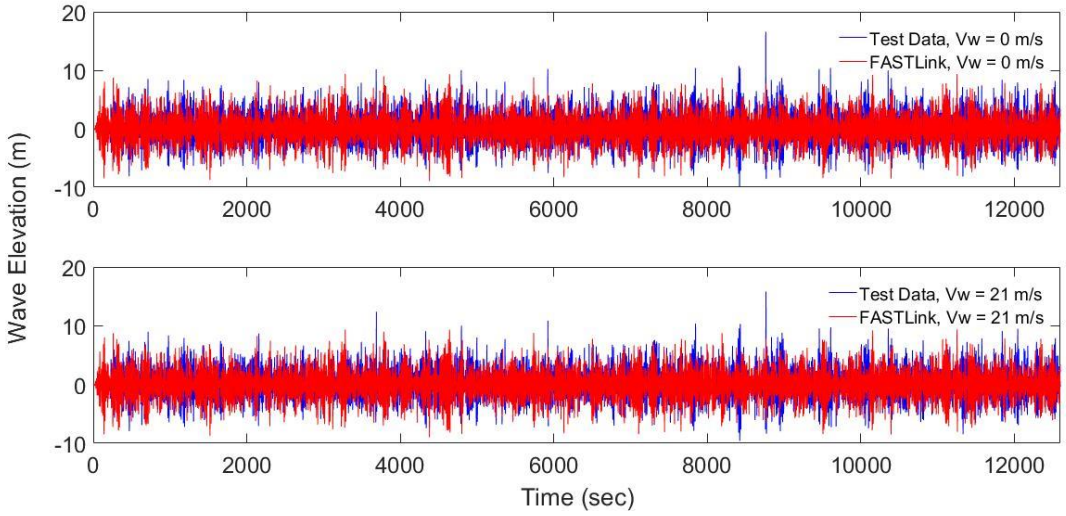

Fig. 5.12 Three-and-one-half hour-long wave elevation time series of test data and FASTLink for no wind (top plot) and 21m/s steady wind speed (bottom plot) cases with a significant wave height of 10.5m and a peak wave period of 14.3s

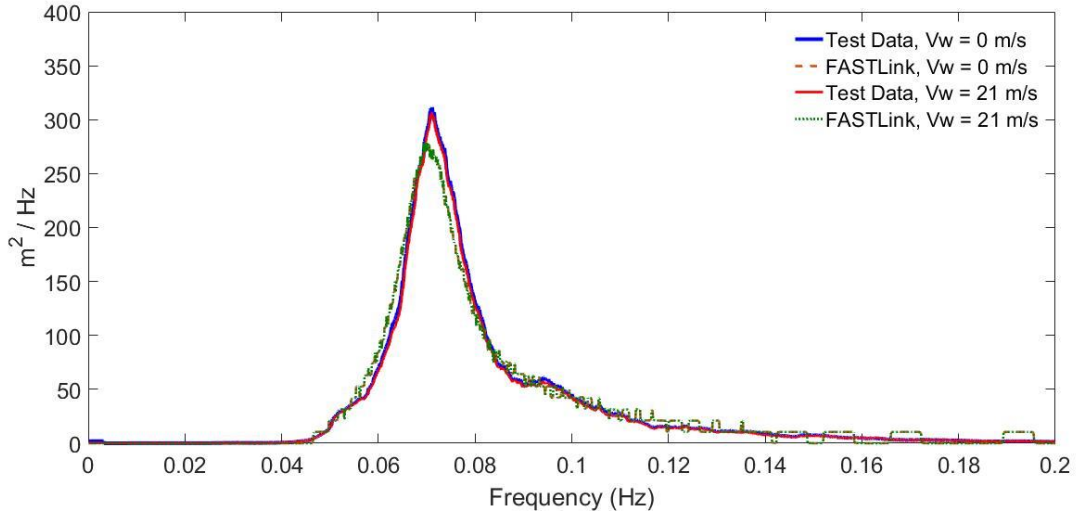

Fig. 5.13 Wave elevation PSDs of test data and FASTLink for no wind and 21m/s steady wind speed cases with a significant wave height of 10.5m and a peak wave period of 14.3s

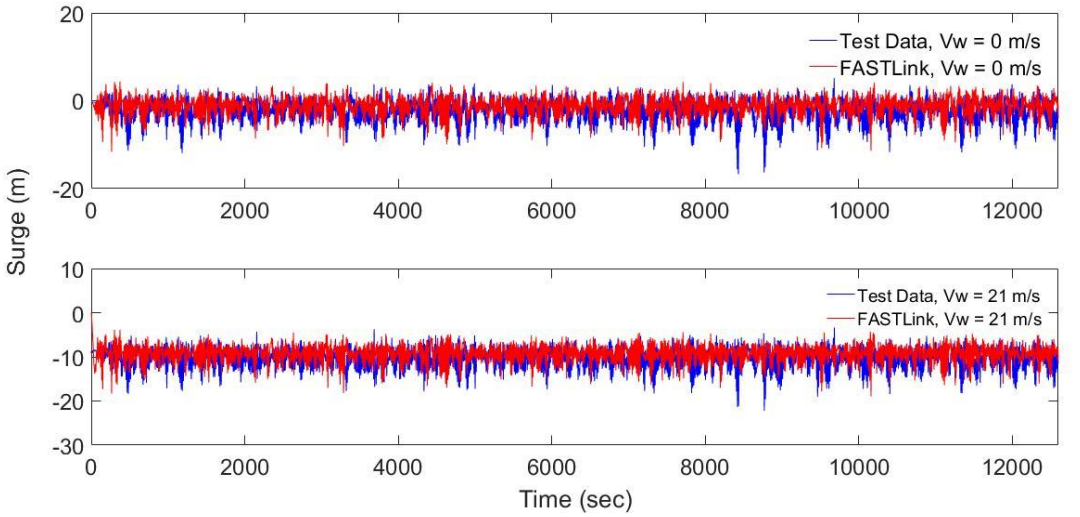

Fig. 5.14 Three-and-one-half hour-long surge motion time series of test data and FASTLink for no wind (top plot) and 21m/s steady wind speed (bottom plot) cases with a significant wave height of 10.5m and a peak wave period of 14.3s

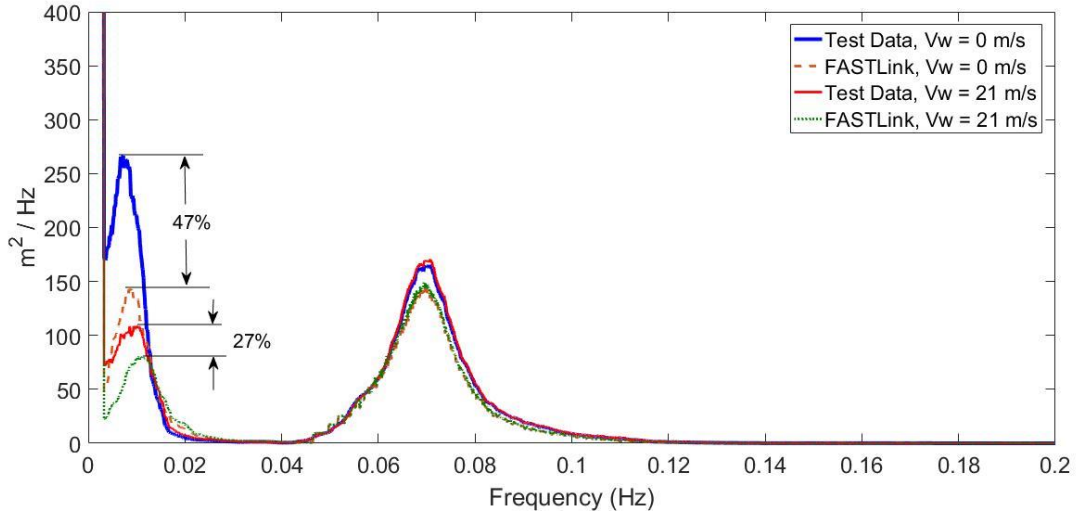

Fig. 5.15 Surge PSDs of test data and FASTLink for no wind and 21m/s steady wind speed cases with a significant wave height of 10.5m and a peak wave period of 14.3s

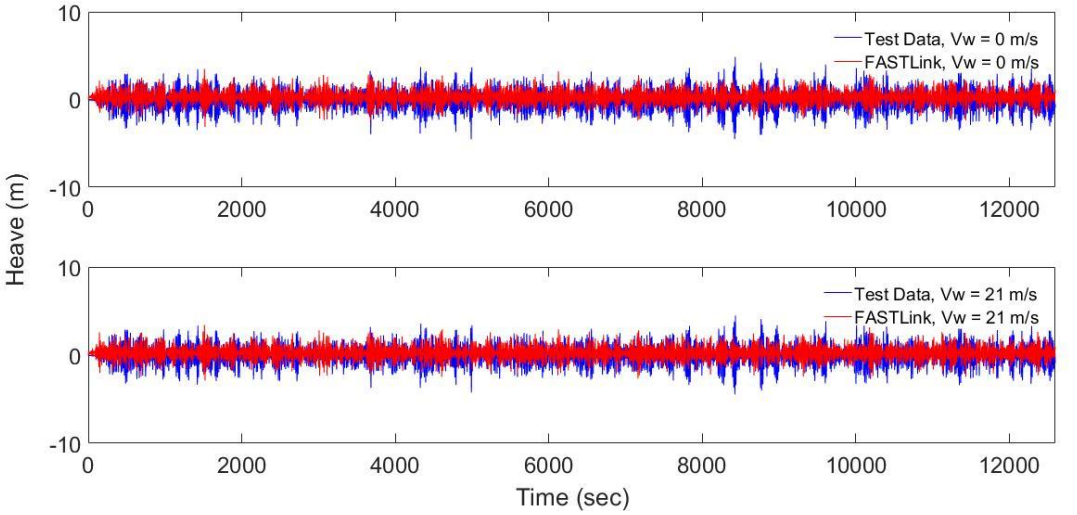

Fig. 5.16 Three-and-one-half hour-long heave motion time series of test data and FASTLink for no wind (top plot) and 21m/s steady wind speed (bottom plot) cases with a significant wave height of 10.5m and a peak wave period of 14.3s

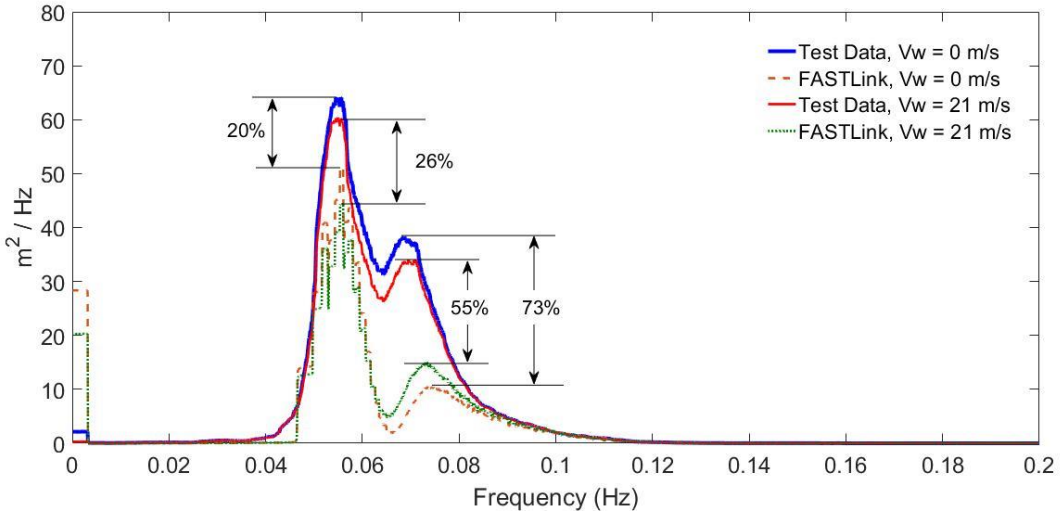

Fig. 5.17 Heave PSDs of test data and FASTLink for no wind and 21m/s steady wind speed cases with a significant wave height of 10.5m and a peak wave period of 14.3s

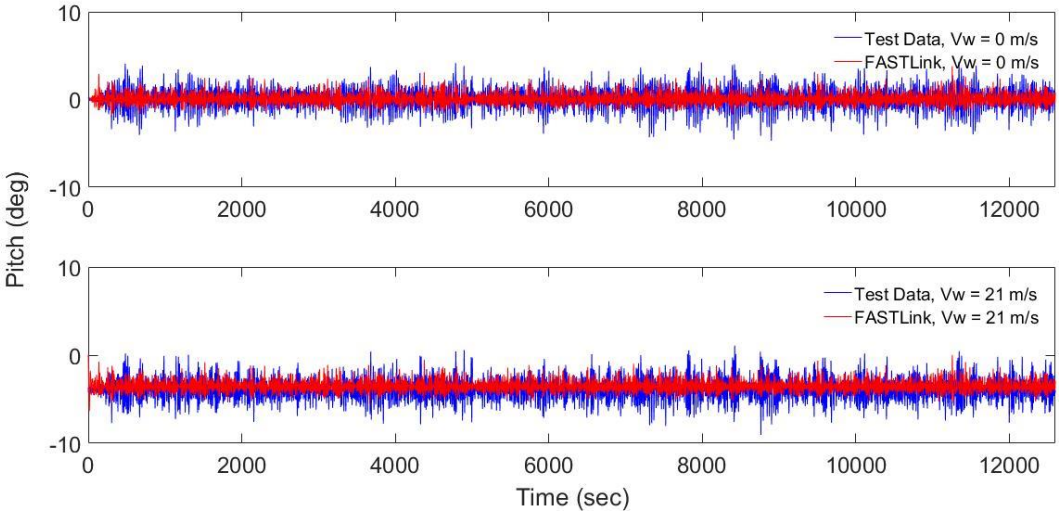

Fig. 5.18 Three-and-one-half hour-long pitch motion time series of test data and FASTLink for no wind (top plot) and 21m/s steady wind speed (bottom plot) cases with a significant wave height of 10.5m and a peak wave period of 14.3s

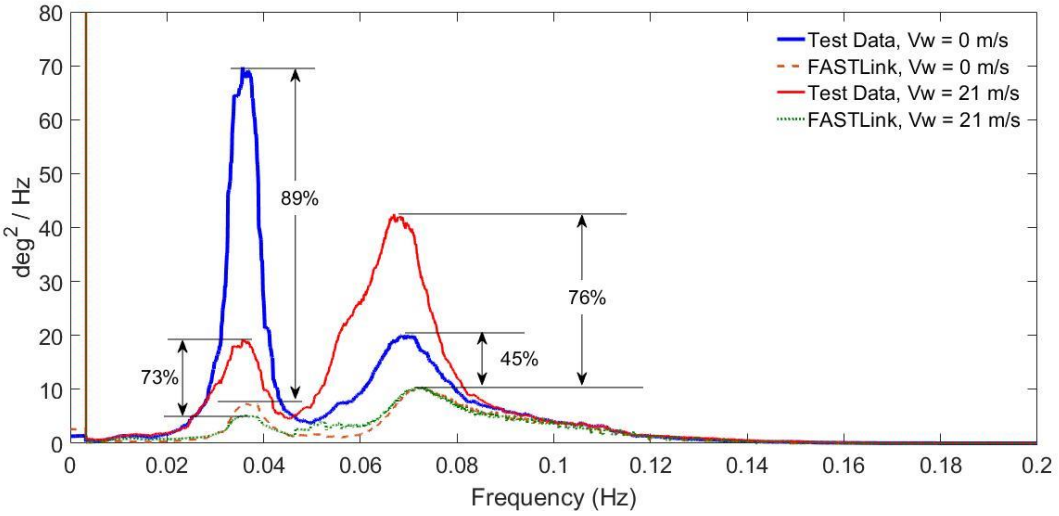

Fig. 5.19 Pitch PSDs of test data and FASTLink for no wind and 21m/s steady wind speed cases with a significant wave height of 10.5m and a peak wave period of 14.3s

Table 5.1 Comparison of FASTLink predictions and test data statistics in wave heights, surge, heave and pitch motions under no wind condition

	Experiments		FASTLink		Difference (%)	
	Mean	Root Mean Square	Mean	Root Mean Square	Mean	Root Mean Square
Wave	2.07	2.61	2.08	2.62	0.19	0.40
Surge	-2.35	3.37	-1.31	2.43	44.21	27.74
Heave	-0.08	1.16	0.30	0.89	73.33	23.63
Pitch	0.06	1.11	0.09	0.65	49.65	41.46

Table 5.2 Comparison of FASTLink predictions and test data statistics in wave heights, surge, heave and pitch motions under the steady wind speed of 21m/s

	Experiments		FASTLink		Difference (%)	
	Mean	Root Mean Square	Mean	Root Mean Square	Mean	Root Mean Square
Wave	2.03	2.57	2.08	2.62	2.07	2.16
Surge	-10.41	10.63	-9.43	9.63	9.41	9.41
Heave	-0.03	1.11	0.25	0.88	88.18	20.80
Pitch	-3.89	4.05	-3.48	3.54	10.53	12.61

5.3.2 Mooring Line Tension

In this section, mooring line tensions at the fairlead are presented. Time series, PSDs and statistical analyses from both simulation exercises and the experimental results are presented successively. Certain common trends are evident. FASTLink results are lower than experiments for mooring line tensions. This is because of the decreased motions of the FOWT in the FASTLink model. Snap load events (large tension spikes) are observed for the upstream mooring line (#1) in the test data and FASTLink simulation output, however, the characteristics are quite different. The magnitude of the spikes is smaller in the simulations. The downstream lines (#2 and #3) do not see any snap load events.

Figs. 5.20, 5.22 and 5.24 respectively show the time series comparisons for line 1, line 2 and line 3 between the test data and the FASTLink results under the no wind and steady wind conditions. Figs. 5.21, 5.23 and 5.25 respectively show the PSD comparisons for line 1, line 2 and line 3 between the test data and the FASTLink results under the no wind and steady wind conditions. The mooring line tension history of line 1 shows lower mean values under the no wind condition than the values under the steady wind condition. Moreover, the mooring tension histories of lines 2 and 3 show higher mean values under

the no wind conditions than the values under the steady wind condition. The distribution of loads across the lines appears to differ between the static offset tests and the simulations, which possibly could be due to some differences in the experimental setup and the arrangement.

The absolute surge mean value increases from 2.35m to 10.41m under steady wind conditions, thus, the line 1 tension increases and lines 2 and 3 tensions decrease. The wave force effects on the mooring lines are significant which are observed on both of the test model and the FASTLink model because the PSDs at the wave frequency range of 0.04 to 0.2Hz are much higher than the PSDs at the low-frequency range. For line 1, the tension PSDs of the test data of both SF1 and SF2 are higher than the PSDs of the simulation results. The differences are 50% and 43% for the no wind and the steady wind conditions, respectively. Moreover, the dynamic tension of line 1 is underpredicted by the numerical model which could be due to a higher drag coefficient, a higher stiffness of mooring chain or extra damping system in the FASTLink model. Both lines 2 and 3 have similar experiment and simulation results in the tension time histories. The tension PSDs in the low-frequency range differ by 28%. Moreover, the tension PSDs of lines 2 and 3 are larger under the no wind condition than the PSDs for the steady wind condition. This is expected since lines 2 and 3 are downwind and therefore lose more tension under steady wind conditions.

Table 5.3 and Table 5.4 show comparisons of statistics in mooring line tensions (line 1, 2 and 3) for the no wind and the steady wind conditions, respectively. The FASTLink model overall does a fairly good job of predicting mean tensions which differ by 10.63%. For line 1, the root mean squares differ by 3.84% and 8.22% under the no wind and the steady wind

conditions respectively. For lines 2 and 3, the root mean squares differ 10.82% and 10.83% under the no wind and the steady wind conditions, respectively. The underestimation of the line stiffness could cause the root mean square difference between the test data and the simulation results. Maximum and minimum values, being non-statistical, can differ considerably between the experiments and the simulation. In a quasi-static sense, the mean tensions are more important than root mean squares. Hence, the simulation results are acceptable.

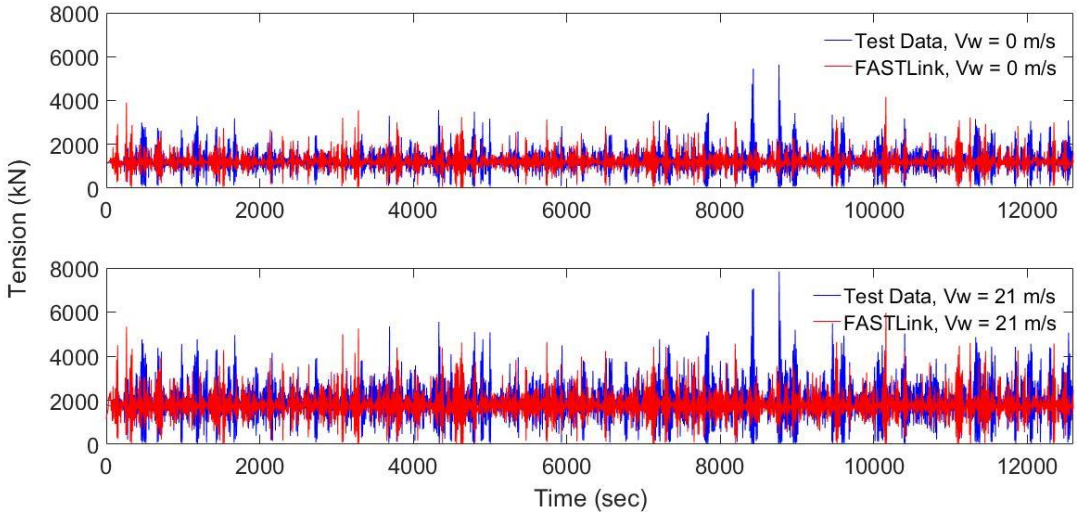

Fig. 5.20 Three-and-one-half hour-long mooring line tension time series (Line 1) of test data and FASTLink for no wind (top plot) and 21m/s steady wind speed (bottom plot) cases with a significant wave height of 10.5m and a peak wave period of 14.3s

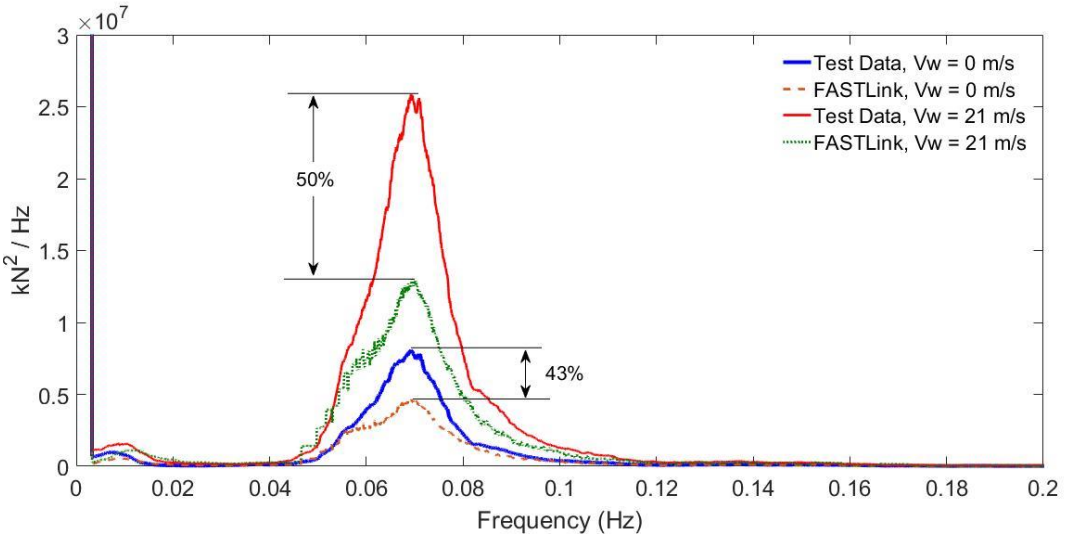

Fig. 5.21 Mooring line tension (Line 1) PSDs of test data and FASTLink for no wind and 21m/s steady wind speed cases with a significant wave height of 10.5m and a peak wave period of 14.3s

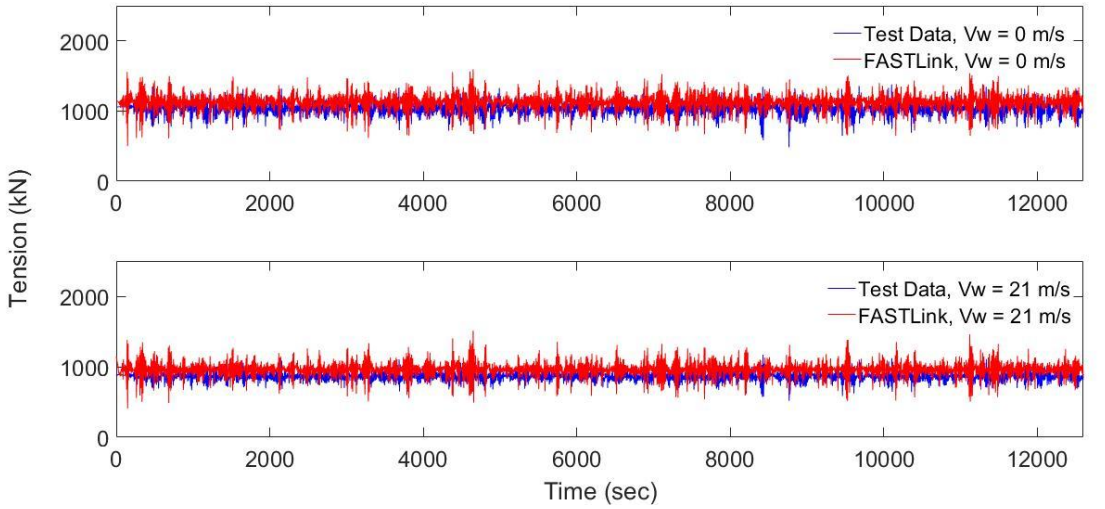

Fig. 5.22 Three-and-one-half hour-long mooring line tension time series (Line 2) of test data and FASTLink for no wind (top plot) and 21m/s steady wind speed (bottom plot) cases with a significant wave height of 10.5m and a peak wave period of 14.3s

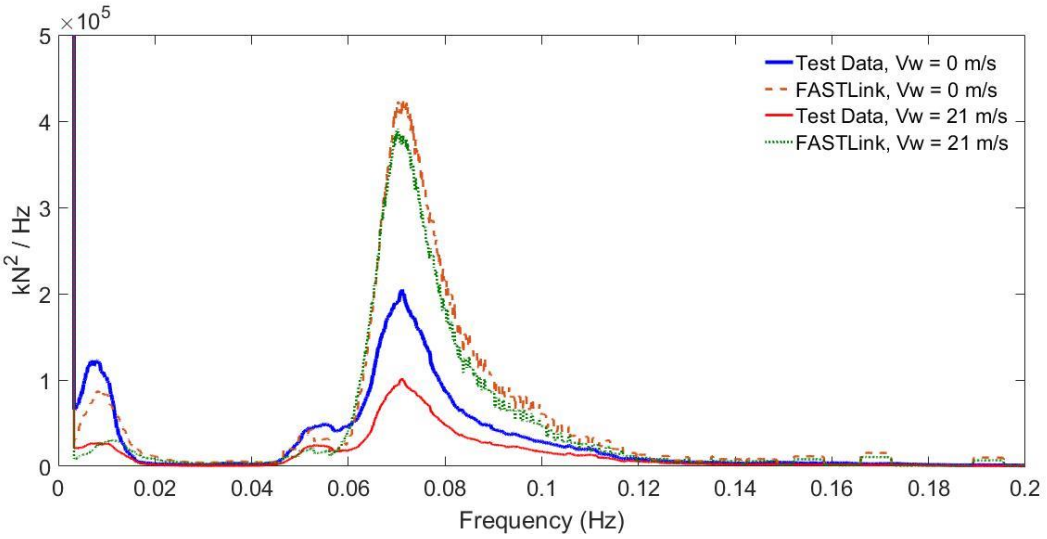

Fig. 5.23 Mooring line tension (Line 2) PSDs of test data and FASTLink for no wind and 21m/s steady wind speed cases with a significant wave height of 10.5m and a peak wave period of 14.3s

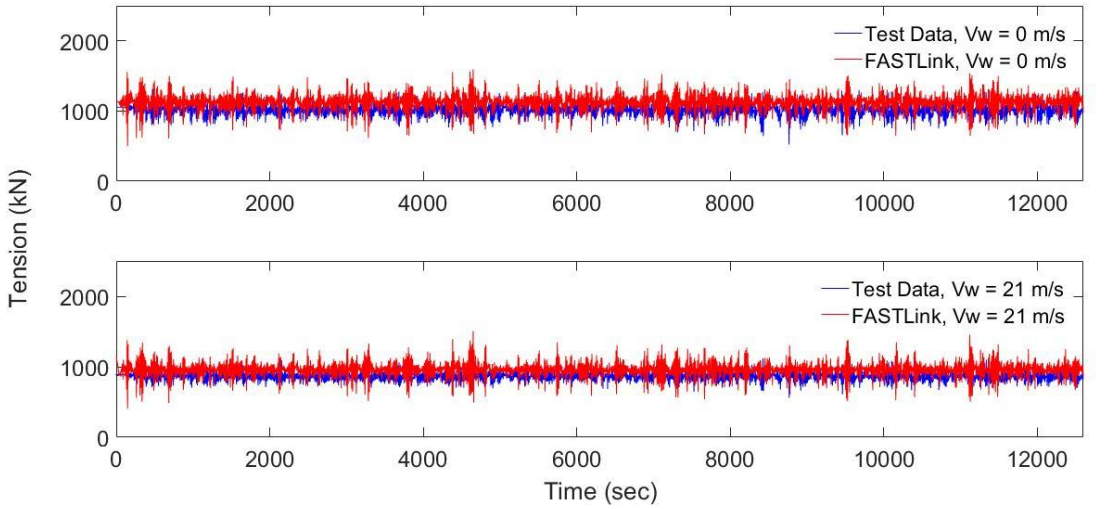

Fig. 5.24 Three-and-one-half hour-long mooring line tension time series (Line 3) of test data and FASTLink for no wind (top plot) and 21m/s steady wind speed (bottom plot) cases with a significant wave height of 10.5m and a peak wave period of 14.3s

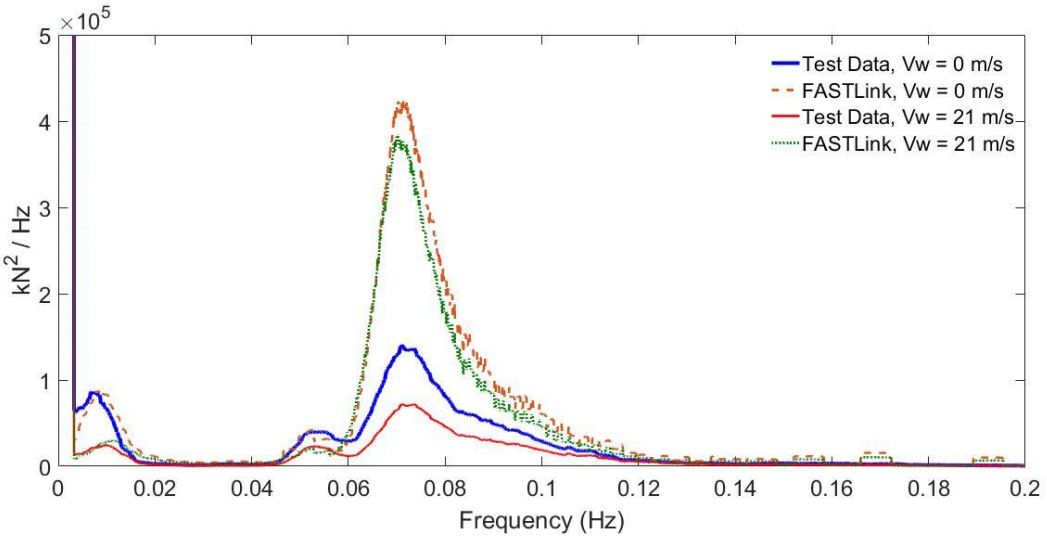

Fig. 5.25 Mooring line tension (Line 3) PSDs of test data and FASTLink for no wind and 21m/s steady wind speed cases with a significant wave height of 10.5m and a peak wave period of 14.3s

Table 5.3 Comparison of FASTLink predictions and test data statistics in mooring line tensions of line 1, 2 and 3 under no wind condition

		Experiments	Simulation	Difference (%)
Line 1	Mean	1256.28	1226.64	2.36
	Root Mean Square	1325.52	1274.65	3.84
	Maximum	5640.23	4162.83	26.19
	Minimum	31.66	10.52	66.77
Line 2	Mean	1028.77	1114.83	8.37
	Root Mean Square	1031.67	1119.42	8.51
	Maximum	1378.27	1595.58	15.77
	Minimum	483.01	500.07	3.53
Line 3	Mean	1007.75	1114.84	10.63

	Root Mean Square	1010.16	1119.42	44.91
	Maximum	1316.18	1595.28	10.82
	Minimum	523.01	500.21	4.36

Table 5.4 Comparison of FASTLink predictions and test data statistics in mooring line tensions of line 1, 2 and 3 under steady wind speed of 21m/s

		Experiments	Simulation	Difference (%)
Line 1	Mean	1938.93	1816.69	6.30
	Root Mean Square	2076.16	1905.41	8.22
	Maximum	7835.23	5968.74	23.82
	Minimum	33.92	4.66	86.27
Line 2	Mean	859.64	950.17	10.53
	Root Mean Square	861.30	954.60	10.83
	Maximum	1171.20	1511.91	29.09
	Minimum	517.14	407.32	21.24
Line 3	Mean	860.45	947.86	10.16
	Root Mean Square	861.90	952.22	10.48

Maximum	1119.41	1504.67	34.42
Minimum	561.33	408.20	27.28

CHAPTER 6

THE COMPOSITE WEIBULL DISTRIBUTIONS OF THE NUMERICAL DATA

This chapter studies three FASTLink results of the FOWT Semi (SF1) under survival storm conditions. The environmental conditions of these three cases are Case 1, 4 and 7 of Table 3.8. For all of these three cases, the significant wave height and wave peak period are held constant at 10.5m and 14.3s, respectively, while the steady wind speed is varied from 0 to 30.5m/s. The directions of the wind and waves were 180^o with respect to the *x*-axis. Several snap events are found to result in the upwind mooring line. The proposed composite Weibull probability distribution described in Chapter 4 is applied to the mooring line dynamic tension predicted by numerical modeling. The proposed distribution model provides a good fit to the simulated tension data and compared with the model of the test data as presented in Chapter 4.

6.1 Analysis of Tension Maxima

In this study, the normalized cyclic dynamic tension ($\hat{T}$), snap-induced tension ($\widehat{T^s}$) and those that are not associated with a snap event ($\widehat{T^n}$) are investigated. Table 6.1 summarizes data on $\hat{T}$, $\widehat{T^n}$ and $\widehat{T^s}$ for all the three cases (Case 1, 4 and 7 of Table 3.8). In general, snap events are infrequent, occurring on average about once for every 25 non-snap cyclic events. The greatest number of snap events is observed for Case 7, where the wind speed is 30.5m/s and for a rotor at zero RPM. The smallest number of snap events occurred when there is no wind (Case 1), which is also observed in the same case for the test data (Table 4.1). For

both $\widehat{T^n}$ and $\widehat{T^s}$, the number of cycles predicted by FASTLink are very similar to the test data. The absolute difference of the number of cycles between test data and FASTLink results range from 5% (Case 1) to 13% (Case4).

Overall, the snap event durations range from 6.1 to 10.7 s. Snap-induced dynamic tension ($\widehat{T^s}$) are in the range of 1.80 to 4.25, while their non-snap counterparts, $\widehat{T^n}$, are in the range of 0.07 to 3.70. In the no-wind condition (Case 1), the largest $\widehat{T^s}$ value of 4.25 is observed. For the test data, the largest $\widehat{T^s}$ value of 4.83 is also found in the no wind condition. The largest $\widehat{T^n}$ and $\widehat{T^s}$ value of the FASTLink results are respectively 29% larger and 14% lower than the value of the test data (Table 4.1) under the same three cases (Cases 1, 4 and 7). It is notable that the FASTLink results of the three cases have larger maximum $\widehat{T^n}$ values and smaller maximum $\widehat{T^s}$ values when compared to the test data. Wind speed could cause $\widehat{T^s}$ values to decrease (Cases 1 vs. 4 and 7). For steady winds, $\widehat{T^s}$ values are higher for higher wind speeds with a stationary rotor (Case 7) compared to lower wind speeds with rotor in operating conditions (Case 4). The same phenomenon is also observed in the test data.

Table 6.1 Normalized tension ranges, number of cycles, and duration for $\hat{T}$, $\widehat{T^n}$ and $\widehat{T^s}$ in the three cases of the test data

Case	$\hat{T}$		$\widehat{T^n}$			$\widehat{T^s}$			
	Tension range		Number	Tension range		Number	Duration range	Tension range	
	Min	Max	of cycles	Min	Max	of cycles	(sec / cycle)	Min	Max
1	0.10 -	4.25	912	0.10	3.70	22	6.2 - 10.2	1.85	4.25
4	0.07 -	3.99	1011	0.07	3.29	26	6.5 - 10.3	1.80	3.99
7	0.08 -	4.09	985	0.08	3.43	27	6.1 – 10.7	1.84	4.09

The exceedance probability (P) of the normalized cyclic dynamic tension ($\hat{T}$), snap-induced tension ($\widehat{T^s}$) and those that are not associated with a snap event ($\widehat{T^n}$) are investigated. The exceedance probability of a line's dynamic tension, $\hat{T}$, was described in Eq. (4.1).

Fig. 6.1. compares the exceedance probabilities of the dynamic tension ($\hat{T}$) for the stationary rotor with different steady wind speeds, Cases 1 and 7, while Fig. 6.2. does the same for different steady wind speeds and different rotor speeds, Cases 4 and 7. The number of data points plotted corresponds to *r*, the total number of measurements (tension values) in the sample. In both figures, the exceedance probability curves for the higher tension ranges are mostly contributed to by $\widehat{T^s}$ and one $\widehat{T^n}$ in the ranges of 3.3 to 3.7. The lower tension range values are mostly related to $\widehat{T^n}$. Compared to the exceedance probability curves of the test data in the same cases (see Fig. 4.1), the transition point associated with a change in the curve characteristics is not obvious. However, there still appears the transition ranges from approximately 2.6 to 3.1 for all the three cases, irrespective of the wind speed and other influences. Over this range of transition, there is some overlap of tension values from non-snap and snap events.

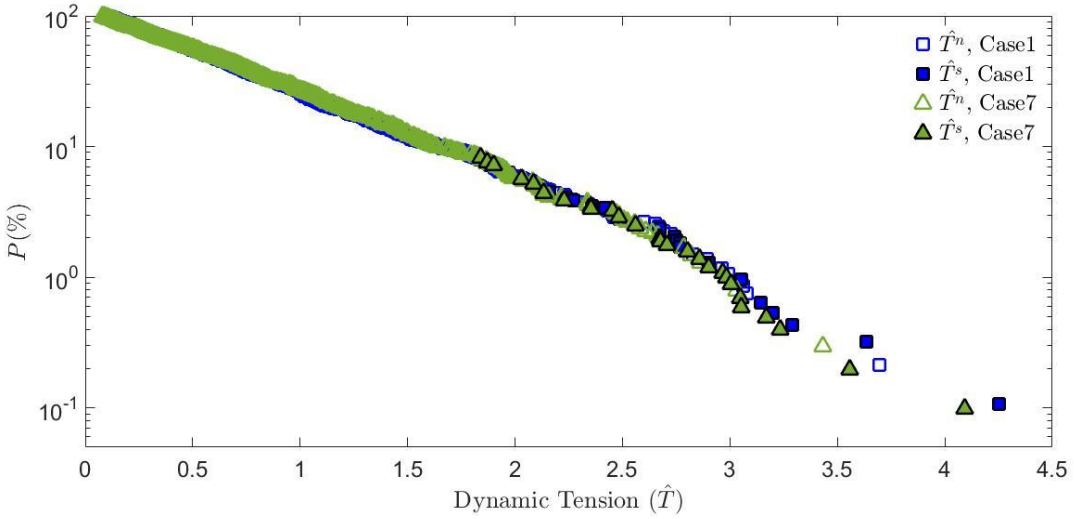

Fig. 6.1 A comparison of exceedance probability curves for $\widehat{T^n}$ (hollow markers) and $\widehat{T^s}$ (solid markers) for Case 1 (square) and Case 7 (triangle)

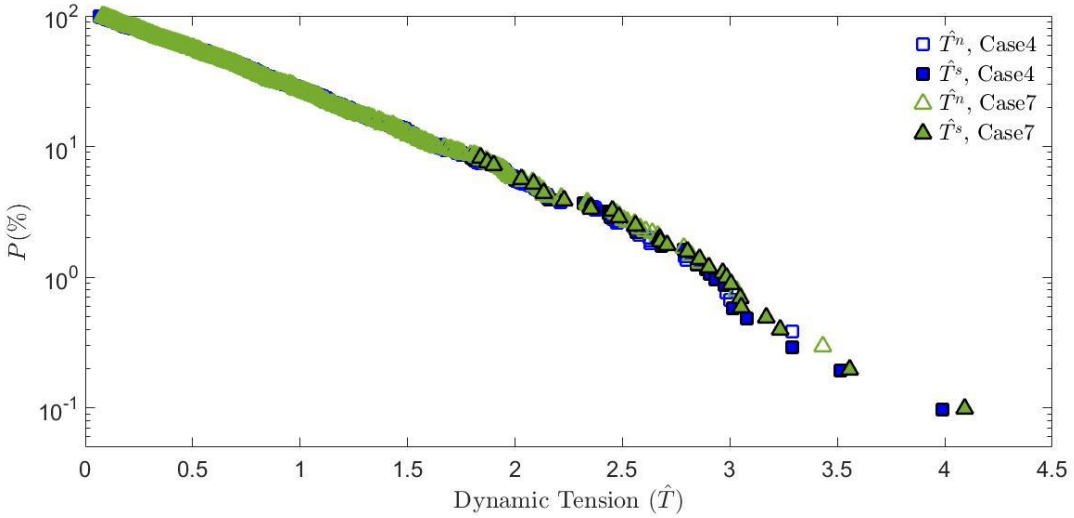

Fig. 6.2 A comparison of exceedance probability curves for $\widehat{T^n}$ (hollow markers) and $\widehat{T^s}$ (solid markers) for Case 4 (square) and Case 7 (triangle)

Fig. 6.3 presents exceedance probability curves for $\widehat{T^n}$ and $\widehat{T^s}$ separately as well as combined together as $\hat{T}$. It appears that at selected tension levels, both $\widehat{T^n}$ and $\widehat{T^s}$ have lower exceedance probability levels under steady wind with the rotor in the operating condition when compared with other wind conditions. It is notable that, for each case, the largest point of $\widehat{T^n}$ are in the higher tension range of 3.3 to 3.7. When compared with the

test data (Fig. 4.3), $\widehat{T^n}$ from FASTLink have larger right tail probability levels. Fig. 6.4 shows the tension history from 0s to 500s. The largest $\widehat{T^n}$ occurred around 260s, which is denoted as a cyclic dynamic tension ii. The cross and the circle marker represent the $\hat{T}^{min}$ and $\hat{T}^{max}$, respectively.

$$\hat{T}^{min} = T^{min} / T_{rms} \tag{6.1}$$

$$\hat{T}^{max} = T^{max} / T_{rms} \tag{6.2}$$

$$\hat{T}_o = T_o / T_{rms} \tag{6.3}$$

$$\hat{T}_\ell = T_\ell / T_{rms} \tag{6.4}$$

Where T^{min} and T^{max} are respectively the local minimum and local maximum tensions and were defined in Eq. (3.1). T_o and T_ℓ are the pretension and slack tension respectively, which were defined in Eq. (3.2). For the three cases, the values of $\hat{T}^{min}$ ranges from 0.28 to 0.32 which is 167% to 273% higher than the values of $\hat{T}_\ell$. For the three cases, the values of $\hat{T}^{max}$ ranges from 3.57 to 4.01 which is 249% to 376% higher than the values of $\hat{T}_o$. This finding suggests that there is a possibility of large dynamic tension levels in which $\hat{T}^{min}$ are about 3 times higher than $\hat{T}_\ell$. However, the causes are a complex blend of the platform motions, wave height and the relative velocities of the mooring line. Moreover, a non-snap event, cyclic dynamic tension i, and a snap event, cyclic dynamic tension iii, are observed around 150s and 320s respectively. It is notable that, there are several other non-snap events observed from 0s to 500s, which are not marked in Fig. 6.4. The dynamic tension values of the non-snap and snap events respectively range from 2.72 to 2.79 and from 2.87 to 2.96, which are very close. $\hat{T}^{max}$ of cyclic dynamic tension i range from 3.01 to 3.02, while $\hat{T}^{min}$ of cyclic dynamic tension iii range from 2.89 to 2.99. The absolute

difference of $\hat{T}^{max}$ between cyclic dynamic tension i (non-snap event) and iii (snap event) range from 1% to 4%, which is very small. Therefore, the local maximum tension and dynamic tension values of the non-snap event are very close to the snap event. The findings above raise the question that of whether the current criteria of snap loads are adequate for the catenary mooring systems.

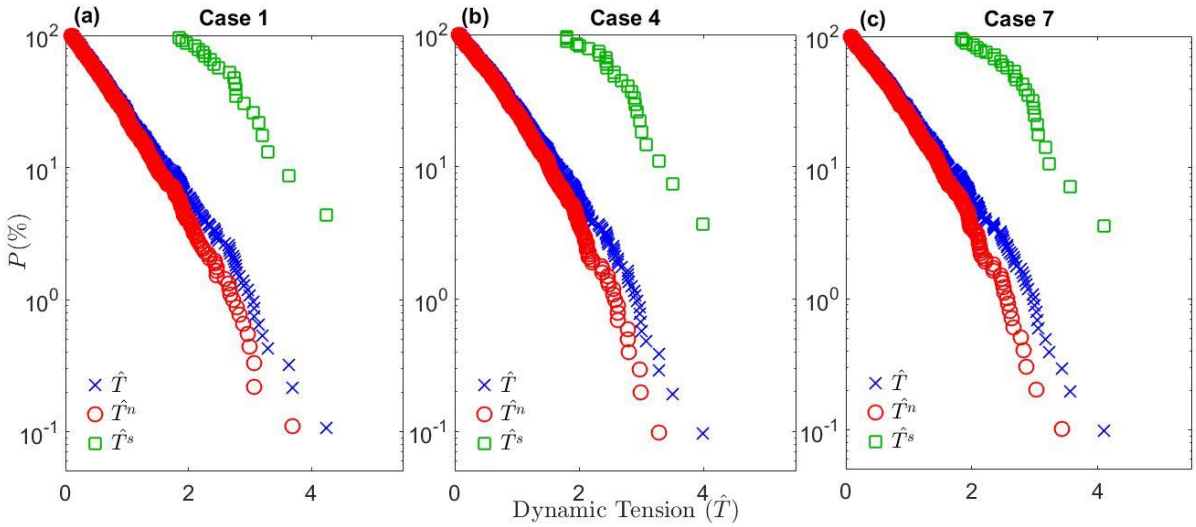

Fig. 6.3 A comparison of exceedance probability curves for $\hat{T}$ (hollow diamonds), $\widehat{T^n}$ (hollow circles) and $\widehat{T^s}$ (hollow squares) for: (a) Case 1, (b) Case 4, and (c) Case 7

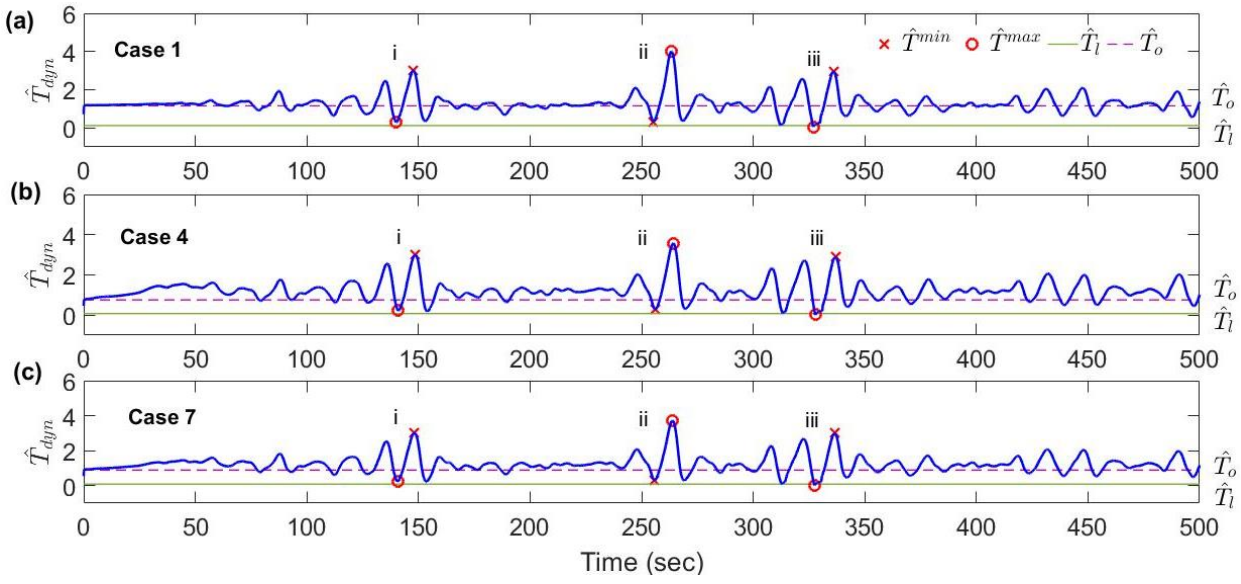

Fig. 6.4 Tension time histories of FASTLink results for (a) Case 1, (b) Case 4, and (c) Case 7

6.2 Estimation of Extreme Tensions

6.2.1 Weibull Distribution

The Weibull distribution (WBL) function (Eq. 4.2) is used to obtain parameter estimations of $\hat{T}$, $\widehat{T^n}$ and $\widehat{T^s}$ for Cases 1, 4 and 7 of the simulation results and are listed in Table 6.2. As can be seen from this table, the estimates of η and ξ for all the cases suggest a weak correlation with wind conditions. The WBL parameter estimates for $\widehat{T^s}$ are larger than those for $\hat{T}$ and $\widehat{T^n}$. η estimates for $\hat{T}$ and $\widehat{T^n}$ are in the range of 0.779 – 0.835, while η estimates for $\widehat{T^s}$ are in the range of 2.832 – 2.916. For all the cases, the values of the shape parameter (ξ) of FASTLink (Table 6.2) are larger than the test data (Table 4.2). This indicates that the curve characteristics of $\widehat{T^s}$ for FASTLink are different to the test data, which can also be observed by comparing Fig. 6.5 and Fig. 4.6.

Table 6.2 Scale (η) and shape (ξ) parameters for WBL distributions fitted to $\hat{T}$, $\widehat{T^n}$ and $\widehat{T^s}$ for Cases 1, 4 and 7 of the FASTLink results

Case	$\hat{T}$		$\widehat{T^n}$		$\widehat{T^s}$	
	Scale (η)	Shape (ξ)	Scale (η)	Shape (ξ)	Scale (η)	Shape (ξ)
1	0.835	1.296	0.792	1.360	2.916	4.654
4	0.831	1.259	0.786	1.317	2.832	5.149
7	0.827	1.259	0.779	1.327	2.886	5.223

Weibull distributions, showing the probability of exceedance, with the estimated parameters for Cases 1, 4 and 7 are shown in Figs. 6.4 – 6.6; these figures serve to assess the WBL fits to the snap and non-snap extreme tension values. Fig. 6.5 suggests that for Case 4 and Case 7, the distribution of $\widehat{T^n}$ is well represented by a Weibull model with a

large shape parameter ($\xi > 1$). Case 1 has heavier right probability tail levels and is not fitted well by the WBL model. For $\xi > 1$, the exceedance probability plots for the Weibull model decrease gradually in the lower tension range but fall more steeply at higher values. This phenomenon is observed in Case 4 and Case 7, while for Case 1, the distribution still falls gradually at higher tension ranges. On the other hand, the exceedance probability plots for $\widehat{T^s}$ deviate considerably from the WBL distribution beyond the lower tension range (Fig. 6.6). The exceedance probability data for $\widehat{T^s}$ stay high initially and decrease only gradually beyond the transition range. The probability distributions of $\widehat{T^s}$ for FASTLink results (Fig. 6.6) fall more steeply at higher tension ranges when compared to the distributions of $\widehat{T^s}$ for test data (Fig. 4.6). This is because FASTLink results have higher minimum $\widehat{T^s}$ values and lower maximum $\widehat{T^s}$ values when compared to the test data. The plots indicate that the WBL model still fits $\widehat{T^s}$ data very well for tension values beyond the transition ranges. Fig. 6.7 shows exceedance probability plots of $\hat{T}$ along with fitted WBL distribution models for Cases 1, 4 and 7. The probability curve over the higher tension ranges are mostly contributed to by $\widehat{T^s}$ and one $\widehat{T^n}$ value. For Case 4 and Case 7, it is seen that $\hat{T}$ data have slightly larger right tail probability levels than the corresponding probability levels predicted by the Weibull distribution. For Case 1, $\hat{T}$ data have obvious larger right tail probability levels than the corresponding probability levels predicted by the Weibull distribution. For Case 1, the large right tail probability levels of $\hat{T}$ data contributes to the heavy tail probability of $\widehat{T^s}$ as well as $\widehat{T^n}$. This finding indicates that $\widehat{T^n}$ data of Case 1 include the non-snap events which have similar dynamic tension levels with the snap events, which is also suggested by Fig. 6.4. Although the non-snap events with high dynamic tension levels are found in the three cases, the dynamic tension levels in Case

1 are larger than the ones in Cases 4 and 7. Thus, the $\hat{T}$ data of Case 1 are considered to have an obvious deviation from the Weibull distribution in the higher tension ranges.

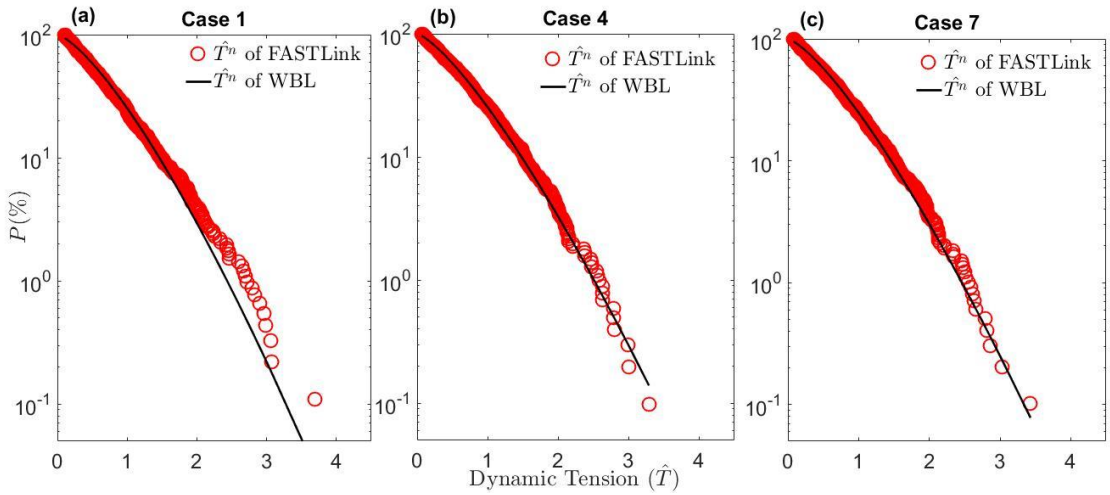

Fig. 6.5 A comparison of exceedance probability curves for $\widehat{T^n}$ between FASTlink (hollow circles) and WBL (solid line) for: (a) Case 1, (b) Case 4, and (c) Case 7

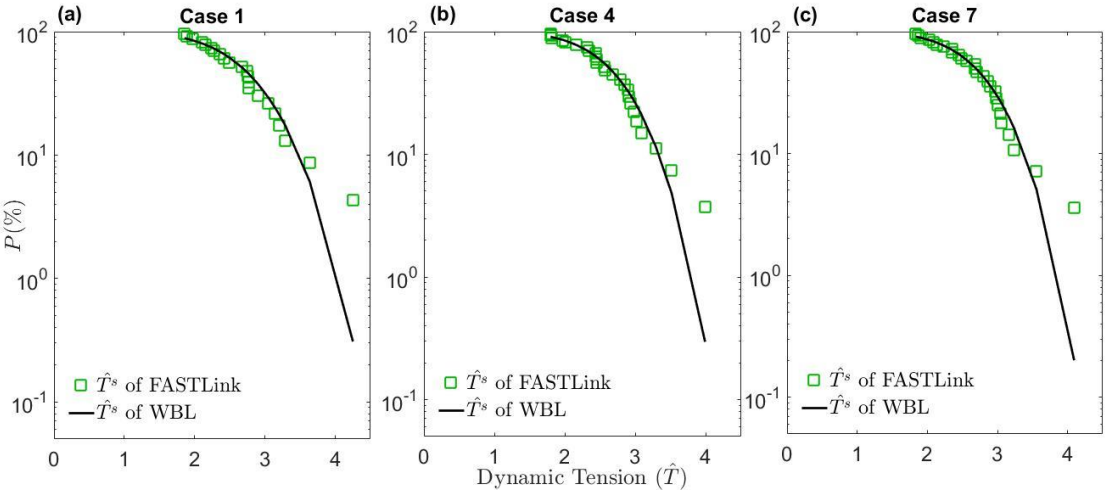

Fig. 6.6 A comparison of exceedance probability curves for $\widehat{T^s}$ between FASTlink (hollow circles) and WBL (solid line) for: (a) Case 1, (b) Case 4, and (c) Case 7

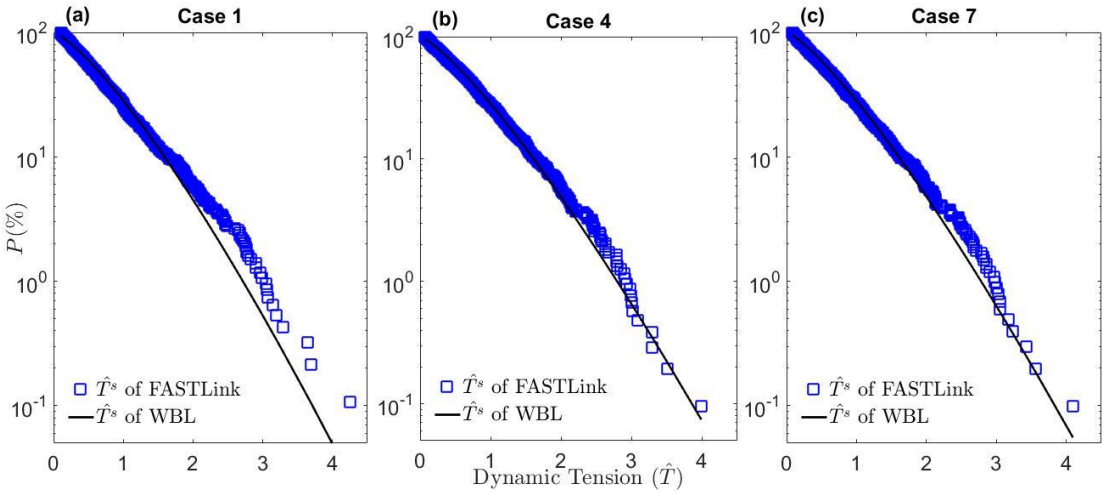

Fig. 6.7 A comparison of exceedance probability curves for $\hat{T}$ between FASTlink (hollow circles) and WBL (solid line) for: (a) Case 1, (b) Case 4, and (c) Case 7

6.2.2 A Composite Weibull Distribution

The proposed composite Weibull Distribution model described in section 4.2.2 is also applied to the simulation results. The CWD models for the FASTLink results are investigated and compared with the test data. Table 6.3 presents the shape parameters $(\beta_1; \beta_2)$, scale parameters $(\hat{T}_1; \hat{T}_2)$ and the transition tension $(\hat{T}_{tr})$ for the CWDs of FASTLink as well as for the CWDs of the test data under Cases 1, 4 and 7.

Table 6.3 The transition tension $(\hat{\boldsymbol{T}}_{\boldsymbol{tr}})$, shape parameters $(\boldsymbol{\beta_1}; \boldsymbol{\beta_2})$ and scale parameters $(\hat{\boldsymbol{T}}_{\boldsymbol{1}}; \hat{\boldsymbol{T}}_{\boldsymbol{2}})$ for the CWD for the three cases of FASTLink and the test data

	Case	$\hat{T}_{tr}$	$\hat{T}_1$	β_1	$\hat{T}_2$	β_2
FASTLink	1	2.620	0.786	1.205	0.642	1.032
	4	2.834	0.801	1.207	0.829	1.230
	7	2.766	0.797	1.218	0.666	1.065
Test data	1	2.710	0.792	1.279	0.345	0.763
	4	2.845	0.855	1.269	0.364	0.741
	7	2.770	0.816	1.243	0.360	0.745

Table 6.3 suggests that the values for $\beta_1, \hat{T}_1$, and $\hat{T}_{tr}$ of FASTLink have a weak correlation with the wind conditions. However, the values for $\beta_2, \hat{T}_2$ of Case 4 are 20% – 30% larger than the values of Cases 1 and 7. This finding indicates that the case with the rotor in operation under steady wind speed have smaller right tail probability levels when compared to the other wind conditions. For FASTLink, the absolute differences of β_1 related to β_2 are 2% (Case 4) to 17% (Case 1), while for test data, the absolute differences are 67% (Case 7) to 71% (Case 4). Thus, for FASTLink, the probability curve differences between higher and lower tension ranges are smaller when compared to the curve differences for test data. When compared to the values for $\beta_2, \hat{T}_2$ of test data, the values of FASTLink are 35% – 133% larger. The larger β_2 values indicate that the right tail probability levels decrease. For larger $\hat{T}_2$ values, the tension data with the values higher than $\hat{T}_{tr}$ which are mostly contributed to by $\widehat{T^S}$ have lower probability levels. Thus, for FASTLink results, the probability distribution curve in the higher tension range do not deviate significantly from the distribution curve in the lower tension range. $\widehat{T^S}$ predicted by the FASTLink model have a lower probability level when compared to the $\widehat{T^S}$ of test data. Since the parameters, β_2 and $\hat{T}_2$, and wind conditions are correlated, it is not suitable to apply the average values of the parameters to the CWD model. For FASTLink, the parameters listed in Table 6.3 are used in the analysis that follows and also applied to Eq. (4.4). Figs. 6.8 – 10 shows exceedance probability plots for $\hat{T}$ estimated using the composite Weibull distribution for FASTLink for Cases 1, 4, and 7 respectively. The graphs support the validity of the CWD model in a qualitative sense.

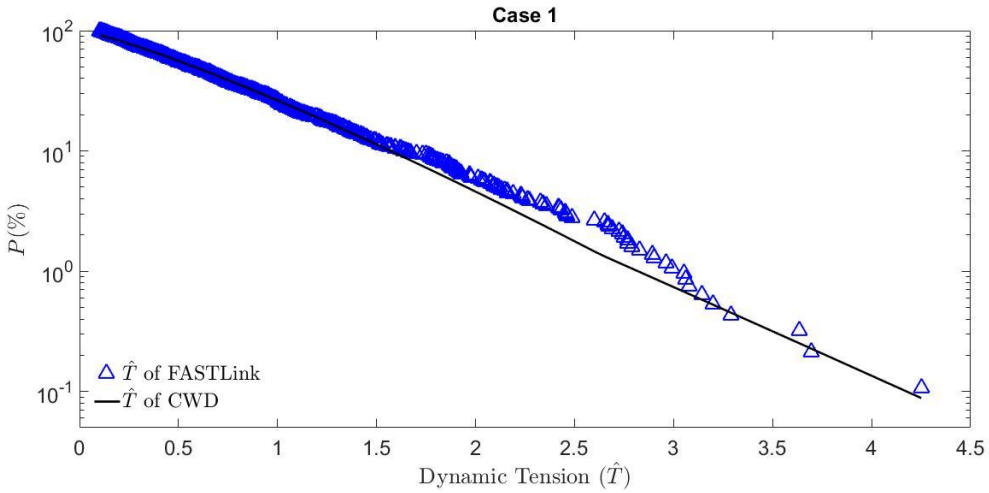

Fig. 6.8 A comparison of exceedance probability curves for $\hat{T}$ between FASTLink (hollow triangles) and CWD (solid line) for Case 1

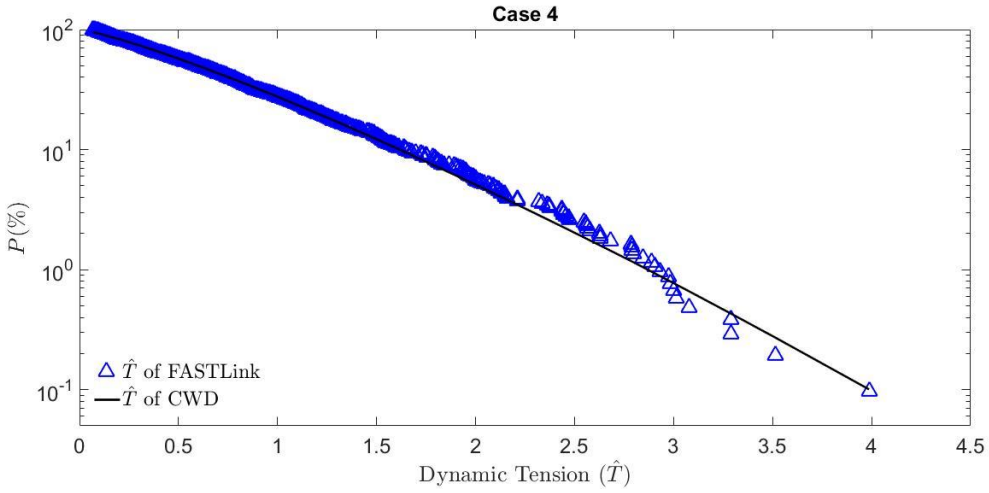

Fig. 6.9 A comparison of exceedance probability curves for $\hat{T}$ between FASTLink (hollow triangles) and CWD (solid line) for Case 4

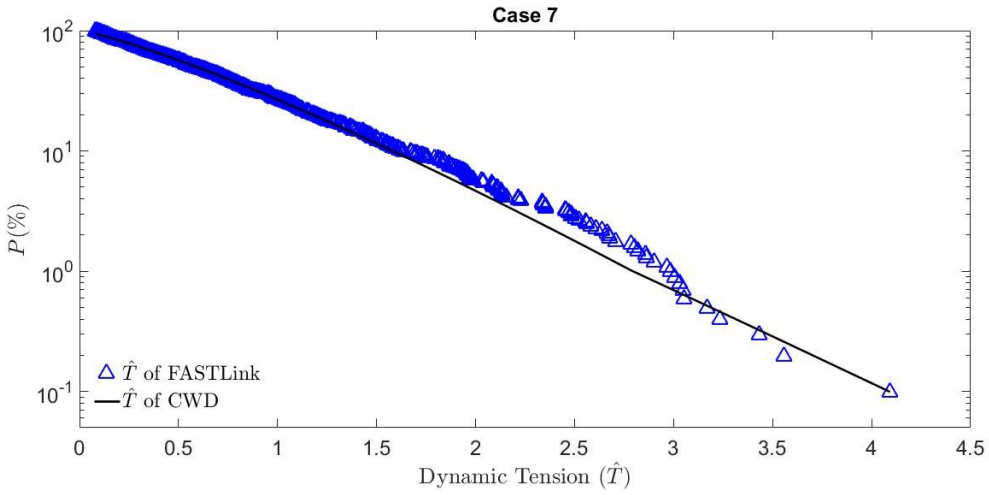

Fig. 6.10 A comparison of exceedance probability curves for $\hat{T}$ between FASTLink (hollow triangles) and CWD (solid line) for Case 7

6.2.3 Extreme Value Prediction by CWD and WBL Models

The goodness of fit estimates for the CWD and WBL distribution function models are evaluated by computing the absolute distribution fitting error, ε_{ABS}, which is defined in Eq. (4.13). It is notable that $\mathrm{P}_{data}(\widehat{T}_j)$ is defined as the exceedance probability in regard of the simulation results as defined in Eq. (4.1), while $\mathrm{P}_{theo}(\widehat{T}_j)$ is the exceedance probability computed using the theoretical distribution model as obtained with the cumulative probability distribution functions for both WBL and CWD defined in Eqs. (4.2) and (4.4) respectively. Fig. 6.11 shows a comparison of the absolute fitting errors for both models in Cases 1, 4 and 7. The fitting errors with the CWD model range from 0.8% (Case 2) to 1.6% (Case 1), while the corresponding errors with the WBL model are slightly higher, ranging from 1.5% (Case 4) to 2.6% (Case 1). Although these errors with both distribution models are lower than 2.6%, the upper tails of the CWD distribution models show better fits with the experimental data.

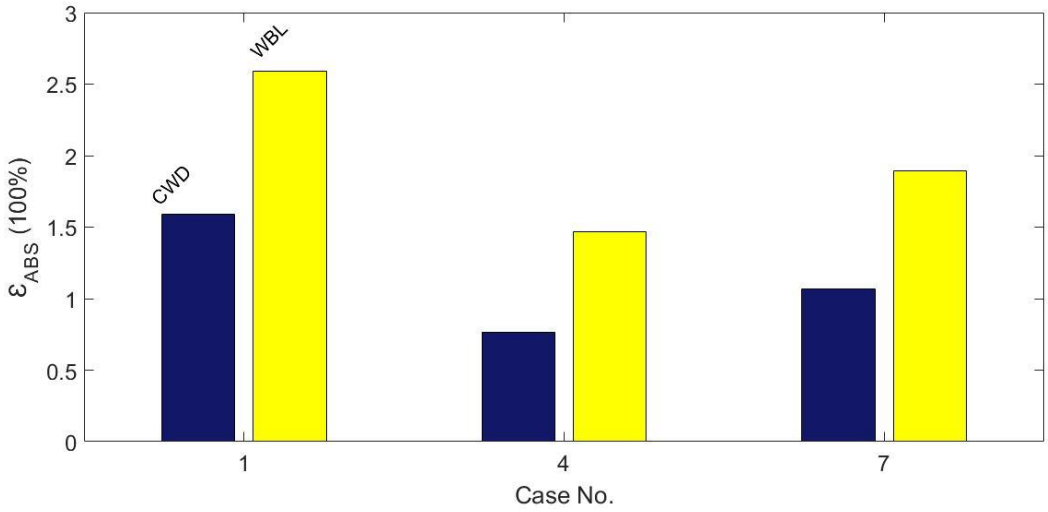

Fig. 6.11 Absolute fitting error ($\boldsymbol{\varepsilon_{ABS}}$) in percent for the exceedance probability distribution based on the CWD (horizontal line pattern) and WBL (vertical line pattern) models for Cases 1, 4 and 7

For extreme value predictions, the MPME values of WBL and CWD are calculated by Eq. (4.14) and Eq. (4.15) respectively. Computed values are shown in Table 6.4, and are also presented in the form of QQ-plots in Fig. 6.12. Table 6.4 compares $\hat{T}_{MPME}^{CWD}$ of the FASTLink results with $\hat{T}_{MPME}^{CWD}$ of the test data for Cases 1, 4 and 7. The $\hat{T}_{MPME}^{FASTLink}$ is also compared with $\hat{T}_{MPME}^{test}$ under the same cases. $\hat{T}_{MPME}^{FASTLink}$ and $\hat{T}_{MPME}^{test}$ represent the maximum value of $\hat{T}$ observed from FASTLink simulations and test data respectively. Note that $\hat{T}_{MPME}^{FASTLink}$ are 6.59% (Case 1) to 12.31% (Case 4) lower than $\hat{T}_{MPME}^{test}$, while the $\hat{T}_{MPME}^{CWD}$ of the FASTLink results are 12.47% (Case 1) to 16.67% (Case 4) lower than the $\hat{T}_{MPME}^{CWD}$ of test data. The maximum dynamic tension values of the FASTLink results are lower when compared to the values of test data. Table 6.4 shows that the MPME values predicted by the CWD model are lower for the FASTLink results when compared to the ones for test data. For the CWD model, the average values for the parameters ($\boldsymbol{\hat{T}_{tr}, \beta_1, \beta_2, \hat{T}_1,}$ and $\boldsymbol{\hat{T}_2}$) are applied to the cases of test data while the parameters listed in Table 6.3 are used for the cases of FASTLink results. Thus, the absolute differences between $\hat{T}_{MPME}^{CWD}$

values and simulation results are all smaller than 3%. For test data, the absolute differences range from 2.07% (Case 1) to 19.06% (Case 4). In Fig. 6.12, QQ-plots of Cases 1, 4 and 7 for FASTLink results are presented. It can be seen that for Case 1, the CWD model performs far more favorably compared to the WBL model. The CWD model fits the numerical results very well, especially so in the upper tail. The deviations of the CWD model over the entire $\hat{T}$ range are relatively small. On the other hand, the WBL model shows maximum discrepancies relative to $\hat{T}$ FASTLink results that are approximately 3.1 for Case 1. For Cases 4 and 7, both the CWD model and WBL model perform very well in the entire $\hat{T}$ range. This is because the absolute differences of β_1 related to β_2 are small, 2% – 17%. Thus, WBL model with constant shape parameter can have similar performance with CWD model. The QQ-plots in Fig. 6.11 also indicate that our proposed CWD model performs very well for potential extreme value prediction.

Table 6.4 The most probable maximum extreme dynamic tension based on FASTLink ($\hat{T}_{MPME}^{FASTLink}$) and test data ($\hat{T}_{MPME}^{test}$), and the predicted MPME value for the CWD model ($\hat{T}_{MPME}^{CWD}$) under the three cases, including the differences between $\hat{T}_{MPME}^{FASTLink}$,$\hat{T}_{MPME}^{test}$ and $\hat{T}_{MPME}^{CWD}$

Case	FASTLink			Test data			Absolute difference w.r.t. test data	
	$\hat{T}_{MPME}^{FASTLink}$	$\hat{T}_{MPME}^{CWD}$	Absolute difference	$\hat{T}_{MPME}^{test}$	$\hat{T}_{MPME}^{CWD}$	Absolute difference	$\hat{T}_{MPME}^{FASTLink}$	$\hat{T}_{MPME}^{CWD}$
1	4.25	4.14	2.58 %	4.83	4.73	2.07 %	6.59 %	12.47 %
4	3.99	4.01	0.50 %	4.04	4.81	19.06 %	12.31 %	16.63 %
7	4.09	4.10	0.24 %	4.55	4.77	4.84 %	10.11 %	14.05 %

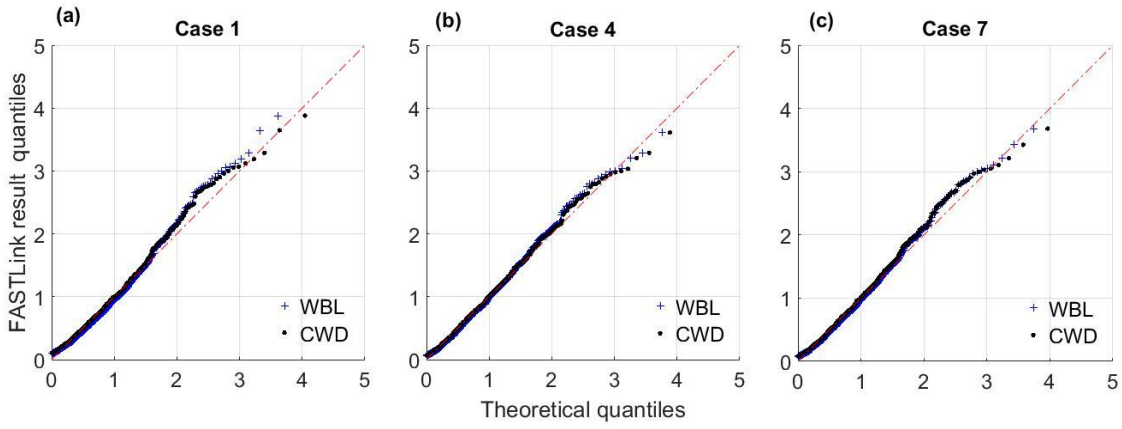

Fig. 6.12 Quantile-Quantile (Q-Q) plots for the WBL and CWD models versus FASTLink results for $\hat{T}$ considering (a) Case 1, (b) Case 4, and (c) Case 7

6.3 Discussion and Conclusions

In this study, we investigated the extreme value distributions of a FOWT mooring tensions predicted by the numerical model. A detailed examination of the mooring line tensions from the simulations revealed that the largest values of snap-induced tension ($\widehat{T^s}$) are 1.2 times that of the cyclic dynamic tension ($\widehat{T^n}$); this suggests that the maximum tension on FOWT mooring systems may be underestimated if snap events are not considered. For each case, the largest point of $\widehat{T^n}$ are in the higher tension range of 3.3 to 3.7. For the largest point of $\widehat{T^n}$, although the local minimum tension values are 167% to 273% higher than the slack tension, its dynamic tension are very similar to the dynamic tension of a snap event. The finding raises the question of whether the current criteria for snap loads is adequate for the catenary mooring systems.

When compared with the test data (Fig. 4.3), $\widehat{T^n}$ of FASTLink have larger right tail probability levels. For Case 1, the large right tail probability levels of $\hat{T}$ data is contributed by the heavy tail probability of $\widehat{T^s}$ as well as $\widehat{T^n}$. This finding indicates that the $\widehat{T^n}$ data of

Case 1 include the non-snap events which have similar dynamic tension levels with the snap events. This is because the non-snap events have higher dynamic tension levels for Case 1 when compared with the levels for Cases 4 and 7. Thus the $\hat{T}$ data of Case 1 are considered to have an obvious deviation from the Weibull distribution in the higher tension ranges.

It is notable that FASTLink simulations of all cases (Cases 1, 4 and 7) have larger maximum $\widehat{T^n}$ values and smaller maximum $\widehat{T^s}$ values when compared to the test data. This phenomenon can reduce the probability curve difference for lower and higher tension ranges. It is clear from this study that for Case 1, WBL models of the FASTLink underestimate the upper tail of dynamic tension that include snap events, while for Cases 4 and 7, both CWD model and WBL model perform very well in the entire $\hat{T}$ range.

The parameters of the proposed a composite Weibull distribution (CWD) model for FASTLink are compared to the parameters of test data. The absolute differences of β_1 related to β_2 of FASTLink (2% – 17%) are much smaller than the differences of test data (67% – 71%). Since the probability curve differences at lower and higher tension ranges are small, the transition between these two probability curves is not obvious (see Figs. 6.7 – 9).

The ultimate limit state design described in section 4.3 is also applied to the simulation results. The characteristic mean line tension (T_{C-mean}) and the characteristic dynamic line tension (T_{C-dyn}) of Eq. (4.16) are calculated in regard to the descriptions in section 4.3. It is notable that the $\hat{T}_{C-dyn}$ of DNV for FASTLink results are very close to the test data and the absolute differences are in the range of 0% to 3.7%. The $\hat{T}_{C-dyn}$ of CWD for FASTLink

are 19.6% to 34.1% lower than the values of test data. For FASTLink, $\hat{T}_{C-dyn}$ values predicted by the CWD model are 2.0 – 2.3 times larger than the $\hat{T}_{C-dyn}$ values based on the DNV criteria (0.5 $\hat{T}_{tr}$), which is 17.9% to 25.9% lower than the ratios of test data. However, both test data and FASTLink results suggest the need for more than a doubling of the partial safety factor, γ_{dyn}.

Table 6.5 The characteristic dynamic line tension ($\hat{T}_{C-dyn}$) with the CWD model and the DNV standard (assuming one-half of transition tension, 0.5 $\hat{T}_{tr}$) for the three cases, along with the ratio between the two

Case	FASTLink			Test data		
	$\hat{T}_{C-dyn}$ of CWD	$\hat{T}_{C-dyn}$ of DNV	Ratio	$\hat{T}_{C-dyn}$ of CWD	$\hat{T}_{C-dyn}$ of DNV	Ratio
1	3.00	1.31	2.3	3.73	1.36	2.8
4	2.86	1.42	2.0	3.80	1.42	2.7
7	2.94	1.38	2.1	3.78	1.38	2.7

CHAPTER 7

SUMMARY AND DISCUSSION

The work of this thesis brought together diverse elements including physical testing, data analysis, numerical modelling and probability distribution development into an integrated study of the extreme tension analysis of mooring system for a FOWT.

7.1 Summary of the Study

As described in Chapter 2, a theoretical basis was used to understand the underlying physics of snap loads on a mooring line system. A parametric study on the dynamic tension of a nonlinear vertical cable system has been performed. The results show that the nonlinearity of the line stiffness and hydrodynamic drag force can play important roles in the formation of snap loads. Moreover, hydrodynamic drag force in conjunction with a small pretension could result in larger normalized dynamic tension within the region of smaller $A/t_p^2\, g$ values. In this study, the snap-like events are observed which have similar formation of snap events. A snap-like event does not follow DNV's criteria of a snap load. However, the dynamic tension levels of the snap-like events are very similar to the snap events.

An investigation of extreme tension in FOWT mooring systems using the 1:50 scale DeepCWind test data was described in Chapter 3. The floater motions and dynamic line tensions of the TLP model are compared with those of the Semi model under a survival sea-state with steady wind speed varying from 0 to 21m/s. For both TLP and Semi models, the wave height and heave motion are strongly correlated with snap events. It thus appears

that wave characteristics play a dominant role in bringing about snap loads on a mooring line. For the no wind condition, the TLP model with a higher pretension value could mitigate the occurrence of the snap loads when compared to the Semi model. For the Semi model, the wind forces cause a 23% increase in the snap events and a 16% decrease in the maximum dynamic tension. For the TLP model, the wind forces cause a 93% increase of snap events and a 42% increase in the maximum dynamic tension.

Chapter 4 presents the theoretical extreme tension distribution models of the test data. The mooring line tensions from the experiments revealed that the largest values of snap-induced tension ($\hat{T}^s$) were 1.6 times that of the cyclic dynamic tension ($\hat{T}^n$). This suggests that the maximum tension on FOWT mooring systems may be underestimated if snap events are not considered. The probability distribution of dynamic tension ($\hat{T}$) in the higher tension ranges is dominated by snap-induced tension maxima ($\hat{T}^s$); as a result, $\hat{T}$ distributions exhibit larger right tail probability levels than are associated with the Weibull distribution. The proposed composite Weibull probability distribution model provides a good fit to the measured tension data particularly in the extreme value range. If snap-induced dynamic tension values are to be included in the ultimate limit state design, the characteristic dynamic line tension ($\hat{T}_{C-dyn}$) based on the CWD model will be 2.6 – 2.8 times larger than the $\hat{T}_{C-dyn}$ values based on the DNV criteria. This suggests the need for more than a doubling for the partial safety factor, γ_{dyn}.

As described in Chapter 5, the comparative analysis of the DeepCWind Semi model exposed to the 100-year storm condition has been performed based on model test data and numerical simulation using coupled OrcaFlex-FAST software. Overall, the dynamic motions in the surge, heave and pitch, and the dynamic tension (line #2 and #3) have good

agreement with the test data in wave frequency ranges. However, the dynamic mooring line (#1) tensions are underestimated by coupled OrcaFlex-FAST (FASTLink). It might be due to FASTLink using a higher drag coefficient, higher stiffness or there is an extra damping system which is not considered in this study. This study has considered the effects of wind forces on the platform motions and line tensions. For both experiment and FASTLink, PSDs of surge, heave and mooring tensions of lines 2 and 3 under no wind conditions are larger at wave frequency range than the PSDs under the steady wind of 21m/s, while the opposite is found for the tension PSDs of line 1. The noticeable discrepancy in pitch motions in the low-frequency ranges is affected by second-order hydrodynamic effects not captured in coupled OrcaFlex-FAST model.

Chapter 6 focuses on the study of the composite Weibull distributions of the numerical data using the FASTLink model. The simulations revealed that the largest values of snap-induced tension ($\hat{T}^s$) are 1.2 times that of the cyclic dynamic tension ($\hat{T}^n$), which is smaller then the test data. When compared with the test data, $\hat{T}^n$ of FASTLink have larger right tail probability levels. FASTLink simulations of the all cases (Cases 1, 4 and 7) have larger maximum $\hat{T}^n$ values and smaller maximum $\hat{T}^s$ values when compared to the test data. The absolute differences of β_1 related to β_2 of FASTLink (2% – 17%) are much smaller than the differences of test data (67% – 71%). Since the probability curve differences at lower and higher tension ranges are small, the transition between these two probability curves is not obvious. For each case, the largest point of $\hat{T}^n$ are in the higher tension range of 3.3 to 3.7. For the largest point of $\hat{T}^n$, although the local minimum tension values are 167% to 273% higher than the slack tension, its dynamic tension are very similar to the dynamic tension of a snap event.

7.2 Discussion

In chapter 2, the snap-like events, which do not follow DNV's criteria of snap loads, were observed. These snap-like events have flat troughs and peak crests with similar dynamic tension levels similar to those of the snap events. In chapter 6, the FASTLink results show that, for each case, the largest point of $\hat{T}^n$ is in the higher tension range of 3.3 to 3.7. For the largest point of $\hat{T}^n$, although the local minimum tension values are 167% to 273% higher than the slack tension, its dynamic tension is very similar to the dynamic tension of a snap event. The findings in both Chapters 2 and 7 raise the question of whether the current criteria for snap loads is adequate for catenary mooring system design. DNV's criteria for a snap load is defined for the crane wire, which is a vertical cable system with linear stiffness. The catenary system provides restoring forces through the suspended weight of the mooring lines and its change in configuration arises from the platform motions. A catenary system has a nonlinear restoring force for the surge motion. The catenary equation as given by Faltinsen [90] is:

$$\mathrm{X} = \mathrm{l} - h\left(1 + 2\frac{a}{H}\right)^{\frac{1}{2}} + a\cosh^{-1}\left(1 + \frac{H}{a}\right) \tag{7.1}$$

$$a = \frac{T_H}{w} \tag{7.2}$$

$$T_{FL} = T_H + wH \tag{7.3}$$

Where X is the horizontal distance from the anchor, H is the water depth, T_{FL} is the line tension at the fairlead position, T_H is the horizontal force from the cable on the vessel and w is the weight per unit length of the mooring line. By substituting these variables with the values listed in Table 3.2, the calculations based on Eqs. (7.1) – (7.3) are illustrated in Fig. 7.1. The black curve in Fig. 7.1 represents the restoring force for the surge motion with

respect to the *x*-axis for the catenary mooring system of the DeepCWind Semi-submersible. The dashed lines show the slope the curve at X_{mean} and X_{max}. X_{max} is the maximum surge motion over the entire 3.5hr surge motion time histories, including the seven experimental datasets and the three FASTLink results. This maximum surge motion is found in Case 4 of the test data, which is about -25m. X_{mean} is the mean surge motion of the same dataset, which is about -10m. These two tangent lines suggest that the catenary mooring line can be approximated by a bilinear curve. The intersection of these two lines can be defined as the critical surge motion, X_{cr}, with a restoring force of 3441kN (T_{cr}). The stiffness equals 93.35kN/m when the platform moves from 0 to X_{cr}, and then it increases to 511.99kN/m while the platform moves from X_{cr} to X_{max}. X_{mean} and X_{max} are selected because there is a high tendency for the platform to move in these ranges. While the platform moves from X_{mean} to X_{max} in a short time duration, it is hypothesized that the mooring line has a higher possibility to follow this bilinear curve than the catenary stiffness curve. When comparing Fig. 7.1 with Fig. 2.4, both the catenary system and the vertical hanging cable system have a bilinear stiffness. The snap-like events are observed in both of these systems. Thus, T_{cr} could be an important factor of the formation of a snap load. Here, let it be assumed that the snap criteria is defined as the slack tension (T_ℓ) is equal to $0.1T_{cr}$ and compare with DNV's criteria, T_ℓ equal to $0.1T_o$. The 3.5hr tension time history of Case 1 predicted by FASTLink is selected for this study. The slack tension (T_ℓ), critical tension (T_{cr}) and local minimum dynamic tension ($\hat{T}^{min}$) are made non-dimensional in the following manner:

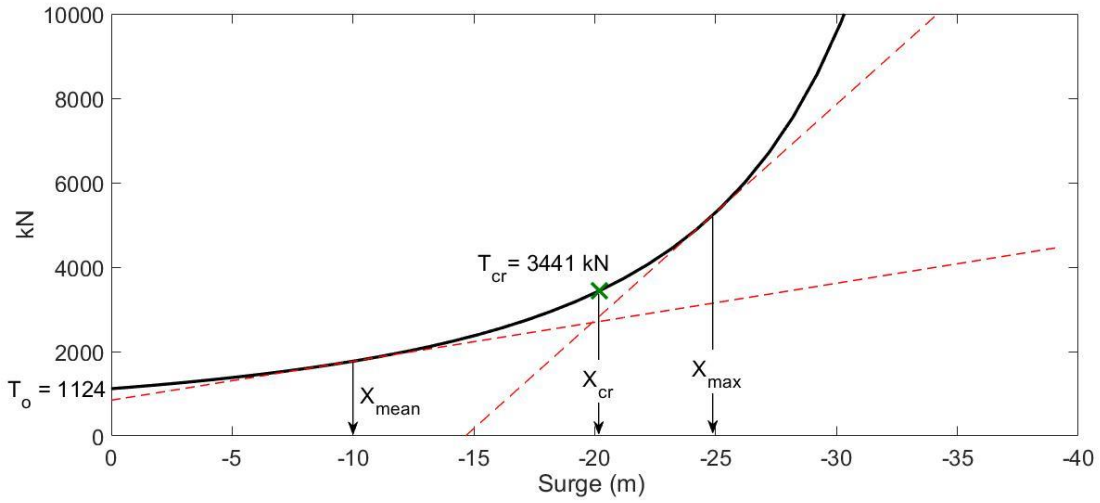

Fig. 7.1 Restoring force vs. surge motion

$$\hat{T}_\ell = T_\ell / T_{rms} \tag{7.4}$$

$$\hat{T}_{cr} = T_{cr} / T_{rms} \tag{7.5}$$

$$\hat{T}^{min} = T^{min} / T_{rms} \tag{7.6}$$

Where $\hat{T}_\ell$ = 0.34 and 0.12 for the proposed criteria and DNV's criteria respectively. Table 7.1 summarizes data on $\hat{T}$, $\hat{T}^n$ and $\hat{T}^s$ for Case 1 under $\hat{T}_\ell$ = 0.34 and $\hat{T}_\ell$ = 0.12. The snap events increase 2.8 times when $\hat{T}_\ell$ increases from 0.12 to 0.34. For $\hat{T}_\ell$ = 0.34, the greatest number of $\hat{T}^n$ equals 2.67 which is 28% smaller than the one for $\hat{T}_\ell$ = 0.12. The smallest number of $\hat{T}^s$ equals 1.34 which is also 28% smaller than the one for $\hat{T}_\ell$ = 0.12. Thus, by applying the new criteria to the data, smaller maximum $\hat{T}^n$ values, smaller minimum $\widehat{T^s}$ values and increased snap events are observed.

Table 7.1 Normalized tension ranges, number of cycles, and duration of $\hat{T}$, $\hat{T}^n$ and $\hat{T}^s$ in Case 1 of the FASTLink results for $\hat{T}_\ell$ =0.34 and $\hat{T}_\ell$ = 0.12

$\hat{T}_\ell$	$\hat{T}$		$\hat{T}^n$			$\hat{T}^s$			
	Tension range		Number	Tension range		Number	Duration range	Tension range	
	Min	Max	of cycles	Min	Max	of cycles	(sec / cycle)	Min	Max
0.34	0.10 -	4.25	873	0.10	2.67	61	5.4 - 10.6	1.34	4.25
0.12	0.10 -	4.25	912	0.10	3.70	22	6.2 - 10.2	1.85	4.25

Beyond the transition range, the exceedance probability curve is contributed to by $\hat{T}^s$ for $\hat{T}_\ell$ = 0.34, while for $\hat{T}_\ell$ = 0.12, there is still some overlap of tension values from non-snap and snap events (Fig. 7.2). In Fig. 7.2, there is a tendency of the cyclical dynamic tension with $\hat{T}^{min}$ ranging from 0.12 to 0.34 to occur with a tension range of 2 to 3.7. For $\hat{T}_\ell$ = 0.12, most of the snap events are also observed in this tension range of 2 – 3.7. This indicates that cyclical dynamic tension, which has similar tension values with snap events, may be ignored by using DNV's criteria. Thus, one might underestimate the effect of snap events on mooring systems if those dynamic tensions are disregarded.

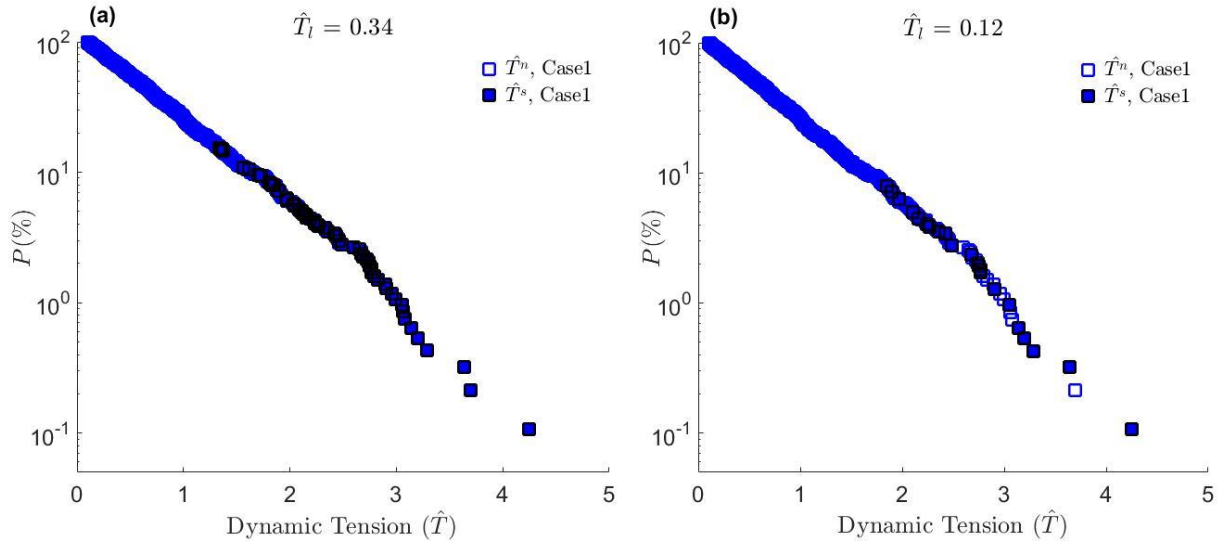

Fig. 7.2 A comparison of exceedance probability curves for $\hat{T}^n$ (hollow markers) and $\hat{T}^s$ (solid markers) for: (a) $\hat{T}_\ell$ = 0.34, and (b) $\hat{T}_\ell$ = 0.12

In Fig. 7.3, the exceedance probability plot of $\hat{T}^n$ deviates considerably from the probability of $\hat{T}$ beyond the lower tension range and falls more steeply in the tension range of 2.6 – 2.8 when compared with $\hat{T}_\ell$ = 0.12. For $\hat{T}_\ell$ = 0.12, the largest value of $\hat{T}^n$ is 3.7, which is in the higher tension range. When compared with $\hat{T}_\ell$ = 0.12, the $\hat{T}^n$ of FASTLink have larger right tail probability levels.

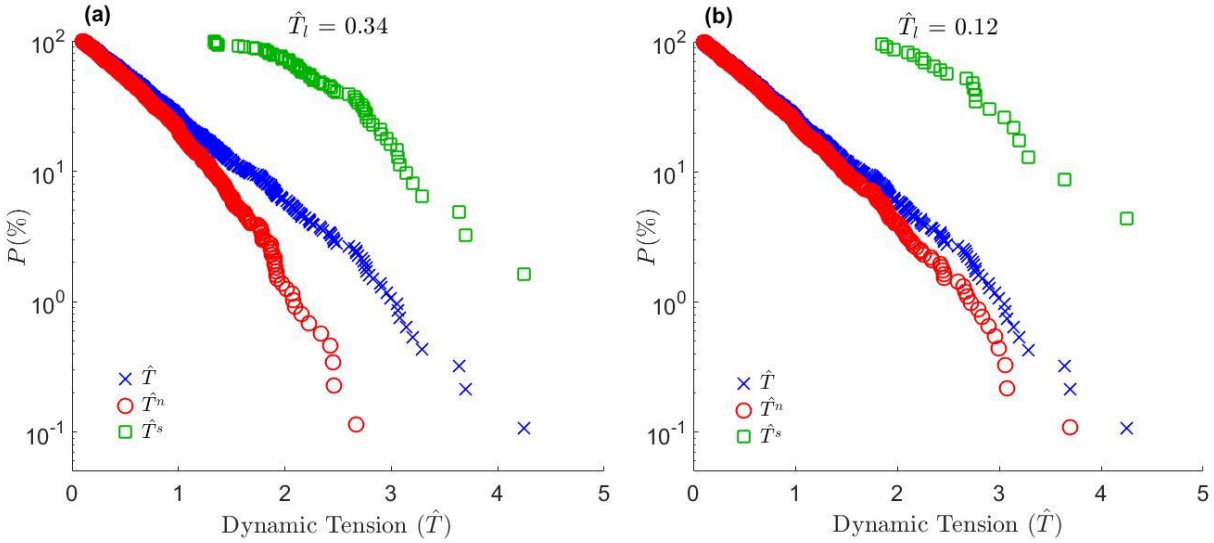

Fig. 7.3 A comparison of exceedance probability curves for $\hat{T}$ (hollow diamonds), $\hat{T}^n$ (hollow circles) and $\hat{T}^s$ (hollow squares) for: (a) $\hat{T}_\ell$ = 0.34, and (b) $\hat{T}_\ell$ = 0.12

In Table 7.2, the value of the WBL shape parameter (ξ) estimated for $\hat{T}^n$ under $\hat{T}_\ell$ = 0.34 is larger than the value under $\hat{T}_\ell$ = 0.12. Thus, $\hat{T}^n$ have smaller right probability tail levels under $\hat{T}_\ell$ = 0.34 when compared to those of $\hat{T}_\ell$ = 0.12. For $\hat{T}_\ell$ = 0.34, the distribution of $\hat{T}^n$ is well represented by a Weibull model (Fig. 7.4). For $\hat{T}_\ell$ = 0.12, $\hat{T}^n$ has heavier right probability tail levels and is not fitted well by the WBL model (Fig. 7.4). Fig. 7.4 shows evidence that $\hat{T}^n$ data might include cyclic dynamic tensions which have similar characteristics with snap events under $\hat{T}_\ell$ = 0.12. Fig. 7.5 shows that the WBL model does not fit the $\hat{T}^s$ data very well for larger tension ranges of $\hat{T}_\ell$ = 0.34 when compared to the one for $\hat{T}_\ell$ = 0.12.

Table 7.2 Scale (η) and shape (ξ) parameters for WBL distributions fitted to $\hat{T}$, $\hat{T}^n$and $\hat{T}^s$ for $\hat{T}_\ell$ = 0.34 and $\hat{T}_\ell$ = 0.12

$\hat{T}_\ell$	$\hat{T}$		$\hat{T}^n$		$\hat{T}^s$	
	Scale (η)	Shape (ξ)	Scale (η)	Shape (ξ)	Scale (η)	Shape (ξ)
0.34	0.835	1.296	0.726	1.477	2.623	4.143
0.12	0.835	1.296	0.792	1.360	2.916	4.654

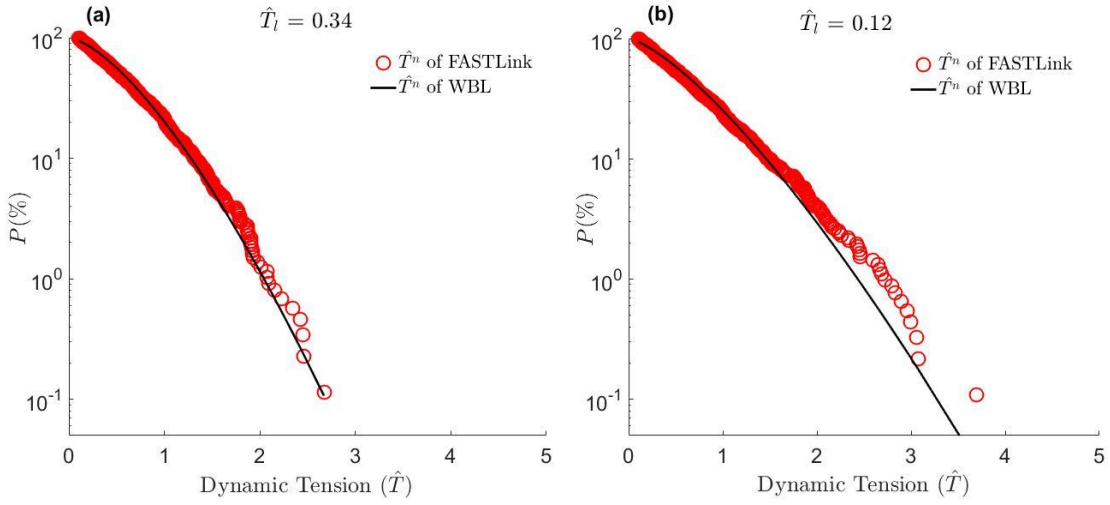

Fig. 7.4 A comparison of exceedance probability curves for $\hat{T}^n$ between FASTlink (hollow circles) and WBL (solid line) for: (a) $\hat{T}_\ell$ = 0.34, and (b) $\hat{T}_\ell$ = 0.12

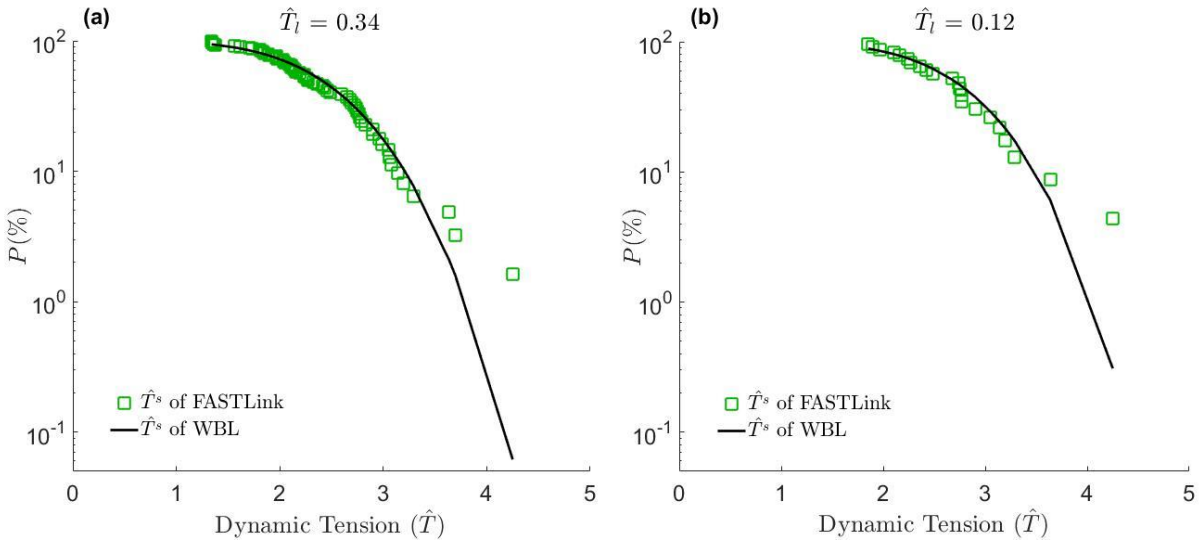

Fig. 7.5 A comparison of exceedance probability curves for $\hat{T}^s$ between FASTlink (hollow circles) and WBL (solid line) for: (a) $\hat{T}_\ell$ = 0.34, and (b) $\hat{T}_\ell$ = 0.12

In this study, the effect of snap load criteria on the tension maxima analysis is performed. This research argues that the bilinear behavior of catenary mooring lines may be expected when snap conditions occur. The values of stiffness are different on either side of a critical point (X_{cr}). In light of the results in Chapter 2 when the line elongation increases from a value smaller than the critical point (X_{cr}) to a value larger than X_{cr}, the dynamic line tension has a strong nonlinear behavior, which can increase the possibility of snap loads. Thus, the critical tension ($\hat{T}_{cr}$) may play an important role in the study of snap loads. Thus, this study proposed a snap load criterion which is defined as $\hat{T}_\ell = 0.1\hat{T}_{cr}$. By applying the proposed criteria to the FASTLink results, the characteristics of snap loads are different to those using DNV's criteria.

For $\hat{T}_\ell$ = 0.34, there appears to be a strong correlation between the point where $\hat{T}$ transitions to a different slope and the point where $\hat{T}^n$ stops changing when compared to $\hat{T}_\ell$ = 0.12 (see Fig.7.3). Table 6.3 shows that the transition tension ($\hat{T}_{tr}$) of Case 1 of FASTLink equals 2.62. This value is very close to the tension range where $\hat{T}^n$ stops changing under

$\hat{T}_\ell$ = 0.34. Since the $\hat{T}_{tr}$ is defined by the maximum dynamic tension value for non-snap tension distribution, for $\hat{T}_\ell$ = 0.13, one may consider the $\hat{T}_{tr}$ value equal to 3.7, where the exceedance probability of $\hat{T}^n$ stops changing (Fig. 3.7). Fig. 7.6 shows the CWD model comparison between $\hat{T}_{tr} = 3.7$ and $\hat{T}_{tr} = 2.62$. It is obvious that, for $\hat{T}_{tr} = 3.7$ the dynamic tension is not well described by the CWD model for larger tension ranges. Moreover, the exceedance probability of the maximum tension value is underestimated by 45%. Table 7.3 shows the parameters of the CWD model for $\hat{T}_{tr} = 3.7$ and $\hat{T}_{tr} = 2.62$. The values of $\hat{T}_1$ and β_1 are the same, because 94% of the $\hat{T}$ data has a value smaller than 2. CWD models in both plot (a) and (b) of Fig. 7.6 fit very well for tension values smaller than 2. Although the values of $\hat{T}_2$ and β_2 for $\hat{T}_{tr} = 3.7$ are very close to $\hat{T}_{tr} = 2.62$, the overestimation of the transition tension results in underpredicting the maximum tension value.

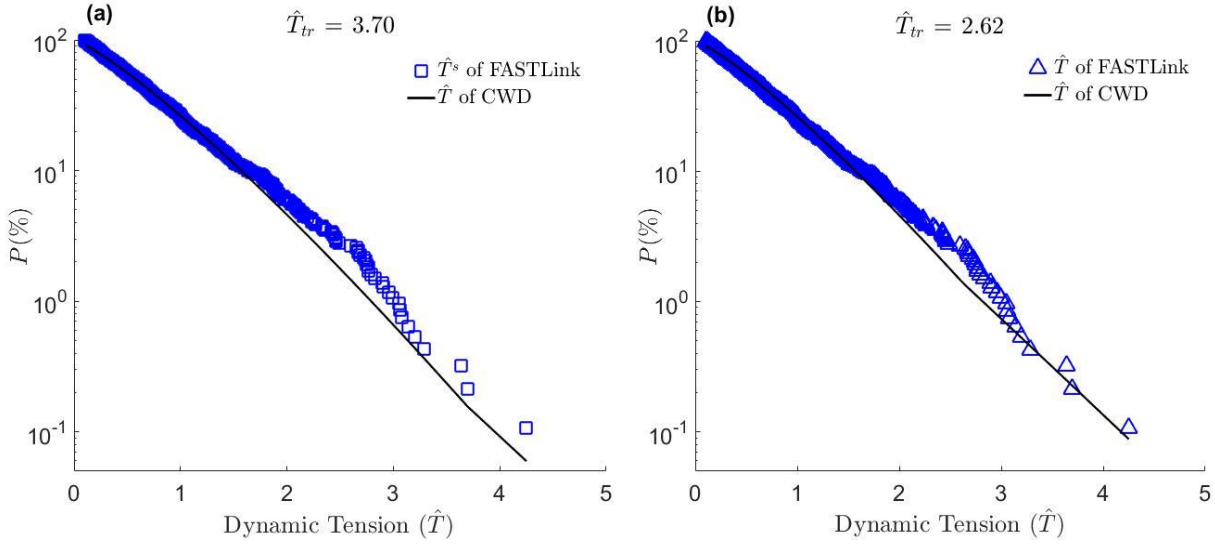

Fig. 7.6 A comparison of exceedance probability curves for $\hat{T}$ between FASTlink (hollow circles) and CWD (solid line) for: (a) $\hat{T}_{tr}$ = 3.70, and (b) $\hat{T}_{tr}$ = 2.62

Table 7.3 The shape parameters ($\boldsymbol{\beta_1}$; $\boldsymbol{\beta_2}$) and scale parameters ($\boldsymbol{\hat{T}_1}$; $\boldsymbol{\hat{T}_2}$) for the CWD for $\boldsymbol{\hat{T}_{tr}}$ = 3.70 and $\boldsymbol{\hat{T}_{tr}}$ = 2.62

$\hat{T}_{tr}$	$\hat{T}_1$	β_1	$\hat{T}_2$	β_2
3.70	0.786	1.205	0.568	0.996
2.62	0.786	1.205	0.642	1.032

For FASTLink, the exceedance probability distribution of $\hat{T}$ has smaller right tail probability levels compared to that for test data. The maximum snap loads predicted by the FASTLink model are 23.82% (V_w = 21m/s) – 26.19% (V_w = 0m/s) lower than that of test data. The dynamic tension PSDs predicted by the FASTLink model are 43% (V_w = 21m/s) – 50% (V_w = 0m/s) lower than the test data in the wave frequency range. This may occur because the FASTLink model: 1) underestimates the surge and pitch motion at low frequency ranges, 2) uses a different drag coefficient, 3) has a different mooring system, and 4) has limitations on dynamic modelling.

The surge and pitch PSDs predicted by FASTLink model are respectively 27% (V_w = 21m/s) – 47%% (V_w = 0m/s) and 73% (V_w = 0m/s) – 89%% (V_w = 21m/s) lower than test data at low frequency ranges. This may be due to second-order hydrodynamic effects not being captured in the numerical model. Moreover, the pitch motions are strongly affected by the turbine aerodynamics with uncharacterized system damping, and hence simulation results often show discrepancies. The drift surge motions are found to be an important factor in the dynamic tension. Thus, underestimation of surge drift motion can result in underpredicting the dynamic tension. Moreover, a higher drag coefficient of the mooring

line can be used in the FASTLink model which could also lead to the underestimation of dynamic tension.

For the DeepCWind tests, there is a small spring attached to the anchor to obtain the correct overall axial stiffness. Thus, the mooring line was composed out of the stud-less chain with a small spring, which is very similar to the bilinear stiffness cable model studied in Chapter 2. In Chapter 2, two springs with constant K_{c1} (top) and K_{c2} (bottom) connect in series supporting the payload, where K_{c1} is 14 times larger than K_{c2}. This model was designed to assure that snap loads could be seen. Regarding the results shown in Chapter 2, significant nonlinear dynamic tension was observed. Moreover, the bilinear stiffness cable system lead to higher dynamic tension ranges and a higher occurrence of snap loads. Also, the model-scale chains behave differently from the full-scale chain. Thus, the mooring system of the tests can result in higher tension ranges when compared to the mooring system of FASTLink model. This indicates that for a full-scale FOWT, the snap load level can be smaller than the test data. However, further study is required to better understand the snap load characteristics of FOWT mooring systems.

For extreme load analysis, it is important to separate the steady-state and transient-state responses. In addition to snap loads, the extreme loads on marine structures also include ringing and springing loads which are resulted from nonlinear wave load impulse. The wave impulse can delay and amplify the ringing responses as well as decrease fatigue life. The delay and amplification are respectively dependent on the ratio of the load period and the natural period and system damping [91]. In Chapter 2, the study found that the maximum snap loads also relate to forced periods and hydrodynamic drag force, which have similar finding as the study of ringing loads on marine structures.

To estimate the maximum tension of a FOWT mooring system during a 3.5-hr operation, one can separate the snap events and regular cyclic tension from the tension time history using snap load criteria. It is expected to have close agreement between experimental and theoretical values for steady tensions. A further analysis method for the snap load contribution is needed to provide an additional reference for investigating the infrequent spike-induced tensions on a FOWT mooring system.

7.3 Future Work

A snap load is defined as a spike in tension as a mooring line re-engages immediately following a slack condition, typically of very short duration. However, the duration from slack to snap varies for different mooring systems. The features that might affect the slack to snap duration include the mooring line stiffness, materials, drag coefficient, wet weight, line length and environmental conditions. The definition of the duration of a snap load is needed. Moreover, DNV suggests that a snap condition is set to occur when the force exceeds 90% of the static load. Thus, a slack condition is defined as the line tension becoming zero or smaller than 10% of the static load. However, this criterion is defined for a crane wire which is a vertical cable system. The suitable criteria for a catenary mooring system are still unknown. It is possible to see the slack condition in part of a catenary mooring line with the rest of the line still having relatively high tension. The formation of snap events is important to investigate by experimental tests or numerical modelling. The work described previously can help the understanding of snap load criteria.

The preceding discussion of CWD models is based on limited test data from seven 100-year storm conditions. Many more numerical simulations are required to further evaluate

the proposed CWD model for predicting long-term extreme values of a mooring line tension in a FOWT. Since the DNV criteria suggest evaluation of a 50-year value of the line tension for ULS design, a reliability analysis on mooring line tensions using a 50-year environmental contour would be interesting to consider in future work.

REFERENCES

[1] Bailey H, Brookes KL, Thompson PM. Assessing Environmental Impacts of Offshore Wind Farms: Lessons Learned and Recommendations for the Future. Aquatic Biosystems. 2014;10:8.

[2] Kimball RW, Goupee AJ, Coulling AJ, Dagher HJ. Model Test Comparisons of TLP, Spar-Buoy and Semisubmersible Floating Offshore Wind Turbine Systems. Proceedings SNAME Annual Meeting. 2012.

[3] Koo B, Goupee AJ, Lambrakos K, Kimball RW. Model Tests for a Floating Windturbine on Three Different Floaters. ASME 2012 31st International Conference on Ocean, Offshore and Arctic Engineering. Rio de Janeiro, Brazil. 2012. p. 455-65.

[4] Martin HR, Kimball RW, Viselli AM, Goupee AJ. Methodology for Wind/Wave Basin Testing of Floating Offshore Wind Turbines. Journal of Offshore Mechanics and Arctic Engineering. 2014;136:021902.

[5] Netherlands MRI. Deepcwind Floating Wind Turbine Model Tests Final Text Report. 2011.

[6] Goupee AJ, Koo BJ, Kimball RW, Lambrakos KF, Dagher HJ. Experimental Comparison of Three Floating Wind Turbine Concepts. Journal of Offshore Mechanics and Arctic Engineering. 2014;136:021903.

[7] DNV. Modeling and Analysis of Marine Operations. Recommended Practice DNV-RP-H103. Hovik, Norway: DET NORSKE VERITAS; 2011.

[8] Musial W, Butterfield S, Boone A. Feasibility of Floating Platform Systems for Wind Turbines. 23rd ASME Wind Energy Symposium. Reno, Nevada 2004.

[9] Hsu W-T, Thiagarajan KP, MacNicoll M, Akers R. Prediction of Extreme Tensions in Mooring Lines of a Floating Offshore Wind Turbine in a 100-Year Storm. Proceedings of the ASME 2015 34th International Conference on Ocean, Offshore and Arctic Engineering. St. John's, NL, Canada: ASME; 2015.

[10] Liu FC. Snap Loads and Bending Fatigue in Diving Bell Handling Systems. Offshore Technology Conference. Houston,TX. 1981.

[11] Niedzwecki JM, Thampi SK. Snap Loading of Marine Cable Systems. Applied Ocean Research. 1991;13:210-9.

[12] Salancy AM, Bea RG. Offshore Single Point Mooring Systems for Import of Hazardous Liquid Cargoes Offshore Southern California. International Society of Offshore and Polar Engineers. Honolulu, USA: International Society of Offshore and Polar Engineers; 1997.

[13] Shah AA, Umar A, Siddiqui NA. A Methodology for Assessing the Reliability of Taut and Slack Mooring Systems against Instability. Ocean Engineering. 2005;32:1216-34.

[14] Gobat JI, Grosenbaugh MA. Dynamics in the Touchdown Region of Catenary Moorings. The Eleventh (2001) International Offshore and Polar Engineering Conference. Stavanger, Norway2001. p. 273-81.

[15] Kvitrud A. Lessons Learned from Norwegian Mooring Line Failures 2010–2013. ASME 2014 33rd International Conference on Ocean, Offshore and Arctic Engineering. San Francisco, California, USA2014.

[16] JTSB. Marine Accident Investigation Report. Japan Transport Safety Board; 2011.

[17] Final Accident Report PK-AXC. The Ministry of Transport of the Republic of Indonesia. 2015.

[18] Burgess JJ. Natural Modes and Impulsive Motions of a Horizontal Sallow Sag Cable: Ocean Engineering; 1985.

[19] Umar A, Datta TK, Ahmad S. Complex Dynamics of Slack Mooring System under Wave and Wind Excitations. The Open Oceanography Journal. 2010;4:9-31.

[20] Chen L, Basu B. A Numerical Study on in-Plane Wave Propagation in Mooring Cables. Procedia Engineering. 2017;173:934-9.

[21] Gerber M, Engelbrecht L. The Bilinear Oscillator: The Response of an Articulated Mooring Tower Driven by Irregular Seas. Ocean Engineering. 1993;20:113-33.

[22] Brommundt M, Krause L, Merz K, Muskulus M. Mooring System Optimization for Floating Wind Turbines Using Frequency Domain Analysis. Energy Procedia. 2012;24:289-96.

[23] Benassai G, Campanile A, Piscopo V, Scamardella A. Ultimate and Accidental Limit State Design for Mooring Systems of Floating Offshore Wind Turbines. Ocean Engineering. 2014;92:64-74.

[24] Fontana CM, Arwade SR, DeGroot DJ, Hallowell ST, Aubeny C, Landon M, Myers A, Hajjar J, Ozmultu S. Multiline Anchors for the OC4 Semisubmersible Floating System. International Society of Offshore and Polar Engineers.

[25] Hall M. Moordyn User's Guide. University of Maine; 2015.

[26] Cordle AJ, JM. State of the Art in Floating Wind Turbine Design Tools. Proceedings of the 21st international offshore and polar engineering conference. Maui, HI2011.

[27] Kim H, Choung J, Jeon G-Y. Design of Mooring Lines of Floating Offshore Wind Turbine in Jeju Offshore Area. 2014:V09ATA042.

[28] Hong S, Lee I, Park SH, Lee C, Chun H-H, Lim HC. An Experimental Study of the Effect of Mooring Systems on the Dynamics of a Spar Buoy-Type Floating Offshore Wind Turbine. International Journal of Naval Architecture and Ocean Engineering. 2015;7:559-79.

[29] Nihei Y, Matsuda Y, Kitamura S, Takaiwa K, Kanda N. Research and Development About the Mechanisms of a Single Point Mooring System for Offshore Wind Turbines. Ocean Engineering. 2018;147:431-46.

[30] Bae YH, Kim MH, Kim HC. Performance Changes of a Floating Offshore Wind Turbine with Broken Mooring Line. Renewable Energy. 2017;101:364-75.

[31] Masciola M, Robertson A, Jonkman J, Coulling A, Goupee A. Assessment of the Importance of Mooring Dynamics on the Global Response of the Deepcwind Floating Semisubmersible Offshore Wind Turbine. The Twenty-third (2013) International Offshore and Polar Engineering. Anchorage, Alaska, USA2013. p. 359-68.

[32] Goeller JE, Laura PA. Analytical and Experimental Study of the Dynamic Response of Segmented Cable Systems. Journal of Sound and Vibration. 1971;18:311-24.

[33] Strengehagen J, Gran S. Supply Boat Motion, Dynamic Response and Fatigue of Offshore Cranes. Offshore Technology Conference. Houston, TX, USA. 1980.

[34] Swenson RC. A Snap-Back Restrained Kevlar Mooring Line. Offshore Technology Conference. Houston, TX, UAS. 1983.

[35] Huang S, Vassalos D. A Numerical Method for Predicting Snap Loading of Marine Cables. Applied Ocean Research. 1993;15:235-42.

[36] Han JS, Son Y-J, Choi HS, Rho JB. The Transient Behavior of Mooring Systems in Line-Broken Condition. The Twenty-first (2011) International Offshore and Polar Engineering Conference. Maui, Hawaii, USA: International Society of Offshore and Polar Engineers; 2011.

[37] Hann M. Statics and Dynamics of Multi-Cable Systems for Submersibles. Marine Structures. 1995;8:555-83.

[38] Cozijn IJL, Bunnik ITHJ. Omae2004-51370. The 23rd International Conference on Offshore Mechanics and Arctic Engineering. Vancouver, Canada2004. p. 1-11.

[39] Zhu K-q, Zheng D-c, Cai Y, Yu C-l, Wang R, Liu Y-l, Zhang F. Nonlinear Hydrodynamic Response of Marine Cable -Body System under Random Dynamic Excitations. Journal of Hydrodynamics, Ser B. 2009;21:851-5.

[40] Zhu K-q, Zhu H-y, Zhang Y-s, Gao J, Miao G-p. A Multi-Body Space-Coupled Motion Simulation for a Deep-Sea Tethered Remotely Operated Vehicle. Journal of Hydrodynamics, Ser B. 2008;20:210-5.

[41] Lu W, Ge F, Wang L, Wu X, Hong Y. On the Slack Phenomena and Snap Force in Tethers of Submerged Floating Tunnels under Wave Conditions. Marine Structures. 2011;24:358-76.

[42] Suhara T, Koterayama W, Tasai F, Hiyama H, Sao K, Watanabe K. Dynamic Behavior and Tension of Oscillating Mooring Chain. Offshore Technology Conference. Houston, TX, USA: Offshore Technology Conference; 1981.

[43] Budiman E, Wahyuni E, Raka IGP, Suswanto B. Experiments on Snap Force in Tethers of Submerged Floating Tunnel Model under Hydrodynamic Loads in Case of Shallow Water. ARPN Journal of Engineering and Applied Sciences. 2016;11:14383-90.

[44] Guo S, Chen W, Fu Y. Non-Linearly Restoring Performance of SFT's Catenary Mooring-Lines under Consideration of Its Dynamic Behaviors. Procedia Engineering. 2016;166:202-11.

[45] Papazoglou VJ, Mavrakos SA, Triantafyllou MS. Non-Linear Cable Response and Model Testing in Water. Journal of Sound and Vibration. 1990;140:103-15.

[46] Van Den Boom HJJ. Dynamic Behaviour of Mooring Lines. Proceedings of Behaviour of Offshore Structures. Delft: Elsevier Science Publishers B.V.; 1985. p. 359-68.

[47] Zhang S-x, Tang Y-g, Liu X-j. Experimental Investigation of Nonlinear Dynamic Tension in Mooring Lines. Journal of Marine Science and Technology. 2012;17:181-6.

[48] Gottlieb O, Yim SCS. Nonlinear Oscillations, Bifurcations and Chaos in a Multi-Point Mooring System with a Geometric Nonlinearity. Applied Ocean Research. 1992;14:241-57.

[49] Palm J, Eskilsson C, Bergdahl L. An Hp -Adaptive Discontinuous Galerkin Method for Modelling Snap Loads in Mooring Cables. Ocean Engineering. 2017;144:266-76.

[50] DNV. Rules for Planning and Execution of Marine Operations. Hovik, Norway: Det Norske Veritas; 1996.

[51] Goeller J, A. Laura P. A Theoretical and Experimental Investigation of Impact Loads in Stranded Steel Cables During Longitudinal Excitation. 1970.

[52] Thiagarajan KP, Troesch AW. Hydrodynamic Heave Damping Estimation and Scaling for Tension Leg Platforms. Journal of Offshore Mechanics and Arctic Engineering. 1994;116:70.

[53] Goupee AJ, Fowler MJ, Kimball RW, Helder J, de Ridder E-J. Additional Wind/Wave Basin Testing of the Deepcwind Semi-Submersible with a Performance-Matched Wind Turbine. 2014:V09BTA026.

[54] Netherlands MRI. Umaine – Deepcwind/OC4 Semi Floating Wind Turbine Repeat Tests. 2013.

[55] Hsu W-T, Thiagarajan KP, Hall M, MacNicoll M, Akers R. Snap Loads on Mooring Lines of a Floating Offshore Wind Turbine Structure. ASME 2014 33rd International Conference on Ocean, Offshore and Arctic Engineering. San Francisco, California, USA. 2014. p. V09ATA036.

[56] DNV. Position Mooring. Offshore Standard DNV-OS-E301. Hovik, Norway. 2008.

[57] Driscoll FR, Buckham B, Nahon M. Numerical Optimization of a Cage-Mounted Passive Heave Compensation System. Proceedings of the OCEANS 2000 MTS/IEEE Conference and Exhibition IEEE2000. p. 1121-7.

[58] Luxmoore JF, Grey S, Newsam D, Johanning L. Analytical Performance Assessment of a Novel Active Mooring System for Load Reduction in Marine Energy Converters. Ocean Engineering. 2016;124:215-25.

[59] Jeon SH, Cho YU, Seo MW, Cho JR, Jeong WB. Dynamic Response of Floating Substructure of Spar-Type Offshore Wind Turbine with Catenary Mooring Cables. Ocean Engineering. 2013;72:356-64.

[60] Thiagarajan KP, Urbina R, Hsu W. Nonlinear Pitch Decay Motion of a Floating Offshore Wind Turbine Structure. Journal of Offshore Mechanics and Arctic Engineering. 2014;137:011902.

[61] Carmona R. Heavy Tail Distributions. Statistical Analysis of Financial Data in R: Springer New York; 2014. p. 69-120.

[62] Shipping AB. Guide for Slamming Loads and Strength Assessment for Vessels. 2011.

[63] Razola M, Olausson K, Garme K, Rosén A. On High-Speed Craft Acceleration Statistics. Ocean Engineering. 2016;114:115-33.

[64] Onorato M, Proment D, Toffolo A. Freak Waves in Crossing Seas. The European Physical Journal Special Topics. 2010;185:45-55.

[65] Petrova P, Cherneva Z, Guedes Soares C. Distribution of Crest Heights in Sea States with Abnormal Waves. Applied Ocean Research. 2006;28:235-45.

[66] Onorato M, Osborne AR, Serio M, Bertone S. Freak Waves in Random Oceanic Sea States. Physical Review Letters. 2001;86:5831-34.

[67] Rinne H. The Weibull Distribution: A Handbook. Boca Raton: CRC Press; 2009.

[68] Abernethy RB. The New Weibull Handbook, 5th Ed. North Palm Beach, Florida. 2006.

[69] Battjes JA, Groenendijk HW. Wave Height Distributions on Shallow Foreshores. Coastal Engineering. 2000;40:161-82.

[70] DNV. Design of Floating Wind Turbine Structures. DNV-OS-J103. Hovik, Norway: Det Norske Veritas; 2013.

[71] Kwan CT. Design Practice for Mooring of Floating Production Systems. Marine Technology. 1991;28:30-8.

[72] Larsen K, Sandvik PC. Efficient Methods for the Calculation of Dynamic Mooring Line Tension. International Society of Offshore and Polar Engineers. Trondheim, Norway. 1990.

[73] McClure AC. Barge Motion Predictions. Marine Technology. 1983;20:366-9.

[74] Lu YJ, Chen Y-N, Tan P-L, Bai Y. Prediction of Most Probable Extreme Values for Jackup Dynamic Analysis. Marine Structures. 2002;15:15-34.

[75] Nahmias S, Olsen TL. Production and Operations Analysis: Waveland Press, Inc.; 2015.

[76] Kimball R, Goupee AJ, Fowler MJ, de Ridder E-J, Helder J. Wind/Wave Basin Verification of a Performance-Matched Scale-Model Wind Turbine on a Floating Offshore Wind Turbine Platform. 2014:V09BTA025.

[77] van Sluihs MF, Blok JJ. The Dynamic Behavior of Mooring Lines. Offshore Technology Conference. Houston, TX. 1977.

[78] Rhinoceros 5 User's Guide. In: Associates RM, editor. 2014.

[79] AQWA User Manual. In: ANSYS I, editor. 2012.

[80] Lopez-Pavon C, Watai R, Ruggeri F, N. Simos A, Souto-Iglesias A. Influence of Wave Induced Second-Order Forces in Semisubmersible Fowt Mooring Design. 2013.

[81] Coulling AJ, Goupee AJ, Robertson AN, Jonkman JM, Dagher HJ. Validation of a Fast Semi-Submersible Floating Wind Turbine Numerical Model with Deepcwind Test Data. Journal of Renewable and Sustainable Energy. 2013;5:023116.

[82] LTD O. Orcaflex User Manual Version 9.7a. Daltongate, Columbia, LA12 7AJ, UK. 2013.

[83] Masciola M, Robertson A, Jonkman J, Driscoll FR. Investigation of a FAST-Orcaflex Coupling Module for Integrating Turbine and Mooring Dynamics of Offshore Floating Wind Turbines. International Conference on Offshore Wind Energy and Ocean Energy. Beijing, China. 2011. p. NREL/CP-5000-52896.

[84] Viselli AM, Goupee AJ, Dagher HJ. Model Test of a 1:8-Scale Floating Wind Turbine Offshore in the Gulf of Maine 1. Journal of Offshore Mechanics and Arctic Engineering. 2015;137:041901.

[85] Jonkman J. Dynamics Modeling and Loads Analysis of an Offshore Floating Wind Turbine. National Renewable Energy Laboratory; 2007.

[86] ABS. Floating Wind Turbines. Bsee Technology Assessment and Research Program. 2012.

[87] Robertson A, M. Jonkman J. Loads Analysis of Several Offshore Floating Wind Turbine Concepts. 2011.

[88] Jonkman JM. Dynamics of Offshore Floating Wind Turbines-Model Development and Verification. Wind Energy. 2009;12:459-92.

[89] Simonoff JS. Smoothing Methods in Statistics. New York: Springer Verlag; 1996.

[90] Faltinsen OM. Sea Loads on Ships and Offshore Structures. United Kingdom: The Press Syndicate of the University of Cambridge; 1998.

[91] Kappos AJ. Dynamic Loading and Design of Structures. New York, NY: Spon Press; 2002.

APPENDIX A

EXPERIMENTS OF VERTICAL HANGING CABLE MODELS

This is a report of the final design of the nonlinear cable model conducted in Tainan Hydraulic Laboratory at National Cheng Kung University during the summer of 2017. This report will cover the procedure of the experiments.

The properties of the prototype and the 1:2 scale vertical hanging cable model is shown in Table A.1. The values of prototype are regarding the paper of Geoller and Laura [51]. The authors conducted the experiments in the water tank with of 30.48m long, 22.86m deep, and 10.7m wide. Because of the limitation of dimension of the water tank, the cable length, diameter and weight of the cable are ignored for the 1:2 scale model tests. The cable was replaced with the spring system with the 1:2 scale stiffness. Table A.2 shows the test matrix of the experimental study of the vertical hanging cable system. The forced amplitude ranged from 0.01 – 0.04m, forced frequency ranged from 0.5 – 2s, weight of the payload ranged from 6.13 – 18.95N. A total of 105 tests were done. Fig. A.1 and A.2 shows the dimensions and the model of the payloads. There were three payload models were manufactured. All of them have the same diameter and height. The densities of the payload model were varied. Fig. A.3 shows the bilinear spring system, which has series springs. Two springs with constants K_{c1} (top) and K_{c2} (bottom) connect in series supporting the payload, where K_{c1} is 14 times larger than K_{c2}. $K_{c1} = 1765.8$N/m and $K_{c2} = 126.55$N/m. The series springs are designed with bilinear stiffness, where the stiffness is equal to $\frac{1}{K_{c1}^{-1}+K_{c2}^{-1}}$ for elongation smaller than x_{cr}, and is equal to K_{c1} when the elongation of the series springs is greater than x_{cr} (see Fig. A3). There is a stopper system connected to the

two ends of the soft spring, which allows the soft spring to have the maximum elongation of x_{cr}.

This vertical hanging cable model includes the series springs and a payload. The top of the model was attached to one side of the tension sensor, and the other side of the load cell is connected to a fish wire, which is looped around two pulleys and attached to the wave maker. With the wavemaker on the left side of the pulleys, it is possible to create oscillation motion acting on the top side of the model.

Table. A.1 Model Dimension

Payload	Model	Prototype
Diameter (m)	0.1	0.2
dry Weight (N)	15.03	120.25
Cable		
Length (m)	-	21.34
Diameter (m)	-	0.20
weight per unit length (Kg/m)	-	0.11
wet weight (Kg/m)	-	0.07
Stiffness (kg/m)	1773.94	7094.88
Forced Amplitude		
forced period (s)	0.5893	0.8333
Amplitude (m)	0.0381	0.0762

Table. A.2 Test Matrix

$\boldsymbol{A}$	0.01 – 0.04m
$\boldsymbol{t_p}$	0.5 – 2s
$\boldsymbol{W_{pl}}$	6.13 – 18.95N

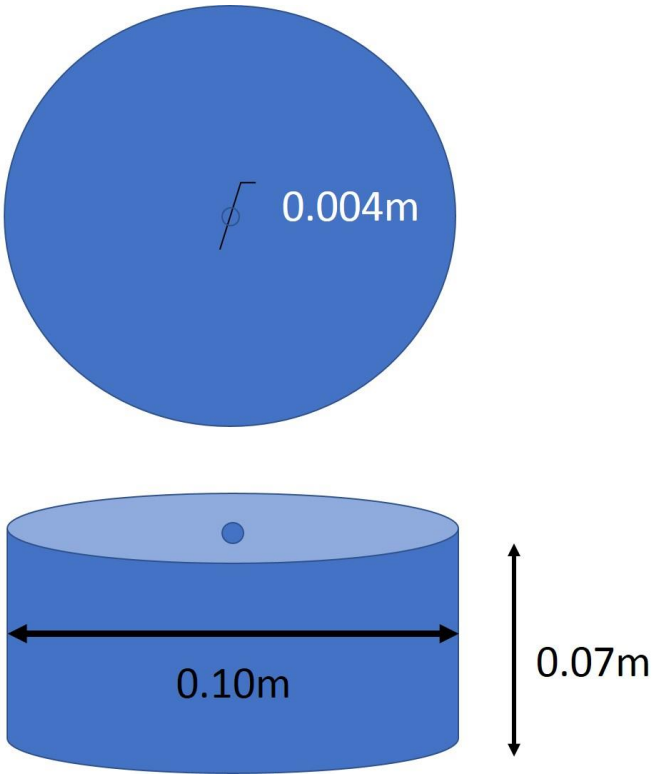

Fig. A.1 Payload model layout

Fig. A.2 Payload model (left: 6.13N, middle: 14.25N, right: 19.95N)

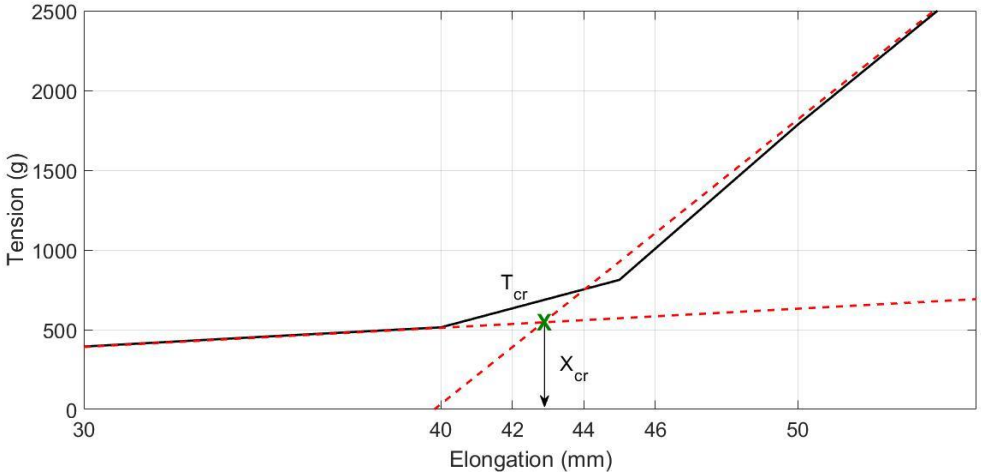

Fig. A.3 Bilinear stiffness of scale model

Model is set up in a wave flume which is 20m long, 0.5m wide and 0.8m deep. The specified stroke is generated using a programmable PC-controlled piston-type wave maker at one end of the flume. The DAQ is a Microsoft NT-based Multi Nodes Data Acquisition System (MNDAS), which was developed by THL. A load sensor is connected to the 2-spring system on the top. The load sensor is LT6 type. Fig. A.4 and A.5 show the load sensor and the configuration of the load sensor. The maximum load is 49N.

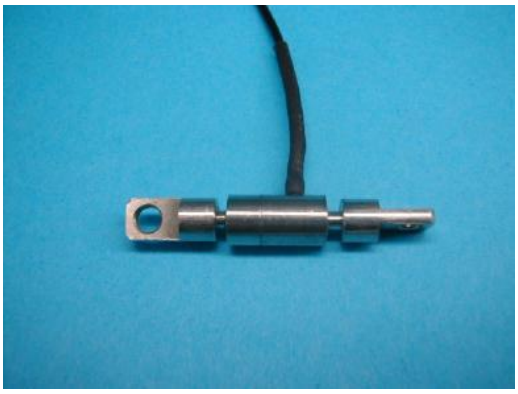

Fig. A.4 Load sensor

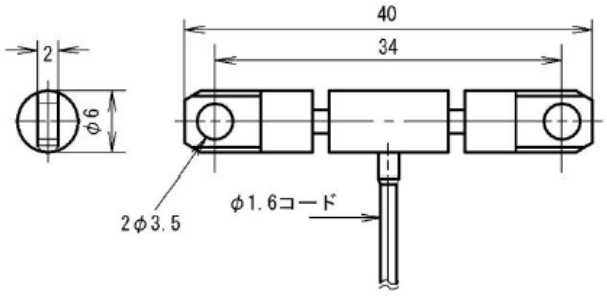

Fig. A.5 Configuration of the load sensor

To compare the results of scale model with the prototype model, Table A.3 shows the maximum tension under the same forced oscillation. The scale model results are up-scaled and compared with the prototype. Fig. A. 6 and A.7 respectively show the tension time history of scale model and prototype under the same oscillation condition. For scale model, the weight of payload is 5.17% lower than the prototype, and the maximum tension is 40.13% lower than the prototype. This is because the bilinear stiffness of scale model differs from the one of prototype. For prototype, the stiffness equals to zero while the line elongation is smaller than zero. For scale model, the stiffness equals to 126.55N/m while the line elongation is smaller than x_{cr}. Also, the weight of payload is smaller than the one of prototype.

Table. A.3 Comparison of the parameters for the scale model and prototype

	A (m)	t_p(s)	W_{pl} (N)	Maximum tension (N)
Scale model	0.08	0.85	114.03	400.00
Prototype	0.08	0.83	120.25	668.06

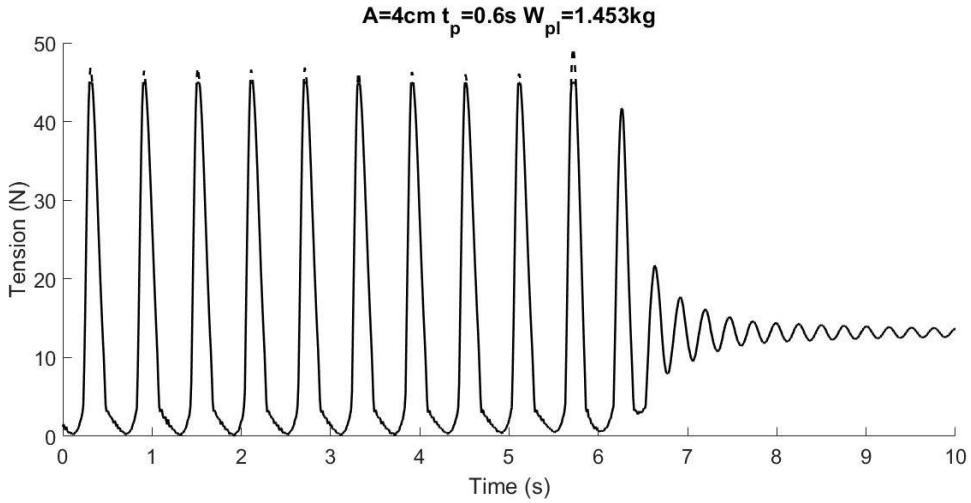

Fig. A.6 Tension time history of scale model result ($A = 0.04$m, $t_p = 0.6$s, W_{pl} =14.25N)

150lb

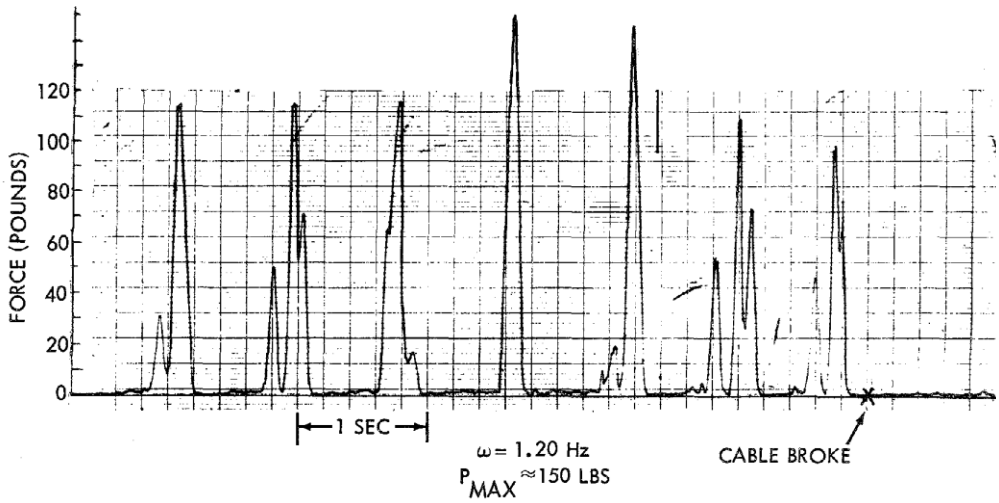

Fig. A.7 Tension time history for prototype ($A = 0.08$m, $t_p = 0.83$s, W_{pl} =120.25N)

APPENDIX B

ANALYSIS OF 3.5HR AND 3HR TEST DATA

The statistical analysis, cycles of non-snap events and snap events and the parameters of composite Weibull distribution for 3.5hr and 3hr (removing the first half hour) test data are compared in this study. SF1 and SF2 are selected in this study. B.1 shows the statistical analysis in platform motions and mooring line tensions for 3.5hr and 3hr test data. B.2 performs the extreme tension analysis and the parameters of the composite Weibull distributions for 3.5hr and 3hr test data.

B.1 Statistical Analysis of 3.5hr and 3hr Test Data for SF

Table B.1 and B.3 respectively show the statistics in wave heights and platform motions for SF1 and SF2. Table B.2 and B.4 respectively show the statistics in mooring line tensions of three lins for SF1 and SF2. For Table B.1–4, the differences of 3.5hr and 3hr test data are smaller than 1.5%.

Table B.1 Comparison of 3.5hr and 3hr test data statistics in wave heights, surge, heave and pitch motions for SF1

	3.5hr Test Data		3hr Test Data		Difference (%)	
	Mean	Root Mean Square	Mean	Root Mean Square	Mean	Root Mean Square
Wave	2.07	2.61	2.08	2.63	1.43	0.76
Surge	-2.35	3.37	-2.38	3.39	1.26	0.59
Heave	-0.08	1.16	-0.08	1.16	0	0
Pitch	0.06	1.11	0.06	1.11	0	0

Table B.2 Comparison of 3.5hr and 3hr test data statistics in mooring line tensions of line 1, 2 and 3 for SF1

		3.5hr Test Data	3hr Test Data	Difference (%)
Line 1	Mean	1256.28	1258.21	0.15
	Root Mean Square	1325.52	1327.35	0.14
	Maximum	5640.23	5640.23	0
	Minimum	31.66	31.66	0
Line 2	Mean	1028.77	1028.43	0.03
	Root Mean Square	1031.67	1031.35	0.03
	Maximum	1378.27	1378.27	0
	Minimum	483.01	483.01	0
Line 3	Mean	1007.75	1007.06	0.07
	Root Mean Square	1010.16	1009.49	0.07
	Maximum	1316.18	1297.18	1.46
	Minimum	523.01	523.01	0

Table B.3 Comparison of 3.5hr and 3hr test data statistics in wave heights, surge, heave and pitch motions for SF2

	3.5hr Test Data		3hr Test Data		Difference (%)	
	Mean	Root Mean Square	Mean	Root Mean Square	Mean	Root Mean Square
Wave	2.03	2.57	2.04	2.58	1.46	0.39
Surge	-10.41	10.63	-10.44	10.66	0.29	0.28
Heave	-0.03	1.11	-0.03	1.11	0	0
Pitch	-3.89	4.05	-3.89	4.06	0	0.25

Table B.4 Comparison of 3.5hr and 3hr test data statistics in mooring line tensions of line 1, 2 and 3 for SF2

		3.5hr Test Data	3hr Test Data	Difference (%)
Line 1	Mean	1938.93	1942.09	0.16
	Root Mean Square	2076.16	2079.26	0.15
	Maximum	7835.23	7835.23	0
	Minimum	33.92	33.92	0
Line 2	Mean	859.64	859.13	0.06
	Root Mean Square	861.30	860.83	0.05
	Maximum	1171.20	1171.20	0
	Minimum	517.14	517.14	0
Line 3	Mean	860.45	859.85	0.07
	Root Mean Square	861.90	861.30	0.07
	Maximum	1316.18	1297.18	1.46
	Minimum	523.01	523.01	0

B.2 Tension Maxima Analysis of 3.5hr and 3hr Test Data for SF

Table B.5 and B.6 respectively summarizes data on $\hat{T}$, $\widehat{T^n}$ and $\widehat{T^s}$ for all the seven cases described in Table 3.8 for the 3.5hr and 3hr test data. For the 3hr test data, the cycles of $\widehat{T^n}$ and $\widehat{T^s}$ are about 13% and 16% lower than the 3.5hr test data, which indicates that several snap events were occurred during the first half hour test for seven cases. Fig. B.1 and B.2 respectively show the exceedance probability curves for $\widehat{T^n}$ and $\widehat{T^s}$ for Case 1 and 7 using 3.5hr and 3hr test data. For 3.5hr test data, the curves in the higher tension ranges are very close to the ones for 3hr test data. Table B.7 shows the comparison of the parameters used for CWD model using 3.5hr and 3hr test data. For 3.5hr test data, all of the parameters are

very close to those for 3hr test data. Therefore, the CWD models for both 3.5hr and 3hr test data are very close.

Table B.5 Normalized tension ranges, number of cycles, and duration for $\hat{T}$, $\widehat{T^n}$ and $\widehat{T^s}$ in seven cases of the 3.5hr test data (SF)

Case	$\hat{T}$		$\widehat{T^n}$			$\widehat{T^s}$			
	Tension range		Number	Tension range		Number	Duration range	Tension range	
	Min	Max	of cycles	Min	Max	of cycles	(sec / cycle)	Min	Max
1	0.09 -	4.83	904	0.09	2.88	21	8.0 - 10.1	1.75	4.83
2	0.06 -	4.50	971	0.06	2.89	37	8.0 - 10.5	1.70	4.50
3	0.06 -	4.27	958	0.06	2.71	38	7.8 - 10.5	1.72	4.27
4	0.05 -	4.04	970	0.05	2.78	30	8.1 - 10.4	1.73	4.04
5	0.06 -	4.43	966	0.06	2.95	38	8.1 - 10.5	1.81	4.43
6	0.08 -	4.65	938	0.08	2.87	30	7.7 - 10.3	1.77	4.65
7	0.07 -	4.55	934	0.07	2.87	25	7.8 – 10.0	1.76	4.55

Table B.6 Normalized tension ranges, number of cycles, and duration for $\hat{T}$, $\widehat{T^n}$ and $\widehat{T^s}$ in seven cases of the 3hr test data (SF)

Case	$\hat{T}$		$\widehat{T^n}$			$\widehat{T^s}$			
	Tension range		Number	Tension range		Number	Duration range	Tension range	
	Min	Max	of cycles	Min	Max	of cycles	(sec / cycle)	Min	Max
1	0.09 -	4.86	786	0.09	2.90	19	8.0 - 10.1	1.76	4.86
2	0.06 -	4.53	844	0.06	2.91	30	8.0 - 10.5	1.71	4.53
3	0.06 -	4.28	836	0.06	2.72	32	7.8 - 10.5	1.73	4.28
4	0.05 -	4.06	848	0.05	2.80	24	8.1 - 10.4	1.74	4.06
5	0.06 -	4.42	845	0.06	2.94	33	8.1 - 10.5	1.81	4.42
6	0.08 -	4.70	818	0.08	2.90	25	7.7 - 10.3	1.79	4.70
7	0.07 -	4.57	816	0.07	2.88	21	7.8 – 10.0	1.76	4.57

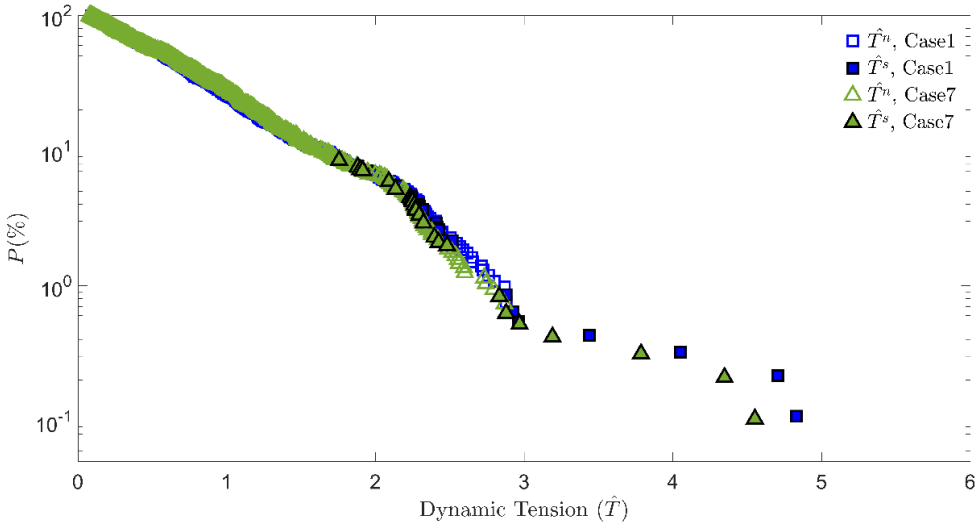

Fig. B.1 A comparison of exceedance probability curves for $\widehat{T^n}$ (hollow markers) and $\widehat{T^s}$ (solid markers) for Case 1 (square) and Case 7 (triangle) using 3.5hr datasets

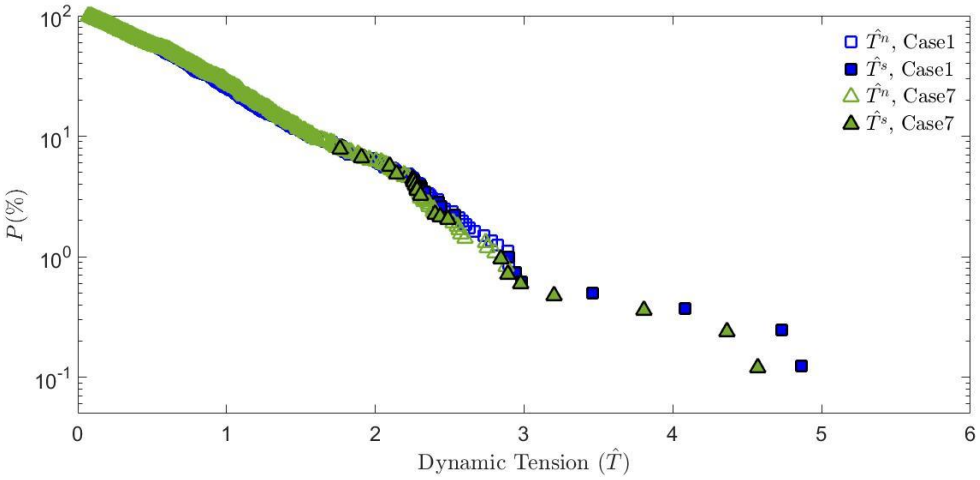

Fig. B.2 A comparison of exceedance probability curves for $\widehat{T^n}$ (hollow markers) and $\widehat{T^s}$ (solid markers) for Case 1 (square) and Case 7 (triangle) using 3hr datasets

Table B.7 The average values for transition tension ($\hat{T}_{tr}$), shape parameters (β_1 ; β_2) and scale parameters ($\hat{T}_1$; $\hat{T}_2$) for the seven cases using 3.5hr and 3hr test data

	$\hat{T}_{tr}$	$\hat{T}_1$	β_1	$\hat{T}_2$	β_2
3.5hr test data	2.81	0.820	1.244	0.360	0.746
3hr test data	2.83	0.821	1.265	0.354	0.752

BIOGRAPHY OF THE AUTHOR

Wei-Ting Hsu was born and grew up in Kaohsiung, Taiwan. She received her B.S in Aeronautics and Astronautics Engineering from National Cheng Kung University, Tainan, Taiwan in 2006. She completed her M.S. in Experimental Fluid Mechanics from National Cheng Kung University, Tainan, Taiwan in 2008. Following two-and-a-half years of research and work experiences on fluid mechanics and heat transfer. She started her doctorate studies in Civil engineering at University of Texas at Austin in September 2011 and transferred to Mechanical engineering at University of Maine at 2012 and graduated with her Ph.D. in December 2017.

Her fields of study are fluid-structure interaction of floating systems, floating structure model test and numerical modeling of floating offshore wind turbine systems. Wei-Ting is a candidate for the Doctor of Philosophy degree in Mechanical Engineering from the University of Maine in December 2017.